Università degli Studi di Padova

Dipartimento di Fisica e Astronomia "Galileo Galilei"

Dottorato di Ricerca in Fisica

Detailed active volume determination of HPGe detectors and its impact on the measurement of the half-life of $2\nu\beta\beta$ decay of ^{76}Ge in the Gerda and LEGEND-200 experiments

Candidata
Valentina Biancacci

Supervisore
Prof. Riccardo Brugnera

Ciclo XXXV

Ai miei genitori

ABSTRACT

An open question still involves the nature of neutrinos: are they their own anti-matter counterpart? The most promising way to test this Majorana nature of neutrinos is by searching for the neutrinoless double beta decay, a hypothetical nuclear process that violates the total lepton number. Among the double beta decay experiments, the GERDA experiment stands out for its ultra-low background and excellent energy resolution. Concluded in November 2019, it demonstrated the outstanding potential of germanium detectors to prepare the next-generation experiment – the tonne-scale LEGEND experiment – able to probe the half-life of the decay up to and beyond 10^{28} yr. The main focus of this dissertation is the determination of the active volume of germanium detectors in GERDA and LEGEND experiments, studying its effects on the measurement of the half-life of the double-beta decay. Gamma spectroscopy setups at the HADES underground laboratory in Belgium are used to characterize the new ICPC detectors. A versatile software framework is developed to automatically determine the active volume with high precision by comparing the data with Monte Carlo simulations, reproducing the overall setup. The GERDA official values for BEGe detectors are affected by the systematic of the unknown growth of the full charge collection depth at room temperature. A re-characterization of nine BEGes has been performed to obtain more reliable estimations. The data collected by GERDA Phase II$^+$ offers a unique opportunity to estimate the active volume *in-situ*. A statistical analysis of the spectrum of low energy events, where the ^{39}Ar decay is the main contribution, has been performed by using Monte Carlo simulations to extract the size of the dead layer and the transition region for each of the active detectors. A new estimation of the half-life of the double beta decay $T^{2\nu}_{1/2} = (2.022 \pm 0.041) \cdot 10^{21}$ yr is extracted using the accurate active volume determination presented in this work. This experimental result is the most precise and reliable estimation of $T^{2\nu}_{1/2}$ ever reported with ^{76}Ge.

SOMMARIO

Una delle domande ancora senza risposta sui neutrini riguarda la loro natura: sono uguali alle loro corrispettive antiparticelle? Il modo più promettente per scoprire questa natura di Majorana dei neutrini è la ricerca del doppio decadimento beta senza neutrini, un processo nucleare ipotetico che viola il numero leptonico totale. Tra i vari esperimenti dedicati al doppio decadimento beta, l'esperimento GERDA si distingue per il background ultra-basso e l'eccellente risoluzione energetica. Conclusosi nel novembre del 2019, esso ha dimostrato l'incredibile potenziale dei rivelatori al germanio. La stessa tecnologia sarà alla base del nuovo progetto LEGEND che ha come obiettivo il miglioramento di un fattore 100 il limite sul tempo di dimezzamento del decadimento doppio beta senza neutrini del ^{76}Ge ($T^{2\nu}_{1/2} > 10^{28}$ anni).

L'obiettivo principale di questo lavoro di tesi è la determinazione del volume attivo nei rivelatori al germanio usati negli esperimenti di GERDA e LEGEND, studiando i suoi effetti sulla misura della vita media del doppio decadimento beta. Per caratterizzare i nuovi rivelatori ICPC per l'esperimento LEGEND, sono state usate diverse installazioni di spettroscopia gamma allestite appositamente nel laboratorio sotterraneo HADES in Belgio. É stato sviluppato un software versatile per determinare automaticamente con alta precisione il volume attivo andando a confrontare i dati e le simulazioni Monte Carlo, che riproducono l'intera configurazione. I valori ufficiali di GERDA per i rivelatori BEGe sono affetti da sistematiche sulla crescita sconosciuta della *full charge collection depth* a temperatura ambiente. Per ottenere delle stime più affidabili, nove rivelatori BEGe sono stati caratterizzati di nuovo. I dati raccolti da GERDA in Fase II$^+$ offrono una opportunità unica per stimare *in-situ* il volume attivo. É stata eseguita un'analisi statistica dello spettro degli eventi a bassa energia, dove il maggior contributo è dato dal decadimento del ^{39}Ar, utilizzando simulazioni Monte Carlo per estrarre le dimensioni dello strato morto e della regione di transizione per ciascun rivelatore attivo. La nuova stima della vita media del doppio decadimento beta di $(2.022 \pm 0.041) \cdot 10^{21}$ anni è stata estratta dalle determinazioni accurate di volume attivo presentate in questa tesi. Questo risultato sperimentale è la stima più precisa e affidabile della vita media del doppio decadimento beta mai riportata con il ^{76}Ge.

CONTENTS

INTRODUCTION

Neutrinos have always fascinated since their discovery, and scientists worldwide are attracted by these elusive elementary particles, aspiring to reveal all their secrets. Because of its extremely low cross-section, the neutrino is the least understood elementary particle in the Standard Model. Studying the properties and interactions of neutrinos has been one of the most exciting purposes in particle physics and will be one of the main focuses of fundamental research for many years to come. From the discovery of neutrino oscillations, which establish a tiny but non-zero neutrino mass, a window to new physics beyond the Standard Model has been opened. Then, the investigation of neutrinos offers an exciting field to study, as it provides a way to test the most fundamental physics laws, reaching implications also in other fields, for instance, in cosmology. After its discovery in 1956, the absolute neutrino mass is still unknown, it is unclear whether its three known eigenstates follow a normal or inverted mass ordering, and the existence of sterile flavor eigenstates is still under investigation. An additional open question involves the nature of this particle: it may be its own antiparticle (Majorana type) or not (Dirac type). The Majorana nature of the neutrino would imply a violation of the total lepton number, which could help to explain the matter-antimatter asymmetry in the universe and, thus, the existence of matter itself. Hence, the discovery of Majorana neutrinos would prove physics beyond the Standard Model and perhaps shed light on the origins of our universe.

The most promising discovery channel to experimentally test if the neutrino is a Majorana particle is identified by the extremely rare nuclear process, the so-called neutrinoless double-beta decay ($0\nu\beta\beta$). The double-beta decay with the contemporary emission of two neutrinos has already been observed for a certain number of nuclei, despite its low rate. If the neutrino is a Majorana particle, another double-beta decay mode can take place, in which no neutrinos are produced at all. Thus, this second-order weak nuclear decay requires physics beyond the Standard Model and it is only possible if the total lepton number is violated. $0\nu\beta\beta$ decay is predicted by many theories extending the Standard Model, and several experiments worldwide are searching for the decay using different isotopes and experimental techniques.

However, none of them reported evidence for the existence of $0\nu\beta\beta$ decay, and, in the absence of a signal, lower limits on its half-life have been set. The current threshold, greater than 10^{26} yr, has been determined by the GERDA and KamLAND-Zen experiments. GERDA looked for $0\nu\beta\beta$ decay of ^{76}Ge operating germanium detectors made from enriched material, i.e. the isotopic fraction of ^{76}Ge nuclei is increased from 7.8% to 86%. In this experiment, the source is equal to the detector, yielding a high detection

efficiency. GERDA operated from 2011 to 2019 at the Laboratori Nazionali del Gran Sasso, in Italy. It has been working in background-free conditions for all its collected exposure, using an array of high purity germanium detectors submerged in liquid argon. This achievement has successfully demonstrated the advantages of the GERDA experimental philosophy, and it has been selected as the basis of the next-generation experiment, which is currently being prepared by the LEGEND collaboration.

The characterization of the detectors before their submersion in the liquid argon is crucial to know their optimal work conditions and to model the detector response. The active volume is one of the aspects of the detector determined during the characterization, and it has large effects on the detection efficiency for many analyses. The dead layers near the n+ electrode must be precisely measured since they do not contribute to the detector's active volume. The active volume enters the computation of the $0\nu\beta\beta$ half-life, and it is of absolute importance for the determination of the $2\nu\beta\beta$ half-life, whose event distribution is of great interest for new physics searches and other low-energy physics analyses. Since the systematic uncertainty on the $2\nu\beta\beta$ half-life in GERDA is currently dominated by the uncertainty of the active volume, more solid estimations of the dead regions in the detectors are needed to improve the precision substantially.

The present thesis work is structured as follows. The first three chapters constitute a general introduction. An overview of the neutrino physics as an approach to search for physics beyond the Standard Model is given in Chap.1. In Chap.2, a description of the various forms of double-beta decay is provided with an overview of current experiments. Finally, Chap.3 introduces the GERDA experiment and its achievements, and the future LEGEND experiment and its goals. The second part focuses on the characterization of the LEGEND detectors. The production and the initial characterization of inverted coaxial detectors employed in the first phase of the LEGEND experiment are described in Chap.4. Chap.5 is devoted to the detailed measurement of the dead layer and its homogeneity around the detector surfaces by irradiating each detector with several radioactive sources. The third part of the thesis illustrates two techniques to obtain the active volume at the time of GERDA data-taking. In Chap.6, nine detectors are re-characterized after being stored at room temperature for a few years before the deployment in liquid argon. Chap.7 explains in detail an innovative technique used to probe the active volume with the data collected at low energy by GERDA. It uses the bath of liquid argon in which the detectors are immersed. The liquid argon contains ^{39}Ar, an isotope mainly produced in the atmosphere. Since the energy distribution of the ^{39}Ar decay events is particularly sensitive to the model and the size of the active volume, it provides an alternative tool to estimate it for each detector operated in GERDA. The final part of the thesis focuses on one of the effects of active volume determination. Chap.8 illustrates the measurement of the $2\nu\beta\beta$ half-life obtained with the more accurate values of active volume estimated in the

previous chapters. This provides a half-life measurement of unprecedented precision.

Part I

Introduction

1

NEUTRINO PHYSICS

1.1 THE STANDARD MODEL

The Standard Model (SM) of Particle Physics aims to explain the nature laws through a finite number of elementary interactions and particles. This physics theory includes electromagnetic interaction, weak interaction, and strong interaction, and it classifies all the particles known until now. It does not include gravity, described instead by general relativity.

The ultimate theory of particle physics would consist of a single equation from which everything else can be derived. Beginning, the scientists tried to construct the Standard Model *ad hoc* to reproduce the experimental data, taking in mind the final goal. They put together different theoretical ideas into the same model: the Quantum Field Theory describing the particles and their interactions, the local gauge principle determining the behavior of these interactions, the Dirac equation of relativistic quantum mechanics providing the dynamics of the fermions, the Higgs mechanism of electroweak symmetry breaking which generates the masses of the particles. Whilst the expectations of the Standard Model have been verified and demonstrated by many experiments [1], this particle physics theory presents different limits because of many unanswered questions, particularly in the realm of neutrinos. Although it is one of the great successes of modern physics, it is not the ultimate theory.

1.1.1 *CPT symmetry and weak interaction*

In the last century, the concept of symmetry in the laws of nature has played an increasingly important role. In physics, one of the most fundamental symmetries is CPT invariance: any Lorentz-invariant quantum field theory with a Hermitian Hamiltonian is invariant under CPT [2]. The charge conjugation operator C turns a particle state into an antiparticle state: $C|\psi>=|\overline{\psi}>$. The parity operator P performs a spatial inversion $P|\psi(\vec{r},t)>=|\psi(-\vec{r},t)>$. The temporal flow is inverted by time reversal T, as it flips the temporal parameter t: $P|\psi(\vec{r},t)>=|\psi(\vec{r},-t)>$. One effect of CPT theorem is that particles and anti-particles share the same mass, same lifetime, and equal but opposite charge and magnetic moment.

In 1956, the Wu experiment demonstrated parity violation during the decay of ultra-cold polarized ^{60}Co. Later experiments showed that parity is indeed maximally violated in weak interactions via Lorentz-invariant left(right)-chiral projections $\psi_{L(R)}$ of the particle fields. A generic spinor

Chirality is a frame-independent property of the weak interaction.

field ψ can be defined in terms of the chiral fields called right-handed (RH) and left-handed (LH)

$$\psi = \psi_R + \psi_L$$

with

$$\psi_{R(L)} = \left(\frac{1 \overset{+}{(-)} \gamma^5}{2} \right) \psi$$

where γ^5 is the chirality matrix.

As it turns out, only left-handed chiral particle states (and right-handed chiral antiparticle states) participate in the charged-current weak interaction. In 1957 at the Padua-Venice conference, Marshak and Sudarshan proposed the left-handed V–A form for the weak Lagrangian [3], shortly followed by the Feynman and Gell-Mann paper [4].

The neutrino was introduced to the SM as a purely left-handed particle after the measurement of γ emitted in the ^{152}Eu K-shell electron capture, passing through polarized iron and absorbed resonantly in a ^{152}Sm target. The results revealed a negative helicity of neutrinos [5] but since helicity and chirality are the same for a massless particle, negative helicity is referred to as left-handed.

The helicity of a particle is defined as the projection of its spin into the direction of its momentum.

Left(right)-handed (anti-)neutrinos and their corresponding charged lepton l form a doublet under weak isospin I_3. The right-handed weak isospin singlet neutrino does not underlay any interactions of the Standard Model. Since there is no evidence of its existence, it is called *sterile*.

1.2 BRIEF HISTORY OF NEUTRINO

The name *neutrino* was coined by Enrico Fermi to differentiate it from the neutron. The neutrino went on stage for the first time through the β radioactive decay research. Only one particle was detected to be emitted in the final state, and a discrete energy spectrum of the beta particle was expected. Instead, in 1914 Chadwick observed that this energy spectrum was continuous, violating the conservation of energy, momentum, and angular momentum. Only in 1930 Pauli hypothesized the existence of the third particle in β decay, although it was not detected yet with the equipment of that time. Four years later, this hypothesis found a theoretical explanation with Fermi's formulation of the weak interaction theory.

The "invention" of the neutrino was confirmed only several years later, in 1956, with the experiment of Cowan and Reines [6] who observed electron antineutrinos emitted together with electrons from nuclear decay inside a reactor. After discovering the muon in 1937, Pontecorvo hypothesized the existence of another flavor of neutrino: the muon neutrino, derived in association with the muon [7]. This prediction was confirmed in 1962 by the experiment of Lederman, Schwartz and Steinberger[8]. Following the discovery of the third charge lepton called tau, in 2000 the corresponding tau neutrino was observed [9]. It completed the list of the three neutrinos

known until now, which are active in the processes of weak interaction that allows their detection.

1.3 TO BE, OR NOT TO BE, A MASSIVE NEUTRINO

According to SM, the neutrino ν is a fermion from the lepton family, with $\frac{1}{2}$ spin, no charge, and no mass. However, this last property is surrounded by an air of mystery even now.

Suppose neutrinos are massive, and the masses of the three neutrinos are not identical. In that case, the neutrino flavor states ν_e, ν_μ, and ν_τ can be expressed as a superposition of the three neutrino mass states:

$$\nu_\alpha = \sum_{k=1}^{3} U^*_{\alpha k} \nu_k \tag{1.1}$$

where α labels the flavor eigenstates and k the mass eigenstates. U is the Pontecorvo-Maki-Nakagawa-Sakata (PMNS) mixing unitary matrix and can be expressed in its standard parametrization as

$$U = \begin{pmatrix} c_{12}c_{13} & s_{12}c_{13} & s_{13}e^{-i\delta} \\ -s_{12}c_{23} - c_{12}s_{23}s_{13}e^{i\delta} & c_{12}c_{23} - s_{12}s_{23}s_{13}e^{i\delta} & s_{23}c_{13} \\ s_{12}s_{23} - c_{12}c_{23}s_{13}e^{i\delta} & -c_{12}s_{23} - s_{12}c_{23}s_{13}e^{i\delta} & c_{23}c_{13} \end{pmatrix} D \tag{1.2}$$

where $s_{ij} = \sin\theta_{ij}$, $c_{ij} = \cos\theta_{ij}$ and δ is the Dirac phase responsible of the CP violation in the neutrino oscillation experiments. D is the diagonal phase matrix $D = \mathrm{diag}(1, e^{i\alpha}, e^{i(\beta+\delta)})$ containing the Majorana phases α and β. Assuming three neutrinos, the matrix is expressed by six physical parameters: three mixing angles θ_{21}, θ_{31}, θ_{32} and three phases α, β, δ.

α, β are physical only if neutrinos are Majorana particles (Sec. 1.4).

The transition probability between neutrino flavors α and β is given by

$$\begin{aligned} P(\nu_\alpha \to \nu_\beta) =& \delta_{\alpha\beta} - 4\sum_{i>j} \mathrm{Re}\{U^*_{\alpha i}U^*_{\beta j}U_{\beta i}U_{\alpha j}\} \sin^2 \frac{\Delta m^2_{ij} L}{4E} \\ &+ 2\sum_{i>j} \mathrm{Im}\{U^*_{\alpha i}U^*_{\beta j}U_{\beta i}U_{\alpha j}\} \sin \frac{\Delta m^2_{ij} L}{2E} \end{aligned} \tag{1.3}$$

where E is the neutrino energy, L is the source-detector distance, and $\Delta m^2_{ij} = m^2_i - m^2_j$. Therefore, neutrino oscillation physics is only sensitive to the squared mass differences. Experimental evidence exists for neutrino oscillations in solar [10], atmospheric [11], reactor [12] and accelerator [13] neutrinos. These data have determined the PMNS matrix elements and the absolute value of the mass squared differences. By exploiting the Mikheyev-Smirnov-Wolfenstein (MSW) effect in the propagation of solar neutrinos, the sign of Δm^2_{21} has been determined as positive [14]. As yet, the sign of Δm^2_{31} is unknown since it requires the observation of muon neutrinos with very long baselines. As a consequence, the ordering of the neutrino masses can be *normal* ($\Delta m^2_{31} > 0$) or *inverted* ($\Delta m^2_{31} < 0$), as it is shown in Fig. 1.1. Future long-baseline reactor oscillation experiments such as Dune [15] and T2HK [16] aim to measure the sign of Δm^2_{31} with high significance.

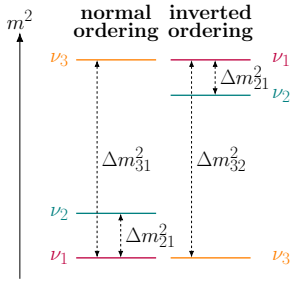

Figure 1.1: Mass ordering scenarios.

1.4 MAJORANA NEUTRINO

The latest observations of neutrino flavor oscillation confirm that neutrinos are not massless. Then, there must be a corresponding mass term in the Lagrangian, and the simplest way of accounting for the neutrino mass is introducing the right-handed singlet ψ_R, as for the other fermions:

$$\mathcal{L}_D = -m_D \, (\overline{\nu_R}\nu_L + \overline{\nu_L}\nu_R). \tag{1.4}$$

Referring to neutrinos, ψ_L creates the left-handed neutrino ν_L, $\overline{\psi}_R = \psi_R^\dagger \gamma^0$ creates the right-handed neutrino ν_R.

Since the left-handed particles transform as weak isospin doublets and right-handed particles as singlets, the two products do not give a scalar like the mass term and the weak isospin is violated. Then, it is required to introduce a doublet in the product, which is typically provided by the Higgs mechanism. The neutrino acquires a Dirac mass

$$m_D = \frac{v}{\sqrt{2}} Y^\nu \tag{1.5}$$

proportional to the non-zero expectation value v of the Higgs field and to the Yukawa coupling Y^ν. Given current upper limits on the neutrino mass of $\mathcal{O}(1)$ eV, and considering v of $\mathcal{O}(100)$ GeV, a Yukawa coupling as small as $Y^\nu < 10^{-11}$ is required, smaller by several orders of magnitude compared to the other fermions. This mechanism does not explain the smallness of neutrino masses and requires undesired fine-tuning.

In the early 1930s, the physicist Ettore Majorana wondered if it were possible to describe a massive neutrino using only the left-handed chiral field, not requiring the existence of the right-handed state as the Dirac mechanism needed. The Majorana field is

$$\psi = \psi_L + \psi_R = \psi_L + \psi_L^c \tag{1.6}$$

by the definition of the charge-conjugate field and the charge conjugate of the Majorana field is

$$\psi^c = (\psi_L + \psi_L^c)^c = \psi_L^c + \psi_L = \psi \tag{1.7}$$

The lepton number L represents the difference between the number of leptons and the number of anti-leptons in an elementary particle reaction. A Dirac (anti-)neutrino has $L = +1(-1)$.

then it means that the charge conjugate of the field is the field itself or, in other words, that the Majorana neutrino is its own antiparticle. Consequentially, the Majorana term mass can be expressed as

$$\mathcal{L}_M = -\frac{1}{2} m_M \, (\overline{\nu_L^c}\nu_L) + h.c. \tag{1.8}$$

Nevertheless, this transition is not invariant under weak isospin symmetry and violates the conservation of the weak hypercharge. Furthermore, while for the Standard Model the lepton number is a conserved quantum number, the Majorana assumption requires the lepton number violation.

With the right-handed neutrinos allowing both a Dirac and a Majorana mass, the Lagrangian term for combined two masses can be written as

$$\mathcal{L}_{DM} = -\frac{1}{2} \left(\underbrace{\overline{\nu_L} \, m_L \, \nu_L^c + \overline{\nu_R^c} \, m_R \, \nu_R}_{\text{Majorana mass}} + \underbrace{\overline{\nu_L} \, m_D \, \nu_R + \overline{\nu_R^c} \, m_D \, \nu_L^c}_{\text{Dirac mass}} \right) + h.c. \tag{1.9}$$

or it can be expressed in matrix form

$$\mathcal{L}_{DM} = -\frac{1}{2}\begin{pmatrix} \overline{\nu_L} & \overline{\nu_R^c} \end{pmatrix}\begin{pmatrix} 0 & m_D \\ m_D & M \end{pmatrix}\begin{pmatrix} \nu_L^c \\ \nu_R \end{pmatrix} + h.c. \tag{1.10}$$

with $m_D << M$.

Diagonalizing the matrix leads to the masses of physical neutrinos: $m_{heavy} \approx M$ and $|m_{light}| \approx \frac{m_D^2}{M}$. This mechanism, called *type-I seesaw* mechanism, predicts the existence of a very light neutrino, the familiar left-handed Majorana neutrino, with a mass much smaller than the other Standard Model fermions and a very massive neutrino state, the heavy sterile right-handed partner, for each neutrino family. This mechanism is one natural explanation of the relative smallness of the neutrino mass. For instance, if the Dirac neutrino mass is $\mathcal{O}(10^2)$ GeV, and $M \sim 10^{15}$ GeV, the neutrino state has a mass $m_\nu \sim 0.01$ eV, which is the plausible scale for the neutrino mass, according to experimental data.

In conclusion, a Majorana mass term arises from oscillations between particle and anti-particle, and hence, the lepton number L stops to be a conserved quantum number. Consequentially, searching for L non-conservation might reveal the nature of neutrinos. The most promising process envisioned to probe the Majorana character of neutrinos is the neutrinoless double beta ($0\nu\beta\beta$) decay, which is discussed in the following chapter in detail.

2

DOUBLE BETA DECAY

2.1 THEORETICAL ASPECT

Two-neutrinos double beta decay ($2\nu\beta\beta$) processes, first suggested by M. Goeppert-Mayer in 1935, can occur when the single beta decay is forbidden by the energy conservation or strongly suppressed because of a large change of spin. It can proceed only if the parent isotope is less bound than the final product, and both must be more bound than the intermediate nucleus. These conditions are satisfied only for some even-even nuclei (see Fig.2.1).

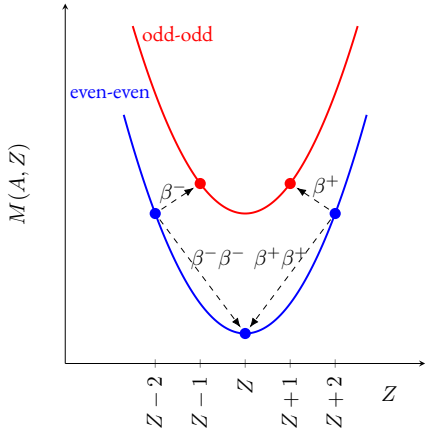

Figure 2.1: Graph of mass as a function of atomic number Z for isobar nuclei with even A split into two cases of even-even and odd-odd nuclei. For certain nuclei the β decay is forbidden but the $\beta\beta$ decay is allowed.

The nuclear charge changes by 2 units and the process can be thought as two simultaneous single β decays (see Fig.2.2):

$$(Z, A) \longrightarrow (Z+2, A) + 2e^- + 2\overline{\nu}_e \quad (2\beta^-) \tag{2.1}$$

$$(Z, A) \longrightarrow (Z-2, A) + 2e^+ + 2\nu_e \quad (2\beta^+) \tag{2.2}$$

Since this decay is a second-order process, the half-life of $2\nu\beta\beta$ decay is typically from 10^{19} to 10^{24} years. The $2\nu\beta\beta$ rate can be computed by invoking the recipe of the Fermi golden rule for simple β decay. To a good approximation, the decay rate can be factorized as a kinematic part, or phase space factor, times the matrix element describing the transition probability between the initial and final nuclear states:

$$\Gamma^{2\nu} = \frac{1}{T^{2\nu}_{1/2}} = |M^{2\nu}|^2 G^{2\nu}(Q_{\beta\beta}, Z) \tag{2.3}$$

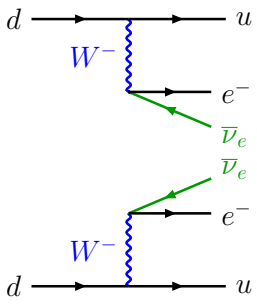

Figure 2.2: Feynman diagram for the double beta decay.

The calculation of the nuclear matrix element (NME) $|M^{2\nu}|$ is a complicated many-body nuclear physics problem. Its value for $2\nu\beta\beta$ depends on the isotope and is of the order of 10^{-1}. The phase space factor $G^{2\nu}(Q_{\beta\beta}, Z)$ is obtained by the integration over the phase space of the four leptons emitted in the decay. Its value for $2\nu\beta\beta$ varies between 10^{-21} and 10^{-17} yr^{-1} depending on the double beta emitter. The so-called Q-value or end-point energy, $Q_{\beta\beta} = M_i - M_f - 2m_e$, is given by the difference of initial mass M_i and final mass M_f of the decaying nucleus, and the mass of the two electrons, $2m_e$. It defines the maximal kinetic energy of the two electrons in the final state of $2\nu\beta\beta$.

The double beta decay without the emission of neutrinos ($0\nu\beta\beta$ decay) is described as

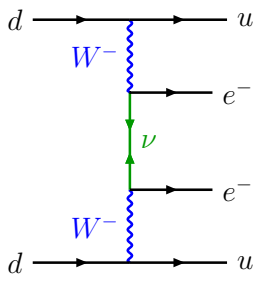

Figure 2.3: Feynman diagram for the neutrinoless double beta decay.

$$(Z, A) \longrightarrow (Z + 2, A) + 2e^- \tag{2.4}$$

$$(Z, A) \longrightarrow (Z - 2, A) + 2e^+ \tag{2.5}$$

This process is forbidden by the Standard Model because it violates the lepton number by two units ($\Delta L = 2$). Although many extensions of the SM include mechanisms that can explain the decay, according to the Schechter–Valle theorem [17] all realizations of Eq.2.4 (or Eq.2.5) are connected to a Majorana neutrino mass. It is possible to classify the mediation process by Majorana neutrinos as the *standard interpretation* of $0\nu\beta\beta$ [18]. It is shown in Fig.2.3, where the emitted left-handed neutrino in the upper β decay is absorbed by the lower decay. For this to happen, the only possibility is $\nu_L = \nu_L^c$, since a particle's absorption is equivalent to its antiparticle emission according to the quantic numbers. Assuming the mediators of the decay are two massive Majorana neutrinos (Fig.2.3), the decay rate is

$$\Gamma^{0\nu} = \frac{1}{T^{0\nu}_{1/2}} = |M^{0\nu}|^2 G^{0\nu}(Q_{\beta\beta}, Z) \left(\frac{m_{\beta\beta}}{m_e}\right)^2 \tag{2.6}$$

where m_e is the electron mass, $|M^{0\nu}|$ the nuclear matrix element, and $G^{0\nu}(Q_{\beta\beta}, Z)$ is the phase space factor which can be considered almost independent of the mechanism when two electrons are emitted during the process. $G^{0\nu}(Q_{\beta\beta}, Z)$ is of the order of 10^{-25} yr^{-1} and can be calculated to a satisfying degree of accuracy [19, 20] , while NME is a problematic parameter and remains terribly affected by large systematic biases [21]. Finally, $m_{\beta\beta}$ is the effective Majorana mass which can be defined in terms of the first row of PNMS matrix as

$$m_{\beta\beta} = \sum_i U_{ei}^2 m_i = c_{12}^2 c_{13}^2 m_1 + s_{12}^2 c_{13}^2 e^{i\alpha} m_2 + s_{13}^2 e^{i\beta} m_3 \quad . \tag{2.7}$$

It is the coherent sum of the mass eigenstates m_i, weighted by their squared U_{ei} contribution.

Since $G^{0\nu}(Q_{\beta\beta}, Z)$ scales with ${Q_{\beta\beta}}^5$, the total decay rate, and hence the inverse half-lives, of $0\nu\beta\beta$ depends strongly on the available Q-value. Therefore, isotopes with high Q-value (above 2 MeV) are usually taken into

account for experiments on double beta decay. For this reason, among the 35 nuclei which can undergo $2\nu\beta\beta$ decay, 11 isotopes could emerge as interesting candidates: ^{48}Ca, ^{76}Ge, ^{82}Se, ^{96}Zr, ^{100}Mo, ^{116}Cd, ^{128}Te, ^{130}Te, ^{136}Xe, ^{150}Nd and ^{238}U. Fig.2.4 shows, as an example, the nuclear level structure of the $2\nu\beta\beta/0\nu\beta\beta$ decay of ^{76}Ge$\rightarrow^{76}$Se.

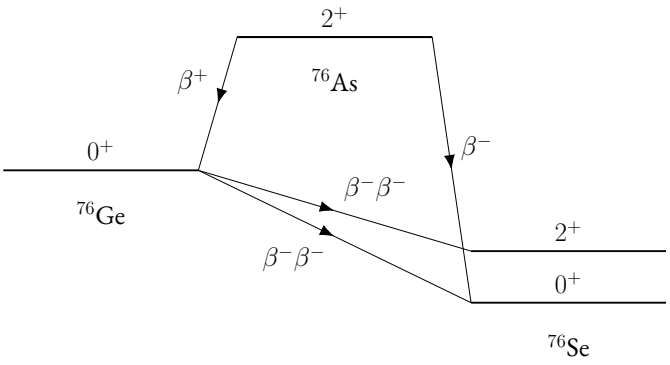

Figure 2.4: Schematic illustration of the energy level structure of the ^{76}Ge$\rightarrow^{76}$Se decay.

2.2 CONSEQUENCES OF $0\nu\beta\beta$ EVIDENCE

The possible discovery of the $0\nu\beta\beta$ decay would have consequences for nuclear and particle physics as well as for astrophysics and cosmology. The CP-violating decay of neutrinos could potentially explain the dominance of matter over antimatter in the universe through leptogenesis, proposed by Fukugita and Yanigada in 1986 [22]. For this model, Majorana neutrinos decayed into lighter leptons and anti-leptons as the universe cooled after the Big Bang. CP-violation by the phases in the Yukawa coupling would lead to an imbalanced lepton anti-lepton production. It would also provide a violation in the baryonic number B, since the quantum number B−L is conserved in the Standard Model both at the classical and quantum level (by *sphaleron* processes).

Sphaleron processes are non-perturbative solutions to the electroweak field equations.

Besides lepton number violation, $0\nu\beta\beta$ decay, if observed, would be of great importance for establishing the mechanism through which the neutrino acquires its mass (Sec.1.4). $0\nu\beta\beta$ decay could provide unique constraints on the neutrino mass scale and mass ordering. Cosmological measurements provide the strongest mass limit on the sum of the three neutrino masses [23]

$$\Sigma = \sum m_i < 0.12\text{eV} \tag{2.8}$$

but they depend on the cosmological model. The direct kinematic (Kurie-plot) searches provide the most model-independent approach to test the neutrino mass, giving limits on the effective electron neutrino mass

$$m_\beta = \sqrt{\sum_i |U_{ei}^2| m_i^2} \tag{2.9}$$

Recent limits by KATRIN experiment constrain $m_\beta < 0.8$ eV [24]. Varying the neutrino oscillation parameters within their 3σ ranges it is possible to plot $\langle m_{\beta\beta} \rangle$, m_β, Σ, as shown in Fig.2.5. The left panel of Fig.2.5 shows the parameter space available for $\langle m_{\beta\beta} \rangle$ as a function of m_{light}. In the case of normal ordering m_{light} corresponds to m_1, whereas for inverse ordering it is m_3. Both ordering scenarios populate individual parameter space, whereas at large values of m_{light}, and respectively large values of $\langle m_{\beta\beta} \rangle$, the two bands overlap. The connection between $\langle m_{\beta\beta} \rangle$ and Σ is shown in the central panel of Fig.2.5 with with the limits on Σ from cosmology. The right panel indicates the connection between $\langle m_{\beta\beta} \rangle$ and m_β with the expected sensitivity of the KATRIN experiment (after 5 years from the results published in 2019). In the normal ordering hypothesis, $\langle m_{\beta\beta} \rangle$ can even vanish, while in the inverted ordering scenario there is a minimum value of about 0.013 eV. This value represents a physics goal for the current and upcoming $0\nu\beta\beta$ experiments.

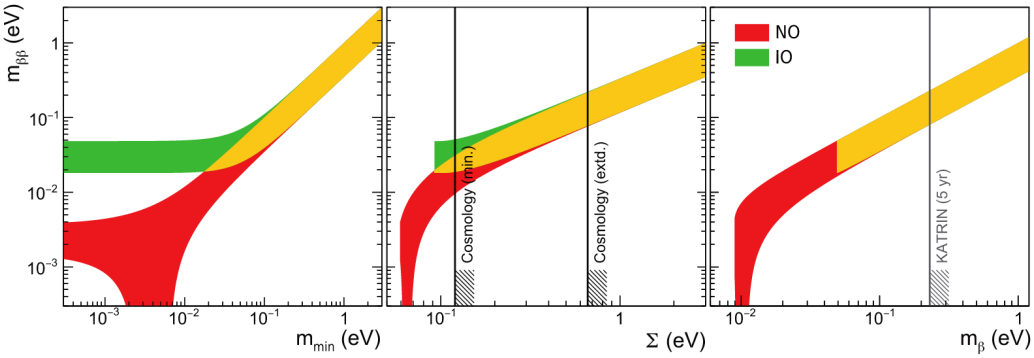

Figure 2.5: $\langle m_{\beta\beta} \rangle$ as a function of the lightest mass eigenstate m_{light} (or here called m_{min}) and other mass observables - namely the sum of neutrino masses Σ and the effective neutrino mass m_β. The region permitted in the case of normal ordering is shown in red, while the region permitted in the case of inverted ordering is shown in green. Where these regions overlap is shown in yellow, called the degenerate region. The figure is adapted from [25].

Unfortunately, no convincing experimental evidence of $0\nu\beta\beta$ decay has been found until now.

2.3 EXPERIMENTAL ASPECTS

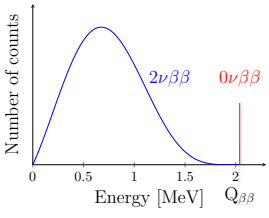

Figure 2.6: Spectrum of the sum of the electron kinetic energies for the $2\nu\beta\beta$ and $0\nu\beta\beta$ decays of ^{76}Ge.

The importance of the topic has encouraged the development of different experimental efforts in the search for $0\nu\beta\beta$ decay. The experimental signature of $0\nu\beta\beta$ decay is a mono-energetic peak in the energy spectrum of the two electrons released in the nuclear decay, see Fig.2.6. Because of the inevitable presence of radioisotope traces, the observation of $0\nu\beta\beta$ is very challenging. Any radioactive decay with a Q-value above the position of the $0\nu\beta\beta$ signal peak may deposit energy in the signal region and be a potential background. Also the $2\nu\beta\beta$ events are considered an unavoidable background source since the decay rate is at least 5-6 orders of magnitude larger

than for $0\nu\beta\beta$ decay, and $2\nu\beta\beta$ signature is a continuous spectrum with tail reaching the $Q_{\beta\beta}$. The two decay varieties can only be distinguished through good energy resolution.

Furthermore, low background techniques need to be applied because of the much higher magnitude of the environmental radioactivity compared to the expected decay rate. Firstly, the experiments must be underground to protect the detectors from cosmic rays. Then, the natural radioactivity needs to be screened by a shield whose radioactivity, and that of the detector material, must be extremely low. Finally, the source material should not only contain a large fraction of the double beta decay isotope but must be available in high purity.

The half life of the $0\nu\beta\beta$ decay is

$$T^{0\nu}_{1/2} = \ln 2 \frac{N_A \epsilon}{m_{enr}\ \lambda_S} \tag{2.10}$$

where N_A is the Avogadro constant, ϵ is the total exposure (product of detector mass M and live time t of the measurement), m_{enr} is the molar mass of the enriched material, λ_S is the detected number of $0\nu\beta\beta$ events. In case of no $0\nu\beta\beta$ events detected and, in the presence of a sizable number of background events the background, the sensitivity of the half life of $0\nu\beta\beta$ scales with:

$$T^{0\nu}_{1/2} \propto \mathcal{E} \cdot a \sqrt{\frac{\epsilon}{BI \cdot \Delta E}} \tag{2.11}$$

where a is the isotopic abundance of the $\beta\beta$ emitter, $\mathcal{E}$ the detection efficiency, ϵ is the total exposure, ΔE is the energy resolution and BI is the background index, namely the number of background events normalized to the width of the Region of Interest (ROI) around the $Q_{\beta\beta}$, source mass and measurement time and expressed in cts/(keV·kg·y). The background-free regime is more advantageous since the half-life scales linearly with exposure

$$T^{0\nu}_{1/2} \propto \epsilon \cdot a \cdot \mathcal{E} \tag{2.12}$$

as opposed to the square root of the exposure in the presence of background. The background-free condition is effectively realized when the expected number of background events in the ROI is less than one in the measurement time: $BI \cdot \epsilon \cdot \Delta E < 1$. The optimal experimental conditions are reached if a zero-background limit is maintained for the majority of the experimental runtime. In case of no signal, a lower limit of $T^{0\nu}_{1/2}$needs to be set.

Numerous experiments have been carried out to search for $0\nu\beta\beta$ decay. They use different isotopes and different detection approaches tracking the particles and measuring the sum of the energies of the two electrons in the $2\nu\beta\beta$. Some experiments use ionization detectors, tracking chambers, cryogenic, scintillating bolometers and more. KamLand-Zen [26] uses a liquid scintillator enriched with ^{136}Xe. Despite their poor energy resolution, the liquid scintillators are easily scalable, which is one of the main advantages of building the next-generation experiment. In the future, KamLAND-Zen

plans to deploy over a tonne of enriched xenon with a goal to the expected $T^{0\nu}_{1/2}$ sensitivity of $\sim 2 \cdot 10^{27}$yr. NEMO-3 [27] used a multi-layer detector to measure the energy and the particle track. It is the only type of detector able to measure the opening angle between the two βs, and this technology is at the basis of SuperNEMO's [28] operation. This long-term experiment plans to reach a sensitivity of $1.2 \cdot 10^{26}$ yr with ^{82}Se, with excellent background discrimination but low energy resolution and detection efficiency. The CUORE experiment [29] uses TeO_2 bolometers operated at 10 mK. Each detector is equipped with a sensitive thermometer for the read-out of the temperature signal. They are characterized by excellent energy resolution which will be used in the future experiment CUPID [30] updated with scintillating crystal. It aims to cover the inverted hierarchy region of the neutrino mass entirely with a sensitivity of $T^{0\nu}_{1/2} > 10^{27}$ yr. EXO-200 [31] is a cylindrical time projection chamber filled with liquid xenon enriched in ^{136}Xe. The combination of ionization and scintillation signal from ^{136}Xe allows the reconstruction of the event topology, energy, position, and particle type. The next experiment nEXO [32] will use five tonnes of liquid xenon with the ability to identify and measure background and signal simultaneously. The sensitivity goal is $T^{0\nu}_{1/2} \sim 10^{28}$ yr.

The experiments studying the decay of Ge usually operate germanium diodes typically made from enriched material, i.e. the isotopic fraction f_{76} is enlarged up to $\sim 90\%$. The source itself acts as a detector as well, yielding high detection efficiency. Additional advantages of this technique are the high radiopurity from the crystal growing procedure and the superior energy resolution of 0.2% at $Q_{\beta\beta} = 2039.061 \pm 0.007$ keV compared to other searches with different isotopes. On the other hand, the disadvantages are the production cost and the relatively low $Q_{\beta\beta}$ value since background typically deposits lower energy.

Two of the first experiments using germanium detectors for studying $0\nu\beta\beta$ decay were Heidelberg-Moscow (HdM) [33] and the International Germanium Experiment (IGEX) [33]. They used p-type high purity germanium detectors (see Sec.3.1.3) enriched to 86% in ^{76}Ge deployed in vacuum cryostats in deep underground laboratories. The HdM collaboration claimed evidence for $0\nu\beta\beta$ [34] with $T^{0\nu}_{1/2} \approx 1.19 \cdot 10^{25}$ yr. It resulted in an upper limit of the effective Majorana neutrino mass of 0.35 eV at 90% C.L.. The assertion had received numerous criticisms from the physicist community and it had to be verified by other experiments because of the large uncertainties on the matrix elements [35]. To push the sensitivity to much higher levels, two experiments were initiated: Majorana Demonstrator [36] and Gerda [37]. They used high purity germanium, which acted as source and detector simultaneously. Majorana refined the background reduction techniques in the traditional approach of operating germanium detectors in vacuum, while Gerda used an innovative technique with Liquid Argon (LAr). A deeper description of Gerda experiment is presented in the following chapter.

Tab.2.1 shows the recent results of different experiments comparing the lower half-life limits $T^{0\nu}_{1/2}$ (90% C.L.) and corresponding upper limits of the effective Majorana neutrino mass $m_{\beta\beta}$. A strong conclusion from the table is that ^{76}Ge experiments reach competitive sensitivities with much smaller isotope exposures compared to the other technologies. Ge-based experiments have indeed an extremely high detection efficiency and operate in a quasi background-free regime. The goal of the next-generation of $0\nu\beta\beta$ experiments is to extend the half-life limit beyond 10^{28} yr and to probe $\langle m_{\beta\beta}\rangle$ in order to cover the parameter range predicted in the case of inverted mass ordering [38]. The comparison of the discovery sensitivity of current and future neutrinoless double beta decay experiments is shown in Fig.2.8. The history of ^{76}Ge experimental achievements is presented in Fig.2.7 in terms of the half-life lower limits.

Table 2.1: Comparison of lower half-life limits $T^{0\nu}_{1/2}$ (90% C.L.) and corresponding upper Majorana neutrino mass $\langle m_{\beta\beta}\rangle$ limits of different $0\nu\beta\beta$ experiments. The experiments, the isotopes, and the exposures are shown in columns 1–3. The lower half-life limits and corresponding upper limits for $m_{\beta\beta}$ are shown in columns 4 and 5, respectively.

Experiment		**Isotope**	**Exposure** [kg· yr]	$T^{0\nu}_{1/2}$ [10^{25} yr]	$\langle m_{\beta\beta}\rangle$ [meV]
GERDA	[39]	^{76}Ge	127.2	18.0	79 – 180
MAJORANA	[40]	^{76}Ge	64.5	8.3	113 – 269
KamLAND-ZEN	[41]	^{136}Xe	970	23	36 – 156
EXO-200	[42]	^{136}Xe	234.1	3.5	93 – 286
CUORE	[43]	^{130}Te	372.5	3.2	75 – 350

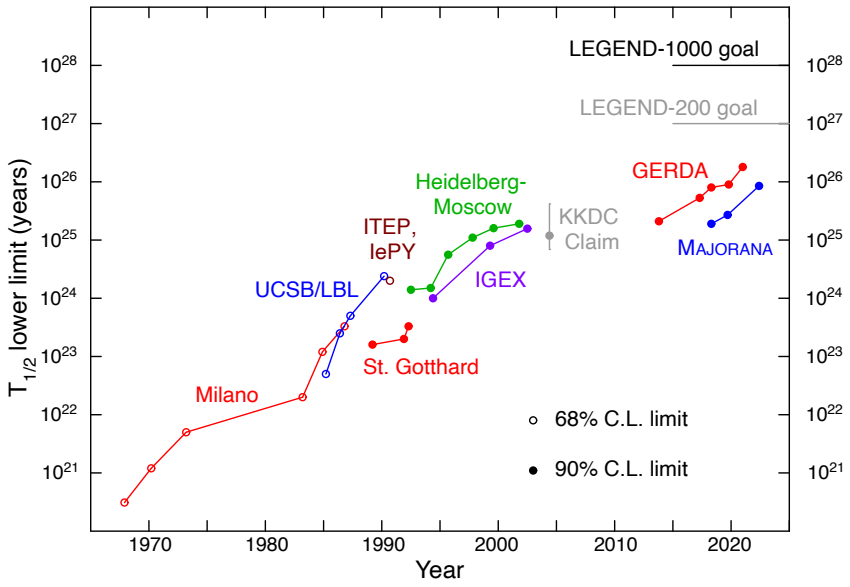

Figure 2.7: A historical timeline of Ge-based $0\nu\beta\beta$ decay experiments and their reported half-life lower limit. The future prospects are indicated by the projections for the LEGEND program. From [44]. References to the named experiments can be found in [38].

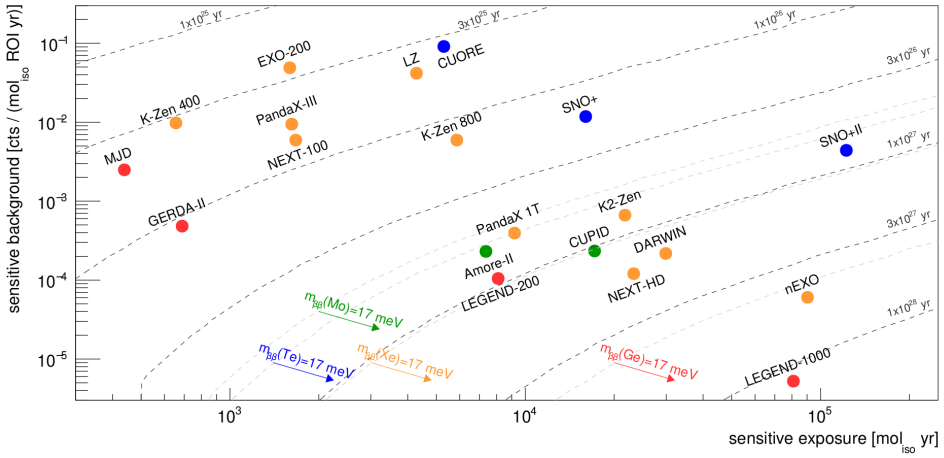

Figure 2.8: Discovery sensitivity comparison between completed or running (top-left side) and future neutrino-less double beta decay experiments. Contours of $0\nu\beta\beta$ half-life are shown. ^{100}Mo (green), ^{130}Te (blue), ^{136}Xe (yellow) and ^{76}Ge (red) projects are considered. From [45].

3

GERDA AND LEGEND EXPERIMENTS

3.1 GERDA EXPERIMENT

The GERDA experiment [37] (GERmanium Detector Array) has searched for the neutrinoless double beta decay ($0\nu\beta\beta$) of ^{76}Ge. It was proposed in 2004 and was built in the INFN Laboratori Nazionali del Gran Sasso (LNGS). A location underground is essential for an experiment searching for an extremely rare process, like $0\nu\beta\beta$ decay, in order to shield it from cosmic rays, a potential source of fake signals. The overburden of the LNGS consists of 1400 m rock, which is equivalent to a 3500 m water equivalent shielding. GERDA submerged high purity germanium (HPGe) detectors (enriched $\sim$ 88% in ^{76}Ge) arranged in strings in a cryostat filled with liquid argon (LAr). The 64 m^3 of LAr acted simultaneously as a shield against external radioactivity and as a cooling medium. The LAr cryostat was placed in a tank (see Fig.3.1) filled with 590 m^3 of ultra-pure water acting as a moderator for neutrons and photons. This tank also acted as a Cherenkov veto detector for traversing muons thanks to 66 photomultiplier tubes (PMTs). Additionally, plastic scintillator panels were set on top of the clean-room, which was above the water tank, in order to enable the detection of muons traversing through the cryostat neck without water. The detectors were lowered into the LAr volume using a lock system located in the clean-room. Fig.3.2 shows a schematic view of the experiment. The GERDA experiment ended its data taking in mid-November 2019.

Figure 3.1: Inside the water tank after the installation of the muon veto system [46]. Photo from [47].

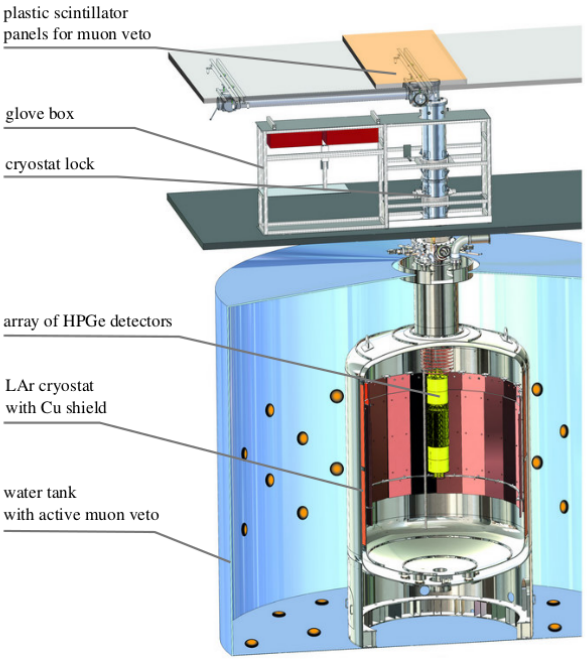

Figure 3.2: Schematic view of the experimental setup of GERDA: the array of HPGe detectors was placed in a LAr cryostat. The cryostat was placed in a tank filled with 590 m^3 pure water. PMTs detected Cherenkov light emitted by muons passing through the detector, the so-called muon veto. The clean room with the lock to the cryostat was on top of the water tank. The lock was surrounded by a glove box which was kept under a nitrogen atmosphere for the detector mounting and installation. The muon veto was complemented by plastic scintillator panels installed on top of the clean room. From [48].

3.1.1 *Phase I*

The GERDA experiment has been developed in two phases. In Phase I, five semi-coaxial diodes from the former Heidelberg-Moscow (HDM) [33] experiment (named ANG1–ANG5) and three from the IGEX [49] experiment (named RG1–RG3) were deployed; 14.6 kg of semi-coaxial detectors were used overall to take data from November 2011 until May 2013. The detector strings were covered by 60 μm thick copper cylinders, the so-called mini-shrouds, to shield the electric field and prevent the accumulation of ^{42}K on the detector surface. The energy resolution of the semi-coaxial detectors at 2.6 MeV, determined with a ^{228}Th calibration source, was about $4-5$ keV [37]. In June 2012, an additional string with five new enriched Broad Energy Germanium (BEGe) detectors totaling a mass of 3.6 kg was installed. The BI could be lowered to about 10^{-2} cts/(keV·kg·yr). Overall exposure of 21.6 kg yr was collected, and the analysis reported no excess of events above the background at $Q_{\beta\beta}$, setting a lower limit on the $0\nu\beta\beta$ half-life of ^{76}Ge of $2.1 \cdot 10^{25}$ yr at a 90% confidence level [50].

3.1.2 *Phase II*

From 2014 to 2015, GERDA underwent an upgrade, called Phase II, and it started a new data taking in December 2015. The goal of GERDA Phase II$^+$ was to achieve a sensitivity higher than 10^{26} yr on the half-life of the $0\nu\beta\beta$ decay of ^{76}Ge. For this purpose, a background index of the order of 10^{-3} cts/(keV·kg·yr) was required together with an exposure of 100 kg·yr. The LAr veto system was built to reject events with coincident energy deposition in LAr and the Ge detector array (see Fig. 3.3). The array was surrounded by a 2.2 m long shroud. On the top and bottom, 16 PMTs were installed looking toward the detector array. The detector strings were covered by nylon cylinders (the mini-shrouds). The central part of the shroud was made of a cylinder of light guiding fibers coated with wavelength shifter tetraphenyl butadiene (TPB), surrounding the germanium detector array. They were read out at the top end by silicon photomultipliers (SiPMs). TPB was used to shift the wavelength of the light into a range visible to PMTs.

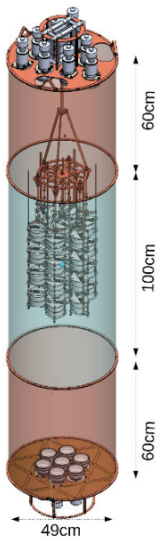

Figure 3.3: LAr instrumentation. From [48].

Furthermore, the mass of enriched germanium was increased by 20 kg, provided by BEGe detectors with good pulse shape discrimination (PSD) properties that further help to identify the background. The first data from Phase II allowed to reach 34.4 kg·yr exposure and improve the limit on the half-life up to $T^{0\nu}_{1/2} > 5.3 \cdot 10^{25}$ yr (90% C.L.) [51]. In May 2018, five inverted coaxial (IC) detectors were introduced in the GERDA experiment through a small upgrade, including also a fiber tube in the central array. From December 2015 to November 2019 (Phase II$^+$), an exposure of 103.7 kg·yr was collected, no signal event was detected, and a final lower limit of $1.8 \cdot 10^{26}$ yr at 90% C.L. was set on the neutrinoless double beta decay half-life.

The Phase II$^+$ upgrade was partly also a test bench for the next-generation successor of GERDA in the field of double beta decay physics with ^{76}Ge, the LEGEND experiment, which is described in detail in Sec.3.2.

In Phase II$^+$, a total of 41 HPGe detectors were arranged in seven detector strings.

- **^{enr}Coax** strings: 7 enriched coaxial detectors were mounted with a total mass of 15.8 kg. They were arranged in two strings.
- **BEGe** strings: 30 enriched BEGe detectors were mounted with a total mass of 20.0 kg. The detectors were arranged in four strings.
- **ICPC** string: the last string consisted of four Inverted Coaxial Point Contact detectors. `IC48B` was arranged in the sixth string with BEGes. The total mass of the five ICPC detectors was 9.6 kg.

Fig.3.4 shows the GERDA strings with the different HPGe detectors. The detectors were suited for γ rays measurements at the energy of MeV scale. Furthermore, each detector was connected to a charge sensitive amplifier optimized for low radioactivity which was operated close to the detectors

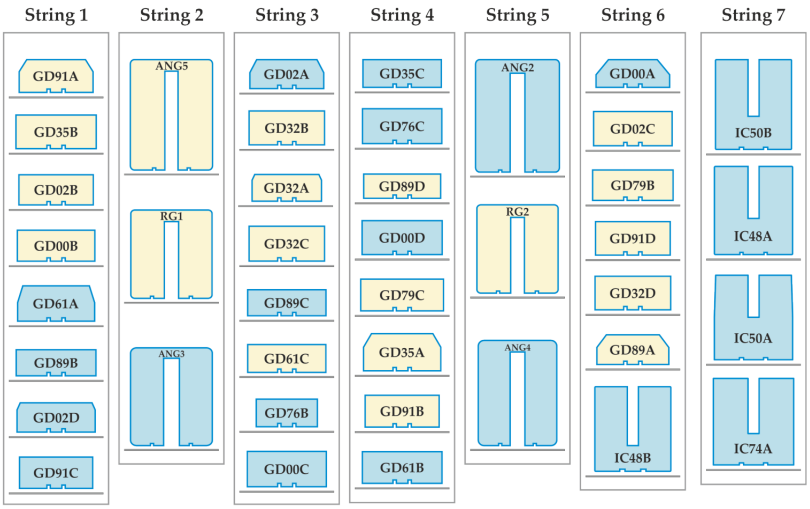

Figure 3.4: Illustration of the strings with the different HPGe detectors and their names and positions inside the experiment. Strings 2 and 5 contain semi-coaxial, Strings 1,3,4, and 6 contain BEGe and IC48A, whereas string 7 contains the other ICPC detectors. From [48].

in the LAr. The analog signal was digitized with Flash Analog-to-Digit Converter (FADC) with 100 MHz sampling frequency and analyzed offline.

Regular calibration measurements, with radioactive γ sources, provided the data necessary to determine the energy calibrations and resolutions of the diodes and to monitor their stability versus time. The LAr veto instrumentation is usually switched off during calibration runs because of the too high source activity of $\mathcal{O}(10)$ kBq. However, special calibration data were acquired with the same sources and the LAr light instrumentation was turned on to study the performance of the LAr veto system. In order to calibrate the detectors within the LAr cryostat, three ^{228}Th calibration sources were lowered into the LAr close to the array. The duration of a calibration run, usually of 1.5-3 hours, was chosen such that stronger lines, and especially the double escape peak, were clearly visible in each detector. Calibration data were taken every 7-10 days.

3.1.3 *Germanium detectors*

The detectors used in GERDA were all p-type (Coax, BEGe, ICPC). They had boron implanted p+ contact, used as a read-out electrode since the majority of charge carriers were collected here.

The germanium detector types used in GERDA are listed below (see Fig.3.5):

(a) The semi-coaxial (Coax) detectors typically had a mass around 2-3 kg and they were enriched to ~87% in ^{76}Ge. The semi-coaxial had a "wrap-around" n+ conductive Li layer and a B implanted p+ contact in the central hole, separated by a groove which was covered by an insulating silicon monoxide layer (*passivation layer*).

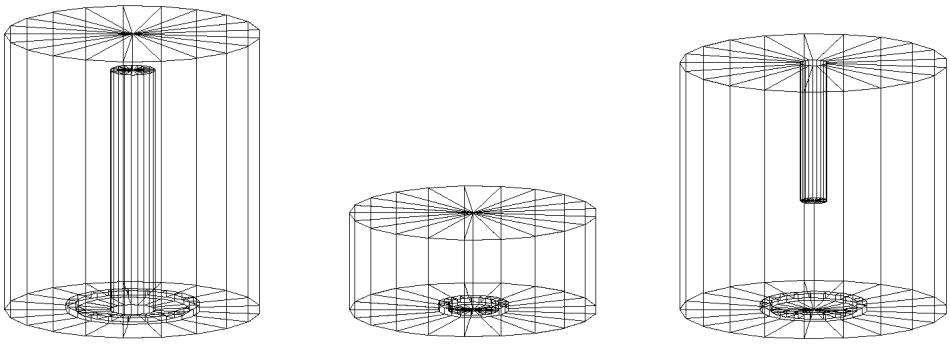

Figure 3.5: Sketch of the HPGe detector types used in GERDA, in scale. (a) Coaxial detector. (b) BEGe detector. (c) ICPC detector. More details in the text.

(b) The BEGe detectors had an average mass ∼670 g and they were enriched to ∼88% in ^{76}Ge. Unlike in the Coax, the p+ contact was very small, called the point contact readout electrode. The special geometry of BEGe allowed enhanced signal discrimination against background events. Compared to Coaxial detectors, they also registered an excellent energy resolution in a broad energy range.

(c) The ICPC detectors had the same advantageous characteristics of BEGe detectors in terms of energy resolution and pulse shape discrimination. Moreover, they provided more active volume per readout channel with a larger mass and lower surface-to-volume ratio. The small p+ contact was located in the middle of the bottom side while the Li-diffused n+ contact covered the whole outer surface, including most of the bottom part. Several studies have demonstrated the excellent performance of ICPC [52, 53].

More details on germanium detectors are available in the next chapter.

3.1.4 *Background reduction techniques*

Phase II came with some upgrades to improve the background rejection performance. GERDA set the goal to keep the expected background below 1 event in the full exposure of Phase II (100 kg yr). The background count rate was higher with respect to Phase I (factor of $\sim$ 4). This could be explained by the increased number of cables and detector holders and by the introduction of the LAr instrumentation [54].

Despite the excellent shielding of GERDA and its radiopure materials, some radioactive isotopes were always remaining from natural radioactivity, and they constituted a major background source. Because of their very small penetration depth, alpha and beta particles only contributed to the background when they were produced at (or very close to) the surface of a detector. Typical α-sources were ^{226}Ra and ^{210}Po and they were peaked at high energies (around 5.3 MeV) in the energy spectrum. Alphas lose energy in a very short range; thus, long low energy tails reached down

to the ROI and did contribute to the background at $Q_{\beta\beta}$. γ lines were distributed along the entire spectrum and they were mostly originating from ^{42}K or ^{40}K, ^{60}Co and from ^{238}U and ^{232}Th chains. The most intense γ lines from the ^{238}U and ^{232}Th chains were resulting from the decays of ^{214}Bi and ^{208}Tl, respectively. The sources could be located at different positions inside the experiment, like cables or holder structures. Especially, ^{40}K isotope was found in all screened materials while ^{42}K came from ^{42}Ar, a cosmogenically-produced isotope in LAr. Finally, $2\nu\beta\beta$ events were considered an unavoidable background source, since the finite energy resolution does not permit efficiently discriminating $2\nu\beta\beta$ events in the ROI. Different types of cuts were employed to increase the rejection efficiency of all of these backgrounds. While $0\nu\beta\beta$ events normally deposit energy in a confined volume of the detector, the background events can deposit energy in different ways. Multiple energy depositions could occur inside a single detector, therefore the Pulse Shape Discrimination (PSD) was employed in order to discriminate against these events. Furthermore, events that took place in multiple HPGe detectors at the same time were rejected (AntiCoincidence cut). Events in the HPGe detector which coincided with a scintillation light in the LAr were rejected (LAr veto). Finally, even cosmic rays were a background source for GERDA. They produced muons that could penetrate the detectors but were rejected by muon veto.

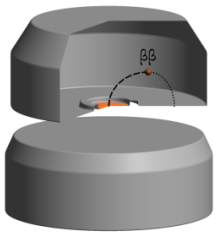

SIGNAL-LIKE

PSD techique

The drift of charges created by an ionizing particle in a voltage-biased germanium detector depends on the electric field in the diode. The $\beta\beta$ signal is a single-site (SSE) event depositing its energy in ~ 1 mm^3 germanium volume and can be considered as a point-like event. On the other hand, gammas undergoing Compton scattering or pair production are mostly multi-site events (MSE) and hence may lead to multiple energy depositions in germanium. Energetic β rays (e.g. from ^{42}K, a daughter of ^{42}Ar in LAr) created at the n+ electrode surface can penetrate the dead layer and deposit energy in the active volume. They can generate slow pulses with incomplete charge collection because of the low electric field in the lithium-diffused region. α events are mainly produced by ^{210}Po accumulated on the surface of the p+ electrode and generate pulses with short rise times and high currents. α particles can trespass the germanium detector only through the p+ electrode and the insulating groove due to their thickness and the absence of the dead layer in the groove. A good parameter to discriminate among different event typologies inside one detector is the (A/E) ratio between the amplitude A of the current pulse and the energy E of the corresponding event (see Fig.3.6). MSEs and surface events at the n+ electrode feature a lower A/E value compared to SSEs since they are characterized by wider current pulses. On the contrary, surface events at the very thin ($< 1\mu$m) p+ electrode show a higher A/E value. While the PSD technique

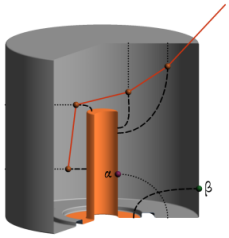

PULSE-SHAPE DISCRIMINATION

Figures at the side of this page are obtained from https://github.com/gipert/gedet-plots.

for point-contact detectors (BEGEs and ICPCs) is based on the A/E ratio of the signal, the coaxial detectors feature a more complicated time structure which requires an artificial neural network (ANN) to discriminate SSEs and MSEs.

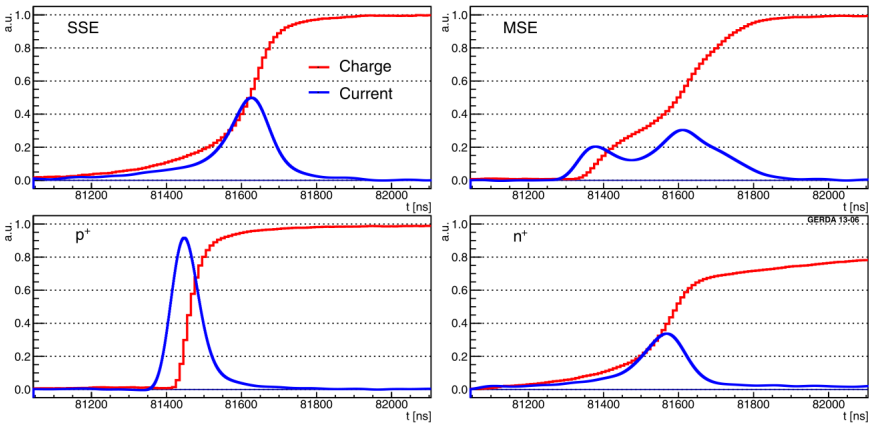

Figure 3.6: Candidate pulse traces taken from BEGe data for a SSE (top left), MSE (top right), p+ electrode event (bottom left) and n+ surface event (bottom right). Figure from [55].

Multiplicity cut

Since the $\beta\beta$ signal is an SSE in one detector, all events in which some energy is simultaneously deposited in more than one detector (i.e. multiplicity higher than one) were tagged and rejected as background. In the offline analysis of a physical event, a trigger algorithm was applied over each germanium trace from all detectors to determine the event multiplicity by checking the presence of other signals above the threshold.

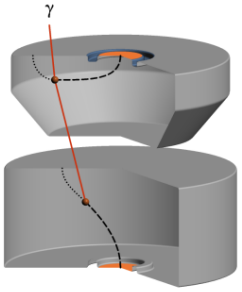

GRANULARITY CUT

LAr veto

The incident particle in LAr deposits its energy mainly by interaction with the electron shell of the argon atom which can be excited or ionized. The decay of an excited argon atom is accompanied by the emission of scintillation light at the typical wavelength of 128 nn and with roughly 40 photons/keV, measured in ultra-pure LAr. Any signal of at least one photoelectron detected by a photosensor within about 6 μs from the germanium detector trigger was classified as background. The signal efficiency of the LAr veto cut can be estimated by evaluating the number of test pulses and baseline events that were randomly flagged as background events. In Phase II$^+$, this efficiency was estimated at $(98.2 \pm 0.1)\%$.

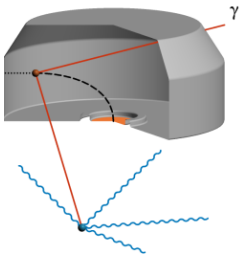

LAr veto

Figures at the side of this page are obtained from https://github.com/gipert/gedet-plots.

Muon veto

The cosmic rays produce muons that could penetrate the detector and lose energy by electromagnetic interactions and inelastic reactions with nuclei. The muon veto was used in order to reject the muons. Every event in a detector that occurs within ± 10 μs after a muon event was rejected as background. The muon veto system was designed to reduce the BI contribution from the direct muon events to a level of 10^{-5} cts/(keV·kg·yr) at $Q_{\beta\beta}$ in the region of interest and its efficiency was estimated to be of $\sim$ 99%.

3.1.5 *Data acquisition*

An FADC system stored traces from germanium detectors and from the PMTs and the SiPMs of the LAr veto, and PMTs of the muon veto, in coincidence with a germanium event. Additional artificial events were recorded by the data acquisition (DAQ) system to study the electronics. The signal waveform collected by the GERDA detectors usually presents the shape shown in Fig.3.7. The rising edge of the signal was typically around 81 μs and lasted $\sim$ 0.3 μs. Then, it decreased exponentially by a time decay τ given by the RC configuration of the electronics in order to prevent saturation. Each event had to survive a series of quality cuts tailored to discard unphysical events such as electrical discharges, pile-ups, bursts of noise, and other problematic traces with very high efficiency. These cuts were based on the flatness of the baseline, polarity, and time structure of the pulse. Physical events at $Q_{\beta\beta}$ were accepted with an efficiency larger than 99.9%.

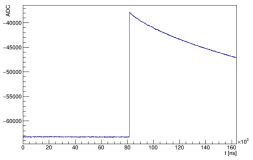

Figure 3.7: Typical waveform in *ns* collected by GERDA detectors.

The offline analysis of data recorded by the germanium detectors is performed with the software tool GELATIO [56] (GErda LAyouT for Input/Output). It handled the data by organizing them into a hierarchical structure, from the raw data to the analysis results. The multi-tier structure is shown in Fig.3.8. The raw data provided by DAQ and Monte Carlo simulations were stored in the lowest level called Tier0. Then, they were encoded and stored as Tier1; even if it contained the same information as the previous tier, it was treated as the starting point for the analysis. Tier2 contained the output information of the digital analysis (risetime, baseline, etc..) on each Tier1 event. Eventually, these files were elaborated to obtain other information, such as the calibrated energy spectrum, and stored in Tier3. More and more sophisticated information (pulse shape discrimination, veto, etc..) was encapsulated in higher-level tiers. The code used for storing the information in Tier1 output was based on ROOT [57] and MGDO [58]. The MGDO objects (MGTEvent and MGTRun) employed in the Tier1 output stored the basic information of individual events (signal traces, time stamps, etc.) and of runs (start and stop times, run type). The processing generating Tier2 file was the core of GELATIO. The analysis was divided

MGDO (MAJORANA-GERDA Data Objects): set of libraries developed by MAJORANA and GERDA collaborations.

into modules, including a chain of elementary digital filters (differentiation, integration, deconvolution, etc.) capable of extracting the information with high precision reducing the background noise.

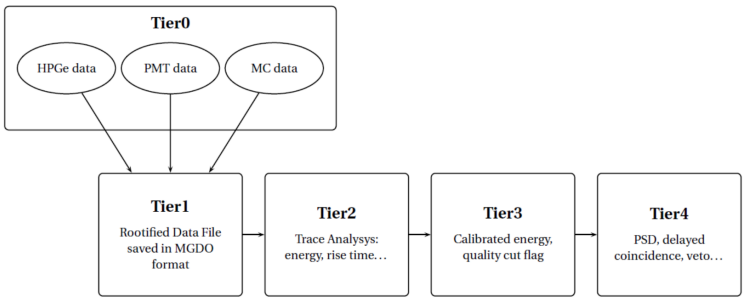

Figure 3.8: The hierarchical organization of the data in GELATIO. The framework organizes the output of each step of the analysis in a different level (Tier) starting from the raw data (Tier0) up to the parameter of the final analysis. From [56].

3.1.6 *Final* GERDA *results and next future*

As already mentioned, a good energy resolution and a low background are the keys to achieving a high $0\nu\beta\beta$ decay sensitivity. It is also crucial to define and maintain a stable energy scale over years of data taking; this is the main goal of the calibration analysis, performed by exposing the germanium detectors to ^{228}Th source. Firstly, a suitable analytical function modeled the positions and widths of the γ peaks. Then, an interpolation function was performed to obtain the energy calibration and resolution at other energies. Gaussian mixtures were used to model peaks in combined spectra, and the effective data set energy resolution was determined as a function of energy by fitting the square root of a linear function to the reconstructed widths of the γ peaks. The energy resolution was stable within 0.1 keV for most of the detectors over the full data-taking period. Noise and gain stability were monitored by test pulses injected into the front-end electronics at a rate of 0.05 Hz. The fraction of data corresponding to stable operating conditions used for physics analysis was about 80% of the total.

Fig 3.9 shows the final energy spectrum collected by GERDA during Phase II$^+$ (after the quality cuts and the multiplicity cut), before and after the LAr and PSD cuts. The LAr cut suppressed background from the ^{228}Th and ^{238}U decay chains. Focusing on the K peaks, the ^{42}K FEP events were reduced up to around 20% while the ^{40}K showed a high survival fraction since these events typically do not deposit energy in liquid argon. The PSD cuts rejected the majority of the alphas at the highest energies.

Since the beginning, GERDA adopted a blind analysis strategy to ensure an unbiased search for $0\nu\beta\beta$ decays. The model describing the energy spectrum predicted a flat energy spectrum around $Q_{\beta\beta}$. Suppose the energies of individual events fell within a range $Q_{\beta\beta}$ $\pm$25 keV, they were not converted

to the data file available for analysis but were stored in backup files only. A range between 1930 keV and 2190 keV was used to determine the BI. The energy regions around significant γ lines were excluded in the latter. The main backgrounds in Phase II in the ROI were due to the β component of ^{42}K, degraded α, ^{208}Tl and ^{214}Bi γ events.

The energy distribution of the events in the analysis window was fitted to search for a signal. The fit model included a Gaussian distribution $\mathcal{G}(Q_{\beta\beta}, \Delta E)$ for the signal and a uniform distribution for the background. The free parameters are the signal strength $S = 1/T_{1/2}$ and the background index B. The expectation value of the number of signal events scales with S as

$$\mu_s = \frac{\ln 2 \mathcal{N}_A}{m_{76}} \epsilon \mathcal{E} S \tag{3.1}$$

where $\mathcal{N}_A$ is the Avogadro number, m_{76} is the ^{76}Ge molar mass, $\mathcal{E}$ is the total detection efficiency and ϵ is the total exposure. The efficiency $\mathcal{E}$ accounts for the enrichment fraction in ^{76}Ge, the electron containment efficiency, the active volume fraction of the germanium detectors, and the analysis cuts (quality cuts, muon veto cut, LAr veto cut, PSD cut). The mean number of background events in the analysis window is given by

$$\mu_b = B \cdot \Delta E \cdot \epsilon \tag{3.2}$$

where $\Delta E = 240$ keV is the effective width of the window. Data from each detector was divided into 408 partitions, i.e. periods of time in which parameters such as the resolution and efficiency were stable. The two free parameters were common to all partitions. The statistical analysis was based on an unbinned extended likelihood function and it was performed in both frequentist and Bayesian frameworks, following the procedure described in [39]. The likelihood function was given by the product of the likelihoods of each partition:

$$\mathcal{L} = \prod_k \left[\frac{(\mu_s + \mu_b)^{N_k} e^{-(\mu_s+\mu_b)}}{N_k!} \cdot \frac{1}{\mu_s + \mu_b} \cdot \prod_{i=1}^{N_k} \left(\frac{\mu_b}{\Delta E} + \frac{\mu_s}{\sqrt{2\pi}\sigma_k} e^{-\frac{(E_i + Q_{\beta\beta})^2}{2\sigma_k^2}} \right) \right] \tag{3.3}$$

where E_i was the energy of the N_k events in the k-th partition, $\sigma_k = FWHM/2.35$ was the energy resolution of the partition, μ_s and μ_b were computed from Eq.3.1 and Eq. 3.2. The frequentist analysis was performed using two-sided test statistics based on the profile likelihood. The probability distributions of the test statistic were computed using Monte Carlo techniques, as they were found to deviate from χ^2 distributions significantly. The analysis of the $N = 13$ events of Phase II returned no indication for a signal and a lower limit was set to $T_{1/2}^{0\mu} > 1.5 \cdot 10^{26}$ yr at 90% C.L. Phase I and Phase II data together gave a total exposure of 127.2 kg·yr. The combined analysis also had the best fit for null signal strength and provided a half-life limit of $T_{1/2}^{0\nu} > 1.8 \cdot 10^{26}$ yr at 90% C.L. The limit coincided with the sensitivity, defined as the median expectation under the no signal hypothesis. GERDA achieved an unprecedentedly low background in Phase II,

as derived from the fit, of $BI = 5.2^{+1.6}_{-1.3} \cdot 10^{-4}$ cts/(keV· kg· yr), and met the design goal to run the entire Phase II data taking in the background-free regime: the background events expected in the signal region ($Q_{\beta\beta} \pm 2\sigma$) was in fact 0.3 cts. The statistical analysis was carried out also within a Bayesian framework. The one-dimensional posterior probability density function $P(S \mid \text{data})$ of the signal strength was derived by marginalizing over the other free parameters. The calculation was performed via a Markov chain Monte Carlo (MCMC), a numerical integration using the Bayesian analysis toolkit BAT [59]. The prior distribution for S was assumed to be constant between 0 and 10^{-24} yr^{-1}, as in the previous GERDA releases. The limit on the half-life was $T^{0\nu}_{1/2} > 1.4 \cdot 10^{26}$ yr (90% C.I.). Uncertainties on the energy reconstruction, energy resolution, and efficiencies were folded into the analysis through additional nuisance parameters, each constrained by a Gaussian probability distribution in the likelihood. Their overall effect on the limit was at the percent level. Potential systematic uncertainties related to the fit model were studied and found to impact the results marginally.

Assuming the $0\nu\beta\beta$ decay is dominated by the exchange of light Majorana neutrinos, the $T^{0\nu}_{1/2}$ limit can be converted into an upper limit on the effective Majorana mass about $m_{\beta\beta} = 79 - 180$ meV. It is comparable to the most stringent constraints from other isotopes [41–43]. GERDA has been a pioneering experiment in the search for $0\nu\beta\beta$ decay, reaching a half-life sensitivity above 10^{26} yr. In about a decade, GERDA improved the experimental sensitivity by one order of magnitude with respect to the previous ^{76}Ge experiments and proved that a background-free experiment with ^{76}Ge is feasible. This sets the stage for the next-generation experiment that is currently being prepared by the LEGEND collaboration.

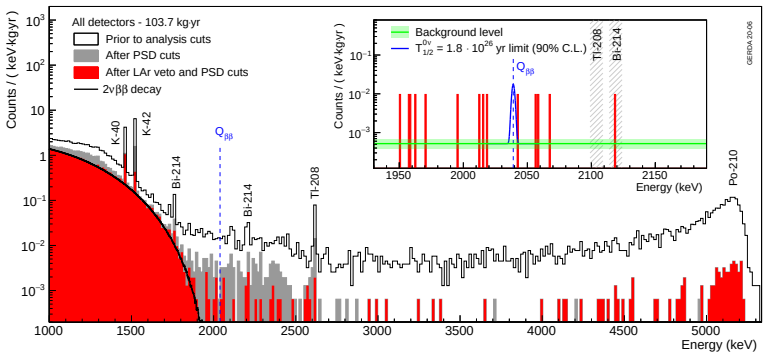

Figure 3.9: Single-detector data from the enriched detectors are displayed in a combined spectrum after indicated cuts. The inset shows unbinned data after all cuts in the analysis window and the fit results.

3.2 LEGEND EXPERIMENT

LEGEND (Large Enriched Germanium Experiment for Neutrinoless double beta Decay) [60] is building on the success of GERDA and MAJORANA DEMONSTRATOR collaborations. MAJORANA located at SURF, operated an

array of 30 kg of Ortec P-type Point-Contact (PPC) detectors, enriched in ^{76}Ge and placed in vacuum-insulated cryostats. It achieved background rate of $(16.6 \pm 0.1) \cdot 10^{-3}$ cts/(FWHM kg yr) in its low background configuration. A characteristic of MAJORANA was the production and use of ultra-pure electroformed copper. It achieved the best energy resolution (in terms of the full width at half maximum, FWHM) of 2.52 keV at $Q_{\beta\beta}$ [40]. These two leading experiments bring together their long experience in the field to help build LEGEND. It also incorporates new international institutions into the project comprising one of the most ambitious searches of $0\nu\beta\beta$ decay to this day.

The first stage of the experiment, LEGEND-200, is fully funded and will improve the GERDA and MAJORANA achievements by entering a new background regime in the region of interest at $Q_{\beta\beta}$. It aims to achieve a discovery sensitivity $> 10^{27}$ yr within 5 years of measurement time and will probe the effective Majorana mass $m_{\beta\beta}$ down to ~ 30 meV. Eventually, LEGEND-1000, the second stage of the experiment, will be able to test the $0\nu\beta\beta$ discovery by LEGEND-200 and reach new discovery sensitivities greater than 10^{28} yr, probing an effective Majorana mass $m_{\beta\beta}$ of around 10 meV. A high sensitivity experiment will clearly need maximum isotope mass as well as minimal backgrounds. These goals will be achieved by increasing the isotope mass in the germanium detectors and improving the background already achieved.

3.2.1 *LEGEND-200*

The LEGEND-200 experiment operates Ge detectors immersed in LAr in an upgrade of the GERDA infrastructure at LNGS. Using the same infrastructure not only facilitates the realization of the first stage but also provides an optimal experimental setup that enables the preservation of the record limits in radiopurity and low background. Fig.3.11 shows a schematic view of the experiment. LEGEND-200 have reached about 200 kg of detector mass, using the existing 70 kg of enriched detectors from the MAJORANA DEMONSTRATOR and GERDA, and an additional 130 kg of newly produced ICPC detectors, all mounted in strings as shown in Fig.3.10.

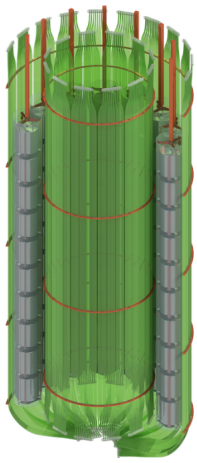

Figure 3.10: LEGEND-200 Ge detectors mounted in strings and surrounded by optical fibers that are used to detect the LAr scintillation light.

To remain nearly background-free for the design exposure of 1 ton-yr, LEGEND-200 requires the reduction of background by a factor of 2.5 w.r.t that already achieved by GERDA. This improvement is easily obtained thanks to firstly, the larger average detector mass. Consequentially, the number of nearby components, cables, and holder materials per kilogram is reduced. The radiopurity of these near-detector components is essential, as well. This can be reduced by using low-mass MAJORANA style components. Underground electro-formed copper reduced the ^{238}U and ^{232}Th chains and the cosmogenic activation of ^{60}Co in copper. The detector supports are made of scintillating plastic such as active Polyethylene naphtalate (PEN) that has replaced the optically inactive silicon plates used in GERDA. They shift 128 nm of LAr scintillation light to 440 nm. Low-noise electronics

has been achieved by combining Liquid Argon-operated preamplifier of GERDA with ultra-clean Low Mass Front-End of MAJORANA. Finally, a new reflector surrounding the detector array has been implemented to improve the scintillation light collection, and higher-purity LAr with better light transmission and light yield has been utilized. LEGEND-200 has also been an asset for the LEGEND-1000 project during its design and construction phases.

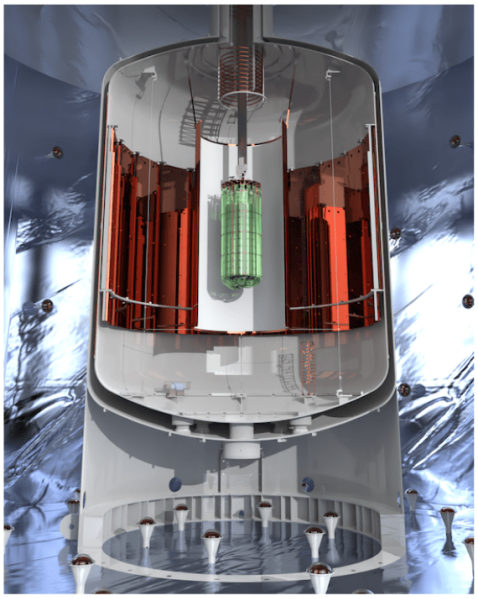

Figure 3.11: Detector systems positioned in the center of a LAr cryostat equipped with wavelength-shifting reflectors. The cryostat is placed in a water tank instrumented with photomultipliers and used as a Cherenkov muon detector.

3.2.2 *LEGEND-1000*

LEGEND-1000 [44] is designed to probe $0\nu\beta\beta$ half-lives beyond 10^{28} years for ^{76}Ge and to reach a background level of less than 10^{-5} cts/(keV kg yr). It utilizes the demonstrated low background and excellent energy performance of high-purity p-type Ge semiconductors, the ICPC detectors. The LEGEND-1000 experiment consists of approximately 400 HPGe detectors, with a total mass of around 1000 kg, made of Ge enriched to more than 90% in ^{76}Ge. They present an average mass of 2.6 kg each and are distributed among four 250 kg modules to allow independent operation and phased commissioning. In each module, the detectors are arranged into 14 vertical strings and are supported by ultra-clean materials and read out using ultra-low-background ASIC-based electronics. The detector strings are immersed in radiopure underground-sourced liquid argon (UGLAr), reduced in the ^{42}Ar isotope and contained within an electroformed copper reentrant tube. Each of the four UGLAr modules is surrounded by LAr produced from atmospheric Ar, contained within a vacuum-insulated cryostat. The LAr

volumes are instrumented with an active veto system comprising optical fibers read out by SiPMs. The cryostat is enveloped by a water tank providing additional shielding. The baseline design assumes installation in the SNOLAB Cryopit.

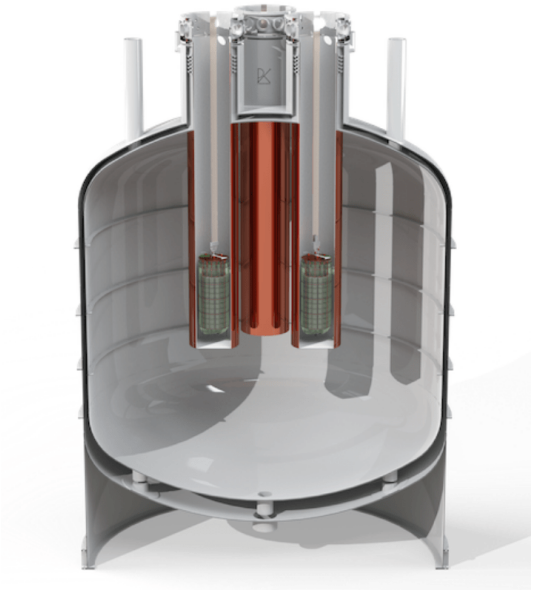

Figure 3.12: Conceptual design of the LEGEND-1000 experiment.

3.2.3 *Future goals*

LEGEND's staged approach provides a low-risk path to world-leading sensitivity. The initial LEGEND-200 phase should easily achieve a modest background improvement over GERDA with a background index of $2 \cdot 10^{-4}$ cts/(keV kg yr) or 0.5 cts/(FWHM t yr) at $Q_{\beta\beta}$. With this background level, LEGEND-200 reaches a 3σ discovery sensitivity of 10^{27} yr with an exposure of only 1 t yr within five years. Using a nuclear matrix element range of 2.66 to 6.04 for ^{76}Ge [61–63], a phase space factor of $2.363 \cdot 10^{-15}$ yr^{-1} [19, 20], and a value of $g_A = 1.27$, the LEGEND-200 discovery sensitivity corresponds to an $\langle m_{\beta\beta} \rangle$ upper limit in the range of $34 - 78$ meV.

LEGEND's ultimate goal is to achieve 3σ discovery sensitivity covering the full parameter space remaining for the inverted neutrino mass ordering, under the assumption of light left-handed neutrino exchange as the dominant mechanism. The LEGEND-1000 experiment should achieve a higher signal/background discrimination than the present generation experiments. The background goal for LEGEND-1000 is a background index of less than $1 \cdot 10^{-5}$ cts/(keV kg yr) or less than 0.025 cts/(FWHM t yr). At this background level, LEGEND-1000 reaches a half-life discovery sensitivity of $1.3 \cdot 10^{28}$ yr, corresponding to a $\langle m_{\beta\beta} \rangle$ upper limit in the range of $9 - 21$ meV in 10 yr of live time.

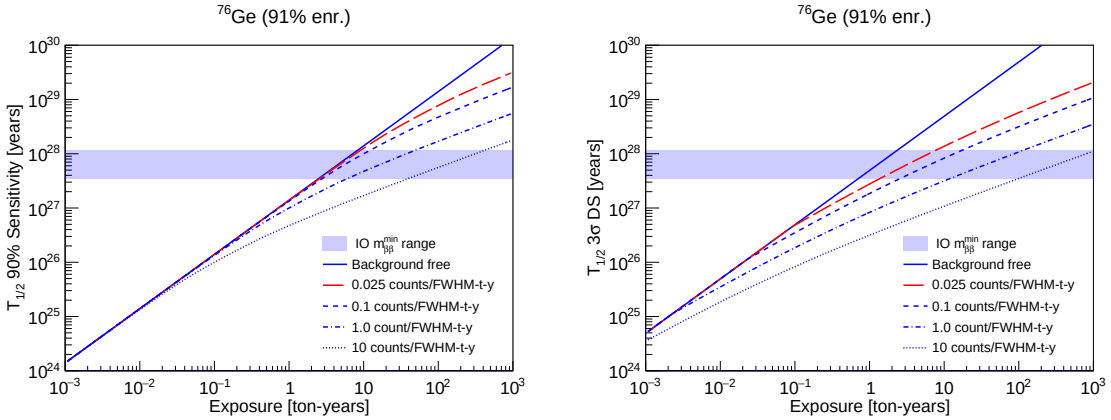

Figure 3.13: Sensitivity to a $0\nu\beta\beta$ decay signal in ^{76}Ge as a function of exposure and background for a (left) 90% CL exclusion sensitivity and (right) 3σ (99.7% CL) discovery sensitivity. Note, the background rates are normalized to a 2.5 keV FWHM energy resolution. From [44].

Part II

Active volume determination of ICPC in LEGEND-200

4

PRODUCTION AND CHARACTERIZATION OF GERMANIUM DETECTORS

The LEGEND experiment integrates the advanced technology of the detectors used in the GERDA and MAJORANA experiments. They operated germanium diodes made from enriched material. These detectors are suited for γ rays measurements at the energy of MeV scale. The crystal growing procedure results in naturally low internal radioactivity and is a well-established technology. The source itself acts as a detector as well, yielding high detection efficiency. On the other hand, since the $Q_{\beta\beta}$ at 2039 keV is relatively low it is more challenging to reach a sufficiently low background. Small abundance of $0\nu\beta\beta$ isotope in nature requires the enrichment process.

The chapter aims to describe the characteristics of the HPGe detectors used in the experiments. Some of the properties of the semiconductor material are summarized in Sec. 4.1. The description of the HPGe detectors, their production process and the importance of the detector characterization are given in Sec. 4.2. Finally, some of the tests performed in HADES are listed in Sec. 4.3.

4.1 SEMICONDUCTOR DETECTORS

Solid materials can be classified into three main categories on the basis of their electrical conductivity: insulators, semiconductors, and conductors. The e^- occupation of the energy bands – the valence band, the conduction band, and their separating barrier called band gap – is different in each category. In a crystal of semiconducting material the valence band is fully occupied and the band gap is typically of the order of 1 eV. Electrons can be promoted from the valence band to the conduction band by a sufficiently energetic primary particle. This is the basis of the operation of the semiconductor particle detector. Many semiconducting materials have to be cooled for operation since a thermal excitation can overcome the band gap promoting electrons to the conductive band and hence, providing free charge carriers for conduction. When a photon interacts in the crystal, its energy is converted to kinetic energy of an electron by photoelectric absorption, Compton scattering or pair production. Valence electrons are excited to the conduction band by the primary electron from the interaction. These secondary electrons, if sufficiently energetic, can create additional electrons, generating a cascading process. The excitation of electrons generates vacancies (or *holes*) in the valence band. The average number of electron-hole pairs is $N = E_{abs}/E_{BG}$ where E_{abs} is the energy

absorbed and E_{BG} is the average energy of the band gap. In the presence of an electric field, the electrons and holes are free charge carriers that drift toward the anode and the cathode, respectively. Semiconductors with a smaller band gap would generally have more free charge carries for a certain E_{abs} and a better intrinsic resolution.

However, even in the absence of an electric field, a small conductivity can be generated by some impurities in a real semiconductor. Additional impurities can be introduced to alter the electric properties of semiconductors (*doping process*). They can provide additional holes (p-type material) or electrons (n-type material). The diode is an electrostatic system with different types of semiconductors placed in contact with each other. Because of the concentration gradient, the electrons and the holes diffuse to the opposite side of the junction. The migration and the recombination of the charge carriers occur in the region called *depletion*. To further enlarge the depletion zone, the detectors are un-doped and present intrinsic impurities only; the outer surface is doped to form the n+ and p+ contact and the interior region can be fully depleted. In this case, the intrinsic impurity concentration determine the (p-, n-) type of the detector. In order to obtain the full depletion (active volume) over the whole detector volume, a reverse bias voltage (p-type material connected to negative voltage and n-type material to positive voltage) of thousands of Volts is applied to the detector. The value of the full depletion bias voltage depends on the size of the detector and the impurity concentration. Generally, the bias voltage recommended by the manufacturer is high enough to provide good charge collection but low enough to minimize the probability of voltage breakdown.

4.2 HPGE DETECTORS

Germanium is one of the predominant materials for semiconductor detectors thanks to its high absorption coefficient and its provision in high purity. The mobility of the charge carriers is relatively high and, the charge collection could proceed rapidly even in large volume detectors. However, increasing the size of the detector, extremely high purity material is required. HPGe detectors are produced in various geometrical configurations for the three experiments (GERDA, MAJORANA, LEGEND), as mentioned in Sec 3.1.3. For p-type HPGe detectors, the p+ electrode is typically small in order to generate a large electric field and reduce the capacitance which is proportional to the surface of the p+ contact . While in ICPC detectors it is point-like, in semi-coaxial detectors the p+ contact fills out the bore-hole and in BEGes it consists of a disk of 7.5 mm radius. The small dimensions of this contact reduce capacitance, and therefore series noise, providing excellent energy resolution at low energy. The thickness of the n+ electrode layer is typically around $0.3 - 2.0$ mm and it depends on the temperature and the time of the generating process (see following section). At room temperature (RT), this thickness can increase in time by thermal diffusion with a speed of 0.1 ± 0.04 mm/yr, according to several authors [64–66].

The thickness of the n+ contact represents a dead layer. It is the region on the surface where electric fields are so weak that electrons and holes cannot be fully collected and so their energy depositions do not result in detector signals (see Sec.5.1). The two contacts are electrically separated on the surface by a groove. In ICPCs, the well on the opposite side of the p+ contact aims to increase the electric field allowing a better charge drifting, which is indeed the dominant process in the bulk of the HPGe detector. The drift velocity of holes and electrons depends on the field orientation with respect to the detector crystal lattice, resulting in a *mobility anisotropy* [67]. The diffusion is the other process transporting the charge carries and it can be relevant only where the electric field is very small. For example, it is especially important for the energy deposition on the n+ contact [68].

4.2.1 *Signal formation*

If energy is deposited in a HPGe detector a charge cloud is formed. The measured current on the electrode is induced by moving charges close to the electrodes, as demonstrated by Shockley-Ramo theorem [69].

$$I(t) = q \cdot v_d(r_q(t)) \cdot E_w(r_q(t)) \tag{4.1}$$

where q is the total electric charge, v_d is the charge carrier drift velocity depending on the $r_q(t)$ trajectory, and the weighting field $E_w(r_q(t)) = -\nabla\phi_w(r_q(t))$ with the weighting potential $\phi_w(r_q(t))$. The latter is given by a combination of the HV applied on the electrodes and the intrinsic potential created by the presence of impurities in the depleted region. The weighting potential for a p-type HPGe is typically null throughout the detector volume and it become significant only around the p+ electrode. Thereby, if an incident radiation creates electron-hole pairs in the bulk volume, there is instantly a small current induced in the electrodes which becomes large when the holes drift into the large weighting potential around the p+ electrode. Fig.4.1 shows the general features (left), the weighting potential (center) and the electric field (right) for a p-type HPGe detector. In the vicinity of the p+ contact the holes drift along the same path (*funnel effect*) and the weighting potential is stronger with respect to the other zones [53]. The weighting potential determines the induced signal on the readout p+ electrode for drifting charges. If pairs are generated inside the n+ electrode they need a considerable time to diffuse first into the electric field; thus, they are called "slow pulses". While, if they are produced close to the p+ electrode, the induced current is immediately large; hence they are said "fast pulses" (see Fig.3.6).

4.2.2 *HPGe detectors production*

The production of the germanium detectors of GERDAand LEGEND consists of different steps. Firstly, the enrichment process of the natural germanium is performed by Isotope JSC, at the Electro Chemical Plant (ECP) in Russia,

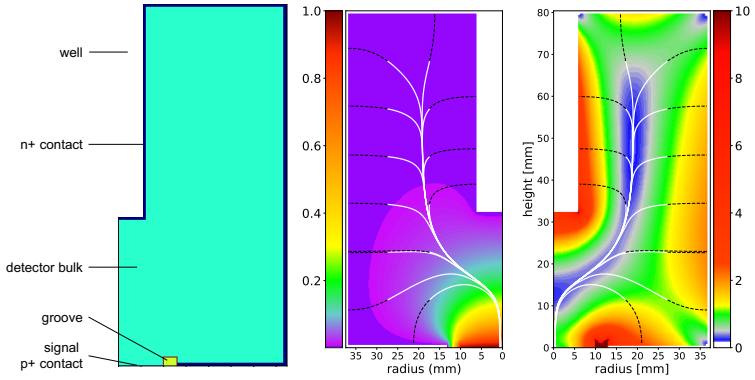

Figure 4.1: Left: main ICPC detector features. Center: calculation of the weighting potential. Right: electric field strength in kV/cm, drift paths in black dashed lines and hole drift in white solid lines. From [70].

About 1–2% of the material is lost in this processing step.

and Urenco in Netherlands. LEGEND-200 purchased material with at least 92% enrichment. The enriched Ge is delivered in the form of GeO_2 with a purity of 99.99%. Secondly, established facilities (PPM Pure Metals, IKZ) reduce the oxide to metallic germanium until 6N purity (99.9999%) and purify the material to the level required by the detector manufacturers. Finally, crystals are grown using the Czochralski process and are converted into diodes. The conversion starts machining of the groove and, for the ICPCs, of a well on the opposite side. Eventually, the Li atoms are diffused into the outer crystal surface to produce the n+ contact. In the end, Boron is implanted in the inner part of the groove for the p+ contact. The n+ contact thickness is determined by the temperature and duration of the lithium diffusion process. The result is a compromise between an efficient absorption of beta particles on the outer surface and the loss of detector active volume. Despite a long-term experience in germanium detector fabrication, the detectors processed by the companies are unique in terms of geometrical properties and internal field configuration. The detector geometry and the impurity profile are optimized to maximize the detector mass while maintaining a depletion voltage below 4000 V and a minimal electric field in the detector bulk above 200 V/cm. These two parameters are of particular importance because of their influence on leakage current and charge collection efficiency, respectively. Both contribute to the event topology discrimination performance and energy resolution. In addition, for the ICPC detectors, the weighting field distribution close to the p-contact has been included in the optimization process to add a constrain to the pulse shape performance. After this process, the crystals are finally converted into working diodes (Fig. 4.2) mounted in vacuum cryostats. Two companies handle the crystal growing and the diode fabrication. Mirion grows germanium crystals in Oak Ridge in the USA and converts them into diodes in Olen, Belgium. ORTEC processes germanium material and produces detectors entirely in Oak Ridge. Shielded storage facilities, like Cherokee Caverns (Oak Ridge) and the HADES underground lab (Mol, Belgium), are used to minimize the time above ground in order to prevent

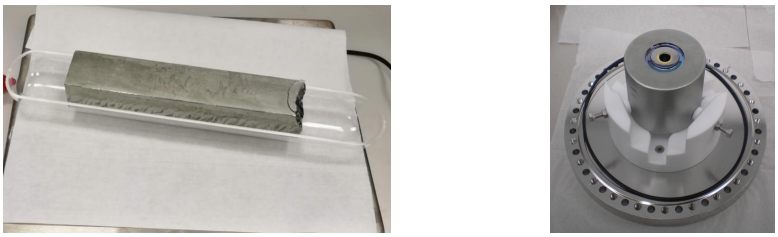

Figure 4.2: Left: starting material, Ge metal ingot. Right: final product, example of Coax detector.

cosmogenic activation of ^{76}Ge and production of intrinsic ^{60}Co and ^{68}Ge background.

4.2.3 *HPGe detector characterization*

The characterization campaign typically lasts a full week per detector.

The working detectors received from the manufacturers undergo a set of specific characterization measurements, performed in a vendor-supplied vacuum cryostat, which cannot be reproduced once the detectors are installed in the final apparatus of the experiment. Before their implementation in the LEGEND cryostat, the detectors undergo extensive acceptance and characterization tests, some of which are fundamental to estimate the rates of physical processes.

As mentioned in Eq.2.11, in the background-free regime the sensitivity of the half life of $0\nu\beta\beta$ decay scales with the product of the detection efficiency $\mathcal{E}$, the isotopic abundance a of the $\beta\beta$ emitter, and the total exposure ϵ. Once the nominal bias voltage has been determined and the homogeneity of the detector's surface has been scanned, the best achievable energy resolution is estimated. Also the determinations of the total detector mass and the material enrichment are essential. The PSD performance needs to be evaluated since it impacts $\mathcal{E}$. The latter depends also on the amount of active volume of the detector, whose analysis is explained in the following chapters. The characterization tests of the detectors are performed in underground sites to reduce the cosmic activation. The European facility is the HADES (High Activity Disposal Experimental Site) laboratory in Belgium while the SURF (Sanford Underground Research Facility) laboratory is the site used in the USA. Furthermore, special campaigns for prototype detectors are ongoing to better understand the surface events or to develop pulse-shape discrimination.

4.3 TESTS IN HADES LABORATORY

HADES is an underground laboratory managed by the Belgian research program EURIDICE [71] regarding the geological disposal of radioactive waste in Mol, Belgium. The laboratory is located about 223 m below ground and it consists of a tunnel reachable via two shafts (see Fig. 4.3). One end of the gallery is equipped with measurement apparatus belonging to the

HEROICA (Hades Experimental Research Of Intrinsic Crystal Appliances) project [72]. It is an infrastructure intended to characterize germanium detectors which are built by the former diode manufacturer CANBERRA [73] located about 30 km from there. It is optimal for this purpose thanks to the clay and sand overburden which is able to reduce the muon flux by three orders of magnitude ($\sim 0.1\ \mathrm{m}^{-2}\mathrm{s}^{-1}$) w.r.t. the ground level. At

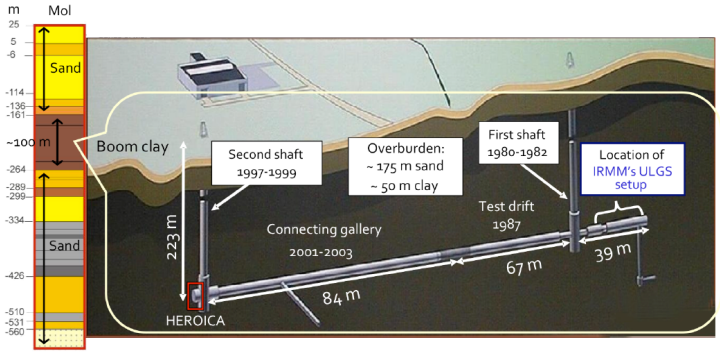

Figure 4.3: Layout of the underground laboratory at HADES. The HEROICA test facility is located behind the second shaft. From [72].

HADES, all the acceptance tests and the characterization of germanium detectors produced for the GERDA experiment have been performed in the past [74]. Starting from September 2019, the LEGEND-200 ICPC detector batches are characterized both at the SURF and HADES underground laboratories in vacuum cryostat before being deployed at LNGS in the LAr cryostat.

The aim of the acceptance tests in HADES is to verify the specifications given by the manufacturer and to characterize the detectors determining several standard parameters and the optimal operational conditions. The characterization comprises data taking with low energy gammas from ^{133}Ba [75] and ^{241}Am [76] radioactive sources and high energy gamma-rays from ^{60}Co [77] and ^{228}Th [78]. In HADES, they are installed inside a vacuum cryostat mounted in a Canberra Dip-Stick vertical dewar.The p+ electrode is AC coupled to a charge sensitive amplifier. The signal is then digitized with a Flash ADC (FADC) at a sampling frequency of 100 MHz.

4.3.1 *HADES Facility*

The details of the geometry and the material of the sources and the cryostat internal components are discussed in Sec.5.3.1.

Measurement tables

Two different setups have been designed for the characterization tests (Fig. 4.4). A measurement table presents a lead castle built on top of it, to shield the diode from the environmental background and protect the operators from the radiation generated by the calibration sources. The tables' design

Figure 4.4: Measurement platform in the HADES underground laboratory. The static tables with the lead castle are visible.

allows to park the cryogenic dewar and the cryostat at the center of the setup and to place the calibration sources in a fixed position around the detector. The other setup presents a movable arm that allows to perform detector surface scans, see Fig. 4.5. The collimated source is mounted on the arm which is parallel to the diode top surface. The source can be moved along the arm with a position resolution better than 1 mm. Moreover, the arm can be rotated around the detector z-axis and the x-axis in steps of 1 degree. The combination of the three movements allows to irradiate the detector top and the lateral surfaces completely.

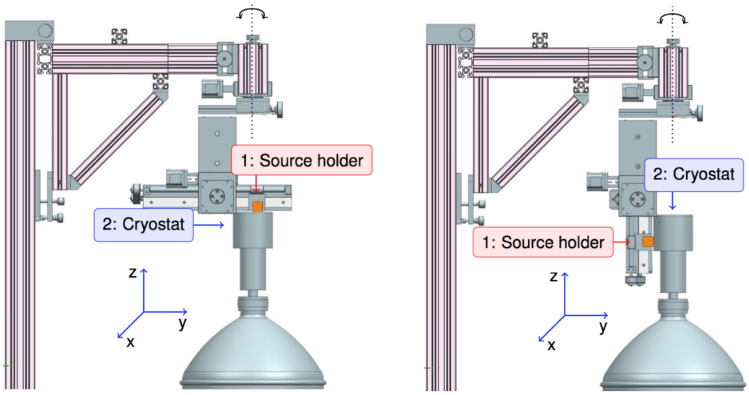

Figure 4.5: Automated measuring setup for surface scans. Left: Position for scanning the top surface. Right: Position for scanning the lateral surface. From [72].

Sources

Several radioactive sources have been provided according to the requirements of the different measurements tests. A 4.33 MBq ^{241}Am collimated source is required for the automated scanning measurements. The typical run time is about 5 minutes. The ^{60}Co source of 413 kBq is chosen for the high voltage scan measurements, which allows a complete test in less than one day. Furthermore, this source is used for active volume determination with typically 1 hour data-taking. The 4.33 MBq ^{241}Am source and the

116.1 kBq ^{133}Ba source are used for the dead layer characterization. The typical run time is about 5 hours for the ^{241}Am source and 30 minutes for the ^{133}Ba source. Finally, the ^{228}Th source of 87 kBq is provided for the pulse shape analysis, with a run time of about 6 hours.

4.3.2 *Characterization tests performed in HADES*

The characterization of several standard parameters describing the performance of the HPGe detectors such as depletion voltage, energy resolution, and pulse shape performance can be done with sources placed at a fixed distance from the detector. The measurements about the dead-layer thickness and its homogeneity are discussed in the following chapter.

Depletion voltage

The depletion voltage measurement is executed as a verification of the detector performance. ^{60}Co scans at different bias voltages are collected and the resolution and peak integral are studied as a function of the voltages. The single run lasts up to 10 minutes and with a voltage step of 100 V. The depletion voltage is set to the first best and stable energy resolution (in term of FWHM) observed in the 1173 keV and 1333 keV lines (Fig. 4.6). The recommended voltage is set to 500 V over the depletion voltage.

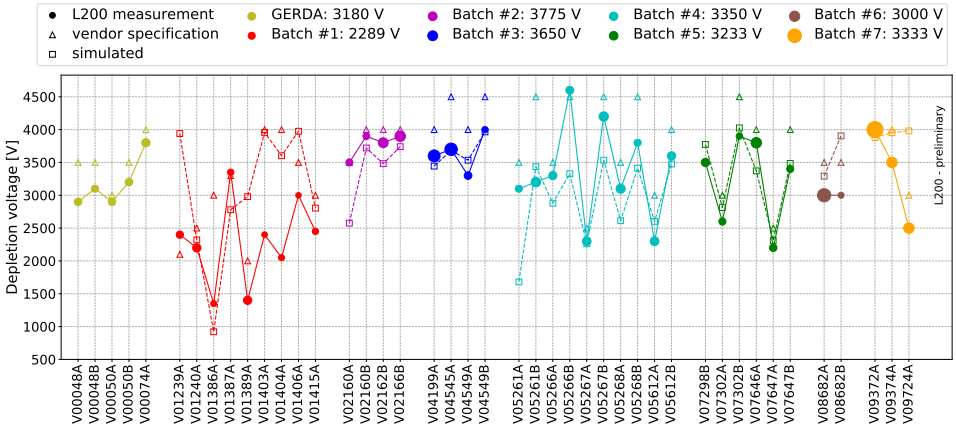

Figure 4.6: Example of depletion voltage comparison between values given by vendor, simulations, and HADES measurements for the detectors tested for LEGEND-200 experiment. The point size indicates the detector's mass. From [79].

Energy resolution

The energy resolution of an HPGe detector is defined as the FWHM of a characteristic γ-line at a given energy. In HADES tests, it refers to the 1333 keV and 2615 keV lines generated by the crystal irradiation with the ^{60}Co source and the ^{228}Th source, respectively (Fig. 4.7). The resolution curves of the points obtained fitting different peaks of ^{228}Th decay is fitted

with the function $\sqrt{a + b \times E}$. The energy-independent term represents the electric noise of the apparatus and it includes the intrinsic equivalent noise charge; the second term is related to the statistics of the charge production and it includes the Fano factor F which is ~ 0.1 for Ge [80]. Even if rare, the impurities in the HPGe detectors can impact the energy resolution. The charge carriers can be captured by the impurity atoms and no longer contribute to the drift current signal. The linear charge trapping correction factor is applied and improves the energy resolution values reported by the manufacturers (by a factor of 2 at 1000 keV) which are referring to the two γ lines at 122 keV and 1333 keV of the ^{57}Co and ^{60}Co sources, respectively.

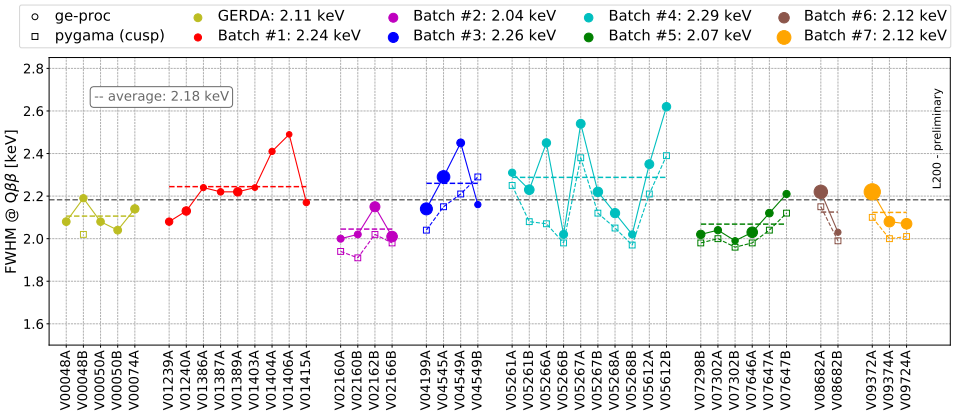

Figure 4.7: Example of interpolated energy resolution FWHM at $Q_{\beta\beta}$ for the detectors tested for LEGEND-200 experiment. Two different available software (*ge-proc* and *pygama*) have been used to compare the final results. The dashed lines show the detector mass weighted average per order. The point size indicates the detector's mass. From [79].

PSD performance

The ^{228}Th source produces a broad energy spectrum up to 2.6 MeV with both single-site and multi-site events topologies. It is appropriate to study pulse shape discrimination (see Sec. 3.1.4), whose diagnostic relies on the fraction of the surviving ^{228}Th MSEs upon the low A/E cut when accepting 90% of the SSEs from ^{208}Tl DEP at 2615 keV (Fig. 4.8). A long run with the ^{228}Th source is collected for at least 8 hours. The ^{241}Am source is used during a fine-grained circular scan on the lateral surface to study the pulse shape response to local surface energy depositions. The pulse shape properties of the detectors are not provided by the manufacturer.

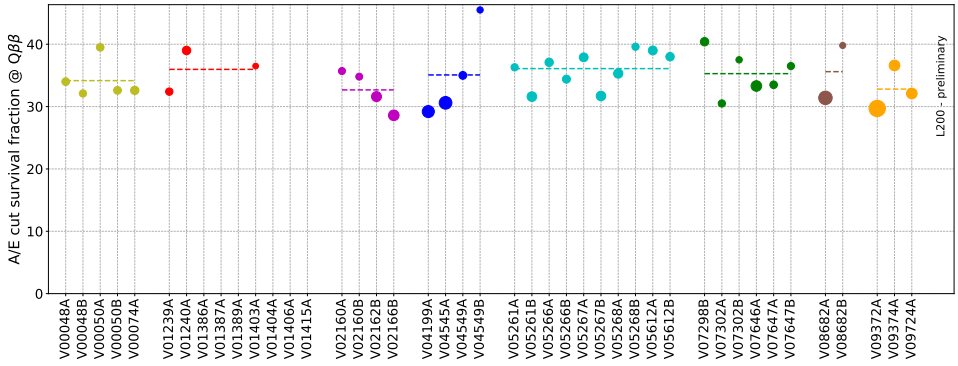

Figure 4.8: Example of PDS performance for the detectors tested for LEGEND-200 experiment. The point size indicates the detector's mass. From [79].

5 AV DETERMINATION IN HADES

The determination of the active volume (AV) of germanium detectors plays a crucial role in the detector response model, and it is fundamental to define the detection efficiency required for many analyses in GERDA and LEGEND. Furthermore, uncertainties on its size contribute linearly to rate estimates of physical processes (e.g. the $2\nu\beta\beta$ decay rate). A precision measurement of the regions nearby the n+ electrode is necessary since they do not contribute to the AV of the detector.

This chapter reports the estimation of the dead regions and the AV of the ICPC detectors of LEGEND-200, using the data collected during the HPGe detector characterization tests performed in the HADES laboratory. The dead layer and the active volume are defined in Sec 5.1 followed by the scheme of the analysis flow. The selection and processing of the data are illustrated in Sec.5.2. Then, Sec.5.3 shows a detailed description of the geometry implementation and the macro construction for the Monte Carlo simulations. Therefore, the post-processing of the simulations is presented in Sec.5.4. After these introductory sections, Sec.5.5 describes the analysis for the determination of the FCCD and the AV, with a previous validation of the MCs with the ^{228}Th source (Sec.5.5.1). The ^{133}Ba (Sec.5.5.2) and ^{241}Am sources (Sec.5.5.3) are used for this purpose but a calibration of the ^{241}Am source is required first (Sec.5.5.4). The study on the systematics uncertainties and final results are reported in Sec.5.5.5 and Sec.5.5.6, respectively. Additional analysis on the FCCD at the bore-hole (Sec.5.5.7) and the homogeneity of the FCCD along the surfaces (Sec.5.5.8) are performed. Finally, Sec.5.5.9 determines the AV for each detector, and Sec.5.5.10 sums up the conclusions of the obtained results.

5.1 ACTIVE VOLUME AND FCCD

The detector's active volume is not equivalent to the entire volume since the charge-collection efficiency (CCE) differs from unity in the regions close to the n+ contact around the outer surface of the detector. The p+ contact is not considered in this analysis since it has a negligible thickness of the order of 1 μm. On the contrary, n+ layer is expected to have a thickness of $\mathcal{O}(1)$ mm. As mentioned in Sec.4.2.2, the n+ contact thickness strongly depends on the lithium diffusion process. The lithium impurities act as recombination centers for charge carriers. Since a measurable signal is created by charge separation in the detector, the impurities cause the reduction of the recollected energy deposited by the events in these regions. Thus, the CCE curve is determined by the lithium concentration profile

which is specific for each detector. The full charge-collection depth (FCCD), defined as the depth at which the CCE reaches unity, consists of a dead layer (DL) where the CCE is negligible and a transition layer (TL) where the charges are partially collected (see Fig.5.1). In this analysis, the TL is ignored, and the FCCD and DL are equivalent. Furthermore, the FCCD has supposed to be the only dead region in the detector with a homogeneous thickness all around the n+ surface. Moving from these assumptions, the active volume can be computed as the difference between the total volume of the detector and its FCCD volume. The FCCD must be characterized for each detector individually due to the singularity of the CCE.

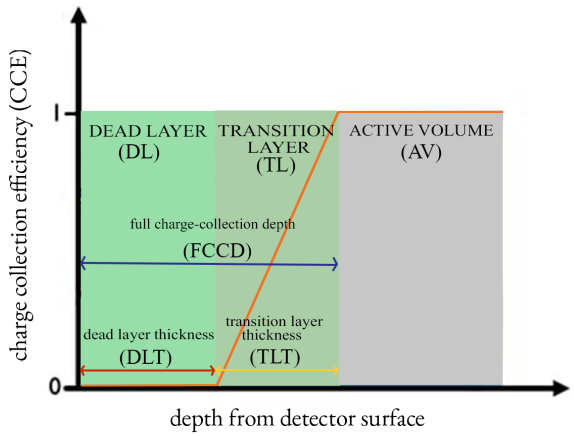

Figure 5.1: Germanium detector's active volume model. The charge-collection efficiency is zero through all the dead layers. Then, the CCE gradually increases in the transition layer until reaching unity in the fully active volume.

The FCCD is determined through gamma spectroscopy which focuses on discrete energy deposition such as full energy peaks (FEP). γ-rays fully contained in the active volume contribute to FEP events, while surface events that occurred in the FCCD region are not detected. The γ-rays can interact with the germanium detectors by three processes dominant at different energies: photoelectric effect, Compton scattering, and pair production. For all processes, the initial γ-ray transfers its energy to a fast electron which creates a measurable effect. When a γ-ray flux of intensity I_0 is incident on the germanium for a distance d, the emerging intensity I is given by the exponential expression:

$$I = I_0 \cdot e^{-\mu \cdot \rho \cdot d} \tag{5.1}$$

where ρ is the germanium density, and μ is the germanium mass attenuation coefficient (expressed in cm^2/g) dependent on the γ-ray energy and the germanium atomic number (Z). The length at which the beam flux has dropped to $1/e$ of its incident flux is called attenuation length d_0. Fig.F.2 and Fig.F.1 show the mass attenuation coefficient and the attenuation length for different interaction processes in the germanium, and for different materials of interest for the analysis.

5.1.1 *Analysis procedure*

The basis idea of the analysis is to compare the gamma spectrum of a calibration source with Monte Carlo simulations of the measurement in which the FCCD of the detector is varied. The data spectrum is calibrated, and the computed energy resolution is used for the energy smearing of the related simulation. The inferred FCCD of the detector is the FCCD in the simulation spectrum that best describes the measured spectrum. Finally, the active volume is computed from the measured FCCD and the dimensions of each detector. This general procedure follows the steps performed for the characterization of the BEGe detectors in GERDA described in [81]. Fig.5.2 shows the workflow of the automated analysis of many detectors.

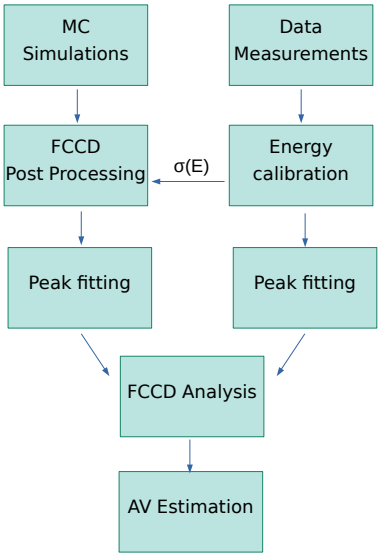

Figure 5.2: Workflow of the FCCD analysis through the comparison of calibrated data and post-processed simulations.

5.2 DATA

The data are taken both in the static and scanning tables. Below, only the measurement campaigns used for the following analysis are listed. Firstly, the HV is set to the depletion voltages estimated for each detector by previous ^{60}Co measurements in HADES (see Sec.4.3). Below, the different measurements are listed ordered by the source used:

1. Detectors are irradiated by the ^{228}Th source placed in a radially centered static position of 38 mm above the detector. The source is encapsulated in the copper holder, which is placed upon a plexiglass volume, called source holder, defining the fixed distance between the source and the cryostat. The run time is about 6 hours. An additional run with the source stably placed along the side of the detector is

taken for 16-17 hours.

2. Measurements with the uncollimated ^{133}Ba source are taken for 30 min at two different distances from the top of the detector in the centered radial position. Only the data with the source at a distance of 78 mm are considered in the analysis because not all the detectors have been irradiated from the two positions.

3. Long measurements with the collimated ^{241}Am source are usually taken with the source in three different positions at the top surface of the detector. The runs with the ^{241}Am source in a radial position away from the bore-hole are selected to better estimate the FCCD at the top side of the detector. The distance of the source from the cryostat is usually less than 10 mm. The runtime is about 5-6 hours.

4. Detailed scans are performed with the low energy ^{241}Am source. The highly collimated γ-rays probe the top and side surfaces of the detector through linear, longitudinal, and circular scans. These positions allow to check for the homogeneity of the detector surface response.

All experimental data are recorded using Flash-Cam digitizer.

5.2.1 *Digital Signal Processing*

lh5 is the LEGEND HDF5 format.

The LEGEND collaboration has developed *pygama*, a proper package for converting physics data acquisition system output to lh5 files and analyze data events. The digital signal processing (DSP) of the HPGe detectors consists of different steps.

Firstly, the baseline is analyzed and restored. Checking the regularity of the baseline provides an efficient tagging of pile-up events and non-physical events, such as pick-up noise or electrical discharges (see Fig.5.3). The noise frequencies are tracked during the data taking since it allows monitoring the setup's stability and the DSP algorithms. The baseline can be restored by subtracting its resting value from the waveform so that the baseline average value is zero.

Secondly, the characterization and correction of the decay tail after the leading edge consists of identifying the decay constant and deconvolution of the exponential function decay. The event's energy can be estimated after the deconvolution when the waveform after the end of the leading edge follows a constant distribution with the mean equal to the maximum voltage amplitude. Finally, this new flat baseline is checked again to remove bad events with a secondary leading edge in the decay tail.

Thirdly, the leading edge analysis is essential for the signal processing since it provides timing information on the evolution of charge collection.

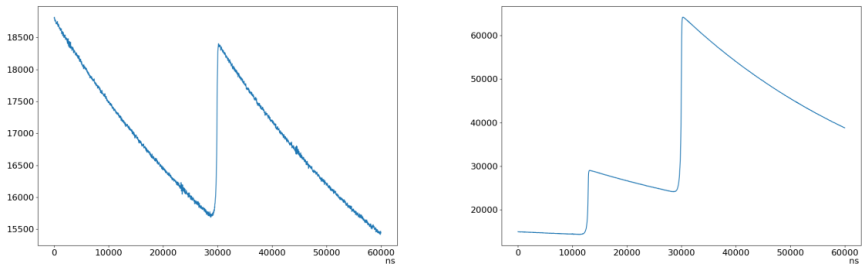

Figure 5.3: Examples of pile-up events. Left: "pre-trace pile-up" sitting on the decay tail of a pulse occurring before the waveform starts. Right: the primary waveform is anticipated by another pulse occurring in the baseline section of the waveform. From [82]

It consists of the estimation of the overall charge collection time defined by the times at which charges are generated and are fully collected. They are respectively established by a walk-back and walk-up leading-edge trigger with respect to a specific threshold. The drift time can be found easily from the difference between the two times, while the rise time of any fraction of the waveform can be found by taking simple fractions of the energy and walking back until the threshold is found.

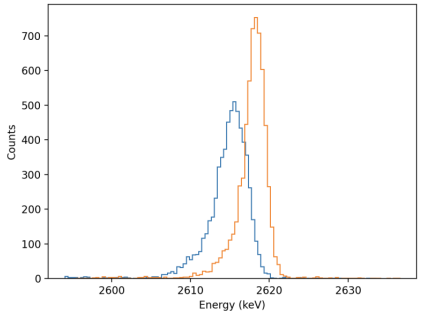

Figure 5.4: γ peak at 2614 keV before (cyan) and after (orange) the charge trapping correction with the Qdrift parameter. From [82]

Finally, the energy is reconstructed by extracting the amplitude of the voltage signal through different energy filters and charge trapping correction (*ctc*) techniques. The charge trapping mainly occurs for events depositing energy at the top of the detector. Since they are affected by long drift, the charge trapping is more likely. The *ctc* is fundamental to improving the energy resolution estimation. In the data analysis and the following calibration, a CUSP filter and the *ctc* with the Qdrift parameter are used (see Fig.5.4) to extract the associated energy deposition. After convolving the filter kernel with the exponential decay added by the electronics, it is then convolved with the waveform. The Qdrift parameter is based on calculating the effective drift time (based on a symmetrical trap filter) considering the uncollected charges. Quality cuts (QC) can be applied to remove pile-up events in the decay tail or baseline.

Filter kernel: an exponentially rising section and a symmetrical falling section separated by a flat section.

5.3 MONTE CARLO SIMULATIONS

The LEGEND collaboration has developed a simulation suite based on GEANT4 called G4simple [83]. It is appropriate for modeling simple geometries such as detector characterization test stands. It is flexible with the format of the output files - ROOT, hdf5, xml, csv. The geometry is supposed to be implemented in GDML files. A significant amount of effort was put into the first stages of the simulation development, starting from collecting precise dimensions, positions, and materials of the set-up components. For instance, improvements in the simulations have been revealed by including the lead castle for the static measurement or by enhancing the material of the source holders. Each component's density and chemical composition have been investigated since some metal components were found to have the wrong specification. Furthermore, the choice of the physics list and the source generator settings played a crucial role in validating the simulations. The ^{228}Th source has been used to validate the simulation settings. Once the geometry and macro files have been finalized and checked, the FCCD analysis with the ^{133}Ba and ^{241}Am sources can proceed. The simulation process has been automatized to handle the next measurements easily.

5.3.1 *Geometry implementation*

The geometries and the materials of the set-up components are listed below. As mentioned in Sec.4.3.1, the lead castle is mounted only in the static table. The movable arms of the scanning table are not simulated since they have no relevant effect on the energy spectra. The cryostat contains the detector, surrounded by the holder and the wrap. In long measurements, the source needs an additional holder to be fixed at a defined distance from the cryostat. The App.A shows drawings, images, and schemes of the components.

Lead Castle

The lead castle has been constructed on top of the static table, and is made of a set of Pb bricks of the same dimensions ($10 \times 10 \times 5$ cm^3). It consists of a cubic shape with an inner cavity where the source components and cryostat inner components are housed. Additional bricks cover the top and the front sides. Fig 5.5 shows the set-up components of a static measurement with the detector irradiated by an uncollimated ^{133}Ba source.

Source

The geometry of the source encapsulations, as well as the size of the active elements, are different among the sources. The 7 mm cylindrical encapsulation of the ^{228}Th source is made of stainless steel, and the activity is located in a 1 mm^3 silicon-dioxide cube 3 mm above the window filled with epoxy wrap. During the top measurements, the source is inserted

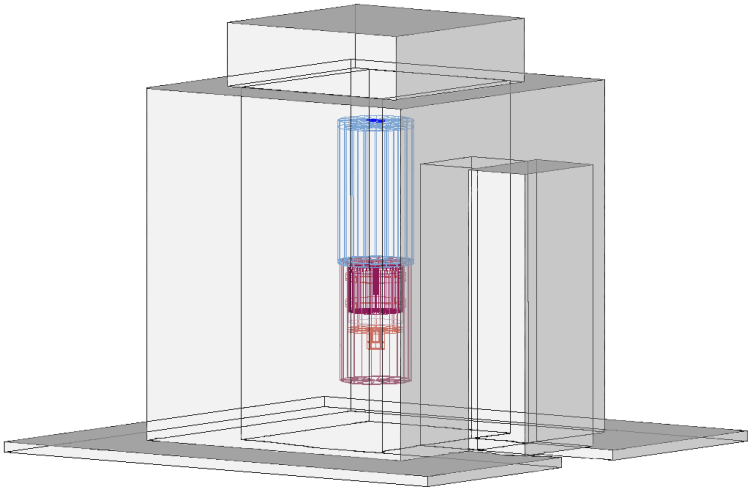

Figure 5.5: Visualization of the simulated overall set-up in the static table. The lead castle shields against the inner components whose zoom-in figures are posted below.

in a copper holder with additional 2 mm thick lead plates at the bottom to prevent the source from falling. The Al encapsulation of the ^{133}Ba has a ring shape with 3 mm height, 20 mm inner radius, and 30 mm outer radius. It surrounds a polyethylene double-foil including the active element, which is implemented as a cylinder with a diameter of 5 mm and a height of 0.01 mm. The cylindrical encapsulation of the 5 MBq ^{241}Am source is made of stainless steel and two 1 mm^3 cubes of an unknown material contain the activity. The front side is only 0.2 mm thick. The source is embedded in a collimator consisting of a copper box. The encapsulation of the uncollimated ^{241}Am source (figure on the side) has a rectangular shape (11.08 $\times$ 23.08 mm^2) with a thickness of 2.02 mm. The activity is located within a diameter of $\sim$ 1 mm, and the best fitting material is acrylic ($C_5H_8O_2$) with a density of 1.15 g/cm^3. The activities of the sources are listed in App.A.

Source Holder

A set of plexiglass source holders have been provided for all top static measurements. They are made from cylindrical segments with fixed heights that can be piled up in series to set the source at different and reproducible distances from the detector. The extensions have a height of about 40 mm, 81 mm, and 160 mm. The cylindrical bottom segments of 38 mm fit the cryostat housing. The top segments have a cavity in the middle, which can house encapsulated sources. For the runs with the ^{228}Th set at the side position, a ring-shaped source holder of 65 mm high is used. It surrounds the detector, and the encapsulated source is placed in a small cavity in the side.

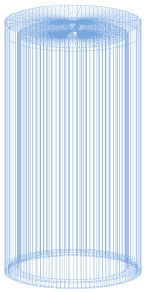

Cryostat

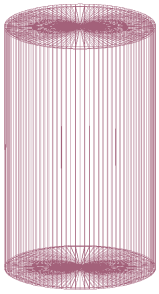

Cryostat consists of the end cap covering the detector, the preamplifier housing and the cooling finger. Despite that, only the end cap and its inner parts have been simulated. This simplified geometry is expected to be a good approximation since the calibration sources have been typically placed above the end cap's top or lateral surface. The standard vacuum cryostat of 101.6 mm diameter and 171 mm height surrounds the detector set-up. Only the detectors of the last orders, at the time of writing, present a larger width requiring a larger cryostat. The thickness is 1.5 mm everywhere. It is made of an aluminum alloy - EN AW-2011T8, which is implemented in the MC simulation as a new material with a density of 2.84 g/cm^3 and the following composition: Cu (6%), Pb (0.4%), Bi (0.4%) and Al (residual part).

Holder

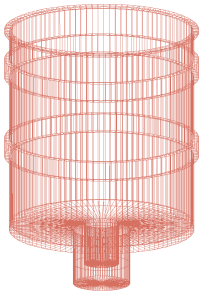

The detector holder is made of the same aluminum alloy as the cryostat, and its dimensions are specific for each diode. Due to missing information, the height of the bottom part in connection with the electronic base has been reasonably set to 25 mm for all detectors. In order to stably mount the diode, the holder can arrange support rings (usually 8.6 mm width and 3 mm thickness). The rigs are equipped with stainless screws for the detector fixation. However, the screws are not relevant for the simulations.

Wrap

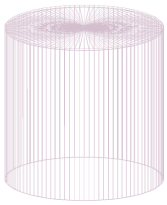

The insulating high-density polyethylene (HDPE) cup surrounds the detector. It presents a cylindrical geometry whose dimensions depend on the size of the detector. Generally, the top width is 1 mm while the side is 0.5 mm. The used HDPE is the HD1000 which has a density of 0.93 g/sm^3.

ICPC detectors

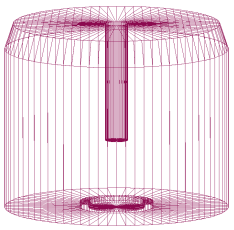

The HPGe detector typically has a cylindrical geometry. However, many of the LEGEND-200 ICPC present some particularities: bulletization on the borders (e.g. `V05261A`), internal and/or external tapered geometries on the top and/or bottom of the diode (e.g. `V04199A`, `V05267A`), a second groove geometry at the top surface (`V02162B`), an asymmetrical crack at the bottom of the diode (`V02160A`), multi-radius at the bottom section (`V07646A`). Minor deviations from the ideal shapes, such as bulletizations, are not simulated and are considered systematic uncertainties.

5.3.2 *Event sampling*

The events from ^{228}Th, ^{133}Ba, and ^{241}Am sources are generated by using the physics list Low Background Experiments (LBE) and the General Particle Source (GPS) tools of GEANT4. The LBE physics list is recommended for underground physics. The opening angles of sources are limited toward

the detector direction to increase the statistics of detected events. The radioactive decay of the ^{228}Th source is implemented by simulating the isotopes of the primary high-energy daughter decay modes ^{208}Tl, ^{212}Bi and ^{212}Pb, according to their branching ratio. As for the ^{133}Ba, the entire decay chain is simulated, generating ten files with 10^7 events each. The radioactive decay of the ^{241}Am source is generated by simulating single peaks of the decay according to their emission probability: 59.5 keV, 99.0 keV, 103.0 keV, 123.1 keV, 125.3 keV, 208.1 keV, 335.4 keV, 662.4 keV. Fifty files are generated with different random seeds containing 10^8 events each for sufficiently high statistics in the low probability γ-lines.

5.3.3 *Automation of the g4simple simulations*

An automation project has been developed to expedite the simulations and the analysis [84]. The components around the detector usually have the same geometry, although the dimensions can be different. This condition allows GDML files to supply the complete implementation of the volumes, leaving the entries of size values empty. The code, then, provides to correctly fill these gaps according to the metadata files of the simulated detector. On the other hand, the geometry of detectors is not standard, and all the possible shapes, shown until the last order arrived at the time of writing, have been implemented in the code. One pre-compiled GDML file is created for each set-up component to flexibly and quickly simulate new measurements. Then, a `main.gdml` file outlines the overall configuration of the measurement by reading the required components' GDML files. For instance, if a component is removed in a data measurement, the simulation can easily reproduce this exceptional configuration without any critical variation to the code. It is enough not to allow the `main.gdml` file to read the related GDML file of that component. The `main.gdml` file is the only file read by the macro file to implement the geometry. The macro file is an ASCII file containing UI commands, and also provides all the information related to the runs, such as the setting of the physics list, the number of events, the source type, the source energy, etc. G4simple uses the GEANT4's generator and the GEANT4's analysis manager with various configurable options like the output format and the sensitive volumes. To decrease the simulation run time, one can split the simulation into different runs. Hence, several macro files can run for the same measurement simulation. The value of the random seed and the name of the output file neatly differ among the macros. Since the run measurements are supposed to follow a protocol, the macros can also be automatically generated. The settings information related to the kind of measurement and the macro commands is given to the code by a proper JSON file. For the standard measurements in HADES, there are pre-compiled JSON files for each kind of measurement - such as ^{228}Th source in static measurement or ^{241}Am in scan table. Thus, the user only needs to change the name of the detector and its position. App.B provides two examples of a GDML file and an ASCII file.

5.4 POST-PROCESSING OF SIMULATIONS

The high amount of MC simulation time required to repeatedly simulate each detector with increasing FCCD resulted in finding a more efficient approach. Firstly, only one simulation of a specific data run is generated without any FCCD in the detector. Hence, the active volume of the detector equals the entire detector volume in the simulations. The position of each MC energy deposition (hit) is recorded. Eventually, in the post-processing the hits are incrementally cut due to the FCCD effect, depending on their distance from the detector surface. An increasing thickness of the FCCD cuts more and more events out of the same sample. The FCCD is increased from 0 mm to 2.0 mm in steps of 0.1 mm. The result of the event cuts clearly has a greater effect for surface events, such as the ones generated from the ^{241}Am source, and for low energy γ-lines, which are affected by attenuation. Finally, the deposited energies of the remaining hits are summed together for each event. They are smeared to model the detector response using a Gaussian function whose parameters are derived from the data calibration.

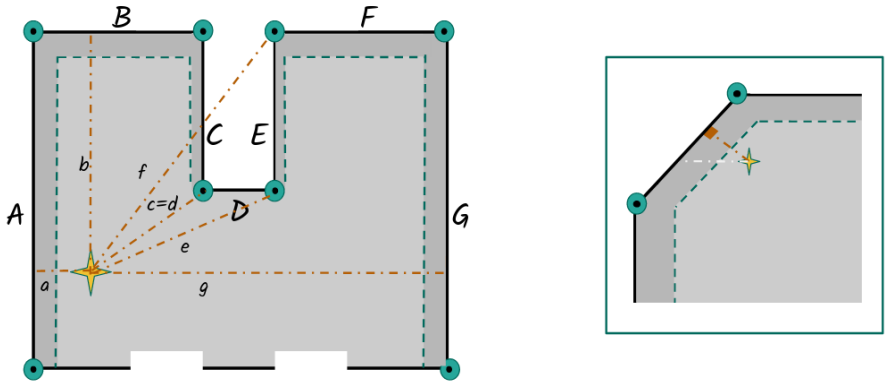

Figure 5.6: Scheme of the distances of an event (star) from all the detector surfaces. The inset shows the case of the correct distance (orange) from a taper surface.

5.4.1 *Automation of the post-processing*

As for the automation of the simulation, the post-processing has been automatized for each detector. The automation code is written in Python to handle the lh5 format of the data easily. Since the diodes are azimuthally symmetric [1], in the following, only the (r, z) coordinates are used. Hence, the analysis treats the z-projection of the detectors, and the borders are represented by segments S with extremes (s_1, s_2). The origin point $(0, 0)$ is set to the top center point of the detector due to the volume construction with the `GenericPolycone` tool in G4simple. The code computes the event's distance in the point v from the detector surface as the minimum distance of the distance set from each border segment (including the taper borders).

1 `V02160A` detector shows an asymmetrical cut at the bottom, nevertheless it is treated in the same way without the cut since the analysis is focusing on the top surface

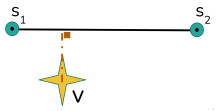

Given a surface segment $\overline{s_1 s_2}$, the distance d is computed as the length of the segment with the event point v and its projection $proj$ on $\overline{s_1 s_2}$ as extremes. $proj$ is defined as

$$proj = s_1 + (s_2 - s_1) \cdot max\left\{0, min\left\{\frac{(v - s_1)(s_2 - s_1)}{length(s_1, s_2)}, 1\right\}\right\} \tag{5.2}$$

where $lenght(s_1, s_2)$ is the length of $\overline{s_1 s_2}$. Finally, the code returns the value of the CCE at the distance of the hit, considering an FCCD step model. Additionally, the analysis at the bore-hole (see Sec.5.5.7) highlights the different FCCDs around the bore-hole surfaces w.r.t. the other n+ surfaces. Hence, the hit is selected only if the minimum of the two CCE values, computed at the minimum distance from the bore-hole and at the minimum distance from the other surfaces, is different from zero. Otherwise, the hit is rejected since it is meant to be in the FCCD region.

5.5 FCCD/AV ANALYSIS

A correct determination of the AV is crucial for a precise detector efficiency calculation in GERDA and LEGEND. Only γ-rays depositing their entire energy in the AV can turn into a FEP, which is required for the identification of the potential $0\nu\beta\beta$ decay. As already mentioned, the basic principle behind the FCCD and AV determination is a comparison of the energy spectra obtained from a calibration source measurement with a MC simulation, which simulates the same experimental setup, and can vary the FCCD. In order to achieve the highest possible precision, an accurate description of the experimental setup in the MC simulation is mandatory. Thereby, a ^{228}Th source is used to validate the goodness of the implementation of the simulation. Afterward, an uncollimated ^{133}Ba source is used for the FCCD analysis. A collimated ^{241}Am source is also meant to be a proper source for this purpose. However, calibration of this source with an uncollimated one was necessary due to unknown details on its material. After examining all potential systematic effects arising from the experiment and the MC, the analysis returns the final estimations of the FCCD with their uncertainties. Furthermore, to better investigate the FCCD in the specific geometry of the ICPC, a detailed analysis of the FCCD at the bore-hole and an investigation of the surface homogeneity on the top and lateral detector sides are carried out. Finally, the FCCD results are translated in terms of AV estimation.

5.5.1 *Simulation validation with the ^{228}Th source*

The energy spectrum of HPGe detectors irradiated by a ^{228}Th [78] source in HADES is easily recognizable. It is mainly characterized by gamma transitions of β products of the elements - ^{212}Pb, ^{212}Bi, ^{208}Tl - of the ^{228}Th decay chain . Detectors hardly see products of α decays due to their short range, which commonly does not allow the achievement of the p+ electrode surface, especially if the source is set at the opposite detector side. Since in

HADES, most of the apparatus set-up is the same for every runs, the ^{228}Th source is appropriate to probe and validate the simulations before starting the FCCD analysis with other sources. An unexpected mismatch between the ^{228}Th energy spectra of the data and the simulation can be due to a wrong geometry implementation in the GDML files or to a wrong Physics List choice.

As already mentioned in Sec.5.3.2, G4simple simulations are produced by implementing only the ^{212}Pb, ^{212}Bi, ^{208}Tl isotopes. Fig. 5.7 shows the simulated hits' space scatterplots in x-y and x-z planes. In the visualizations of the z-x plane, the source is at the bottom side of the plot. The deposited

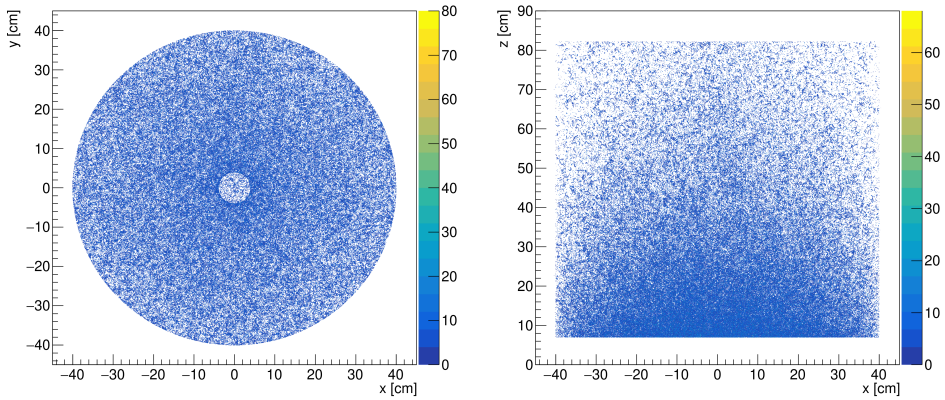

Figure 5.7: Simulated hits in `V02160A` with source set at the top of the detector. Visualizations into the xy-plane (left) and xz-plane (right). The ICPC detector's bore-hole is clearly visible in the center of the xy-plane scatterplot.

energies of the hits undergo Gaussian smearing to model the detector response. The width of the Gaussian is obtained by fitting known peaks of the observed calibrated ^{228}Th spectrum. The fitting function is a combination of a Gaussian signal peak, a constant background, a low energy tail accounting for phenomena such as incomplete charge collection or ballistic deficits, and a Step function representing a possible difference between each side of the peak (Fig. 5.8). The full width half maximum (FWHM) of the Gaussian peaks are then fitted by the resolution curve $\sqrt{a + bE}$. The term a describes the electric noise of the apparatus independent of the energy, and it includes the intrinsic equivalent noise charge called ENC; the term b is related to the statistics of the charge production, and it includes the Fano factor F, which is ~ 0.1 for Ge [80]. Then, the event energies are adjusted according to random samples from the normal distribution $\mathcal{N}(\mu, \sigma)$ with μ equal to the original energy and σ derived by the resolution curve. Finally, the simulated energy histograms of ^{212}Pb, ^{212}Bi, ^{208}Tl (Fig. 5.9) are weighted and combined according to their known branching ratios.

The simulation framework underwent several improvements, including more sophisticated measurements of the dimensions and materials of the setup components, to achieve its final version. The additional lead plate at the bottom of the source holder allowed to better reflect the data spectrum

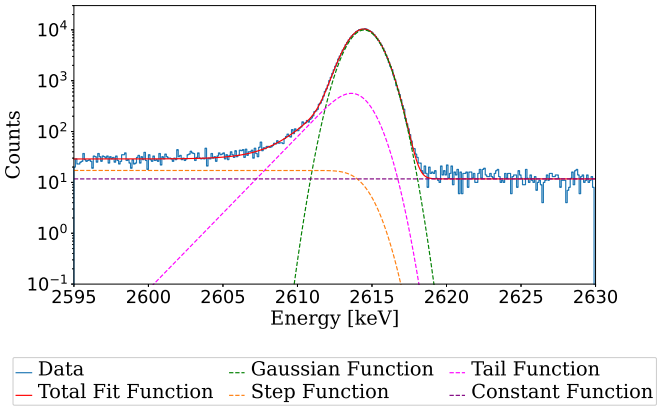

Figure 5.8: Example fit of the γ peak at 2614 keV with the functions described in the text.

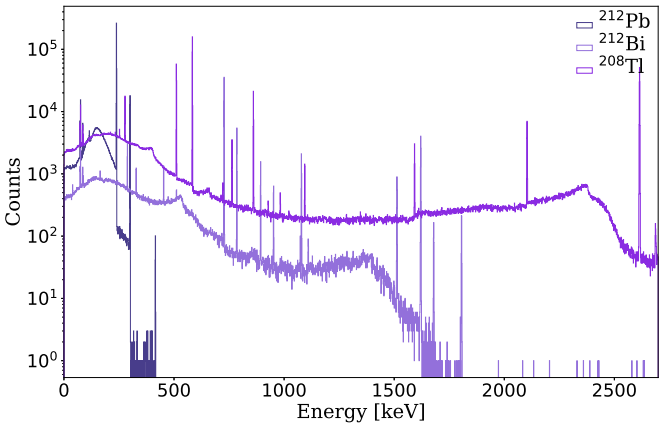

Figure 5.9: Energy spectra of ^{212}Pb, ^{212}Bi, ^{208}Tl. These main components can be summed to reproduce the ^{228}Th energy spectrum of the data.

at low energy. Once added the lead castle, a significant similarity of the simulated Compton continuum slope to the data was observed thanks to the additional back-scattering off of the lead bricks. Furthermore, different source positions were tried to better probe the correct distances among the volumes. Fig. 5.10 shows the components inside the lead castle when the ^{228}Th source is at the top and along the side of the detector. The simulated energy spectra are directly compared to the measured data to judge the accuracy. The spectra with the source at top and side positons are presented in Fig. 5.11 and Fig. 5.12, respectively. They clearly show a good agreement in the whole range, and the simulations are able to reproduce the data. The mismatch at low energies and at the left of the peaks, especially at 2614 keV, is due to the lack of transition layer effects which have not been implemented in the ^{228}Th simulations.

In App.E, a linear transition layer model is applied to the ^{228}Th spectrum to estimate the TL through peak ratio analysis.

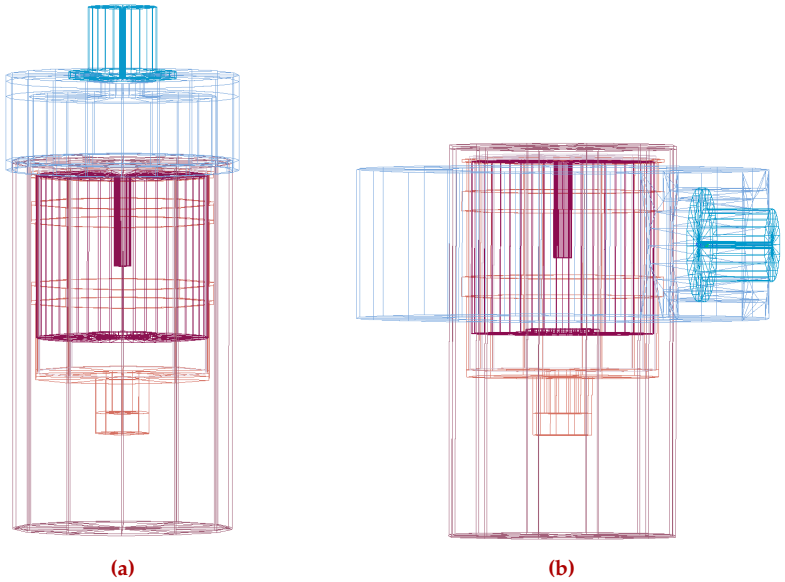

(a) (b)

Figure 5.10: Visualization of the simulated inner components of the lead castle for the runs with the ^{228}Th source at the top (a) and side (b) positions.

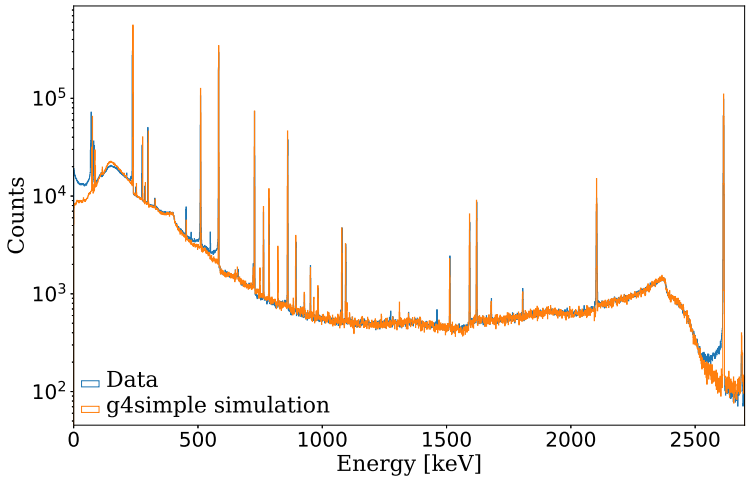

Figure 5.11: Comparison between the data and the final MC energy spectrum with the source at the top position after several improvements.

5.5.2 ^{133}*Ba experimental signature*

One of the methods used to estimate the FCCD is measuring the CCE attenuation of the detector surfaces with a surface probe, like the ^{133}Ba source and the ^{241}Am source. An ICPC detector irradiated by the uncollimated ^{133}Ba source (*ba_HS4*), placed at 78 mm from the top of the detector, typically generates the energy spectrum shown in Fig.5.13 (left). The A/E distribution as a function of the energy is plotted in Fig.5.13 (right). The straight vertical lines along the whole energy range correspond to the main γ emission of the ^{133}Ba source. The double peak at around 80 keV presents a long tail at lower energies mainly due to slow pulses, i.e. degraded energy

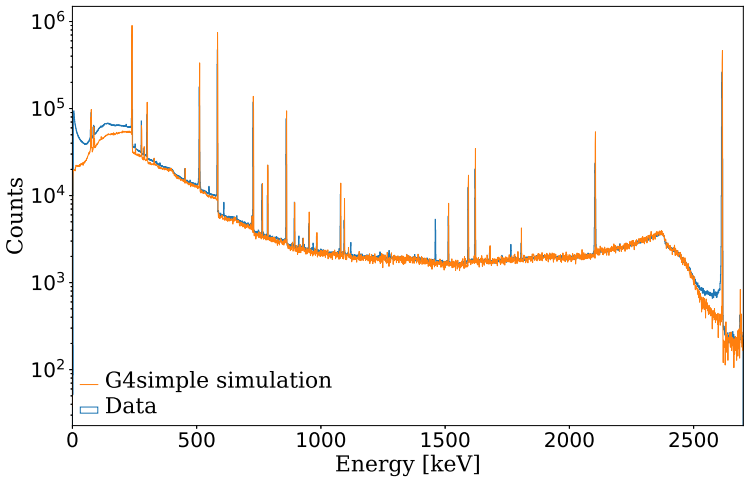

Figure 5.12: Comparison between the data and the final MC energy spectrum with the source at the side position after several improvements.

events with long rise time that diffuse slowly into the active volume. The plot also indicates the events which survived the QC (see Sec.5.2.1). The

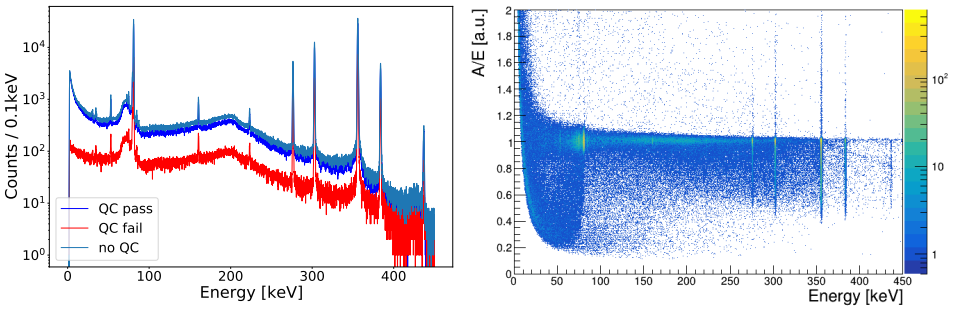

Figure 5.13: Left: typical energy spectrum of an ICPC irradiated by the uncollimated ^{133}Ba source. The different spectra indicate the events that survive or do not the QC. Right: spectrum of A/E versus energy featuring vertical lines corresponding to the typical ^{133}Ba γ-lines. The double peak around 80 keV shows slow pulses at lower energies.

analysis method consists of computing the count ratio of the main ^{133}Ba γ-lines for the data and the simulation. The double peak around 80 keV and the γ-line at 356 keV are used as observable:

$$O_{^{133}Ba} = \frac{C_{79.6keV} + C_{81.0keV}}{C_{356keV}}. \tag{5.3}$$

The emission probabilities are $p_{79.6\text{keV}} = 2.63(19)\%$, $p_{81.0\text{keV}} = 33.31(30)\%$ and $p_{356.0\text{keV}} = 62.05(19)\%$ [75]. Fig.5.14 shows the distributions of the events, weighted with the emission probability, depositing energy in the detector volume for γ lines at 81 keV (top) and at 356 keV (bottom). In the visualizations of the z-x plane, the source is at the bottom side of the plot. The color scale describes the event density and can be directly compared in between each plot. The large number of interactions occurring close to the

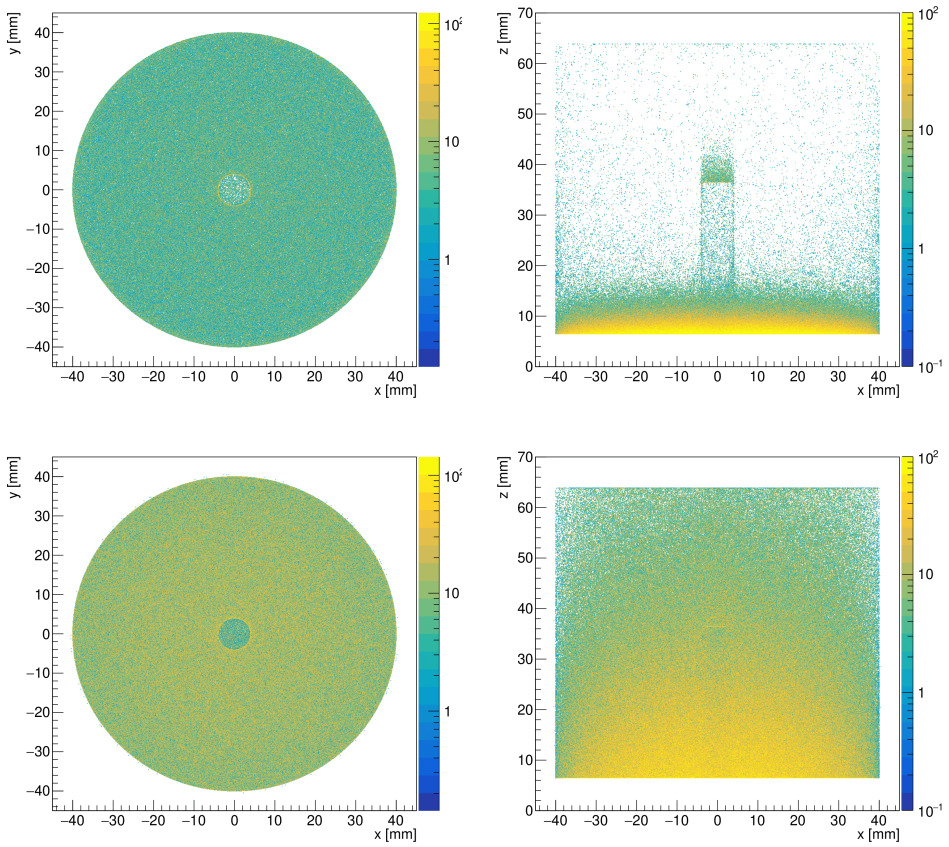

Figure 5.14: Scatterplots in x-y plane (left) and x-z plane (right) of hits from the ^{133}Ba source placed centered at the top of the detector. Top: hits from the 81 keV γ line only. Bottom: hits from the 356 keV γ line only.

top detector surface, even at the higher energies, verify the use of the ^{133}Ba source as a surface probe. The bore-hole is clearly visible when the source is placed at the center of the x-y plane. The FCCD is expected to differ around the bore-hole surfaces due to the detector production chain. Sec.5.5.7 describes a detailed analysis to estimate the FCCD relation between the thicknesses at the bore-hole and at the outer detector surface, using the ^{241}Am source. However, a check on the post-processing simulations has proven that a different FCCD value at the bore-hole does not affect the estimation of the FCCD using the ^{133}Ba source. Then, the FCCD relation between bore-hole and external surfaces is fixed to the expected value of 50% in post-processed simulations for each detector.

As shown in the analysis flow diagram in Fig.5.2, data and simulations must undergo an initial preparation process before running into the peak counts analysis [85]. Firstly, the data are calibrated. Although ^{228}Th calibration parameters may be used for this purpose, a new linear calibration on the ^{133}Ba peaks is performed to have better accuracy in the comparison with the simulations. The data are calibrated fitting the peaks at 81.0 keV, 160.6 keV, 223.2 keV, 276.4 keV, 303.9 keV, 356.0 keV, 383.9 keV with a combination of a Gaussian function and a Step function. The centered values

are extrapolated and compared with the known peak values found in the literature. The MCs are generated simulating the entire ^{133}Ba decay, and the resulting spectra are binned and treated in the same way as the observed spectra to compare them easily. A Gaussian function smears the hits energies with the parameters obtained from the FWHM curve of the ^{133}Ba data peaks, as done before for the ^{228}Th source. The ^{133}Ba simulations are post-processed (see Sec. 5.4.1) setting different values of the FCCD thickness, in a range of $[0, 2]$ mm with a step of 0.1 mm. As expected looking at Fig.5.14, the effects of the post-processing (see Fig.5.15) are stronger in the double peaks, which generates more events near the top surface.

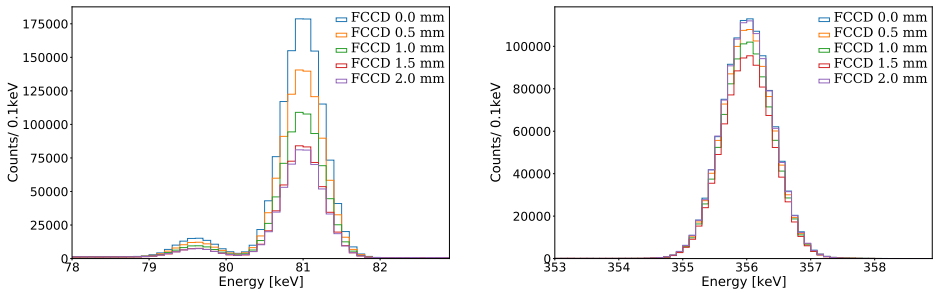

Figure 5.15: Variation of the ^{133}Ba peaks for different FCCD values. The lower energy peak at 81 keV is more affected by the post-processing. For clarity, only some FCCDs are shown.

Secondly, the peak fitting procedure is performed to determine the peak counts entering Eq. 5.3. The fitting functions of the peaks are shown in Fig. 5.16. The best fit function for the double peak is obtained by Gaussian

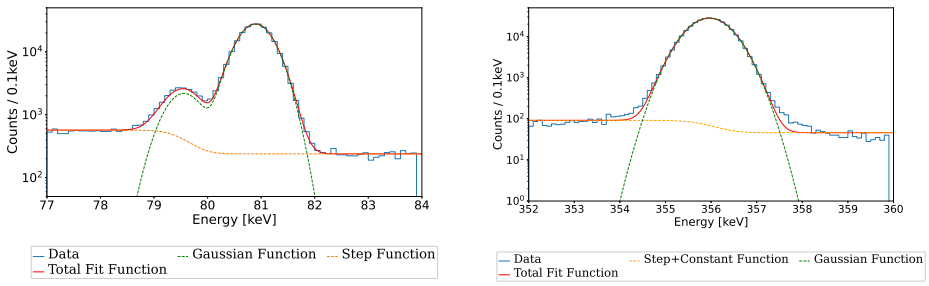

Figure 5.16: Example fit of the observed γ peak at 356 keV and the region of the double peak.

functions on the two peaks and one Step function on the 79 keV peak. The fit of the 356 keV peak is a combination of a Gaussian function and a Step function. Only the green Gaussian components of the fit are selected to represent the peak signal of each line. The counts are computed by the integral of the Gaussian peak at 356 keV within 3σ and the double Gaussian at 79 keV and 81 keV. This fitting procedure allows to exclude different backgrounds in data and simulations since it extracts only the Gaussian peaks in regions without prominent background γ lines. Furthermore, both the MC spectra and the measured spectrum include some random coincidences. While the simulations present coincidence with a second

γ-ray of the same nuclear decay arriving at the same time, the data also include coincidences originating in different decays. However, these effects are canceled by the peak ratio procedure since the probability for γ-ray coincidence is the same for any γ-lines.

Finally, the observable in Eq 5.3 is computed for the measured spectrum and for the set of MC spectra. The values are then compared and plotted as a function of the FCCD. In Fig. 5.17 (top), the black line is the exponential fit of the MC count ratios describing the dominated attenuation effect. The value of the measured observable is shown as a horizontal black line. The uncertainties are taken into account by the dashed lines. Sec. 5.5.5 is dedicated to a detailed description of the systematics uncertainty. The intersection with the data count ratio returns the estimation of the FCCD value and its uncertainty for the current detector. The simulated spectrum post-processed with the best FCCD is compared with the observed spectrum in Fig.5.17 (bottom).The mismatch in some energy ranges is due to the lack of the TL in the simulation. This process is repeated automatically for all detectors. The final results are listed in Table 5.7 and shown in Fig.5.30 .

5.5.3 ^{241}Am *experimental signature*

The analysis procedure described in the previous section has been repeated with the collimated ^{241}Am source to validate the FCCD results. Fig. 5.18 shows that interactions of ^{241}Am γ occur only on the top surface of the detector. This evidence makes the ^{241}Am even more suitable for the FCCD analysis since a larger FCCD sensitivity is reached if the hit distribution is closely concentrated on the surface. The events are less spread and less deep than the events of ^{133}Ba shown in Fig.5.14 because this ^{241}Am is collimated and the peaks of interest are at lower energies.

The typical spectrum (see Fig.5.19(left)) generated by the ^{241}Am source is mainly characterized by the prominent γ peak at 59.54 keV. The particular shape around the region of interested is mainly characterized by the background (see Fig.5.19(right)), obtained by removing the source during the data-taking. It features a long tail on the left due to Compton scatterings at the source holder and to events of partial charge collection origin, assumed to be slow pulses. They are clearly visible in Fig. 5.20, showing the A/E spectrum as a function of the energy. At higher energies, the interesting lines are at 98.97 keV and 102.98 keV and they are visible as SSE events in the A/E versus E plot.

The analysis method is based on the count ratio of three peaks described above:

$$O_{^{241}Am} = \frac{C_{59.5keV}}{C_{99keV} + C_{103keV}}. \tag{5.4}$$

The probabilities of the γ emission are $p_{59.5\text{keV}} = 35,92(17)$ %, $p_{99\text{keV}} = 0,0203(4)$ % and $p_{103\text{keV}} = 0.0195(4)$ % [76]. As explained in the previous section, the analysis needs pre-processed data and simulations. The data, with the source placed at the top of the detector, are calibrated by fitting the

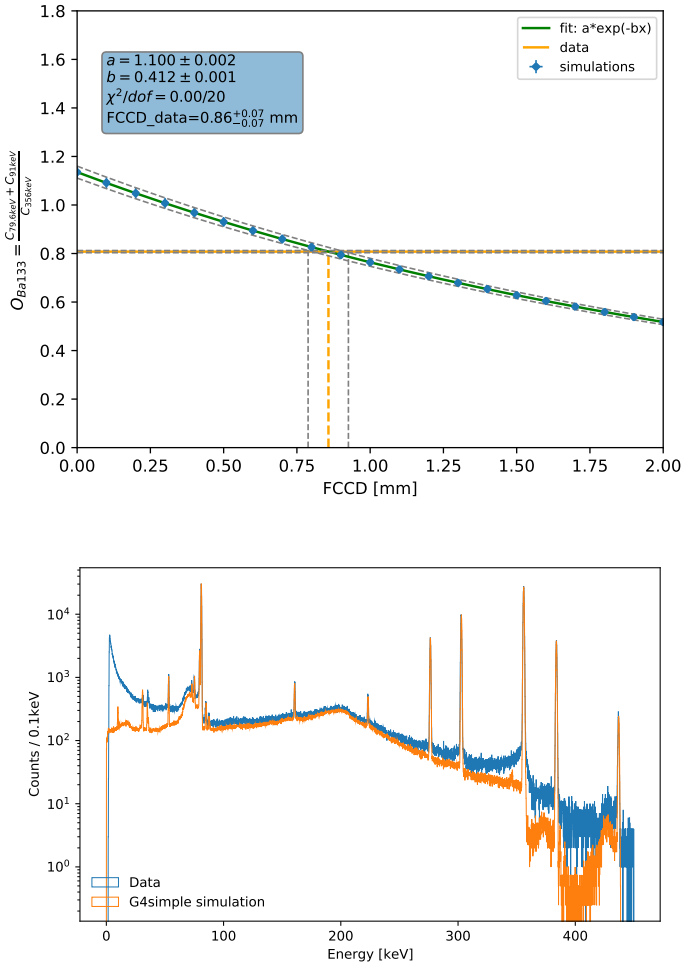

Figure 5.17: Top: count ratio as a function of simulated FCCD (see text). Bottom: comparison of the simulated and observed energy spectra; the simulated peaks are normalized to the run time of the data taking.

peaks at 59.5 keV, 99 keV, 103 keV, and 123 keV with a Gaussian function plus a Step function. As far as concerned simulations, only some ^{241}Am γ peaks are simulated via G4simple. Even though the analysis focuses on the three peaks nominated so far, other main γ lines of the ^{241}Am spectrum till $\sim$ 700 keV are simulated to better check the energy spectrum on a broader energy window. The MC spectra are then binned, smeared, and post-processed as done for the ^{133}Ba source. Since a large number of ^{241}Am interactions occur close to the detector surface, the post-processing has a stronger effect on the events in the spectrum (see Fig. 5.21).

Then, the peaks entering the ratio in Eq. 5.4 are fitted. The fitting functions for the observed spectrum and the simulated spectrum are shown in Fig. 5.22 and Fig.5.23, respectively. The functions used on the double peak of data and simulations are different since the observed X-ray line at 101.1 keV, between the double peak, has not been implemented in the simulation because of its low emission probability. The best fit function

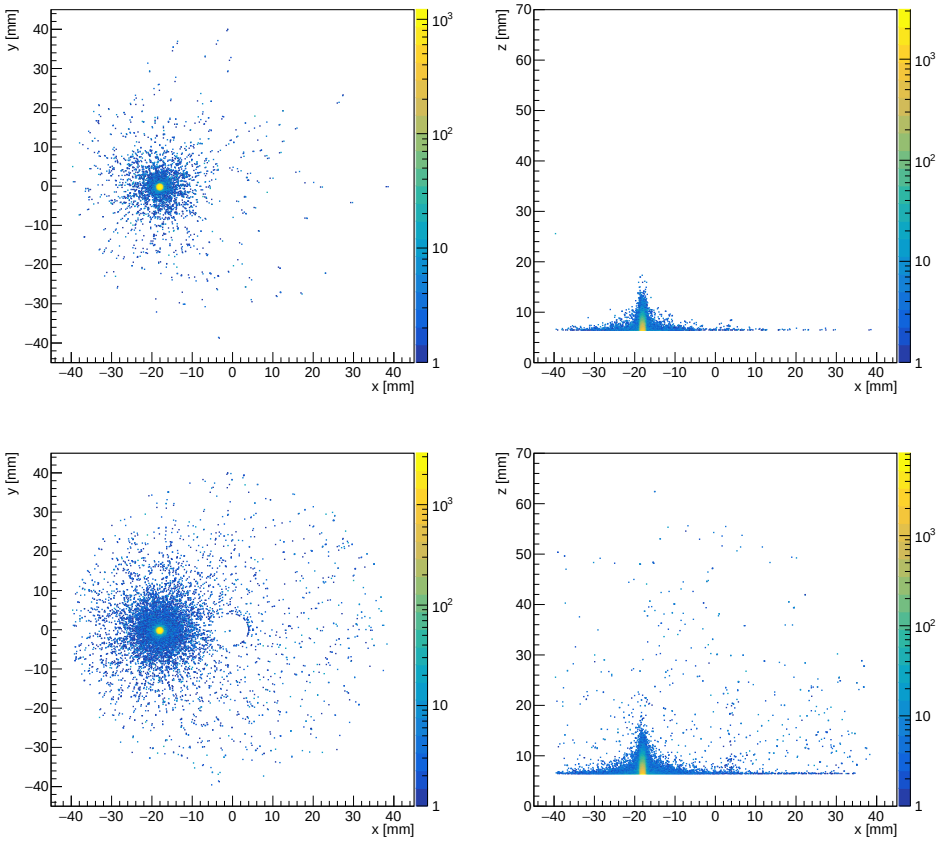

Figure 5.18: Scatterplots in x-y plane (left) and x-z plane (right) of hits from the ^{241}Am source placed off-centered at the top of the detector. Top: hits from the 59.5 keV γ line only. Bottom: hits from all the gamma lines (till $\sim$ 700 keV) generated in MC.

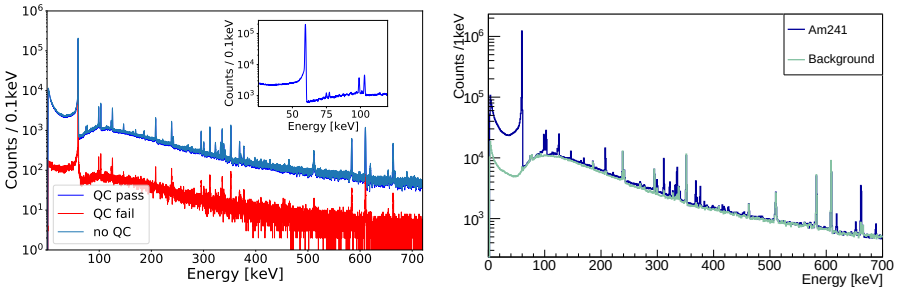

Figure 5.19: Left: observed energy spectrum from ICPC detector irradiated by ^{241}Am source placed at the top of the detector. The inset shows a zoom-in on the three main peaks used in the analysis. Right: Energy spectra with and without (only background) the source.

for the data is a combination of three Gaussian and two Step functions. The best fit function for the MC is obtained by Gaussian functions on the two peaks and one Step function on the 103 keV. Only the green Gaussian components of the fit are selected to represent the peak signal of each line. The counts are computed by the integral of the Gaussian components of the peak at 59.5 keV within 3σ and the double Gaussian at 99 keV and 103 keV. In the end, $O_{^{241}Am}$ is computed for the data spectrum and for

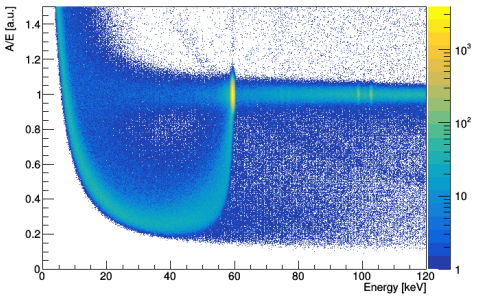

Figure 5.20: A/E data as a function of energy using ^{241}Am source. The 59.5 keV peak shows the FEP events, SSE events from the Compton scattering effect out of the detectors, and pulses depositing energy in the n+ electrode.

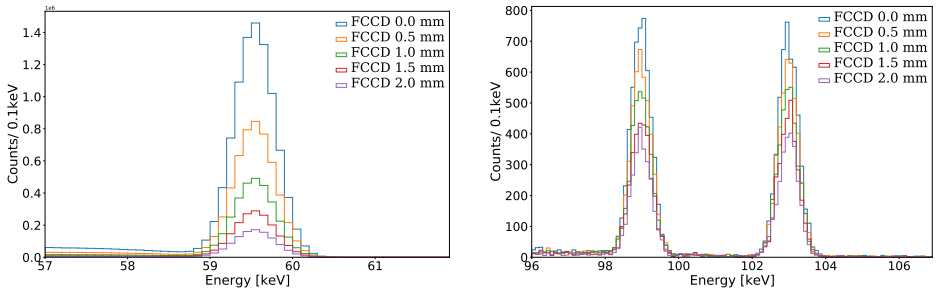

Figure 5.21: Variation of the ^{241}Am peaks for different FCCD values. The lower energy peak at 59.5 keV is more affected by the post-processing. For clarity, only some FCCDs are plotted.

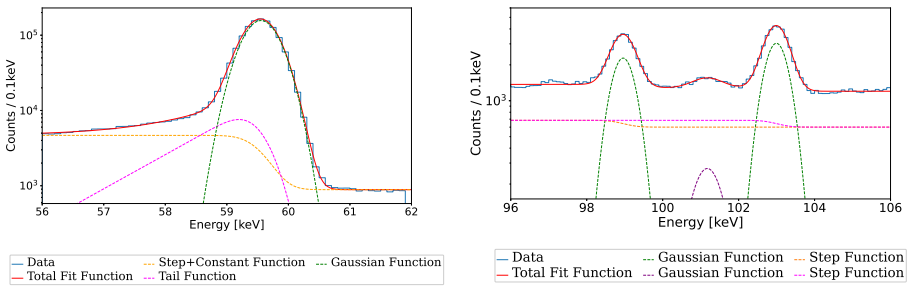

Figure 5.22: Example fit of the observed γ peak at 59.5 keV and the region of the double peak. The peak at 101 keV is visible.

the set of MC spectra, and Fig. 5.24 compares the results as a function of the FCCD values. The MC count ratios are fitted with the exponential line (in black), and the value of the measured observable is indicated by the horizontal black line. The intersection with the data count ratio is expected to return the estimation of the FCCD value but Fig. 5.24 shows no intersection up to 2 mm. It is even clearer looking at the comparison between the data spectrum and the MC spectrum post-processed with an expected FCCD around 1 mm. While the 59.5 keV lines appear to overlap well, the double peaks are too different from having a reasonable matching. The problem must be accounted to the simulation side because the data

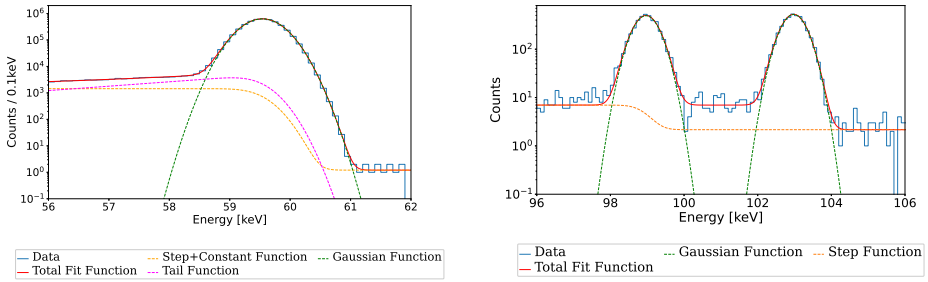

Figure 5.23: Example fit of the simulated γ peak at 59.5 keV and the region of the double peak. The peaks are smeared with the energy resolution calculated from the data calibration.

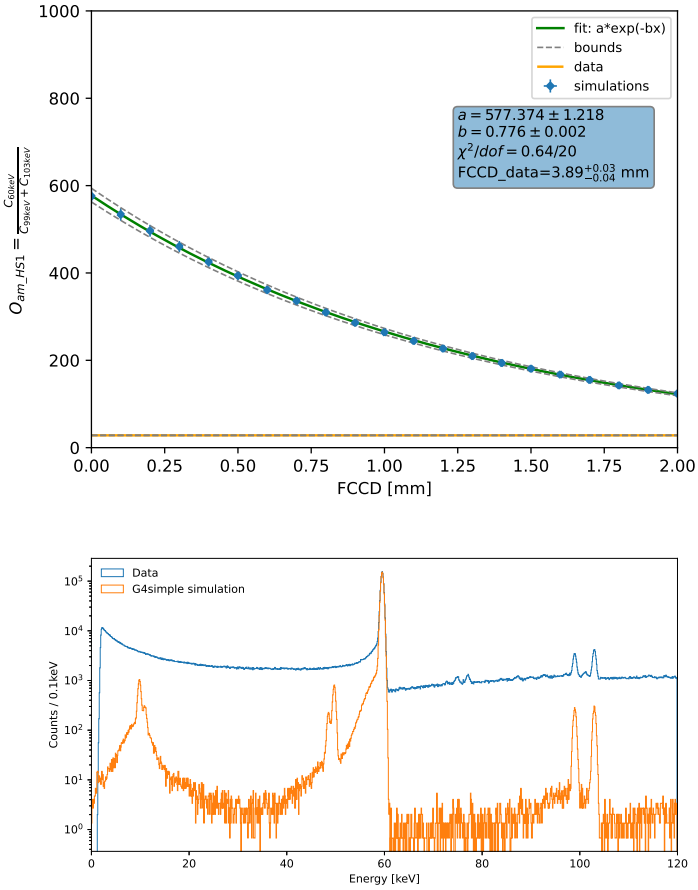

Figure 5.24: Top: count ratio as a function of simulated FCCD (see text). Bottom: comparison of the simulated and observed energy spectra; the simulated peaks are normalized to the run time of the data taking.

The effect of the lead castle used only for the ^{228}Th data taking has been fully tested prior, and it cannot be related to this issue.

measurement has passed all checks on runs, components, HV value, etc. Since the simulation components have been previously verified by the ^{228}Th source, the only plausible cause of the discrepancy can be attributed to the volume of the ^{241}Am source, which is the only difference between the two setup components. Numerous tests on the simulations, such as

changing the position or the dimensions of the source or the collimator, did not give any better results. The only parameter left is the source's material which can produce very different shapes on the energy spectrum. The documentation provided by the manufacturer is not clear about the material of the volume where the radioactivity is placed. Since there is no additional information on this essential aspect, a new approach is required. A solution can be found by calibrating the source with a new ^{241}Am source.

5.5.4 *Calibration of the collimated ^{241}Am source*

Since the radioactivity is set in a volume of unknown material, a calibration is required to be able to obtain results on the FCCD estimation from data taken with the collimated source (*am_HS1*). The uncollimated point-like ^{241}Am source (*am_HS6*) proves helpful for this purpose. The main idea of the calibration is to compare the FCCD analysis of the two sources. The silicon dioxide (acrylic) is the prior material chosen in the simulations for both sources. However, since the *am_HS6* is point-like, the effects of the material, such as absorption effects, are not evident. The analysis of the uncollimated source follows the same steps described in the previous section. After calibrating the data spectrum and extracting the energy resolution parameters, the analysis proceeds with the peak fitting of the measured spectrum and the set of MC spectra. The *am_HS6* shapes appear slightly different from those obtained with the *am_HS1* source. It is due to the different distances, geometry, activity, and the absence of the collimator. The fit function used for the data double peak is given by three Gaussian centered at the peaks at 99 keV, 101 keV, and 103 keV and a Step Function. The function on the simulation double peak is provided by two Gaussian centered around the 99 keV and 103 keV peaks, a Step Function and a Linear Function. The peak at 59.5 keV is fitted by an empirical combination of a Gaussian and Step Function centered at 59.5 keV peak, and other two Gaussian centered at the tiny bumps at lower energies, precisely at 57 keV and 53 keV. All the fitting functions of the observed and simulated spectra are shown in Fig. 5.25 and in Fig.5.26, respectively. Then, the count

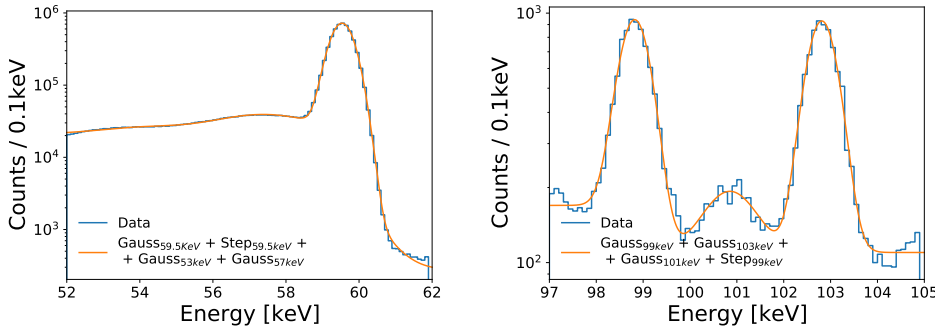

Figure 5.25: Example fit of the observed γ peak at 59.5 keV and the region of the double peak. Two little bumps at lower energy respect with the peak at 59.5 keV are also fitted. The peak at 101 keV is clearly visible.

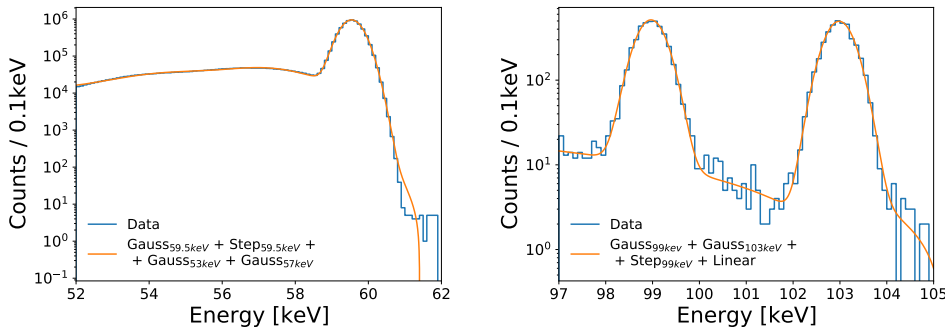

Figure 5.26: Example fit of the simulated γ peak at 59.5 keV and the region of the double peak. The peaks are smeared with the energy resolution calculated from the data calibration. An additional linear function is summed to the empirical fitting function on the double peak.

ratios in Eq. 5.4 are computed by taking into account only the Gaussians of the three main peaks. Fig.5.27 shows the observable as a function of the FCCD. The MC points are fitted with an exponential function. The MC observable at FCCD = 0 mm has a value around 900, consistent with the γ-ray emission ratio corresponding to the observable count. It is reasonable because there is no absorption effect related to the source geometry or component volumes since this source is uncollimated and has a point-like geometry. In this analysis, there is clearly an intersection of the fit function with the data line returning the best FCCD estimation for the detector. This value appears reasonable since the expected value is of the order of 1 mm from previous FCCD analysis on the ICPC detectors used in GERDA [86].

Once the FCCD is estimated from the *am_HS6* source, a comparison between the plots of the Fig. 5.24 and Fig. 5.27 is required to proceed with the calibration analysis. The physical dependence is based on an exponential function since the dominating effect is the attenuation, expressed in Eq.5.1. This attenuation law can be simply written as:

$$I = I_0 \cdot e^{-\mu x}$$

where I_0 depends on the source itself while the absorption factor μ depends on the detector material. This implies that the difference between the black exponential curves of the two sources accounts only for the normalization I_0 (named I_1 for *am_HS1* and I_6 for *am_HS6*) while the shape must be the same. The estimation of I_1 is sufficient for the calibration of the source, and the precise knowledge of the source material is not required anymore. The ratio between the observable events surviving the FCCD thickness, named R_1 and R_6 for the *am_HS1* and *am_HS6* sources respectively, is

$$\frac{R_1}{R_6} = \frac{I_1 \cdot e^{-\mu \cdot \tilde{x}}}{I_6 \cdot e^{-\mu \cdot \tilde{x}}} \tag{5.5}$$

where $\tilde{x} = FCCD$. For the same detector, the expected FCCD value must be the same for both ^{241}Am sources, and the above equation can be simplified as:

$$\frac{R_1}{R_6} = \frac{I_1}{I_6} \quad \text{and so} \quad I_1 = \frac{R_1 \cdot I_6}{R_6}.$$

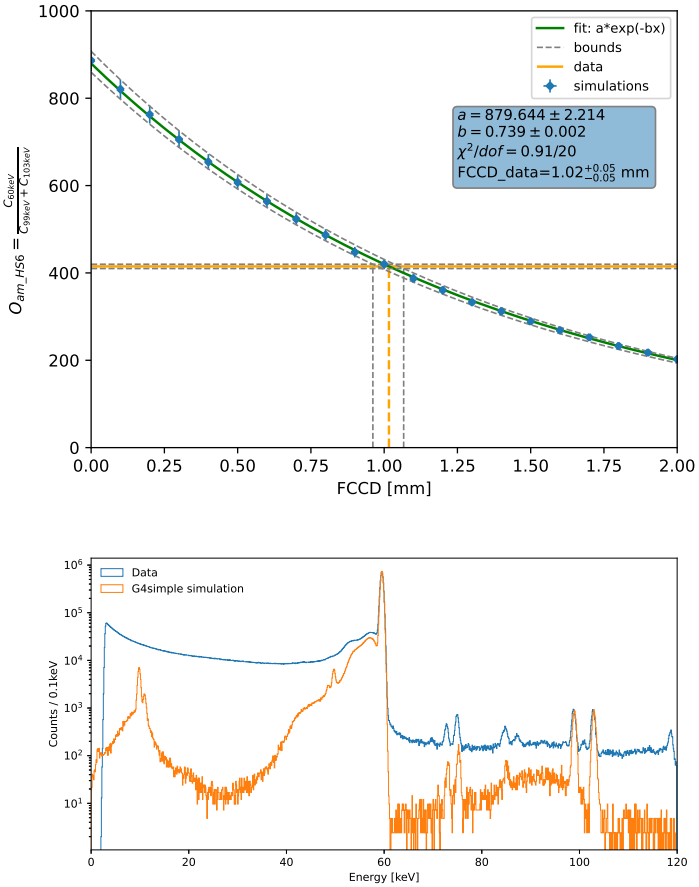

Figure 5.27: Top: count ratio from *am_HS6* as a function of simulated FCCD. Bottom: comparison of the simulated and observed energy spectra; the simulated peaks are normalized to the run time of the data taking. With respect to Fig.5.24, the simulated peaks here are more consistent with the data peaks.

However, since the last relation is purely theoretical, an additional correction on the MC shapes may be needed:

$$I_1 = \frac{R_1 \cdot I_6}{R_6} \cdot e^{-(\mu_6 - \mu_1)}. \tag{5.6}$$

This final equation returns the calibration factor for the I_1 parameter of the collimated source. This factor can be computed for more detectors to get an average calibration. Two options have been pursued and compared: using ICPC detectors; using BEGe detectors. The option to use BEGe detectors has arisen to avoid the in-homogeneity of the FCCD value that appears between the top surface and the bore-hole in the ICPCs (see Sec.5.5.7). The ICPCs detectors chosen for the calibration are taken from the order 7 [2], presenting data for both sources : `V07298B`, `V07302A`, `V07302B`, `V07647A`, `V07647B`. The BEGe chosen are: `GD00B`, `GD32B`, `GD0091B`. They have been firstly used in GERDA and then subjected to a re-measurement before their

2 `V07646A` has not been chosen because of its special geometry.

installation in LEGEND-200 to better investigate the FCCD-growth issue (see Chap.6). The analysis on these new BEGes data with *am_HS1* and *am_HS6* sources follows the same steps as those used for the ICPCs. More details are provided in Sec.6.1.2. The uncertainties of I_1 can be categorized in the correlated and uncorrelated components among the detectors used in the calibration. The correlated uncertainty stems from the propagation of the uncertainties of I_6 and μ_6 derived by propagating all systematics listed in Tab.5.2 summed in quadrature. The uncorrelated uncertainty is given by the propagation of the statistical uncertainty of data (in R_1 and R_6) and the statistical uncertainties of simulations (propagated in the fit parameter I_6, μ_6, and μ_1). For both options, these uncertainties are calculated for all detectors and enter the error matrix $\mathbf{E}$ [87] to compute the weighted average of I_6 and its total uncertainty, which are given by

$$\tilde{I}_1 = \sum_i \alpha_i I_{1i} \tag{5.7}$$

and

$$\sigma^2 = \sum_i \sum_j E_{ij} \alpha_i \alpha_j \tag{5.8}$$

with the weighting factors α_i whose vector $\boldsymbol{\alpha}$ is

$$\boldsymbol{\alpha} = \mathbf{E^{-1}U}/(\tilde{\mathbf{U}}\mathbf{E^{-1}U}). \tag{5.9}$$

n equals the number of the detectors used in the two options, with ICPCs and BEGes

where $\mathbf{U}$ is a vector whose n components are all unity, $\tilde{\mathbf{U}}$ is its transpose, and $\mathbf{E^{-1}}$ is the inverse error matrix.

The final calibration corrections $\tilde{I}_1$ from the two detector types options are listed in Table 5.1. The two values appear consistent inside the uncertainty

	Calibration correction
BEGe	62 ± 2
ICPC	60 ± 2

Table 5.1: Factors for the calibration correction obtained with the two options - using BEGe or ICPC detectors.

ranges. However, the ICPC method looks more solid since changing the set of the ICPCs does not affect the final calibration correction, while it does for the BEGes set. Moreover, it has been proven that the bore-hole does not affect the FCCD analysis with an uncollimated source set at the top. Fig. 5.28 shows the plots of the calibrated observable of one detector as a function of FCCD for both calibration factors. Only the calibration derived by the ICPCs is used in the final FCCD estimation for the ICPC detectors.

5.5.5 *Systematics uncertainties*

The uncertainties of the observables required for estimating the FCCD uncertainty are described below. Statistical uncertainty comes from the peak

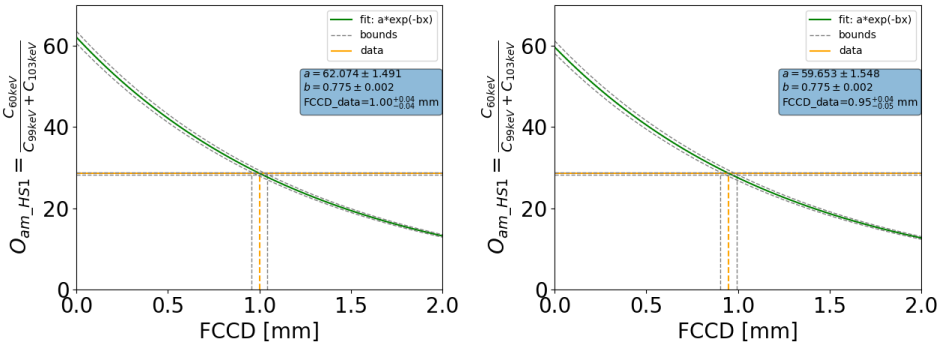

(a) (b)

Figure 5.28: Count ratio from *am_HS1* as a function of the FCCD after the calibration with the factor stemmed from the BEGes analysis (a) and the ICPCs analysis (b).

fitting procedure. The systematic uncertainties on MCs are summarized in Tab. 5.2. Some contributions are given by the MC process, such as the uncertainty on the gamma line emission, the physics process implemented in GEANT4 itself [88, 89], and the MC statistics. For the latter, the number of primaries was chosen so that the statistics would not be relevant compared to the other systematics. Another category of systematics comes from the geometry of the simulated setup. Several variations on the source's dimension, composition, and density have been tried for the uncollimated ^{241}Am and ^{133}Ba sources. The ^{133}Ba and ^{241}Am fluxes cross the cryostat and the wrap when the sources are placed at the top position. Systematics of the top thickness ($\pm$0.01 mm) of the two volumes and of wrap material are taken into account. All these individual systematics are uncorrelated among each other, they can be added in quadrature.

The intersection between the data band and the MC band gives the total uncertainty ΔFCCD, as shown in Fig.5.29. All uncertainties can be classified according to their nature as correlated or uncorrelated among the detectors. The MC statistical uncertainty is uncorrelated since it is individual for each detector. While, all other systematics are correlated since they define the method of the AV determination, which is the same for each detector. $\Delta FCCD_{uncorr}$ is the uncertainty obtained propagating into the FCCD value the statistical uncertainty of data and simulations. $\Delta FCCD_{corr}$ of the FCCD computed with the ^{133}Ba source is the uncertainty obtained by adding all the correlated uncertainties of simulations in quadrature and propagating into the FCCD value. For the collimated ^{241}Am source, the systematics is given by the uncertainty on the calibration process, reported in Tab.5.1. Distinguishing the correlated and uncorrelated components of the uncertainty is useful in the final application of the AV (see Chap.8). Checks have proven that the linear sum of the obtained correlated and uncorrelated uncertainties gives the total uncertainty of the FCCD value.

Systematics	$\Delta O_{^{241}Am}$ [±%]	$\Delta O_{^{133}Ba}$ [±%]
γ line probability	1.81	0.69
GEANT4	2	2
Source thickness	0.01	0.02
Source material	0.01	0.01
Cryostat thickness	0.37	0.28
Wrap thickness	0.03	0.07
Wrap material	0.01	0.03

Table 5.2: List of the systematics (in %) affecting the simulated observable for the analysis with ^{241}Am source and ^{133}Ba source.

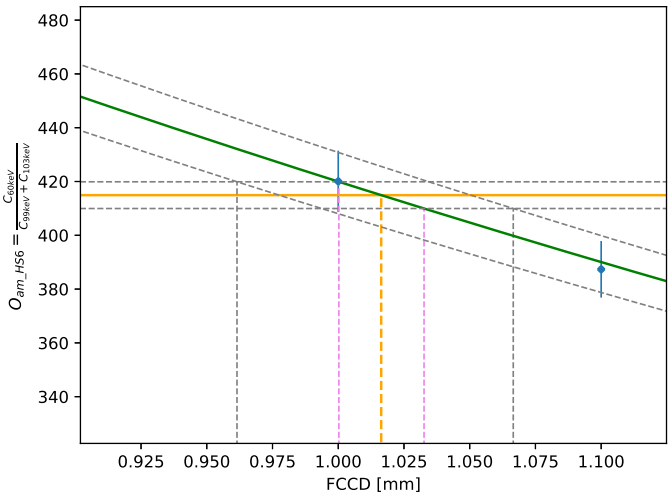

Figure 5.29: Propagation of the total (gray) and statistical (pink) uncertainty in the FCCD fitting for the ^{241}Am analysis.

5.5.6 *Results*

The FCCD determination processes shown so far have been automatically repeated for all detectors characterized in HADES. Unfortunately, for the analysis with the ^{241}Am source, a bunch of detectors could not be analyzed due to incorrect data taking. The `V05261A`, `V05267A`, `V05258B` detectors present only scan runs, not run with run-time long enough to have good statistics on the peaks of interest. During the run of `V02162B` detector, the source was set at the top of its top-groove (see Fig.A.15 (center)), so it has not been analyzed since this position could affect the results. For `V02160A` detector, only the run with the source at the top-center was collected, while the run with the source far from the bore-hole was selected for the other detectors. Only the result obtained from the uncollimated source is available for `V07646A` detector and is listed as ^{241}Am result in Fig.5.30 and Tab.5.7.

Due to unknown materials of the collimated ^{241}Am source, two different calibrations are performed. One calibration uses 3 BEGe detectors irradiated by the same source during the re-measurements (see Sec.6.1.2).The other calibration, chosen for the final FCCD results, uses the spectra of five ICPCs of the order 7 irradiated by the uncollimated ^{241}Am source. Fig. 5.30 compares the sets of results from the calibrated ^{241}Am and the ^{133}Ba analysis. The error bars indicate the total uncertainties of the FCCD. The detectors are shown in several colors to highlight better the different orders of production sequence at the manufacturer. This representation allows for investigating a potential change in FCCD values due to a variation in the production process. The mean values obtained by the ^{133}Ba source are commonly shifted at lower values - except for order 2 and order 4. The cause might be related to a potential energy dependence of the FCCD. A qualitative discussion on potential explanations is reported in Sec.8.1. Tab.5.7 lists the FCCD values with the correlated and uncorrelated uncertainties separated for each detector. App.D reports and compare the FCCD values obtained from the three radioactive sources.

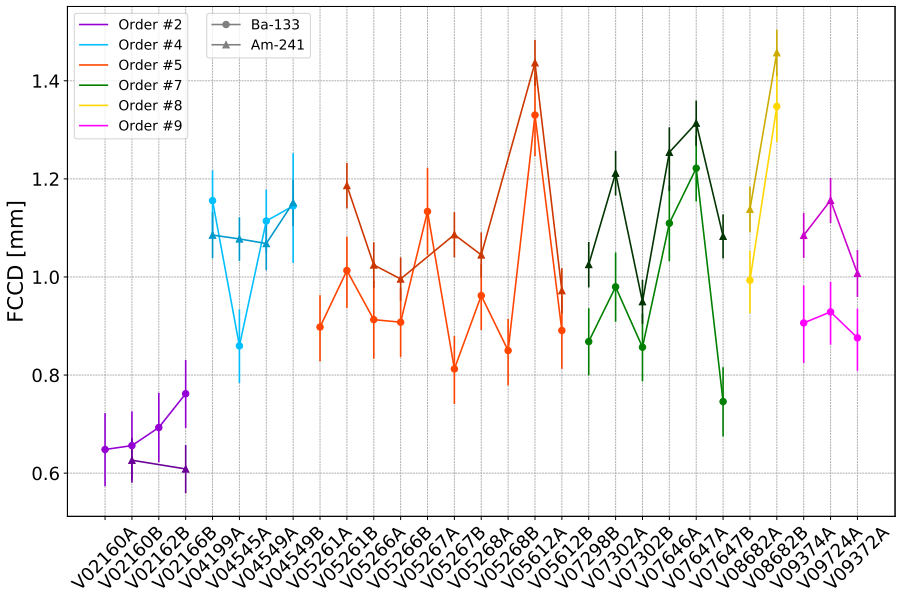

Figure 5.30: Best FCCD values estimated by the ^{241}Am and ^{133}Ba analysis. A systematic offset is observed between the two measurements for each detector.

5.5.7 *FCCD analysis at bore-hole*

In the detector production chain, the n+ electrode is created by the diffusion of lithium into the surface with two annealing cycles. The ICPC bore-hole is created in the time between the two processes [90]. Because of these steps, the FCCD value at the bore-hole surfaces is supposed to be half that at other n+ contact surfaces. The spectra of a collimated source are required to better determine the FCCD at the bore-hole. The ^{241}Am source has been

used to take three different long-run measurements at the top of each detector. This analysis considers runs with the source centered upon the bore-hole and with the source outside the bore-hole radius. The following plots are related to the V05266A detector, which presents a simple geometry. Eventually, the results are verified for other ICPC detectors. Fig. 5.18(right) shows the x-z scattering plot of the MC hits with the source off-centered. None of the hits appear at the bottom bore-hole while less than 1% of all the hits appear at its sides. Looking at these plots, it is clear that the FCCD analysis with the collimated ^{241}Am source at the off-centered position is not affected by the value of the FCCD at the bore-hole. However, a better knowledge of the FCCD at the bore-hole can account for the FCCD analysis using volume probe sources, such as ^{60}Co, which bread its hits more deeply and broadly than the surface probe sources. Furthermore, it is essential to have a more accurate estimation of the AV of the detector.

According to the attenuation law in Eq. 5.1, the ratio of the runs at the two different source positions is expressed as

$$\ln\left(\frac{I_{n+}}{I_b}\right) = -\mu \cdot \rho \cdot (FCCD_{n+} - FCCD_b) \tag{5.10}$$

where I_{n+} and I_b are the counts of the 59.5 keV γ peak in the two data spectra (off-centered and centered source, respectively), μ is the mass attenuation coefficient of germanium at 59.5 keV (1.941 cm^2/g), ρ is the Ge density (5.45 g/cm^3), and the difference between $FCCD_{n+}$ and $FCCD_b$ gives the information on the FCCD at the bore-hole, once the FCCD at the n+ top surface has been defined by previous analyses. The strategy consists of the comparison of peak ratios of data and MC sets for different values of $FCCD_b$ expressed as a fraction of $FCCD_{n+}$. After calibrating data runs and processing the simulations by setting several $FCCD_b$ values, the analysis proceeds with the computation of peak counts via the integral of the Gaussian fit function inside 3σ. The $FCCD_{n+}$ is set to the value obtained by the previous analysis for the V05266A detector (see Tab.5.7). Finally, the ratios of the peak counts are plotted in Fig.5.31 as a function of ΔFCCD, which is the difference between the two FCCDs at the n+ contact and the bore-hole.

As for the FCCD analysis described in previous sections, the intersection between the data line and the exponential fit of the simulation points returns the best value in terms of the ΔFCCD. For this selected detector, $\Delta FCCD = 0.21 \pm 0.03$ mm which translates in terms of fraction as $FCCD_b/FCCD_{n+} \sim 78\%$. Hence, it appears to be different from 50%, which was expected the first time. In addition, a quick analysis can be performed by looking only at the data spectra to verify the obtained result. A possibility is computing the peak ratio of the spectra with the centered and off-centered source (see Fig.5.32), and then substituting it to the Eq. 5.1 to extract ΔFCCD. The obtained result, $\Delta FCCD = 0.210 \pm 0.003$ mm, looks extremely consistent with the previous value got through the comparison strategy. However, this only-data method is only used as a double-check because of additional unknown systematics uncertainties on the different

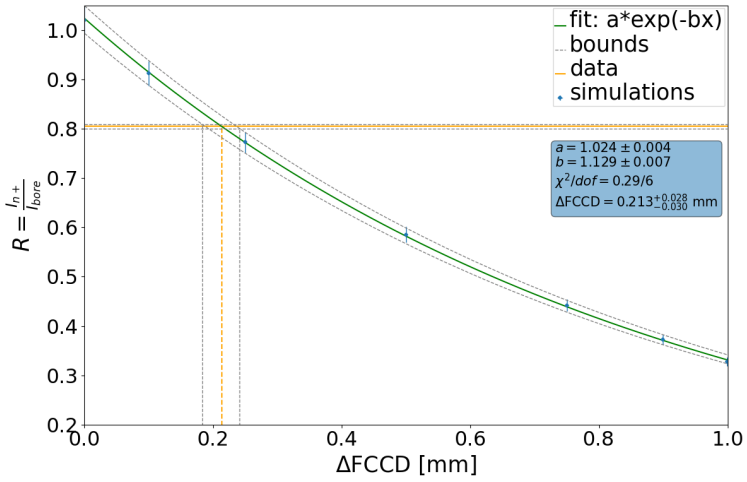

Figure 5.31: Ratio between the counts of the 59.5 keV peak when the source is centered and off-centered as a function of the FCCD difference between the two cases.

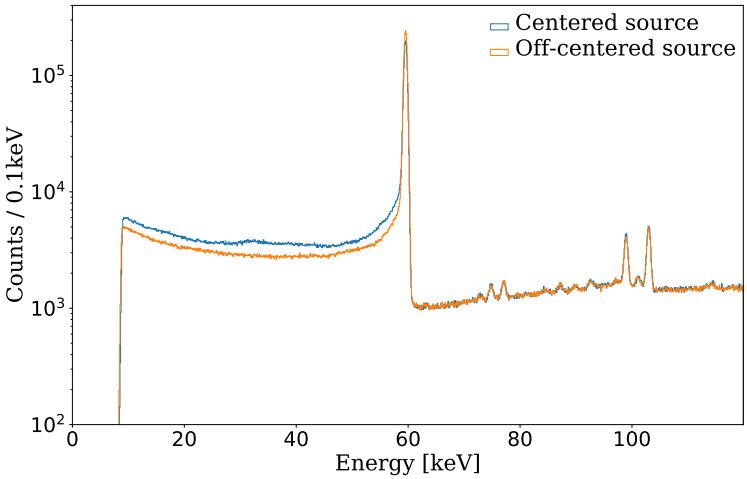

Figure 5.32: Observed energy spectra with the source at the two positions of interest for this analysis.

distances between the source and detector side of the two run measurements.

Additional systematics uncertainties have to be taken into account in this analysis.

1. The analysis cannot precisely select only the events occurring at the bottom side of the bore-hole. To quantify these systematics, an option would be to set different FCCD fractions between the bottom and the side surfaces of the bore-hole and check how it affects the final $FCCD_b$.

2. None of the documentation on the bore-hole's geometry can assure the bottom surface's flatness. Consequently, some simulations with different curvatures on the bore-hole have been run.

3. There is an uncertainty related to the position at which the source is set ($\pm$1mm). Since the radius of the bore-hole is only about a few millimeters, a slight difference in the position can strongly affect the final $FCCD_b$ estimation. Simulations with different positions of the source have been tried.

As far as the first point, the aim is to quantify the uncertainty related to possible differences in the FCCD values among the surfaces of the bore-hole. The default assumption in the analysis has the FCCD homogeneous in the entire bore-hole. The analysis is repeated, changing the ratio between the FCCDs at the sides and the bottom of the bore-hole. The Table 5.3 shows the final results in terms of $\Delta FCCD = FCCD_{n+} - FCCD_{bore\text{-}hole}$. The last raw is related to the condition used so far, fixing the same FCCD at the sides and the bottom. A potential difference between the FCCDs would not

Table 5.3: Estimation of the observable $\Delta FCCD = FCCD_{n+} - FCCD_{bore\text{-}hole}$ setting different FCCD fractions between the two surfaces of the bore-hole in the analysis.

$FCCD_{side}/FCCD_{bottom}$	$\Delta FCCD$ [mm]
20%	0.20 ± 0.03
50%	0.21 ± 0.03
80%	0.20 ± 0.03
100%	0.21 ± 0.03

be relevant in light of the uncertainties already obtained from the standard analysis. For completeness, Fig.5.33 describes the x-z scattering of the hits when the ^{241}Am source is at the center ($r = 0$). In this case, the events at the bottom of the bore-hole are apparently $\sim$ 79% of the total. Actually, looking at the energy spectra, $\sim$ 96% of the total hits happen at the bore-hole in the region of interest around the 59.5 keV peak. Fig.5.34 shows, indeed, the ratio between the simulation energy spectra with and without the selection on the hits at the bore-hole. Around the energy range of interest, the two spectra are almost the same.

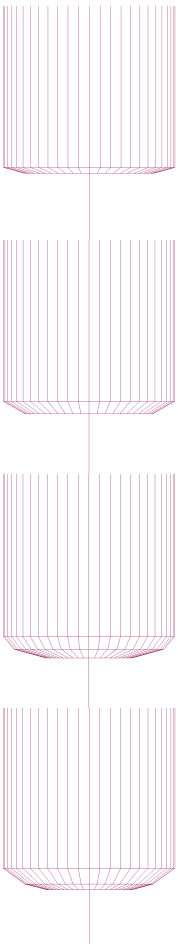

Regarding the second point, several geometries on the bottom side of the bore-hole are applied in the simulations. The analysis is done quantitatively in terms of one or more parameters related to the curvature, but different geometries are applied to qualitatively observe the effect on the FCCD estimation. Since G4simple does not allow simply adding curvatures to a cylinder surface, additional taper-sides are applied to the bottom surface once per time. Fig.5.35 shows how the no-flat geometry of the bottom bore-hole appears in the x-z scatterplot of the simulated hits. Different angles of the tapered side are tried, as shown in the figures at the side of the page. The FCCD analysis is repeated for each geometry in terms of the count ratios at the 59.5 keV peak as a function of $\Delta FCCD$. No effects are seen in the final result. A strongly no-flat surface has been tried as a test to verify the consistency of the analysis. In this case, a different result is observed. No differences are spotted even for the energy spectra with the

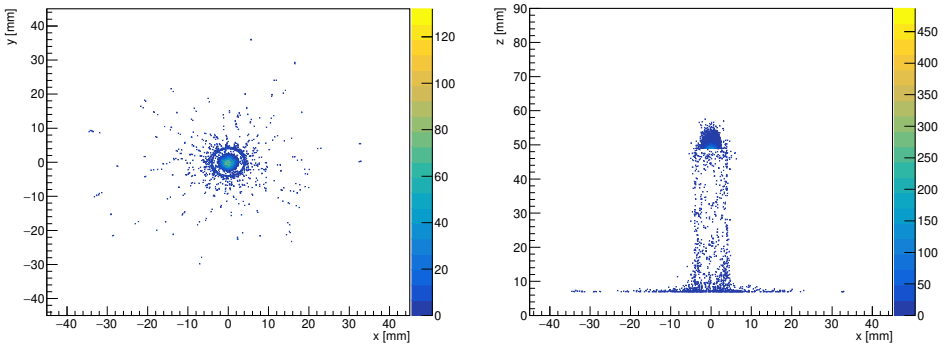

Figure 5.33: Simulated hits with source set at the top of the detector with $r = 0$ position. Visualizations into the xy-plane (left) and xz-plane (right). The ICPC detector bore-hole is clearly visible in both scatterplots.

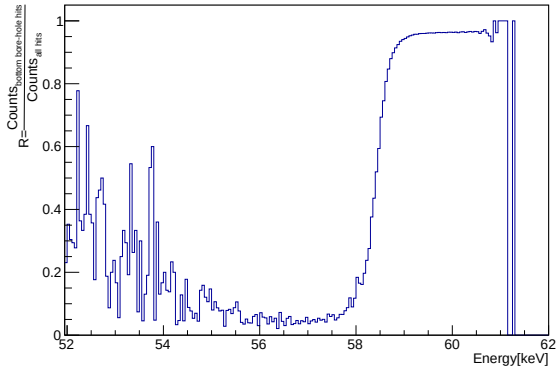

Figure 5.34: Ratio between the simulated energy spectra with and without the selection on the hits at the bottom bore-hole. The ratio almost reaches unity in the region of interest around the 59.5 keV peak.

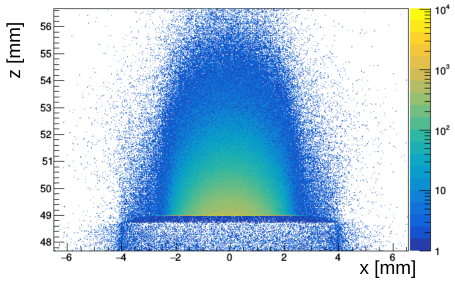

Figure 5.35: Visualization of the bottom bore-hole shape via the deposited energies by simulated hits in the x-z plane.

source at the off-centered position. As expected from Fig.5.36, the counts are not affected by the geometry of the bore-hole. On the other hand, for the spectra with the source at the centered position, only the spectrum of the strongly different geometry (Curvature 4) is found to be distinctive from the other, as expected.

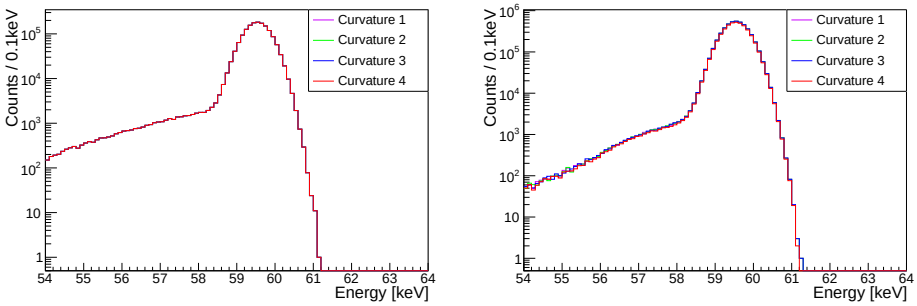

Figure 5.36: Simulated energy spectra with the four curvatures applied to the bottom surface of the bore-hole. Left: with the source at the off-centered position no difference can be noticed. Right: with the source at the centered position only the very no-flat curvature is recognizable among them.

Finally, a simulation with the source at $r = 1$ mm is run to check how the uncertainty of the source position may propagate to the ΔFCCD determination. The uncertainty on the r-position is of the order of 1 mm and since the detector is azimutally symmetrical, only the position at $x = 1$ mm ($y = 0$) is tried. The final result obtained from this new analysis appears to be equal to the estimation obtained by setting the position $x = 0$ mm.

To conclude, all these new settings give a result not different from the original one, inside its error range. Thereby, no additional uncertainties are considered. The two strategies (simulation-data comparison and only-data) are repeated for several detectors. Table 5.4 lists the results obtained so far. The FCCD fractions appear to be not homogeneous among the analyzed detectors. An expansion of the analysis on more detectors is needed to understand better the meaning of this behavior.

Table 5.4: Estimation of the FCCD at the bore-hole as a fraction of the FCCD at top surface, obtained by the previous analysis, for several detectors.

ICPC	$FCCD_{bore\text{-}hole}/FCCD_{n+}$
V05266A	(78 ± 6) %
V05266B	(75 ± 6) %
V02160B	(50 ± 4) %
V02166B	(59 ± 5) %

5.5.8 *Am scans - homogeneity*

The FCCD homogeneity over the top and lateral side of the detector is one of the assumptions for the AV determination, obtained from the difference between the total volume and the FCCD volume. The homogeneity is verified using the scans taken with the scanning table described in Sec.4.3.1 and the collimated ^{241}Am source at a fixed distance (up to 10 mm) from the detector. The analysis considers the top linear scan along the diameter of

the detector and the lateral scan moving from the top to the bottom of one side of the detector. The scanning step length is typically of 1 or 2 mm. The measuring time for a single position of 300 s allows sufficient statistics in the 59.5 keV peak, which is the only peak required for the FCCD homogeneity analysis. Similar conditions on the scanning measurement are followed for all detectors such that only the FCCD difference affects the count rate difference between detectors. Fig.5.37 shows typical energy spectra of a top and lateral scan. To automatically treat all spectrum scans, the energy

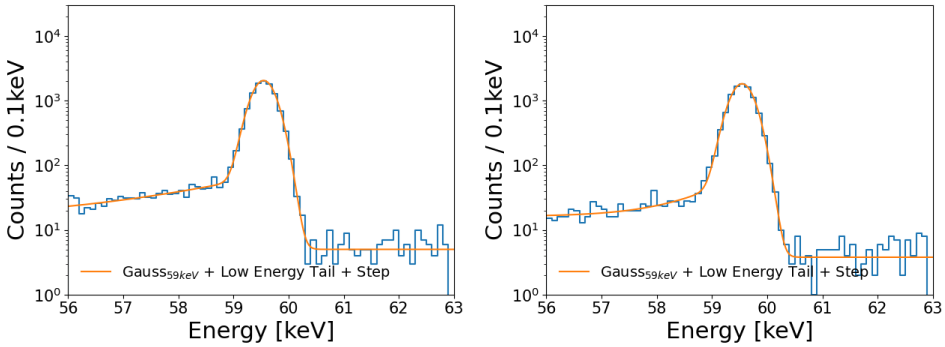

Figure 5.37: Typical ^{241}Am 59.5 keV peak collected during a top (left) and lateral (right) scan.

calibration is firstly performed, and the 59.5 keV peak is fitted, with the same function used for the FCCD analysis, to determine the peak counts R under the Gaussian by the integral counts in the $\pm 3\sigma$ region around the mean. Fig.5.38 shows the ^{241}Am 59.5 keV peak counts of the detector `V05266A` plotted for different source positions of the top and lateral scans. The scans are fitted with a constant function. The only top scan points fitted

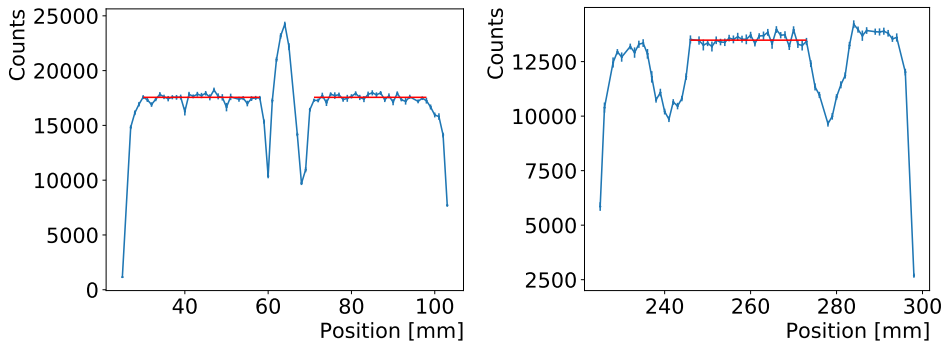

Figure 5.38: Top and lateral surface scans of `V05266A`. The surface regions are fitted with a constant.

are the points along the top surface (without the bore-hole) far from the borders. The lateral scan usually shows three different regions according to the different thicknesses of the detector holder. Some detectors can present only two regions if the scans do not cover the entire detector height. The fit is performed only in the middle region with smaller thickness where the distribution of points is clearer. To compare the counts R_{TOP} and R_{LAT} of

the two runs, they need to be normalized by the correction factors f_{TOP} and f_{LAT}, which take into consideration the different attenuation on the top and the side due to different materials and thicknesses that the ^{241}Am 59.5 keV beam crosses. The cryostat has the same thickness of 1.5 mm aluminum alloy at the top and the lateral sides. The HDPE wrap has a thickness of 1.0 mm at the top and 0.5 mm at the side. On the lateral scan, the beam has to pass additional 1.5 mm thick aluminum alloy detector holder. Table 5.5 summarizes the thicknesses, the material densities, and the mass coefficient at 59.5 keV required to compute the f_{TOP} and f_{LAT} by the attenuation law expressed in Eq. 5.1. The uncertainties are propagated as Gaussian errors.

Table 5.5: Properties of the geometry and material of the volumes needed for the computation of the attenuation factors.

	Thickness [cm]	Mass coefficient [cm^2/g]	Density [g/cm^3]
Cryostat Top/Side	0.15 ± 0.01	0.354	2.84
Holder Lat	0.15 ± 0.01	0.354	2.84
Wrap Top	0.1 ± 0.01	0.189	0.93 ± 0.03
Wrap Lat	0.05 ± 0.01	0.189	0.93 ± 0.03

The peak counts are normalized as $R'_{TOP(LAT)} = R_{TOP(LAT)}/f_{TOP(LAT)}$. The count ratio r between lateral and top side and its uncertainty are:

$$r = \frac{R'_{LAT}}{R'_{TOP}} \qquad \sigma_r = r \cdot \sqrt{\left(\frac{\sigma_{R'_{TOP}}}{R'_{TOP}}\right)^2 + \left(\frac{\sigma_{R'_{LAT}}}{R'_{LAT}}\right)^2} \tag{5.11}$$

where $\sigma_{R'_{TOP}}$ and $\sigma_{R'_{LAT}}$ are the fit errors of the constant fit. The difference in FCCD between top and lateral surface is estimated by:

$$\Delta FCCD = -\frac{1}{\mu \cdot \rho} \cdot \ln r \qquad \sigma_{\Delta FCCD} = \frac{1}{\mu \cdot \rho} \cdot \frac{\sigma_r}{r} \tag{5.12}$$

where μ and ρ are the attenuation and density of germanium, respectively. For a given surface, the variation of the FCCD can be determined by looking at the population variation of individual scans:

$$\delta FCCD_i = \frac{1}{\mu \cdot \rho} \cdot \ln\left(\frac{R_i - \tilde{\sigma}_{R_i}}{R_i}\right) \tag{5.13}$$

where i stands for TOP or LAT side and $\tilde{\sigma}_{R_i}$ is given by the standard deviation between the scan counts at the surface. Table 5.6 lists the final homogeneity results obtained for several ICPCs. The correlations between the counts at top and lateral scans are graphically shown in Fig.5.39 (left) for each order. A smaller count rate in the lateral side is observed for the `V05266A` detector, while a larger count is observed for `V07647A` and `V07298B` detectors. Fig.5.39 (right) shows the correlation between the counts and the FCCD for each order. The count rates are correlated with the FCCD

values of the detectors since determined with the ratio methods. Detectors of the same order, indicated with the same color, do not show a common behavior among each other. The results of this analysis indicate that the first assumption of the FCCD homogeneity is proved.

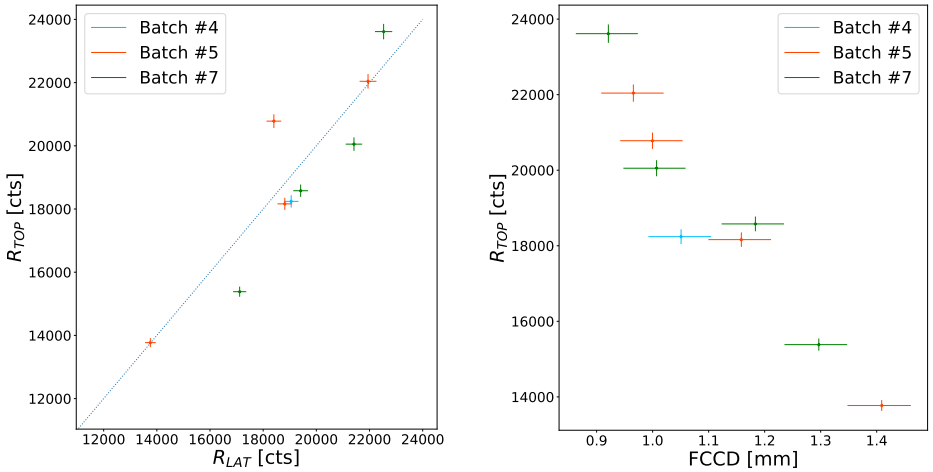

Figure 5.39: Correlation between count ratios from the top and lateral scans (left) and between the count ratio and the estimated FCCD from ^{241}Am analysis (right) for each detector whose order is marked with different color.

Table 5.6: Surface FCCD variation from scanning measurements. The first column indicates the FCCD difference between the top and later surface while the other two columns lists the FCCD variation on the top surface and the lateral surface, respectively.

ICPC	ΔFCCD $\pm \sigma_{\Delta FCCD}$ [mm]	$\delta FCCD_{TOP}$ [mm]	$\delta FCCD_{LAT}$ [mm]
V04199A	-0.04 ± 0.02	0.01	0.01
V05261B	-0.03 ± 0.02	0.01	0.01
V05266A	0.10 ± 0.02	0.01	0.01
V05266B	0.004 ± 0.02	0.01	0.01
V05612A	0.001 ± 0.02	0.01	0.01
V07298B	-0.06 ± 0.02	0.01	0.01
V07302A	-0.04 ± 0.02	0.01	0.01
V07302B	0.04 ± 0.02	0.01	0.01
V07647A	-0.09 ± 0.02	0.01	0.01

5.5.9 *Active volume determination*

To complete the AV model analysis, the final step would be to apply the results collected from the FCCD characterization to compute the AV of each detector. The dimensions of the detectors that affect the determination of the active volume are taken from the manufacturer's documentation. They are listed in Table C.1. The AV calculation is shown in Eq. 5.14 and consists

of the difference between the bulk and bore-hole volumes, decreased in size by the FCCD, cutting the groove. Due to its negligible dimension, the p+ electrode thickness is not included either in the FCCD analysis or in this analysis. For a standard ICPC, the AV is

$$\begin{aligned} V_{cilinder} &= \pi \cdot (H_c - 2 \cdot FCCD) \cdot (R_c - FCCD)^2 \\ V_{bore\text{-}hole} &= \pi \cdot (h_w + FCCD_{bh} - FCCD) \cdot (r_w + FCCD_{bh})^2 \\ V_{groove} &= \pi \cdot r_g \cdot (r_{g_o}^2 - r_{g_i}^2) - \pi \cdot FCCD \cdot r_{g_o}^2 \\ AV_{standard} &= V_{cilinder} - V_{bore\text{-}hole} - V_{groove} \end{aligned} \tag{5.14}$$

where all the h and r refer to the dimensions shown in Fig. 5.40. For detectors with particular geometries, additional attention is required to compute the correct AV. App. C explains how to compute the AV calculation for those detectors properly. Finally, Table 5.7 lists the FCCD, the AV, and

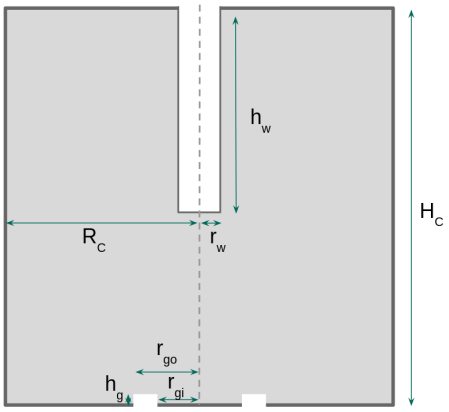

Figure 5.40: Sketch of the r-z plane of a typical ICPC detector. All the dimensions required for the AV computation are labeled.

the AV fraction $f_{AV} = AV/V$ for each detector. All the uncertainties are expressed in correlated and uncorrelated uncertainties.

5.5.10 *Conclusion*

The FCCD is determined by irradiating the detector with the uncollimated ^{133}Ba source and the collimated ^{241}Am source in the HADES laboratory. In this analysis, the observable is given by the count ratio of the three main peaks of ^{133}Ba and ^{241}Am energy spectra. The measured observable needs to be compared with the observable obtained from the energy spectra of MC simulations varying the FCCD. Looking at the simulated energy spectra, it is clear that the validation of simulations by a ^{228}Th source is not enough, but a calibration of the ^{241}Am source is required due to unknown features of the source. Once the source is calibrated with an uncollimated ^{241}Am source, the analysis is performed and the FCCD are obtained for each detectors. This method probes the top surface FCCD with high precision. A systematic offset between the values from the analysis with the two

Table 5.7: List of the FCCD, AV and f_{AV} for each detector, obtained with the ^{133}Ba and ^{241}Am analyses. The uncertainties are separated into correlated and uncorrelated components.

ICPC	FCCD [mm]		AV [mm^3]		f_{AV}	
	^{133}Ba	^{241}Am	^{133}Ba	^{241}Am	^{133}Ba	^{241}Am
V02160A	$0.65^{+0.05\,+0.03}_{-0.5\,-0.03}$	-	$298.0^{+1.5\,+0.7}_{-1.4\,-0.7}$	-	$0.945^{+0.005\,+0.002}_{-0.005\,-0.002}$	-
V02160B	$0.66^{+0.05\,+0.03}_{-0.05\,-0.03}$	$0.63^{+0.03\,+0.01}_{-0.3\,-0.01}$	$293.9^{+1.4\,+0.6}_{-1.3\,-0.6}$	$294.6^{+0.8\,+0.3}_{-0.8\,-0.3}$	$0.947^{+0.004\,+0.002}_{-0.004\,-0.002}$	$0.949^{+0.003\,+0.001}_{-0.003\,-0.001}$
V02162B	$0.69^{+0.05\,+0.02}_{-0.05\,-0.02}$	-	$423.8^{+1.7\,+0.7}_{-1.7\,-0.8}$	-	$0.950^{+0.004\,+0.002}_{-0.004\,-0.002}$	-
V02166B	$0.76^{+0.05\,+0.02}_{-0.05\,-0.02}$	$0.61^{+0.03\,+0.02}_{-0.03\,-0.02}$	$450.3^{+1.8\,+0.7}_{-1.8\,-0.7}$	$455.4^{+1.1\,+0.5}_{-1.1\,-0.5}$	$0.946^{+0.004\,+0.001}_{-0.004\,-0.002}$	$0.957^{+0.002\,+0.001}_{-0.002\,-0.001}$
V04199A	$1.15^{+0.05\,+0.01}_{-0.06\,-0.03}$	$1.09^{+0.03\,+0.01}_{-0.03\,-0.01}$	$510.9^{+2.1\,+0.9}_{-1.6\,-0.5}$	$513.3^{+1.2\,+0.5}_{-1.2\,-0.5}$	$0.942^{+0.004\,+0.002}_{-0.003\,-0.001}$	$0.947^{+0.002\,+0.001}_{-0.002\,-0.001}$
V04545A	$0.86^{+0.05\,+0.03}_{-0.05\,-0.03}$	$1.08^{+0.03\,+0.01}_{-0.03\,-0.01}$	$533.8^{+2.0\,+1.0}_{-1.9\,-1.0}$	$525.7^{+1.2\,+0.4}_{-1.2\,-0.4}$	$0.943^{+0.004\,+0.002}_{-0.003\,-0.002}$	$0.929^{+0.002\,+0.001}_{-0.002\,-0.001}$
V04549A	$1.11^{+0.05\,+0.02}_{-0.05\,-0.02}$	$1.07^{+0.03\,+0.02}_{-0.03\,-0.02}$	$320.9^{+1.4\,+0.4}_{-1.4\,-0.4}$	$322.1^{+0.9\,+0.5}_{-0.9\,-0.5}$	$0.914^{+0.004\,+0.001}_{-0.004\,-0.001}$	$0.917^{+0.003\,+0.002}_{-0.002\,-0.002}$
V04549B	$1.15^{+0.05\,+0.06}_{-0.06\,-0.07}$	$1.15^{+0.03\,+0.01}_{-0.03\,-0.01}$	$268.5^{+1.3\,+1.5}_{-1.1\,-1.3}$	$268.4^{+0.7\,+0.3}_{-0.7\,-0.3}$	$0.931^{+0.004\,+0.005}_{-0.004\,-0.004}$	$0.930^{+0.003\,+0.001}_{-0.003\,-0.001}$
V05261A	$0.90^{+0.05\,+0.02}_{-0.05\,-0.02}$	-	$305.1^{+1.3\,+0.5}_{-1.2\,-0.4}$	-	$0.937^{+0.004\,+0.002}_{-0.004\,-0.001}$	-
V05261B	$1.01^{+0.05\,+0.02}_{-0.06\,-0.03}$	$1.19^{+0.03\,+0.01}_{-0.03\,-0.01}$	$403.7^{+1.7\,+0.9}_{-1.5\,-0.7}$	$398.4^{+1.0\,+0.4}_{-1.0\,-0.4}$	$0.931^{+0.004\,+0.002}_{-0.003\,-0.002}$	$0.919^{+0.002\,+0.001}_{-0.002\,-0.001}$
V05266A	$0.91^{+0.05\,+0.03}_{-0.05\,-0.03}$	$1.02^{+0.03\,+0.01}_{-0.03\,-0.01}$	$349.8^{+1.5\,+0.8}_{-1.5\,-0.9}$	$346.7^{+0.9\,+0.4}_{-0.9\,-0.4}$	$0.932^{+0.004\,+0.002}_{-0.004\,-0.002}$	$0.924^{+0.002\,+0.001}_{-0.002\,-0.001}$
V05266B	$0.91^{+0.05\,+0.02}_{-0.05\,-0.02}$	$1.00^{+0.03\,+0.01}_{-0.03\,-0.01}$	$335.2^{+1.5\,+0.6}_{-1.4\,-0.6}$	$332.8^{+0.9\,+0.3}_{-0.9\,-0.3}$	$0.931^{+0.004\,+0.002}_{-0.004\,-0.002}$	$0.924^{+0.003\,+0.001}_{-0.002\,-0.001}$
V05267A	$1.13^{+0.05\,+0.04}_{-0.05\,-0.04}$	-	$360.7^{+1.5\,+1.0}_{-1.5\,-1.1}$	-	$0.920^{+0.004\,+0.003}_{-0.004\,-0.003}$	-
V05267B	$0.81^{+0.05\,+0.02}_{-0.05\,-0.02}$	$1.09^{+0.03\,+0.01}_{-0.03\,-0.01}$	$403.0^{+1.7\,+0.7}_{-1.5\,-0.6}$	$394.7^{+1.0\,+0.4}_{-1.0\,-0.4}$	$0.945^{+0.004\,+0.002}_{-0.004\,-0.001}$	$0.926^{+0.002\,+0.001}_{-0.002\,-0.001}$
V05268A	$0.96^{+0.05\,+0.02}_{-0.05\,-0.02}$	$1.04^{+0.03\,+0.01}_{-0.03\,-0.01}$	$388.3^{+1.6\,+0.7}_{-1.4\,-0.5}$	$385.9^{+1.0\,+0.4}_{-1.0\,-0.4}$	$0.936^{+0.004\,+0.002}_{-0.003\,-0.001}$	$0.930^{+0.002\,+0.001}_{-0.002\,-0.001}$
V05268B	$0.85^{+0.05\,+0.02}_{-0.06\,-0.02}$	-	$306.0^{+1.4\,+0.6}_{-1.2\,-0.5}$	-	$0.945^{+0.004\,+0.002}_{-0.004\,-0.001}$	-
V05612A	$1.33^{+0.05\,+0.03}_{-0.06\,-0.04}$	$1.44^{+0.03\,+0.01}_{-0.03\,-0.01}$	$362.2^{+1.6\,+1.0}_{-1.4\,-0.8}$	$359.3^{+0.9\,+0.4}_{-0.9\,-0.4}$	$0.908^{+0.004\,+0.002}_{-0.003\,-0.002}$	$0.901^{+0.002\,+0.001}_{-0.002\,-0.001}$
V05612B	$0.89^{+0.05\,+0.02}_{-0.06\,-0.03}$	$0.97^{+0.03\,+0.01}_{-0.03\,-0.01}$	$356.6^{+1.6\,+0.9}_{-1.3\,-0.7}$	$354.4^{+0.9\,+0.3}_{-0.9\,-0.4}$	$0.943^{+0.004\,+0.002}_{-0.004\,-0.002}$	$0.937^{+0.003\,+0.001}_{-0.002\,-0.001}$
V07298B	$0.87^{+0.05\,+0.02}_{-0.05\,-0.02}$	$1.03^{+0.03\,+0.01}_{-0.03\,-0.01}$	$351.0^{+1.5\,+0.6}_{-1.5\,-0.6}$	$346.6^{+0.9\,+0.4}_{-0.9\,-0.4}$	$0.934^{+0.004\,+0.002}_{-0.004\,-0.002}$	$0.923^{+0.002\,+0.001}_{-0.002\,-0.001}$
V07302A	$0.98^{+0.05\,+0.02}_{-0.05\,-0.02}$	$1.21^{+0.03\,+0.01}_{-0.03\,-0.01}$	$299.4^{+1.4\,+0.6}_{-1.3\,-0.6}$	$293.6^{+0.8\,+0.3}_{-0.8\,-0.3}$	$0.923^{+0.004\,+0.002}_{-0.004\,-0.002}$	$0.905^{+0.003\,+0.001}_{-0.003\,-0.001}$
V07302B	$0.86^{+0.05\,+0.02}_{-0.05\,-0.02}$	$0.95^{+0.03\,+0.01}_{-0.03\,-0.01}$	$266.8^{+1.3\,+0.5}_{-1.2\,-0.5}$	$264.6^{+0.8\,+0.3}_{-0.8\,-0.3}$	$0.929^{+0.004\,+0.002}_{-0.004\,-0.002}$	$0.921^{+0.003\,+0.001}_{-0.003\,-0.001}$
V07646A	$1.11^{+0.06\,+0.06}_{-0.03\,-0.03}$	$1.25^{+0.03\,+0.06}_{-0.03\,-0.05}$	$456.7^{+2.0\,+0.8}_{-1.9\,-0.9}$	$452.0^{+1.8\,+1.7}_{-0.9\,-0.8}$	$0.964^{+0.004\,+0.002}_{-0.004\,-0.002}$	$0.954^{+0.004\,+0.004}_{-0.002\,-0.002}$
V07647A	$1.22^{+0.05\,+0.02}_{-0.05\,-0.02}$	$1.32^{+0.03\,+0.01}_{-0.03\,-0.01}$	$312.3^{+1.4\,+0.5}_{-1.3\,-0.5}$	$310.0^{+0.8\,+0.3}_{-0.8\,-0.3}$	$0.909^{+0.004\,+0.001}_{-0.004\,-0.001}$	$0.902^{+0.002\,+0.001}_{-0.002\,-0.001}$
V07647B	$0.75^{+0.05\,+0.02}_{-0.06\,-0.02}$	$1.08^{+0.03\,+0.01}_{-0.03\,-0.01}$	$304.2^{+1.4\,+0.5}_{-1.4\,-0.5}$	$295.9^{+0.8\,+0.3}_{-0.8\,-0.3}$	$0.942^{+0.004\,+0.002}_{-0.004\,-0.002}$	$0.916^{+0.003\,+0.001}_{-0.002\,-0.001}$
V08682A	$0.99^{+0.05\,+0.01}_{-0.06\,-0.02}$	$1.14^{+0.03\,+0.01}_{-0.03\,-0.01}$	$567.7^{+2.1\,+0.8}_{-1.8\,-0.5}$	$562.2^{+1.3\,+0.5}_{-1.3\,-0.5}$	$0.944^{+0.004\,+0.001}_{-0.003\,-0.001}$	$0.935^{+0.002\,+0.001}_{-0.002\,-0.001}$
V08682B	$1.35^{+0.05\,+0.02}_{-0.06\,-0.02}$	$1.46^{+0.03\,+0.01}_{-0.03\,-0.01}$	$242.2^{+1.3\,+0.5}_{-1.3\,-0.5}$	$239.7^{+0.8\,+0.3}_{-0.8\,-0.3}$	$0.883^{+0.005\,+0.002}_{-0.005\,-0.002}$	$0.874^{+0.003\,+0.001}_{-0.003\,-0.001}$
V09374A	$0.91^{+0.05\,+0.03}_{-0.05\,-0.04}$	$1.08^{+0.03\,+0.01}_{-0.03\,-0.01}$	$452.6^{+1.8\,+1.2}_{-1.6\,-1.0}$	$446.8^{+1.1\,+0.4}_{-1.1\,-0.4}$	$0.944^{+0.004\,+0.002}_{-0.003\,-0.002}$	$0.932^{+0.002\,+0.001}_{-0.002\,-0.001}$
V09724A	$0.93^{+0.05\,+0.02}_{-0.05\,-0.02}$	$1.16^{+0.03\,+0.01}_{-0.03\,-0.01}$	$449.8^{+1.8\,+0.7}_{-1.6\,-0.5}$	$442.5^{+1.1\,+0.4}_{-1.1\,-0.4}$	$0.942^{+0.004\,+0.001}_{-0.003\,-0.001}$	$0.927^{+0.002\,+0.001}_{-0.002\,-0.001}$
V09372A	$0.88^{+0.05\,+0.02}_{-0.05\,-0.02}$	$1.01^{+0.03\,+0.01}_{-0.03\,-0.01}$	$700.3^{+2.4\,+1.0}_{-2.1\,-0.7}$	$694.5^{+1.5\,+0.6}_{-1.5\,-0.6}$	$0.955^{+0.003\,+0.001}_{-0.003\,-0.001}$	$0.947^{+0.002\,+0.001}_{-0.002\,-0.001}$

sources is observed. The detectors of the order 2 present a much smaller FCCD with respect with the others probably due to different production process. Additional analysis are proceed up to complete the view of the FCCD distribution on all surfaces. Considering the typical ICPC geometry, the FCCD is studied also inside the bore-hole surfaces. The FCCD at the bore-hole does not seem to be just half of the FCCD at the top surface and presents different values among detectors. Moreover, scan runs are used to validate the homogeneity assumption on the top and lateral sides. No significant in-homogeneity is observed within the uncertainties. Finally, the AV and its fraction are computed from the FCCD results paying attention on the geometry of each detector.

The next step would be a deeper study of the CCE before reaching unity. In App. E a count ratio analysis is performed in the ^{228}Th energy spectrum to find the best DLF (dead layer fraction) using a linear model. Another option could be developing an analysis with Machine Learning techniques to estimate the best DLF comparing energy spectra of the ^{133}Ba source. This source appears more suitable for this purpose without using count ratio analysis.

Part III

Active volume determination at the time of GERDA

6

FCCD GROWTH

All BEGes used in GERDA were characterized in the HADES facility following almost the same procedure then used for the ICPC detectors of LEGEND. After the ^{133}Ba and ^{241}Am measurements in vacuum cryostat, all BEGes were stored at room temperature (RT) for nearly 3 years before the GERDA deployment in 2015. Under such conditions, the Li-diffused FCCD of HPGe detectors can increase. The final results of GERDA [38] took care of this effect setting the average speed of the FCCD growth at RT at 0.1 mm/yr with a variance of ± 0.04 mm/yr, according to several authors [65][66] [64] using p-type HPGe detectors from different vendors. However, this assumption results in being poorly motivated, and a deeper investigation of this effect is required. Nine GERDA BEGe detectors were re-characterized in the HADES laboratory before being arranged in LEGEND arrays. Three BEGes – `GD00B`, `GD32B`, `GD91B` – are re-measured shortly after GERDA in 2021. While the second batch of 6 detectors – `GD35A`, `GD35B`, `GD00D`, `GD02C`, `GD61C`, `GD76C` – are re-measured in February-March 2022. Before this second measurement, the detectors were stored at RT, the first batch for 0.9 y and the second batch for $(0.9 + 1.2)$ y. Furthermore, two detectors – `GD35B` and `GD76C` – were immersed in LAr for ~ 0.6 y during the post-gerda test (PGT). The total time spent at RT, listed in Tab.6.1, are different for each detector.

Table 6.1: Period of time at room temperature between the first measurement in HADES and the GERDA Phase II deployment (first column), and between GERDA and the second measurement in HADES (second column) for each detector. Two BEGes were immersed in LAr during PGT.

BEGe	Time at RT before deployment in LAr [yr]	Time at RT after GERDA [yr]
`GD00D`	2.9	$0.9 + 1.2 = 2.1$
`GD02C`	2.8	$0.9 + 1.2 = 2.1$
`GD35A`	3.4	$0.9 + 2.1 = 2.1$
`GD35B`	2.3	$0.9 + 1.2 - 0.6 = 1.5$
`GD61C`	2.4	$0.9 + 1.2 = 2.1$
`GD76C`	2.9	$0.9 + 1.2 - 0.6 = 1.5$
`GD00B`	2.8	0.9
`GD32B`	2.5	0.9
`GD91B`	2.8	0.9

6.1 RE-CHARACTERIZATION OF NINE BEGES

The re-characterization process of nine BEGe detectors mainly follows the same steps described in the previous chapter. Two different surface probes – ^{241}Am and ^{133}Ba sources – are used to estimate the FCCD, measuring the CCE attenuation around the n+ surface of detectors. The setting of these measurements follows the GERDA program for the first characterization. Compared to 10 years before, the measurement run time has been increased due to lower activity of the sources (see Fig.A.2), especially for ^{133}Ba source whose activity is reduced by $\sim$ 92%. The ^{133}Ba source (*ba_HS4*) is set at 198 mm from the top of the detector in a central radial position. Each run lasts 2 hours w.r.t. a run-time of 1 hour used during the first characterization. For the first batch, a second measurement is taken with a distance of 78 mm, the typical setting in the LEGEND program. For these detectors, the final ^{133}Ba results are obtained from a combination of the estimated values from both runs, allowing a reduction of the systematics uncertainties. The uncollimated ^{241}Am source (*am_HS6*) is set in a central radial position at 198 mm from the top of the detector and the run is taken for 2 hours.

Regarding MCs, the simulated setup components are the same as those used in the LEGEND characterization. Only the Milar foil is added between the detector and the wrap, but its thickness is so small that it does not affect the FCCD results. The cryostat presents slightly different dimensions w.r.t. the one surrounding the ICPC detectors. For simplicity, the peculiar geometry of the electronic base is not simulated, and the detector holder presents a cylinder shape (see Fig.6.1). The validation of the simulations is straightforward since the main verification has already been proven by the ^{228}Th source in LEGEND. The few differences are verified by looking at the visualization outputs showing the entire simulated setup; this allows checking the positions of MCs. The same automation code used for the ICPC detectors in the LEGEND campaign is adapted to these BEGe measurements.

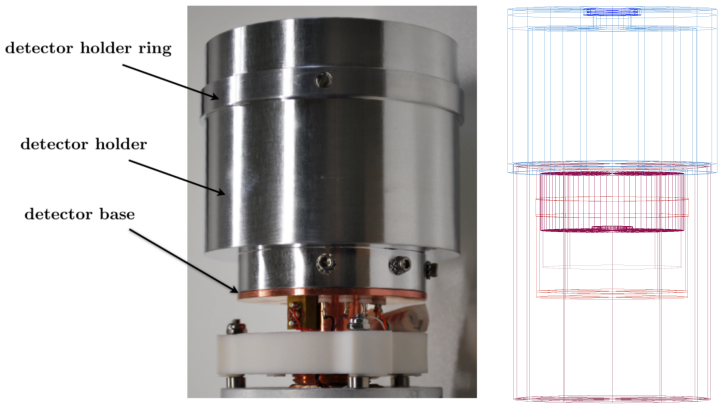

Figure 6.1: Set-up components used in the BEGe characterization. Left: image of the detector holder, the electronic base is not simulated. Right: visualization of the simulated volumes inside the lead castle.

6.1.1 ^{133}*Ba analysis*

The analysis procedures for the ^{133}Ba and ^{241}Am sources are the same as those used for the ICPC characterization in LEGEND. For completeness, the main points of the BEGe measurements are listed below; see Sec.5.5.2 and Sec.5.5.3 for details. Fig.6.2 shows the spatial distribution of the energy deposition on the BEGe when the ^{133}Ba is placed at 78 mm (top) and 198 mm (bottom) from the top side. The events are weighted with the related emission probabilities. The lack of the bore-hole at the top of the BEGe allows not to separate areas with different FCCD, as instead it was made for the ICPC analysis. The hits are closely concentrated on the surface, as for ICPCs (see Fig.5.14). The events from the source set at a greater distance are more degraded due to the increase of the solid angle of the source window. The data are calibrated and the MC are post-processed

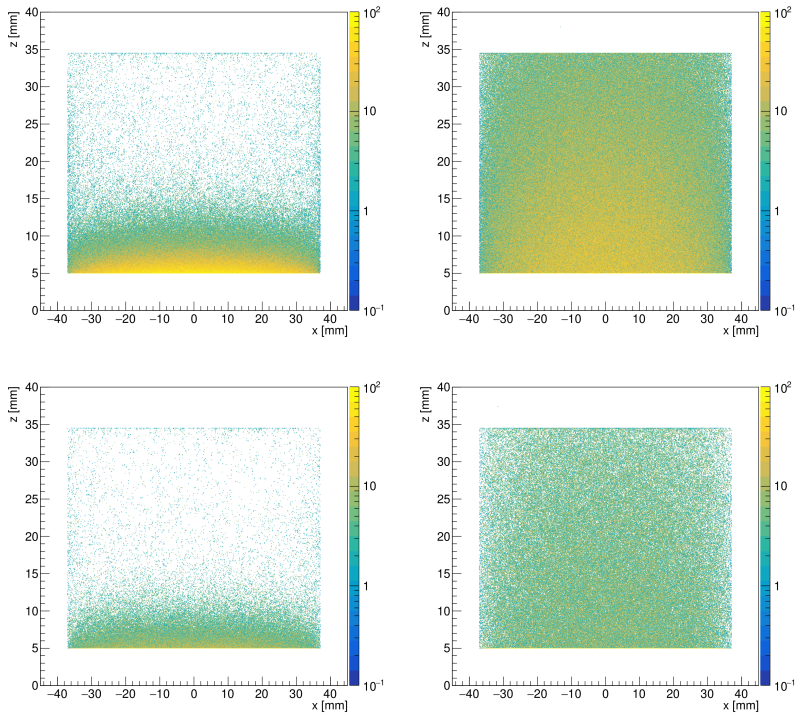

Figure 6.2: Scatterplots in x-z plane of hits from the ^{133}Ba source placed centered at the top of the detector at a distance of 78 mm (top) and 198 mm(bottom) . Left: hits from the 81 keV γ-line only. Right: hits from356 keV γ-line only.

varying the FCCD. The effects of the FCCD at the main peaks used in the analysis are shown in Fig.6.3. Fig.6.4 shows the typical fit at 80 keV double-peak and at 356 keV peak, whose integrals are required for the computation of the observable in Eq.5.3. Finally, the estimated FCCD is obtained from the intersection of the exponential fit of the simulation observable with the data observable. The result and the final comparison between the data spectrum and the MC spectrum post-processed with the estimated FCCD are shown in Fig.6.5.

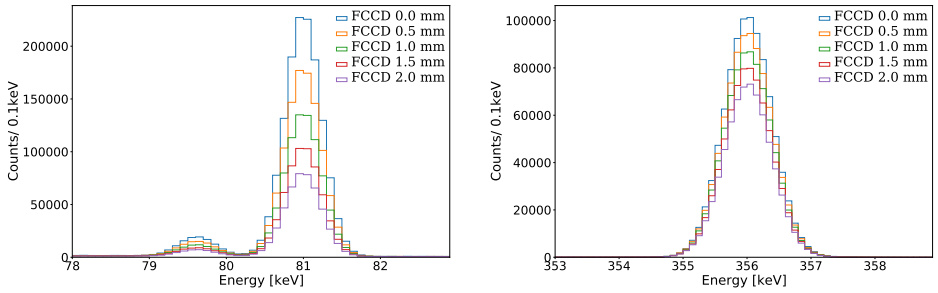

Figure 6.3: Variation of the ^{133}Ba peaks for different FCCD values. The lower energy peak at 81 keV is more affected by the post-processing.

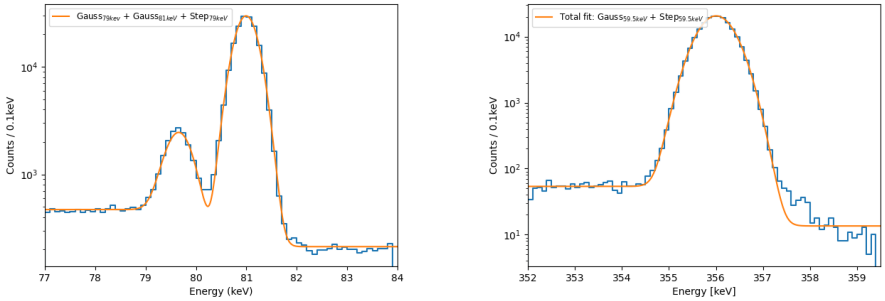

Figure 6.4: Example fit of the observed γ peak at 356 keV and of the double peak around 80 keV.

6.1.2 ^{241}*Am analysis*

The FCCD determination with the ^{241}Am source is obtained with the uncollimated ^{241}Am source also used during the ICPCs characterization in LEGEND to calibrate the collimated ^{241}Am source. Below, the typical figures of FCCD estimation of the BEGe are included. As shown in Fig.6.6, the energy depositions from the uncollimated ^{241}Am source are mostly distributed at the top surface. Mainly due to the lack of the collimator, the events are more spread inside the detector bulk w.r.t. the distribution in ICPC for the collimated ^{241}Am source shown in Fig.5.18. The events are weighted with the related emission probabilities for the 59.5 keV peak (top) and all main γ-lines till $\sim$ 700 keV (bottom). Fig.6.7 shows how the main peaks are cut with different FCCD. As usual, the data are calibrated and the MC are post-processed varying the FCCD. As done for the ICPC, the fitting functions of the main peaks are different for the data spectrum and MC spectra, as displayed in Fig.6.8. After computing the integral of the peaks, the observable in Eq.5.4 is calculated for the data and the MCs. Fig.6.9 (top) shows the typical graph of the FCCD estimation stemmed from the intersection between the exponential fit of the simulated observable and the data observable. The comparison between the data spectrum and the MC spectrum with the FCCD set at the estimated value is displayed in Fig.6.9 (bottom).

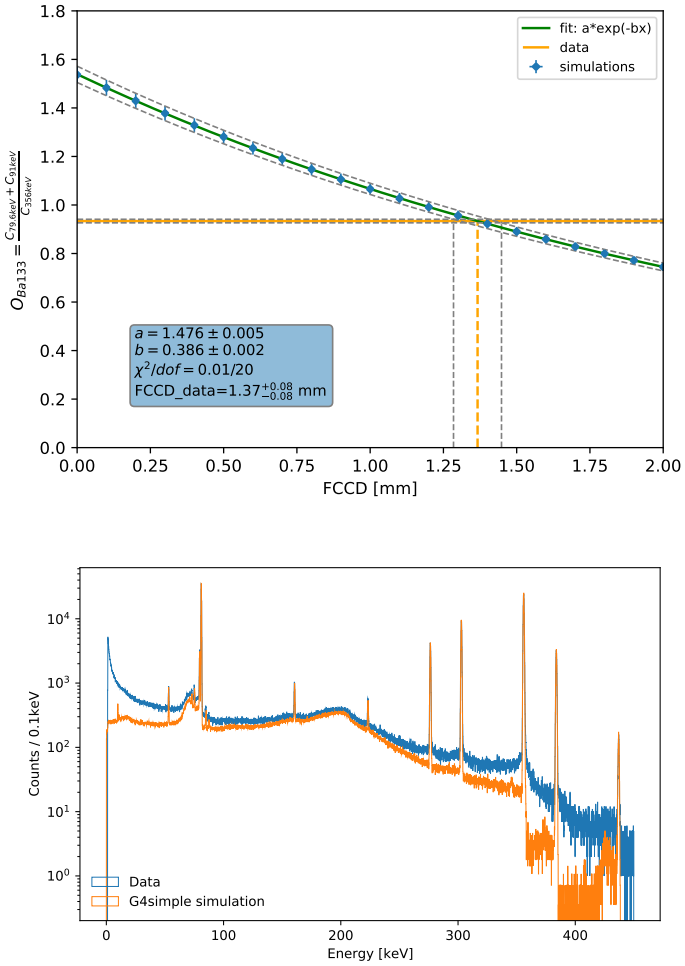

Figure 6.5: Top: count ratio as a function of simulated FCCD; the intersection of the data count ratio and the exponential fit of the simulated count ratio gives the estimated FCCD. Bottom: comparison of the simulated and observed energy spectra; the simulated peaks are normalized to the run time of the data taking.

6.2 RESULTS

The systematic uncertainties on MCs are summarized in Table 6.2 and are described in Sec.5.5.5. As done for ICPC analysis, these uncertainties are categorized by their origins, such as the MC process or the geometry of the simulated setup. The number of primaries of MC is chosen so that the MC statistics would not be relevant compared to the other systematics. Only the MC statistical uncertainty is an uncorrelated uncertainty since it is individual for each BEGe and it does not define the AV determination method, common for each BEGe. The systematics are expected to be very similar to those of the first measurement since the two characterizations are entirely consistent. The results from the two ^{133}Ba measurements (with the source at 78 mm and 198 mm from the detector) of the 3 BEGes of the first batch are combined, weighting in the systematics.

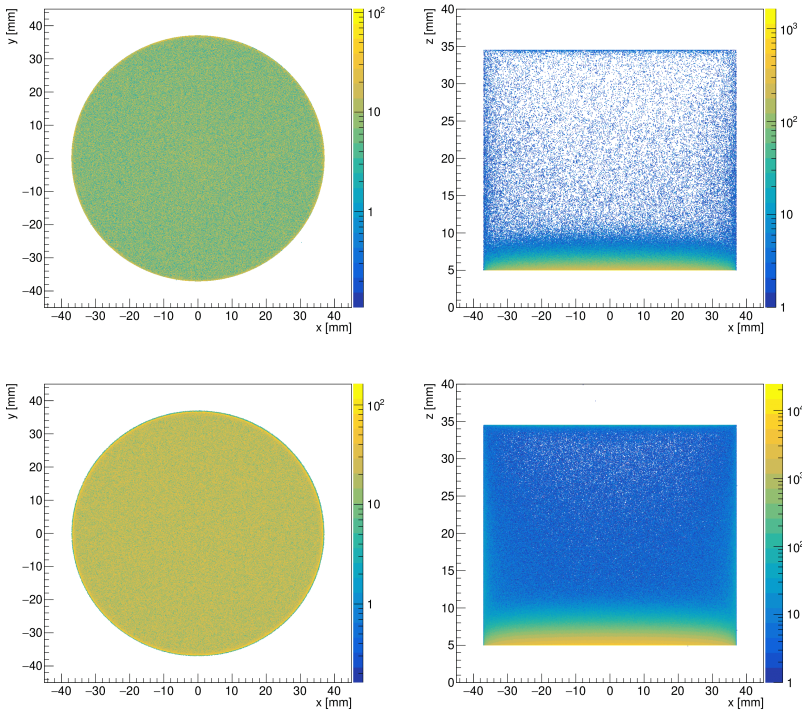

Figure 6.6: Scatterplots in x-y plane (left) and x-z plane (right) of hits from the ^{241}Am source placed centered at the top of the detector. Top: hits from the 59.5 keV γ line only. Bottom: hits from all the gamma lines (till $\sim$ 700 keV) generated in MC.

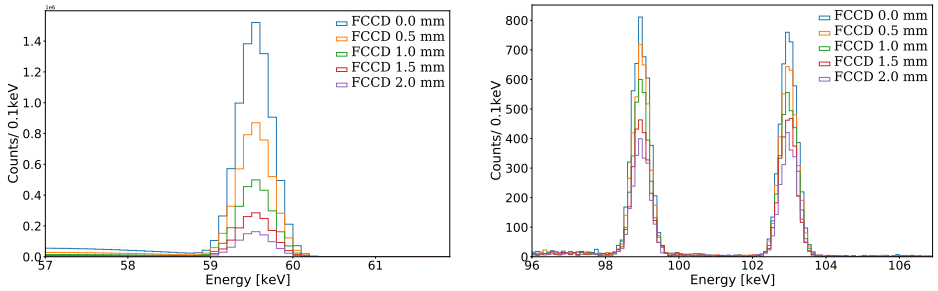

Figure 6.7: Variation of the ^{241}Am peaks for different FCCD values. The lower energy peak at 59.5 keV is more affected by the post-processing.

The FCCD analysis has been automatically repeated for all detectors, and Fig.6.10 shows the final results from the ^{241}Am source, the ^{133}Ba source, and the combined results of the two analyses. There is a systematic offset between the two results, as already shown for the first measurement [38] and even for the ICPC characterization (Sec.5.5.6). The stability of the results is checked by applying the QC to the data. QC are mainly meant to remove pile-up events in the decay tail or baseline. Even if they are not expected in the FEP, a slightly improvement on the feasibility of the fitting procedure of the analysis has been noticed. However, the final results of FCCD are not affected by the application of the QC. Tab.6.3 lists the ^{241}Am and ^{133}Ba results without QC. Their combination is chosen to analyze the

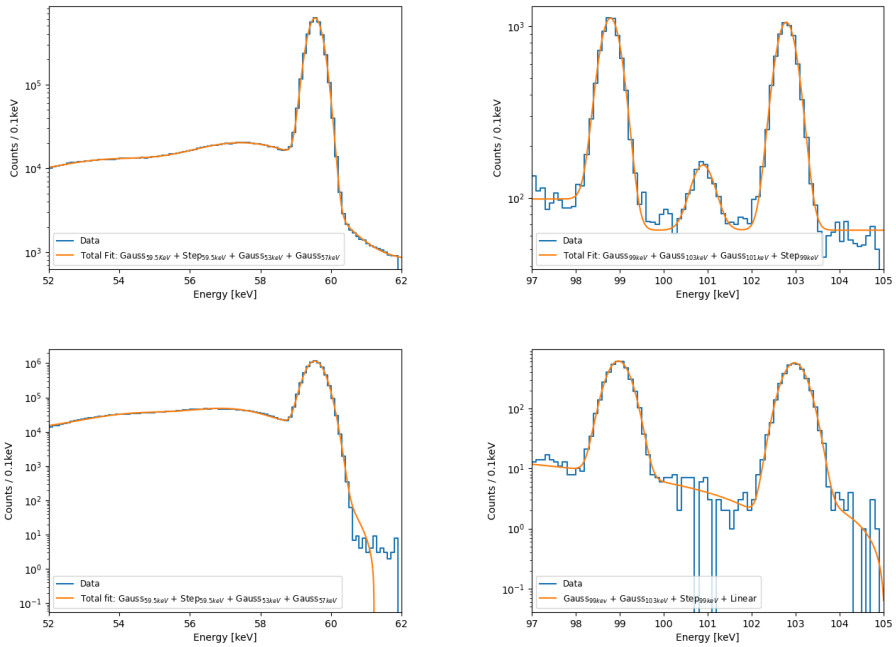

Figure 6.8: Example fit of the γ peak at 59.5 keV (left) and the region of the double peak (right). Top: fit on the observed spectrum; two little bumps at lower energy respect with the peak at 59.5 keV are fitted as well. The peak at 101 keV is clearly visible. Bottom: fit on the simulated spectrum; the peaks are smeared with the energy resolution calculated from the data calibration. An additional linear function is summed to the empirical fitting function on the double peak.

Table 6.2: List of the systematics (in %) affecting the simulated observable for the BEGe analysis with ^{241}Am source and ^{133}Ba source.

Systematics	$\Delta O_{^{241}Am}$ [±%]	$\Delta O_{^{133}Ba}$ [±%]
γ line probability	1.81	0.69
GEANT4	2	2
Source thickness	0.02	0.02
Source material	0.01	0.01
Cryostat thickness	0.31	0.28
Wrap thickness	0.03	0.07
Wrap material	0.01	0.03

FCCD growth for each detector. In Fig.6.11, these results are compared with those derived by the first characterization in 2012 and with the official ones, which are meant to be the estimations of the FCCD at the start of GERDA Phase II.

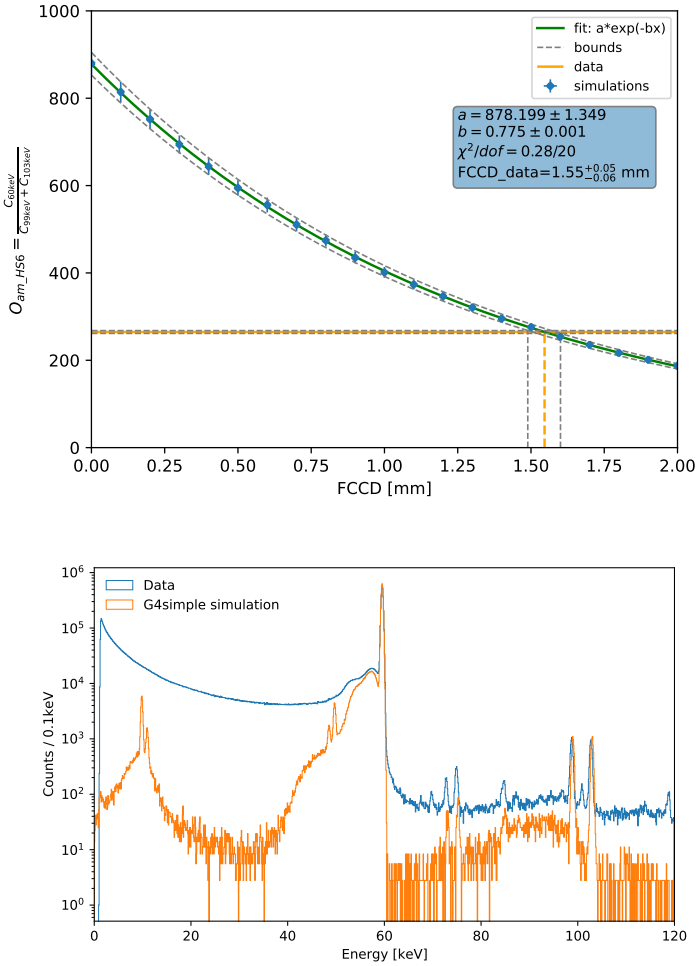

Figure 6.9: Top: count ratio as a function of simulated FCCD (see text). Bottom: comparison of the simulated and observed energy spectra; the simulated peaks are normalized to the run time of the data taking.

6.3 FCCD HOMOGENEITY

In 2012, a dedicated analysis verified the homogeneity of the FCCD over the top and lateral sides of BEGes. This assumption needs to be checked after the growth, as well. Due to the lack of a complete model, there is no guarantee that the FCCD has grown homogeneously over the surfaces, and analysis similar to the one performed on the ICPC in Sec.5.5.8 is required. The GD35A detector is not analyzed due to its tapered geometry at the top side. The measurement scans used for the analysis are the top linear scan and the lateral linear scan with the collimated ^{241}Am source at 5 mm and 3.5 mm from the cryostat, respectively. The time of a single measurement is 180 s with a step of 0.5/1 mm. Many detectors present additional top and lateral linear scans at different angular coordinates. They can be helpful to double-check the results also on other projection-planes of the detector. Furthermore, circular scans can verify the FCCD homogeneity around the

Table 6.3: FCCD and total uncertainties obtained from the ^{133}Ba and ^{241}Am analyses without the application of QC. The ^{133}Ba values of the BEGes of the first batch (last three lines) are obtained from a mean of the two runs with the source at 78 mm and 198 mm.

BEGe	^{133}Ba FCCD [mm]	^{241}Am FCCD [mm]
GD00D	0.87 ± 0.07	1.05 ± 0.05
GD02C	0.99 ± 0.07	1.13 ± 0.06
GD35A	1.59 ± 0.06	1.69 ± 0.08
GD35B	1.25 ± 0.07	1.38 ± 0.07
GD61C	0.81 ± 0.07	0.99 ± 0.06
GD76C	0.95 ± 0.07	1.09 ± 0.06
GD00B	1.36 ± 0.06	1.55 ± 0.05
GD32B	1.14 ± 0.06	1.38 ± 0.05
GD91B	1.15 ± 0.06	1.35 ± 0.05

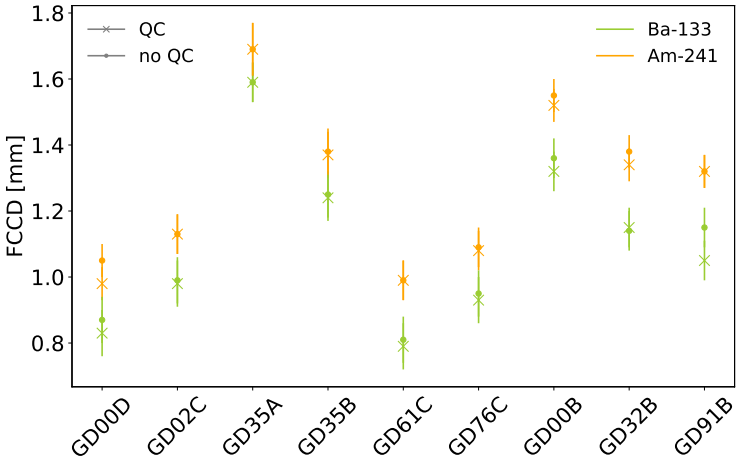

Figure 6.10: FCCD results obtained from the ^{133}Ba and ^{241}Am analyses with and without the QC application. Also the weighted mean between the two analysis is plotted for each detector.

z-axis at a precise source position. A circular scan has a duration of 120 s with a step of 5/10 deg.

As for the ICPC detectors, the energy spectrum collected in each run undergoes the energy calibration and the fitting of the 59.5 keV peak. The integral counts in the $\pm 3\sigma$ region around the mean of the Gaussian determine the peak counts. This process is repeated automatically for each top and lateral scan. For instance, the top linear distribution of the peak counts for different source positions of GD00D detector is compared in Fig.6.12 with the distribution obtained from the first characterization (top-left). The right column of the figure shows the distribution along two different projection-planes of the second characterization. The scale of the first and second characterization results is not supposed to be the same because of the potential difference in the integration range around the

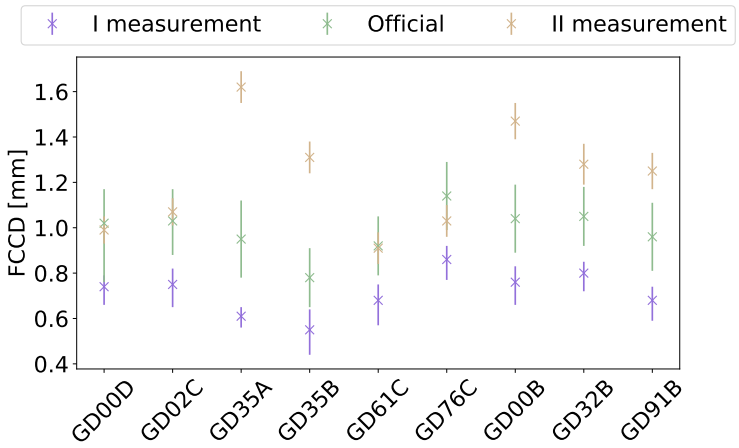

Figure 6.11: Comparison of the FCCD results with the values obtained from the first measurement and the values estimated at the time of measurement considering an average speed of the FCCD growth at ~ 0.1 mm/yr.

59.5 keV peak, in the run-time, and in the source distance set during the single measurement. Looking at the peak counts' shape, it is clear that the FCCD is no longer homogeneous on the top surface after its growth. Furthermore, the plot at the right-bottom shows the result, normalized to the run-time of the linear scans, from the top radial scan of the second characterization with the source set at $x = 29.5$ mm in the scanning table frame. This position corresponds to the slight depression visible on the linear scans and seems to vary for different angular coordinates.

Fig.6.13 shows the number of counts of the 59.5 keV peak for the source set at the lateral side of the `GD02C` detector. In this case, constant distribution of the counts is not expected because of the different thicknesses of the detector holder. The column on the right represents two lateral linear scans of the second characterization from the top to the bottom of one side of the detector at different angular coordinates. Comparing them with the plot at the right-top obtained during the first characterization, it is evident that even along the lateral side the FCCD homogeneity assumption is no longer valid. The plot at the right-bottom is the lateral circular scan of the second characterization with the source set at $z = 242$ mm in the scanning table frame. At that position, the detector seems to have the same trend around the z-axes. The points are normalized to the run-time of the linear scans to compare them better.

Then, the distributions are fitted by a constant function excluding the extreme points to avoid any border effect. The points of the lateral scans related to the different thicknesses of the holder are not considered in the fit. The fits return the counts $R_{TOP(LAT)}$ of the top (lateral) side, and for the detectors with two scans on the same side, the results of the two fits are combined with a weighted average with the fit error as the weights. Moreover, the final counts need to be normalized by the correction attenuation factors (see Tab.5.5). Once computed the count ratio r (see Eq.5.11), the related difference in FCCD and its variation is estimated by Eq.5.12

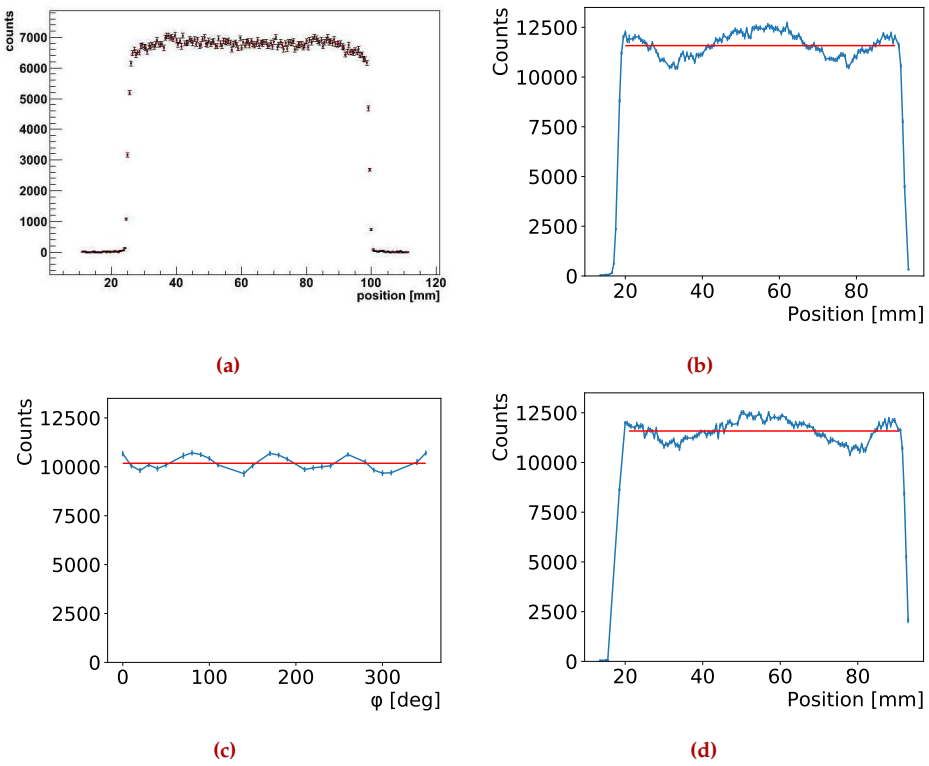

Figure 6.12: Number of counts at 59.5 keV for different source positions at the top of GD00D detector. (a) : distribution obtained from the first characterization in 2012 [91]. (b-d): distributions obtained from the second characterization along two perpendicular lines at the top of the detector. (c): distribution of the points obtained during the top circular scan at $x = 29.5$ mm of the second characterization. In the plots of the second characterization, the fit of the points is indicated by the constant red lines.

and Eq.5.13. Tab.6.4 lists the results for the 8 BEGes, comparing them with those obtained from the first characterization in 2012. The results of the detectors – GD00B, GD032B, GD091 – of the first batch measured in 2021 appears generally less affected by this in-homogeneity, probably because of the shorter time spent at RT. Fig.6.14 plots R_{TOP} counts as a function of the R_{LAT} (left) and the FCCD values estimated before (right). The two batches, indicated by different colors, seem to belong to two different populations.

In conclusion, the homogeneity is no longer proved and the FCCD distribution along the top and lateral sides appear different for each detector. However, the uncertainties related to this in-homogeneity are much smaller than the total uncertainty related to the final FCCD estimation reported in Tab.6.5. Identifying a potential model that can explain these FCCD values and the related distribution along the surfaces is crucial to estimate the FCCD for the other BEGes, but it is beyond the scope of this work.

6.4 CONCLUSION

To find the best FCCD estimations at the time of GERDA, the results of the first and second measurements are plotted as a function of the time in

Table 6.4: Surface FCCD variation from scanning measurements of BEGe detectors of the first [81] and second characterizations. The first column indicates the FCCD difference between the top and later surface while the other two columns list the FCCD variation on the top surface and the lateral surface, respectively. The detector results of the first and second characterization refer to different FCCD value estimations.

ICPC	First characterization			Second characterization		
	$\Delta FCCD \pm \sigma_{\Delta FCCD}$ [mm]	$\delta FCCD_{TOP}$ [mm]	$\delta FCCD_{LAT}$ [mm]	$\Delta FCCD \pm \sigma_{\Delta FCCD}$ [mm]	$\delta FCCD_{TOP}$ [mm]	$\delta FCCD_{LAT}$ [mm]
GC00D	0.01 ± 0.00	0.03	0.02	0.10 ± 0.02	0.04	0.06
GD02C	0.00 ± 0.00	0.01	0.03	-0.03 ± 0.02	0.05	0.05
GD35B	0.03 ± 0.01	0.01	0.00	-0.12 ± 0.02	0.04	0.04
GD61C	0.02 ± 0.00	0.02	0.05	0.04 ± 0.02	0.04	0.04
GD76C	0.00 ± 0.01	0.01	0.01	-0.02 ± 0.02	0.06	0.07
GD00B	0.01 ± 0.00	0.03	0.05	-0.03 ± 0.02	0.01	0.01
GD32B	0.07 ± 0.01	0.03	0.02	-0.09 ± 0.02	0.04	0.02
GD91B	0.02 ± 0.00	0.02	0.03	-0.01 ± 0.02	0.01	0.03

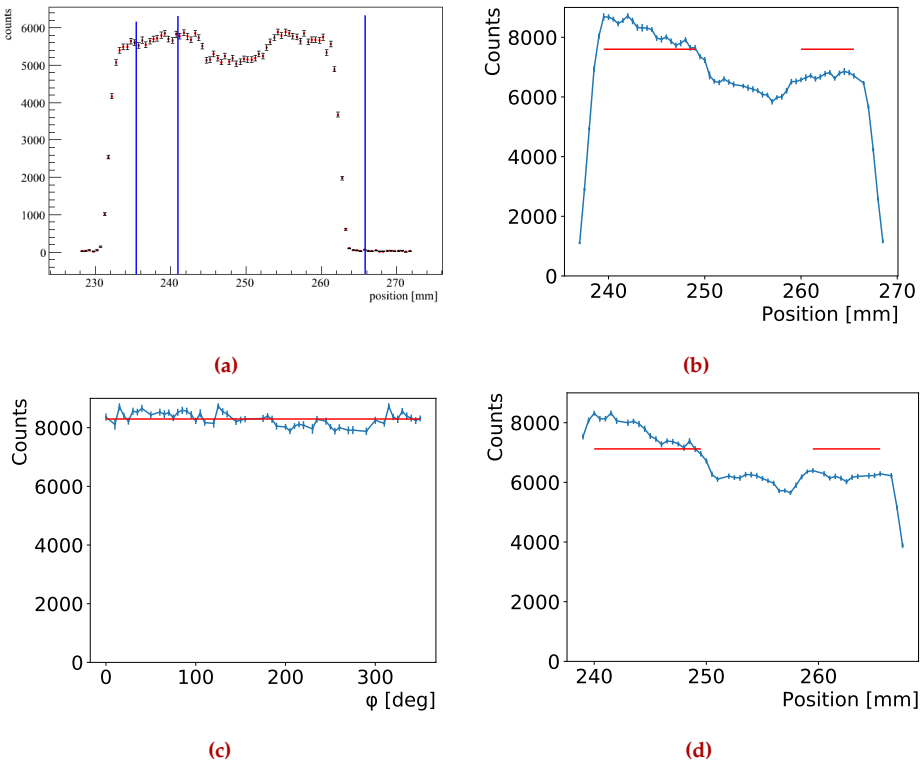

Figure 6.13: Number of counts at 59.5 keV for different source positions on the lateral side of GD02C detector. (a): distribution obtained from the first characterization in 2012 [91]; the blue lines indicate the points sampled in the circular scans. (b-d): distributions obtained from the second characterization along the z-axis starting from two different sides. (c): distribution of the points obtained during the lateral circular scan at $z = 242$ mm of the second characterization. In the plots of the second characterization, the fit of the points is indicated by the constant red lines.

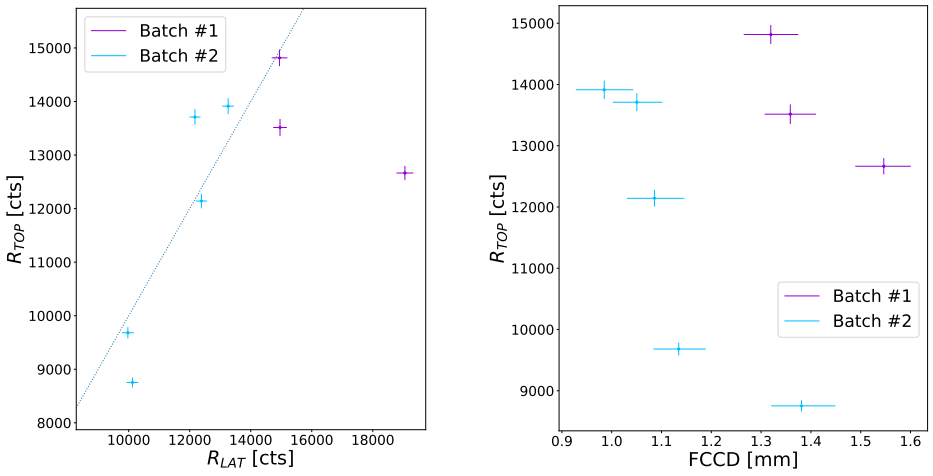

Figure 6.14: Correlation between count ratios from the top and lateral scans (left) and between the top count ratio and the estimated FCCD from ^{241}Am analysis (right) for each BEGe whose batch is marked with different color.

Fig.6.15. The nearly three years of GERDA Phase II data-taking collapses in 0. The results obtained from ^{133}Ba and ^{241}Am sources are firstly treated

separately. Different growths among detectors are observed and a linear interpolation is performed for the nine BEGes. The detectors can be divided

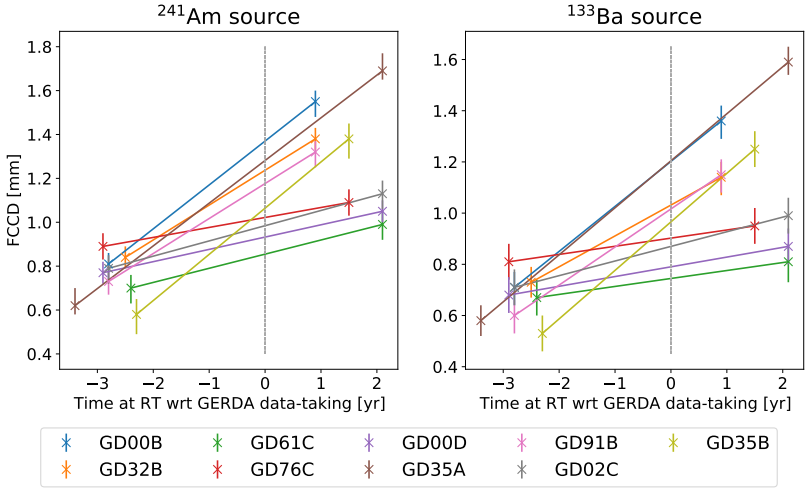

Figure 6.15: First and second measurements as a function of the time at RT for each detector. The 3 years of GERDA are collapsed in 0. Two different distributions of FCCD growth are visible.

into two groups with different growth speeds. `GD32B, GD35A, GD35B` detectors belong to the same production batch and show a large growth. All the others belong to another batch but show an unexpected difference between the growths. In the absence of a reliable growth model appropriate for all BEGe detectors, the conclusions can be related only to the nine BEGes. The two growth populations are clearer in Fig.6.16 (left) which shows the linear growth - the slope of the interpolation - for each detector. The uncertainties are negligible because the systematic uncertainties between the two measurements are the same. The interpolated values at the time of GERDA are

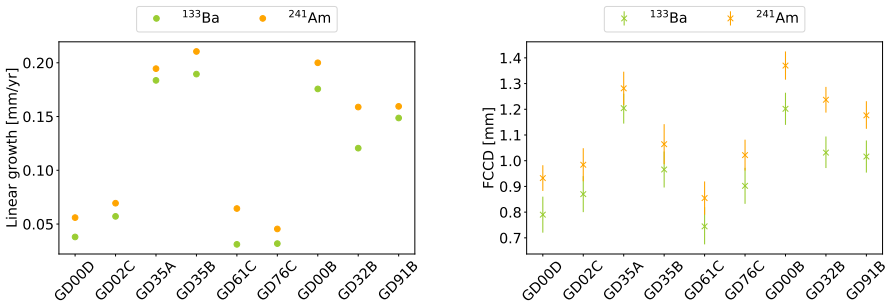

Figure 6.16: Left: slope of the linear interpolation between the two measurement results for each detector for ^{133}Ba and ^{241}Am sources. Right: interpolated FCCD at the time of GERDA from ^{133}Ba and ^{241}Am analyses.

displayed with propagated uncertainties in Fig.6.16 (right) for ^{133}Ba and ^{241}Am analysis. The values from the two sources are consistent and present the systematic offset. The mean between interpolated values is compared in Fig.6.17 with the value used previously in the official GERDA results for each detector. Moreover, additional uncertainty is computed considering the two

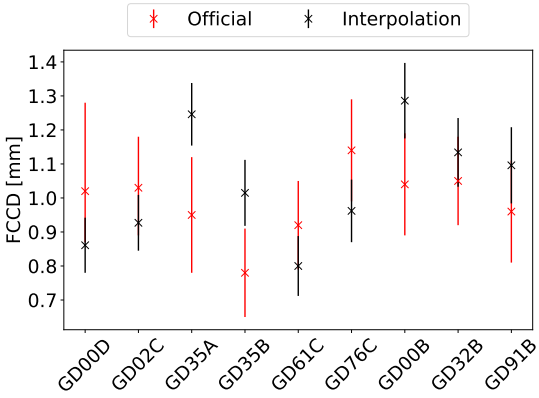

Figure 6.17: Comparison between the weighted mean of the FCCD estimated at the time of GERDA from the ^{133}Ba and ^{241}Am analyses and the estimated FCCD with the ~ 0.1 mm/yr speed of the FCCD growth.

different growth speeds (slow and fast) to take into account the uncertainty of the growth. As the data do not indicate significant correlations between the growth in different detectors, this uncertainty is treated as uncorrelated. A typical uncorrelated uncertainty is displayed in Fig.6.18.

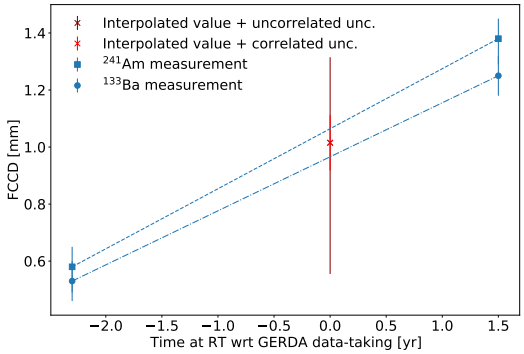

Figure 6.18: Example of the additional uncorrelated uncertainty of the mean of the two estimated FCCD from ^{133}Ba and ^{241}Am analyses. It accounts for the unknown growth model.

Finally, Tab.6.5 lists the FCCD mean value with correlated and uncorrelated uncertainties and the related active volume fraction with the propagated uncertainties for each detector.

This second measurement is crucial to verify the assumption of the FCCD growth speed used so far without a reliable model. Furthermore, the AV uncertainty impacts the detection efficiency, and so the half-life, of the $2\nu\beta\beta$ decay. These effects are described in detail in Chap.8. In the future, to prevent dead layer growth for new detectors, a freezer with a temperature range of $[-45°, -10°]$ C could be available to control the detector temperature while waiting to be installed.

Table 6.5: List of the weighted mean between the FCCDs obtained from the interpolation at the time of GERDA of the two measurements of ^{133}Ba and ^{241}Am sources. The second column indicated the active volume fractions. The uncertainties are separated into correlated and uncorrelated components.

BEGe	FCCD [mm]	f_{AV}
GD00D	$0.86^{+0.08+0.10}_{-0.08-0.14}$	$0.904^{+0.009+0.010}_{-0.009-0.015}$
GD02C	$0.93^{+0.08+0.13}_{-0.08-0.18}$	$0.897^{+0.009+0.014}_{-0.009-0.019}$
GD35B	$1.02^{+0.10+0.30}_{-0.10-0.46}$	$0.888^{+0.010+0.032}_{-0.010-0.050}$
GD35A	$1.25^{+0.09+0.40}_{-0.09-0.65}$	$0.868^{+0.009+0.040}_{-0.009-0.067}$
GD61C	$0.80^{+0.09+0.10}_{-0.09-0.12}$	$0.900^{+0.010+0.013}_{-0.010-0.014}$
GD76C	$0.96^{+0.09+0.06}_{-0.09-0.11}$	$0.895^{+0.010+0.006}_{-0.010-0.012}$
GD00B	$1.29^{+0.11+0.17}_{-0.11-0.53}$	$0.850^{+0.013+0.018}_{-0.013-0.060}$
GD32B	$1.13^{+0.10+0.13}_{-0.10-0.35}$	$0.872^{+0.011+0.014}_{-0.011-0.038}$
GD91B	$1.10^{+0.11+0.14}_{-0.11-0.43}$	$0.871^{+0.013+0.016}_{-0.013-0.049}$

7

ACTIVE VOLUME ESTIMATION VIA EVENTS

The typical procedure to determine the HPGe active volume is by probing the detector with radioactive sources in a dedicated setup, as explained in the previous sections. The recommended FCCDs obtained by the GERDA characterization campaign are reported in Tab.7.1 and are briefly described in the following. The Coax values are extracted from ^{60}Co data as documented in [92], while the BEGe values are obtained by combining ^{241}Am and ^{133}Ba data [93]. ICPC values are extracted from ^{241}Am measurements [86]. As described in the previous chapter, the BEGe detectors have been stored at room temperature and must be therefore corrected for the dead-layer growing effect. They present the growth estimation of $\sim$ 0.1 mm/yr, with a standard deviation of 0.04 mm/yr [93]. While the FCCDs estimated at the time of the GERDA data-taking for the nine BEGes recently re-characterized are listed in Tab.6.5.

An alternative procedure to have more homogeneous results among all detectors would use the GERDA physics data itself to extract the model of the detectors' active volume. The results would be directly usable in any analysis of the data collected during Phase II without any need to correct for unknown dead-layer growth effects. Since effects of partial charge collection are mostly present at low energies, the analysis focuses on events with energies of a few hundred keV deposited in germanium. In this domain, data are dominated by ^{39}Ar decays, naturally occurring in atmospheric LAr. As evident in the following sections, the model of the active volume mainly influences the shape of the energy distribution of these events.

This chapter reports the analysis to extract the FCCD and DLF by studying the ^{39}Ar energy spectrum. Firstly, Sec.7.1 describes the data-set used for the analysis. The physics behind the ^{39}Ar decay in GERDA and how it is affected by the AV is explained in Sec.7.2, which also defines the MC simulations and the observed anomaly on the ^{39}Ar rate. Then, the statistical analysis is reported in Sec.7.3, explaining how the mean values of the parameters are obtained and how the toys MC are generated to compute the confidence intervals. Sec.7.4 lists and explains the systematic uncertainties considered in the analysis. Some tests on the ^{39}Ar rate, the event statistic, and the ^{39}Ar simulation volume are described in Sec.7.5. Finally, Sec.7.6 discusses the results of FCCD and DLF parameters.

Table 7.1: FCCD and DLF values for each detector deployed in GERDA Phase II, calculated from detector characterization data. The Coax values are extracted from ^{60}Co data [92] while the BEGe FCCD values are obtained by combining ^{241}Am and ^{133}Ba data [93] and correcting the dead-layer growing effect. The uncertainties are split into correlated and uncorrelated contributions. The DLF values have been estimated in [81] and do not include any growing effect at room temperature. The ICPC values are obtained from ^{241}Am data [86].

Detector	FCCD (mm)	DLF
ANG1	1.80 ± 0.5	–
ANG2	2.30 ± 0.7	–
ANG3	1.90 ± 0.8	–
ANG4	1.40 ± 0.7	–
ANG5	2.60 ± 0.6	–
RG1	1.50 ± 0.7	–
RG2	2.30 ± 0.7	–
GD00A	$0.91^{+0.14\,+0.04}_{-0.15\,-0.03}$	$0.13^{+0.05}_{-0.04}$
GD00B	$1.04^{+0.14\,+0.04}_{-0.15\,-0.04}$	$0.20^{+0.03}_{-0.04}$
GD00C	$1.01^{+0.16\,+0.02}_{-0.17\,-0.02}$	$0.17^{+0.03}_{-0.03}$
GD00D	$1.03^{+0.15\,+0.02}_{-0.16\,-0.02}$	$0.37^{+0.02}_{-0.02}$
GD02A	$0.88^{+0.12\,+0.03}_{-0.13\,-0.03}$	$0.02^{+0.03}_{-0.04}$
GD02B	$0.97^{+0.14\,+0.04}_{-0.15\,-0.04}$	$0.24^{+0.04}_{-0.04}$
GD02C	$1.03^{+0.14\,+0.04}_{-0.15\,-0.04}$	$0.49^{+0.03}_{-0.03}$
GD02D	–	–
GD32A	$0.91^{+0.17\,+0.02}_{-0.18\,-0.02}$	$0.17^{+0.03}_{-0.03}$
GD32B	$1.05^{+0.13\,+0.02}_{-0.14\,-0.02}$	$0.21^{+0.03}_{-0.02}$
GD32C	$0.97^{+0.13\,+0.02}_{-0.14\,-0.02}$	$0.28^{+0.02}_{-0.03}$
GD32D	$0.77^{+0.13\,+0.03}_{-0.14\,-0.03}$	$0.31^{+0.04}_{-0.04}$
GD35A	$0.95^{+0.17\,+0.01}_{-0.17\,-0.01}$	$0.13^{+0.03}_{-0.02}$
GD35B	$0.78^{+0.12\,+0.06}_{-0.13\,-0.05}$	$0.16^{+0.09}_{-0.07}$
GD35C	$0.79^{+0.12\,+0.02}_{-0.13\,-0.02}$	$0.34^{+0.02}_{-0.02}$
GD61A	$1.00^{+0.15\,+0.05}_{-0.15\,-0.04}$	$0.15^{+0.04}_{-0.05}$
GD61B	$1.00^{+0.14\,+0.04}_{-0.15\,-0.04}$	$0.37^{+0.03}_{-0.03}$
GD61C	$0.93^{+0.12\,+0.04}_{-0.14\,-0.04}$	$0.44^{+0.03}_{-0.03}$
GD76B	$1.14^{+0.14\,+0.04}_{-0.16\,-0.03}$	$0.32^{+0.03}_{-0.03}$
GD76C	$1.15^{+0.15\,+0.03}_{-0.16\,-0.03}$	$0.45^{+0.02}_{-0.02}$
GD79B	$1.03^{+0.16\,+0.03}_{-0.17\,-0.03}$	$0.25^{+0.02}_{-0.03}$
GD79C	$1.09^{+0.13\,+0.03}_{-0.14\,-0.03}$	$0.45^{+0.02}_{-0.02}$
GD89A	$1.00^{+0.16\,+0.04}_{-0.17\,-0.03}$	$0.19^{+0.02}_{-0.04}$
GD89B	$1.12^{+0.16\,+0.02}_{-0.17\,-0.02}$	$0.28^{+0.02}_{-0.02}$
GD89C	$0.99^{+0.15\,+0.03}_{-0.17\,-0.03}$	$0.33^{+0.03}_{-0.03}$
GD89D	$1.03^{+0.14\,+0.03}_{-0.15\,-0.02}$	$0.36^{+0.02}_{-0.03}$
GD91A	$1.00^{+0.15\,+0.04}_{-0.16\,-0.03}$	$0.14^{+0.02}_{-0.04}$
GD91B	$0.95^{+0.14\,+0.03}_{-0.15\,-0.03}$	$0.19^{+0.02}_{-0.03}$
GD91C	$0.95^{+0.14\,+0.04}_{-0.15\,-0.04}$	$0.13^{+0.03}_{-0.05}$
GD91D	$0.99^{+0.16\,+0.04}_{-0.17\,-0.04}$	$0.36^{+0.04}_{-0.03}$
IC48A	$0.82 \pm 0.05_{\text{stat}} \pm 0.05_{\text{sys}}$	–
IC48B	$0.80 \pm 0.03_{\text{stat}} \pm 0.05_{\text{sys}}$	–
IC50A	$1.03 \pm 0.06_{\text{stat}} \pm 0.06_{\text{sys}}$	–
IC50B	$0.79 \pm 0.03_{\text{stat}} \pm 0.05_{\text{sys}}$	–
IC74A	$1.14 \pm 0.06_{\text{stat}} \pm 0.05_{\text{sys}}$	–

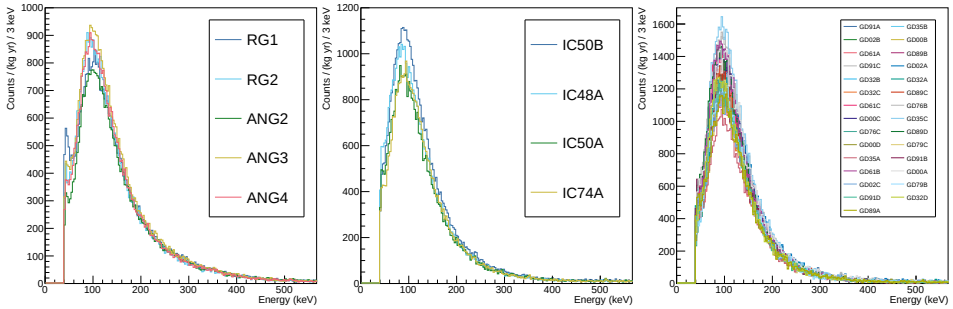

Figure 7.1: Low-energy, single-detector data spectrum for each Phase II$^+$ detector type (Coax, BEGe, ICPC) separately, normalized by detector exposure (see Tab.F.2).

7.1 DATA SET

Since `Run 87`, the online trigger threshold has been reduced from 150 keV to about 16 keV, in order to record events for low-energy analyses. This is ideal for studying the ^{39}Ar event distribution since it peaks at $\sim$ 100 keV. Data taken with the Phase II$^+$ setup from `Run 95` to `Run 114` (excluding `Run 102`, which is a special calibration run) are considered in this analysis. An offline energy threshold of 40 keV, well above any detector online threshold, is chosen to process the data, which must be split on a detector-by-detector basis to study the active volume model for each detector separately. The analysis data set is thus further divided into 38 sub-data-sets, one for each active detector[1] in Phase II$^+$. The multiplicity cut is applied to select single-detector events, which constitute the majority of ^{39}Ar events. LAr veto cut and Pulse Shape Discrimination (PSD) cut are not applied as they do not help in isolating the ^{39}Ar signal. Histograms of the selected data are shown in Fig.7.1, for each detector separately, normalized by exposure (reported in Tab. F.2). Differences in the shape and number of events in the distributions are mainly determined by the detectors' CCE profiles.

7.2 BACKGROUND AND SIGNAL EXPECTATIONS

7.2.1 *Physics of ^{39}Ar decays in* GERDA

^{39}Ar decays via pure first-forbidden unique β^- transition to the ground state of ^{39}K with a Q-value of 565(5) keV [94] . An overview of the ^{39}Ar production mechanism in atmosphere can be found in [95]. The specific activity of ^{39}Ar in the atmospheric LAr has been constrained to about 1 Bq/kg by several experiments [96–98]. The interaction of the ^{39}Ar decay products with an HPGe detector is sketched in Fig.7.2. β particles travel less than 1 mm in LAr and less than 0.2 mm in germanium. They can be directly detected when produced on the p$^+$ contact and insulating groove, where the dead layer is shallow enough. A low β event rate is expected

1 Data from `GD02D`, `ANG5` and `IC48B` in Phase II$^+$ is not usable

in point-contact detectors due to the small penetrable surface, while this contribution is expected to be higher in Coax detectors, which feature a large p^+ contact.

Beyond the direct β particle detection, the ^{39}Ar decay can induce HPGe signals through secondary particles. The charged β can emit *bremsstrahlung* radiation by interacting with the nuclear medium. This radiation travels much farther than the β (up to 10–15 cm) and can be originated by decays happening far from the detectors. It probes the full HPGe volume, and its detection is therefore conditioned by the detector charge-collection profile. Even if the *bremsstrahlung* cross-section is small, a large number of these events can be detected with an ^{39}Ar specific activity of 1 Bq/kg. The signature of such "soft" radiation in the energy spectra is a broad peak-like structure at about 100 keV (see Fig.7.1), which dominates over the β continuum.

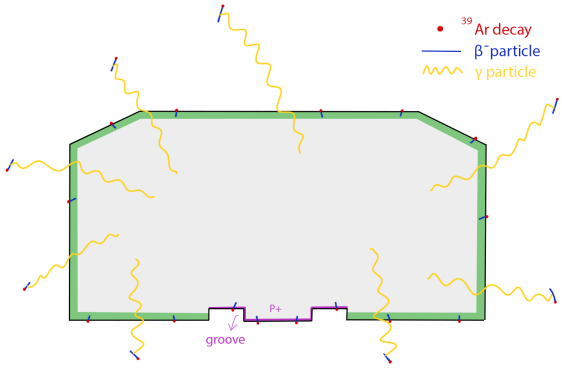

Figure 7.2: ^{39}Ar decays as detected by an HPGe detector. Emitted β particles probe germanium down to a depth of $\sim$ 200 µm (800 µm in LAr), and thus cannot travel the thick n^+ contact. They can reach the active volume through the p^+ contact and insulating groove, where the dead layer is thinner (less than 1 µm). On the other hand, *bremsstrahlung* radiation emitted by β particles in LAr probe the entire germanium volume. The energy distribution of β and γ interactions is shown in Fig.7.3.

7.2.2 *Monte Carlo simulation*

MAGE *is a* GEANT4*-based software tool to produce background and signal for the* GERDA *experiment*

Simulations of ^{39}Ar decays in the GERDA setup are carried on with the MAGE framework [99] , by using the implemented entire Phase II^+ experimental geometry. Primary decays are simulated inside a LAr cylindrical volume whose size is compatible with the expected physics described above. The cylinder is centered on the detector array, and has a height of 70 cm and a radius of 30 cm, considering that the HPGe array has a radius of about 15 cm (see Tab.F.1 for reference to the HPGe dimensions and relation between detector name and channel number). These dimensions have been chosen by looking at the sampling distribution of vertices of ^{39}Ar decays with associated energy deposition in germanium (see Sec.7.5.3 for details). The statistics generated in the MC is greater by a factor of 10 than the data. The output of the simulation is further processed with a specific software

suite to include run-time configuration (detector status, live time), energy resolution (*super*-calibration), and detector's active volume model. The last step is described in detail in the next section.

The distribution of energy depositions in a point-contact detector due to ^{39}Ar, assuming full charge-collection efficiency in the entire germanium volume, is shown in Fig.7.3, leftmost plot. The distribution has been further divided into the pure β and *bremsstrahlung* contributions, as described in the previous section. The β component is computed with standalone MaGe simulations, killing the Geant4 `eBrem` (*bremsstrahlung*) process. The *bremsstrahlung* part is obtained by using 100 μm dead layer on the p+ and groove, which kills all the β events. As anticipated, the most recorded events are due to *bremsstrahlung* radiation.

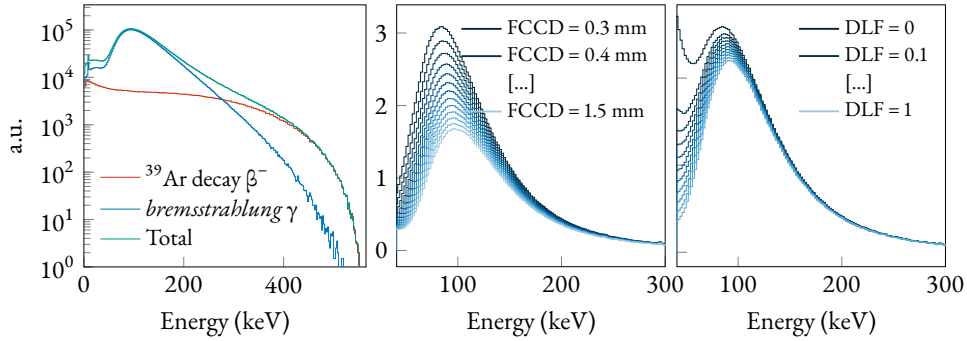

Figure 7.3: Left: simulated ^{39}Ar energy spectrum seen by all GERDA detectors decomposed into β and γ components. Center: impact of the FCCD, varied between 0.3 mm and 1.5 mm in steps of 0.1 mm, on the ^{39}Ar energy spectrum shape, fixing the DLF at 1 (i.e. hard step model) and keeping the ^{39}Ar activity in LAr fixed. Right: impact of the DLF, varied between 0 (i.e. no dead layer) and 1 (i.e. no transition layer, on the ^{39}Ar energy spectrum shape, fixing the FCCD at 0.9 mm and keeping the ^{39}Ar activity in LAr fixed.

7.2.3 *Active volume model folding*

As explained in Sec.5.1, the CCE curve strongly depends on the lithium concentration profile, which is in turn strongly dependent on the diode fabrication process and is different for each detector. Consequently, the FCCD and TL must be individually characterized for each detector. Because of its simplicity, the linear active volume model has been selected to process Monte Carlo simulations for this analysis. It is characterized by the two parameters FCCD and DLF. The latter is defined as

$$\mathrm{DLF} = \frac{\mathrm{DLT}}{\mathrm{FCCD}} \in [0,1] \,,$$

where DLT (dead layer thickness) is the starting point of the transition region (see Fig.5.1). Alternative models have been considered in the study of systematic uncertainties. The active volume model is applied to the Monte Carlo simulations by re-weighting energy depositions in a germanium detector according to the charge-collection efficiency value at the corresponding detector coordinate.

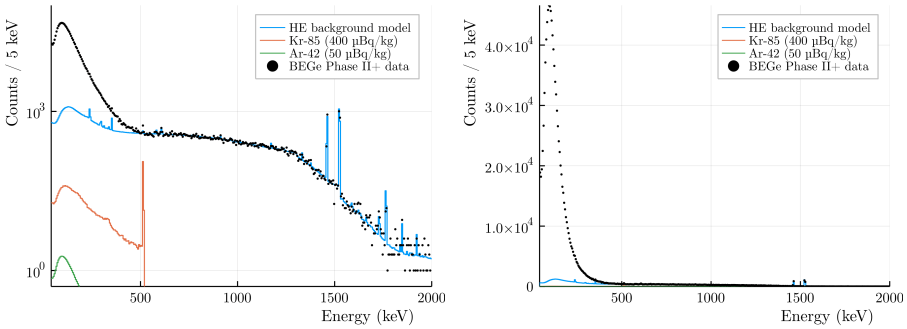

Figure 7.4: Extrapolation of the high-energy background model to the ^{39}Ar energy domain. Left: log-scale; right: linear scale.

The effect of the active volume model on the ^{39}Ar *pdf* (probability density function) is shown in Fig.7.3. In the central plot, the FCCD is varied between 0.3 mm to 1.5 mm in steps of 0.1 mm, keeping the DLF $= 1$ (hard step model). The parameter significantly impacts the total number of recorded events and distorts the distribution at the same time (note the position of the mode). In the rightmost plot, the DLF is varied between 0 and 1 in steps of 0.1 on a fixed FCCD value. In this case, the stronger variations in shape and number of detected events are seen in the low-energy part of the distribution.

7.2.4 *Low-energy background model: ^{39}Ar rate anomaly*

From the higher energy background model [100] of Phase II$^+$ physics data, it is possible to extrapolate the expected number of background events below the ^{39}Ar Q-value. The extrapolation to lower energies is shown in Fig.7.4. In addition, known background sources below the ^{39}Ar Q-value and above 40 keV are ^{212}Pb, ^{42}Ar and ^{85}Kr. The ^{212}Pb content can be constrained with the higher energy ^{232}Th contributions and is included in the high-energy background model *pdf*. ^{42}Ar decays β with a Q-value very close to the ^{39}Ar Q-value. An upper limit on its presence can be obtained from ^{42}K, its progeny, in the high-energy background model. The ^{42}Ar activity in LAr is less than 50 µBq/kg, four orders of magnitude less than ^{39}Ar [101]. ^{85}Kr, on the other hand, is visible in the physics data via the full-energy γ line at 514 keV. Combining information from the line event content and Monte Carlo simulations, a specific activity of $\sim$ 0.4 mBq/kg is obtained in the GERDA LAr, much lower than what was reported by other experiments. It is known, however, that the ^{85}Kr concentration in LAr is sample dependent since it is influenced by the details of the distillation process. The ^{42}Ar and ^{85}Kr contributions are shown in Fig.7.4. At the ^{39}Ar peak, where the signal-to-noise ratio is best, other events are expected to occur at $1 - 3\%$ of the total event rate, depending on the detector type. Detailed numbers are reported in Tab.7.2.

Table 7.2: Expected counts in the [45, 160] keV energy region for each data set: BEGe, Coax and ICPC. Percentages are relative to the physics data.

	BEGe	Coax	ICPC
DATA	778072 / 100%	326367 / 100%	326367 / 100%
TOTAL BKG	22484 / 2.9%	7562 / 2.3%	6733 / 1.2%
^{42}K	14874 / 1.9%	4821 / 1.4%	4197 / 1.2%
^{40}K	2732 / 0.4%	1052 / 0.3%	1042 / 0.3%
$2\nu\beta\beta$	1828 / 0.2%	855 / 0.3%	673 / 0.1%
^{214}Pb/^{214}Bi	1553 / 0.2%	415 / 0.1%	399 / 0.1%
^{212}Bi/^{208}Tl	884 / 0.1%	231 / $<$ 0.1%	228 / $<$ 0.1%
^{228}Ac	408 / $<$ 0.1%	130 /	122 /
^{85}Kr	729 / 0.1%	292 /	188 /
^{42}Ar	1 /	1 /	1 /

A simple comparison between the total number of counts expected with a ^{39}Ar activity of 1 Bq/kg and in data reveals a significant mismatch. Several cross-checks have been performed, but no obvious problems have been spotted (see Sec.7.5.1). The reason could be a potential mis-modeling of the *bremsstrahlung* contribution, which was not detected by previous experiments. A detailed fit model with β/γ split seems to reproduce well the β component, fixed to the ^{39}Ar activity of 1 Bq/kg.

7.3 STATISTICAL ANALYSIS

7.3.1 *Test statistic*

Among the various testing procedures available in the statistics literature, the test statistic chosen to analyze different active volume models on the available data is the likelihood-ratio-based test statistic t_s, defined as [102]:

$$t_s = -2 \log \lambda_p(\boldsymbol{\theta})$$

where $\lambda_p(\boldsymbol{\theta})$ (using the same notation as in [103]) is the *profile-likelihood ratio*

$$\lambda_p(\boldsymbol{\theta}) = \frac{\mathcal{L}(\boldsymbol{\theta}, \widehat{\widehat{\nu}}(\boldsymbol{\theta}))}{\mathcal{L}(\widehat{\boldsymbol{\theta}}, \widehat{\nu})}$$

where $\boldsymbol{\theta}$ is the vector of parameters of interest (the FCCD and the DLF defined in Sec.7.2.3) and ν is a vector of nuisance parameters (e.g. those that regulate systematic uncertainties). The likelihood $\mathcal{L}$ that measures the chance of obtaining the observed data given a certain model specified by determined values of $\boldsymbol{\theta}$ is defined so that the t_s is based on $\Delta\chi^2_{Pearson}$. The

likelihood at the numerator is maximized, for a specified value of $\boldsymbol{\theta}$, only on the $\boldsymbol{\nu}$. The denominator is the maximum likelihood function and $\widehat{\boldsymbol{\theta}}$ and $\widehat{\boldsymbol{\nu}}$ are their maximum likelihood estimators.

The data collected by each detector are compared with different models scanning the t_s; the minimum t_s determines the best-fit. The models are given by MC *pdf*s (Sec.7.2.2) expected in a 2D discrete grid defined by varying the FCCD in a range of $[650, 2850]$ μm with a step of 25 μm and the DLF in a range of $[0.15, 0.85]$ with a step of 0.01. To optimize the generation of only the required *pdf*s, a coarser grid with smaller FCCD and DLF ranges was first built and then gradually enlarged checking the obtained best-fit and the likelihood profiles. In the end, all the best-fit results arise far from the grid borders and the grid is fine enough to well define the likelihood profile projected on the two parameters.

7.3.2 *Analysis range and binning*

The frequentist analysis focuses on the energy window around the ^{39}Ar peak, where the signal to background ratio is maximum between 45 keV and 160 keV. The lower threshold of the fit range is chosen just above the offline energy threshold. Tests on the data have been performed to verify the stability of the fit with respect to the upper edge value. It has varied from 150 keV to 180 keV with a step of 2 keV. The scanning result is shown in Fig.7.5(top) in terms of the FCCD and DLF best-fit values. This variation does not affect the analysis results within the statistical uncertainties of the best-fit of FCCD and DLF computed in Sec.7.6.2.

A 5 keV binning is enough to avoid uncertainties due to the energy scale, and it does not remove features of the energy spectrum. Additional tests have checked the stability of the fit with respect to the binning on the data. Fig.7.5(bottom) shows the distribution of the best-fit values of FCCD and DLF varying the binning from 1 keV to 10 keV with a step of 0.5 keV. This parameter gives an idea about the fit performance, which seems not to be affected by a reasonable changing of the binning within the statistical uncertainties.

The binning choice and the collected high statistics allow to have Gaussian uncertainties in each bin, which permit the equality $t_s = \Delta\chi^2$.

7.3.3 *Performance: toy experiments*

Model testing relies on the knowledge of the t_s distribution. According to Wilk's theorem, under certain regularity conditions the t_s distribution asymptotically follows a $\Delta\chi^2$ distribution with a number of degrees of freedom (*dof*) defined by the number of parameters of interest. In this analysis, the statistics collected during Phase II$^+$ is sufficient for each detector, and different values of parameters of interest, defining distinct models, are tested inside their parameters space which is shared among all the models. Although all these conditions (asymptotic, interior, identifiable,

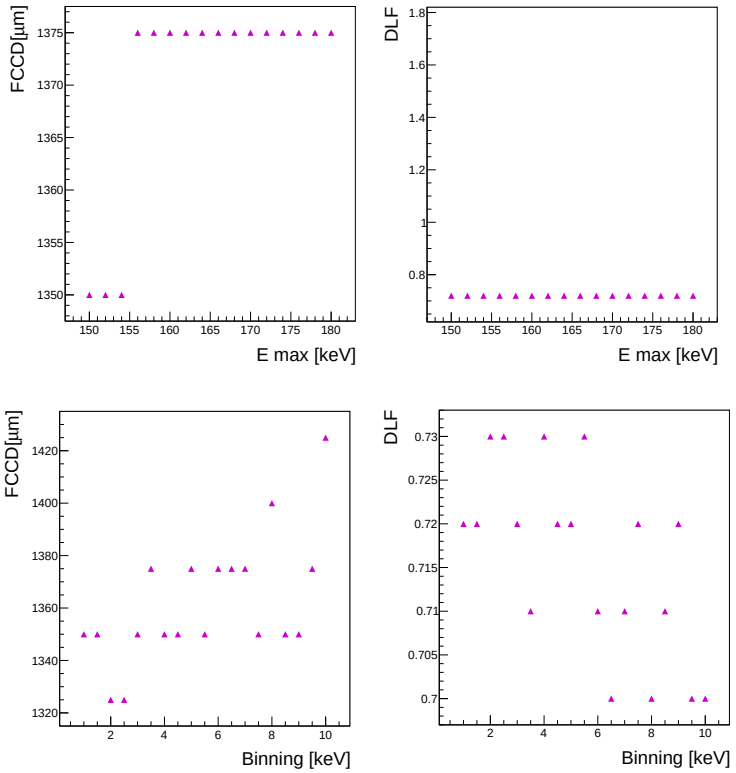

Figure 7.5: Best-fit distribution of the FCCD (left column) and DLF (right column) parameters as a function of the analysis energy range (top row) and the binning (bottom row). The fit performance is stable, especially for the DLF parameter as a function of the energy maximum as expected, and the upper edge of 160 keV and the binning of 5 keV are chosen.

nested conditions from [104]) are guaranteed, uncertainties of the nuisance parameters do not ensure the correctness of the models, and potential deviations from the theoretical $\Delta\chi^2$ distribution of the t_s are expected.

Toys Monte Carlo are generated from the *pdf*s, overcoming the inability to use Wilk's theorem, to verify the validity of the analysis by checking not only the shape of the t_s distribution but also the best-fit parameter distributions. Therefore, thanks to the ability to distort toys according to systematics, the confidence intervals are determined by computing the t_s critical threshold, as described in the next section. Toy experiments are firstly generated for each detector by including only the ^{39}Ar component, whose number of counts equals the number of data counts in the analysis range. The ^{39}Ar is differentiated in beta and gamma components by computing their ratio from the MC *pdf*s at the best-fit. These MC data are then processed by the analysis tools in place of the data, and compared with the MC grid. Each best-fit is collected and the distribution, in terms of the t_s, obtained with 10^4 toys MC is shown in Fig.7.6 in normal (left) and log (right) scale. A good agreement with the χ^2 distribution with two degrees of freedom (in red) is observed [102]. The blue dashed line indicates the critical threshold set at 68%.

Toy experiments can be validated by checking the distribution of the FCCD and DLF corresponding to the best-fit. Their comparison with the injected value can give an indication of potential biases in the analysis. Fig.7.7 shows an example of the parameter distributions and their correlation for a BEGe and, for completeness, it also displays the distribution of the activity of the γ component of ^{39}Ar and the goodness-of-fit defined by the p-value. The parameter distributions have a Gaussian shape centered at the injected values, which are FCCD $= 1375$ μm and DLF $= 0.72$ in the example of the figure. The activity of the γ component of the ^{39}Ar is a free parameter, and it results in being larger than the one fixed for the β component at 1 Bq/kg, as already mentioned in Sec.7.2.4. An expected significant correlation between FCCD and activity is observed. By definition, the p-value is expected to have a uniform distribution, with the mean at 0.5, under the null hypothesis (the best-fit).

Furthermore, background sources from the low energy background model can be set as additional components above the ^{39}Ar. The other systematic effects listed in the following section can be treated as global distortions applied to every component or as specific distortions applied only to the ^{39}Ar *pdf*. These distortions are randomly chosen when generating the toys. The effects of the systematics can be observed, for instance, in the width of the distribution variance, the bias of the distribution mean with respect to the injected value, and the p-value distribution.

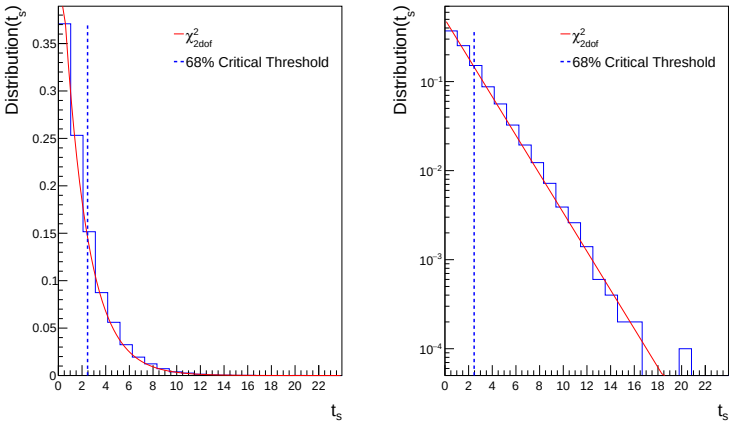

Figure 7.6: Test statistic distribution computed from 10^4 toy Monte Carlo in linear (left) and logarithm (right) scale. The χ^2_{2dof} distribution is shown by the red line. The blue dashed line indicates the critical threshold set at 68%.

7.3.4 *Confidence intervals*

The uncertainties of the best values of the FCCD and DLF parameters are estimated by extracting the 68% confidence interval (C.I.) for each detector. For instance, to find the uncertainty of the FCCD, its likelihood profile on data is computed by fixing the DLF at its best-fit. Sets of 10^4 toys with

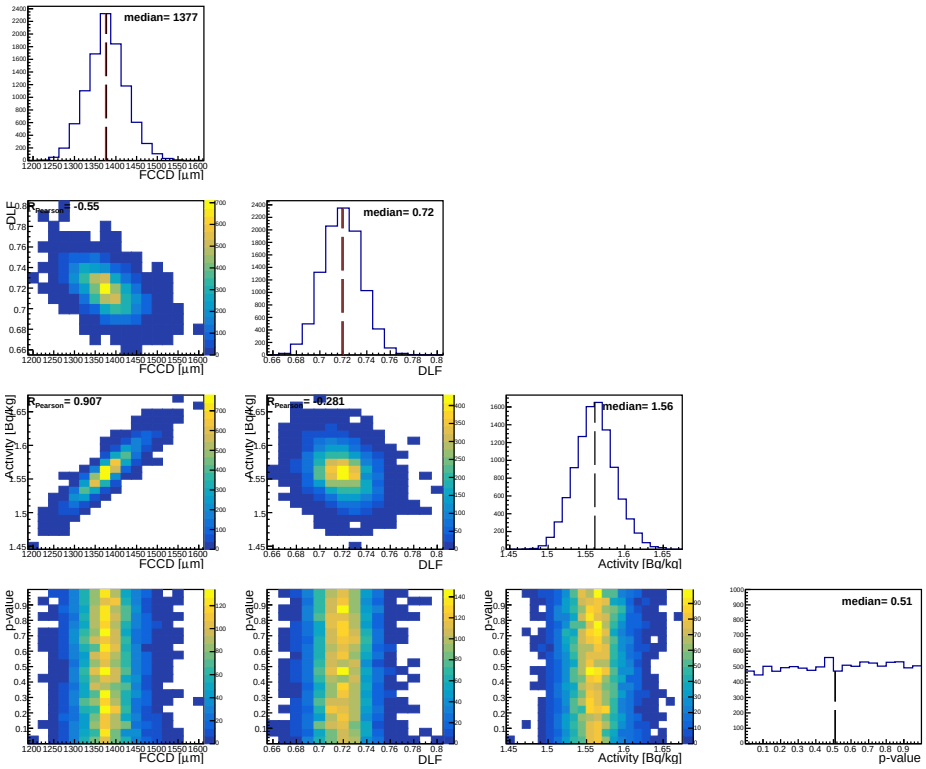

Figure 7.7: Distribution (on the diagonal) and correlations among FCCD, DLF, ^{39}Ar activity, and p-value.

the DLF at its best-fit are generated with different FCCDs. The toys of each set are scanned on the grid to take the minimum of the t_s. From the collected distribution of each set, the 68% quantile is computed, and a complete function of the critical threshold is generated with respect to the FCCD values. Finally, the C.I. region is obtained by intersecting the toy function with the data likelihood profile. The same procedure is repeated for the DLF parameter. Toys with only ^{39}Ar counts are processed to obtain the statistical uncertainties. Toys with additional background counts and distortions provide the total (statistic+systematic) uncertainties.

7.4 SYSTEMATIC UNCERTAINTIES

Below, the systematics uncertainties considered in this analysis – Q-value of ^{39}Ar decay, background model, TL model, energy calibration, and *bremsstrahlung* model in GEANT4 – are illustrated in detail.

7.4.1 ^{39}*Ar-decay theoretical model*

The Q-value of the ^{39}Ar decay is measured as 565 ± 5 keV. Simulated ^{39}Ar energy spectra with different Q-values are shown in Fig.7.8. The effects of the Q-value uncertainties have been firstly treated as a specific distortion on

the ^{39}Ar component in the toy generation, setting the value at its extreme edges (at 560 keV and 570 keV). However, preliminary tests have proven that these effects are negligible and do not contribute to the systematic uncertainty.

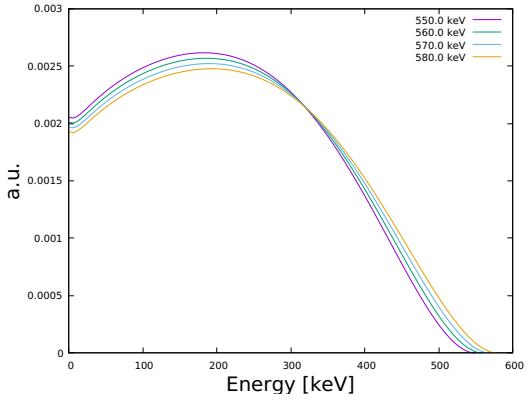

Figure 7.8: Simulated ^{39}Ar energy spectra with different Q-value of the β-decay process.

7.4.2 *Background model*

The sources of background listed in Tab.7.2 are treated as additional components in the toy production. The reference fit model accounts only for the dominant background source locations in the setup. ^{214}Pb and ^{214}Bi are assumed to be located on cables in the fit model. While ^{40}K is found on the mini-shroud, ^{42}K is set in the far location in the LAr volume outside the mini-shroud. Finally, $2\nu\beta\beta$ is located in the germanium detectors. A preliminary test has verified that different choices of the background source location are negligible. The *pdf*s have all the same shape due to *bremsstrahlung* as shown in Fig.7.9 with all the background *pdf*s extracted from the high-energy model. Only the shape of $2\nu\beta\beta$ distribution is clearly different.

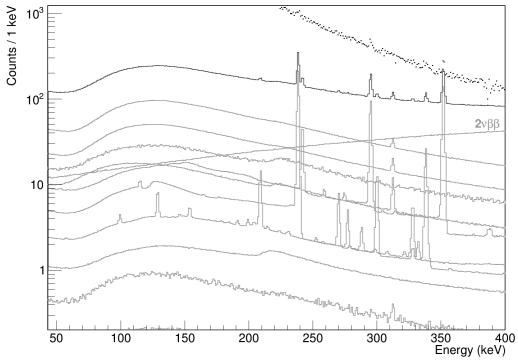

Figure 7.9: High-energy background decomposition below the ^{39}Ar peak. Except for $2\nu\beta\beta$, all *pdf*s have a similar shape due to *bremsstrahlung*.

7.4.3 *Transition layer model*

In this analysis, the transition layer has been modeled with a linear function. However, the real shape of the CCE from the surface of the detector to the active volume is unknown. Systematic effects can be estimated by changing the analytic model of the transition layer. Alternative models, expressed in terms of the two parameters FCCD and DLF, are

- the error function with $M = 3$ (see Fig.7.10(left))

$$0.5 + 0.5 \cdot \mathrm{erf}\left(\frac{x - (1 + DLF)/(2 \cdot FCCD)}{(1 - DLF) \cdot FCCD \cdot \sqrt{2}/M}\right)$$

- the hyperbolic cosine

$$\frac{\left(\frac{\cosh(x/FCCD - 1)}{\cosh 1 - 1}\right)^{0.55}}{(1 - DLF)^{1.3}}$$

Fig.7.10(right) shows the comparison of the linear function, the error function, and the hyperbolic cosine function for different DLF values. The transition layer model is treated as a global distortion of the toy generation.

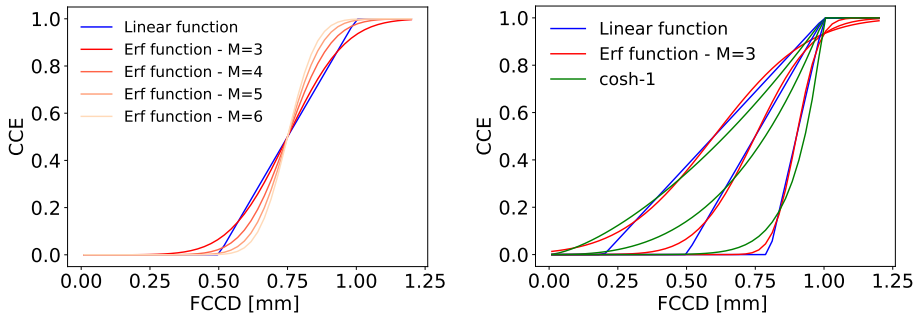

Figure 7.10: Left: examples of error function setting different values of the parameter M. The value $M = 3$ is chosen due to its better similarity with the linear function. Right: linear function, error function, and hyperbolic cosine function compared with different DLF values.

7.4.4 *Energy scale*

The energy calibration parameters applied to the spectrum collected during Phase II$^+$ is known precisely. However, the calibration starts from 238 keV and extrapolation at lower energy is required for this analysis. Fig.7.11 evaluates the extrapolation obtained for each detector by studying the discrepancy of some peaks from their nominal values. An overall shift of ± 1 keV is registered on the energy axis while only few channels have a larger shift. The energy scale is applied as a global distortion in the toy production.

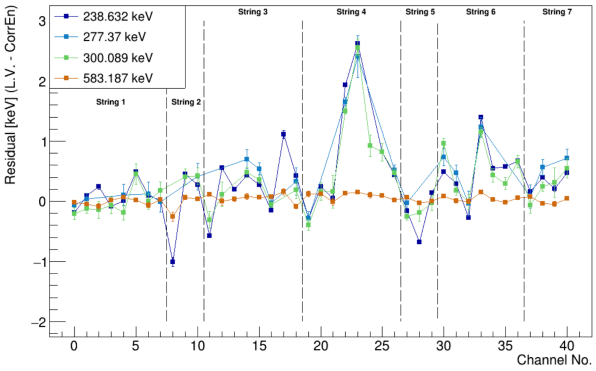

Figure 7.11: Distortion of some peaks from their nominal values for all detectors after extrapolating the calibration at lower energies. A shift of ± 1 keV is taken into account as a systematic. Only few detectors present a larger shift.

7.4.5 GEANT4 *implementation*

A likely source of systematic in the analysis is the implementation of the physics processes into GEANT4. GEANT4 is a broadly-used and heavily-tested software suite in the high-energy physics community and no systematic effects due to the implementation of particle generation and propagation routines are expected. However, potential bias might be originated from the *bremsstrahlung* model, which may be related to the origin of the ^{39}Ar rate anomaly of the γ component. The full simulation chain has been re-run with different electromagnetic low-energy process models available in GEANT4 (Livermore is the default). Fig.7.12 shows ^{39}Ar energy spectra obtained with different Physics Lists. As already tested in previous works [105], the *pdf*s are observed to change at the sub-percent level, and the associated contribution to the systematic uncertainty is negligible [106]; thus, it can not explain the rate anomaly.

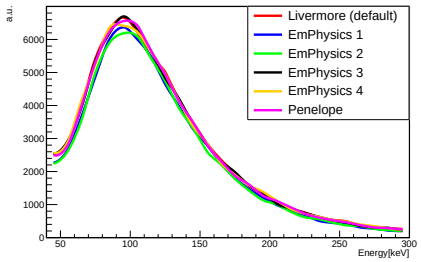

Figure 7.12: Simulated ^{39}Ar energy spectra obtained by setting different Physics Lists on GEANT4. The *bremsstrahlung* yields are not so different among each other and the related systematic uncertainty is negligible.

7.5 VALIDATION AND CROSS-CHECKS

7.5.1 ^{39}Ar rate anomaly

Previous analysis performed by other experiments claimed a ^{39}Ar activity of 1 Bq/kg. Although the β component in this activity can well reproduce the data collected by GERDA, a mismatch of the γ component is observed, as explained in Sec.7.2.4. Below, some tests to verify the origin of this anomaly are reported. Unfortunately, they are not enough to solve the inconsistency.

Correlation test

Fig.7.7 shows a strong correlation between FCCD and ^{39}Ar activity, as already expected looking at the effect of the FCCD on the shape of ^{39}Ar *pdf*s in Fig.7.3(center). To check if the anomaly of the ^{39}Ar activity can be compensated by this correlation, the variation of the FCCD value is observed fixing the parameter of the ^{39}Ar activity to 1 Bq/kg in the analysis. The toys MC are generated with the same statistics found in the data, corresponding to the ^{39}Ar activity of 1.6 Bq/kg. Fig.7.13 shows a bad fit in FCCD (and DLF) out of the expected range; this correlation is not enough to explain the anomaly.

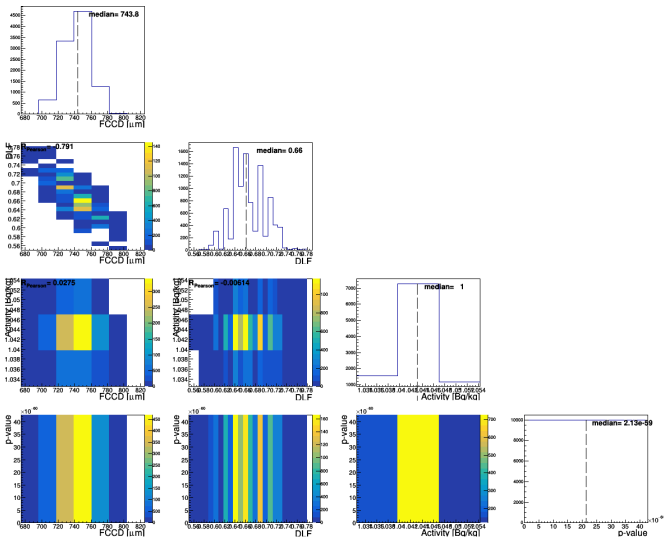

Figure 7.13: Parameter distributions and correlations with the ^{39}Ar activity fixed to the nominal value of 1 Bq/kg. The best-fit FCCD and DLF are out of range. The correlation between ^{39}Ar activity and FCCD can not explain the rate anomaly.

A/E check

It is interesting to observe the A/E distribution of the events in the energy range of the analysis. Fig.7.14 shows two different low-energetic populations (banana and drop shapes) of data collected by `channel 1` (`GD35B`

detector) in `Run 95-114`. The projections in the energy and current amplitude are displayed in Fig.7.15 with the two shapes separated by the hyperbolic ($\propto 1/E$) line shown in Fig.7.14. In the A spectrum, the banana events are distributed in a narrow peak. This spectrum deformation is due to the electronic noise which is not treated properly at low energies and is not covered in the MCs of the analysis. Fig.7.16 shows the comparison of waveforms of banana and drop events at the same energy, highlighting a smoother rising edge for the banana waveforms. An improvement on the algorithm used for the current reconstruction is required for better discrimination of the noise in order to be able to perform signal analyses at low energy. This could be achievable in the next future with the LEGEND experiment.

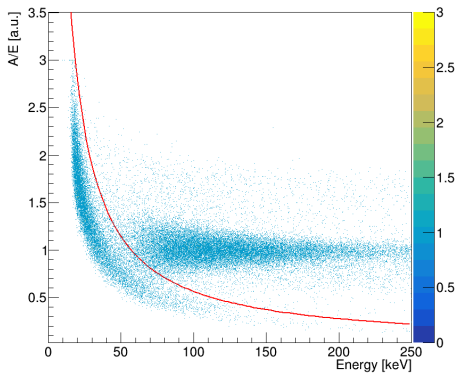

Figure 7.14: Distribution of the A/E as a function of the lower energy of the data collected, for instance, by `channel 1` in `Run 95-114`. It features two different event shapes (banana, drop). The banana shape at lower energy is a distortion due to electronic noise.

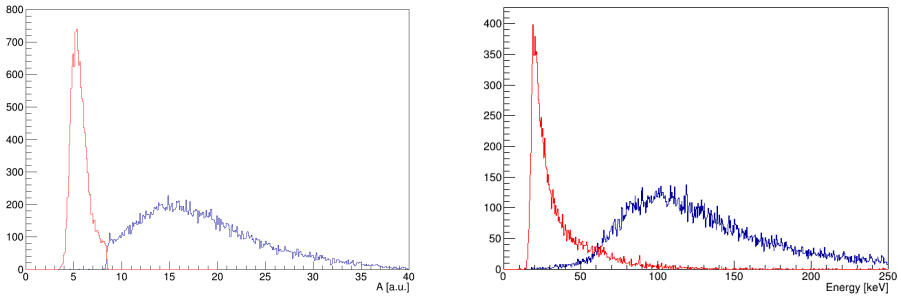

Figure 7.15: Distributions of the current amplitude (left) and the energy (right) with the banana (red) and drop (blue) events separated.

Trigger efficiency

GERDA measurements on the trigger efficiency are not detailed below $\sim$ 60 keV (Fig.7.17). In order to avoid any potential inefficiency, the energy threshold of the analysis has been moved from 45 keV to 60 keV. Therefore, this procedure cuts most of the banana events shown previously. This test

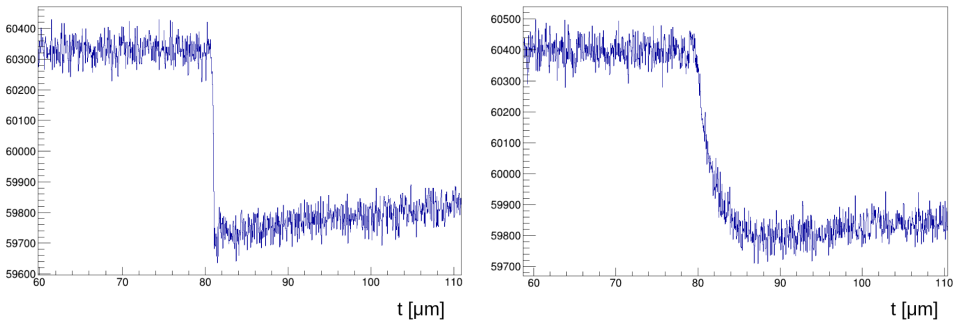

Figure 7.16: Examples of typical waveforms of an event in the banana shape (left) and an event in the drop shape (right), both at the energy equal to 70 keV.

does not improve the analysis showing a more deformed likelihood profile (see Fig.7.18 (left)).

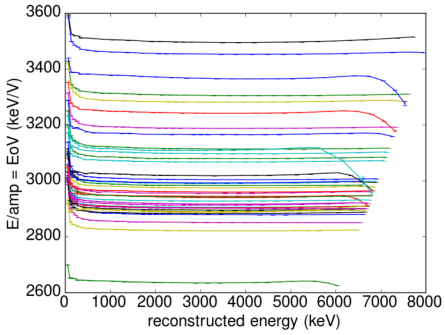

Figure 7.17: Test on the linearity of the reconstructed energy using test pulses for each channel. From [107].

In addition, a counting analysis has been performed. A single large bin is set for the entire energy range and the DLF is fixed to a reasonable value. The likelihood profile shown in Fig.7.18(right) has a rectangular shape because the value of the DLF is fixed and the best-fit is not reproduced well within the analysis range (see the little white bin at 650 μm in the likelihood projection). Even trying different DLF values gives bad results. It implies that even if the trigger efficiency could affect the shape, it would not solve the ^{39}Ar rate anomaly.

Other background sources

An additional test can be performed to check some of the background sources listed in Tab.7.2 that are not considered in the analysis due to their small amount of counts. There may be the possibility that they are so sensitive to the FCCD and/or DLF parameters to deform their shape and explain the activity anomaly extremely. Fig.7.19 shows the comparison of the *pdf*s of ^{39}Ar with ^{42}Ar (top) and ^{228}Ac (bottom) for different FCCD and DLF values. The two background sources have the same statistics of data. The large difference between the amplitude of the *pdf*s implies that the

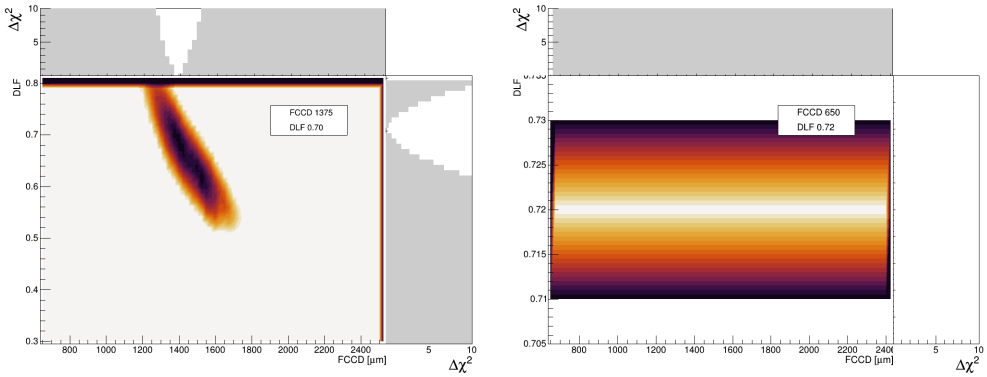

Figure 7.18: Test on the trigger efficiency. Left: shift of the left edge of the analysis range to 60 keV to cut lower energy events that may be affected by potential trigger inefficiency and that are mainly distributed in the banana-shape (see Fig.7.15(right)). The likelihood profile is more deformed than the nominal one in Fig.7.22. Right: counting analysis on `channel 1`. A single bin is set for the analysis on the data. The obtained best-fit of FCCD is out of the range, suggesting that the shape of the *pdf*s does not explain the ^{39}Ar rate anomaly.

FCCD/DLF effect on the two background sources is insufficient to solve the rate problem.

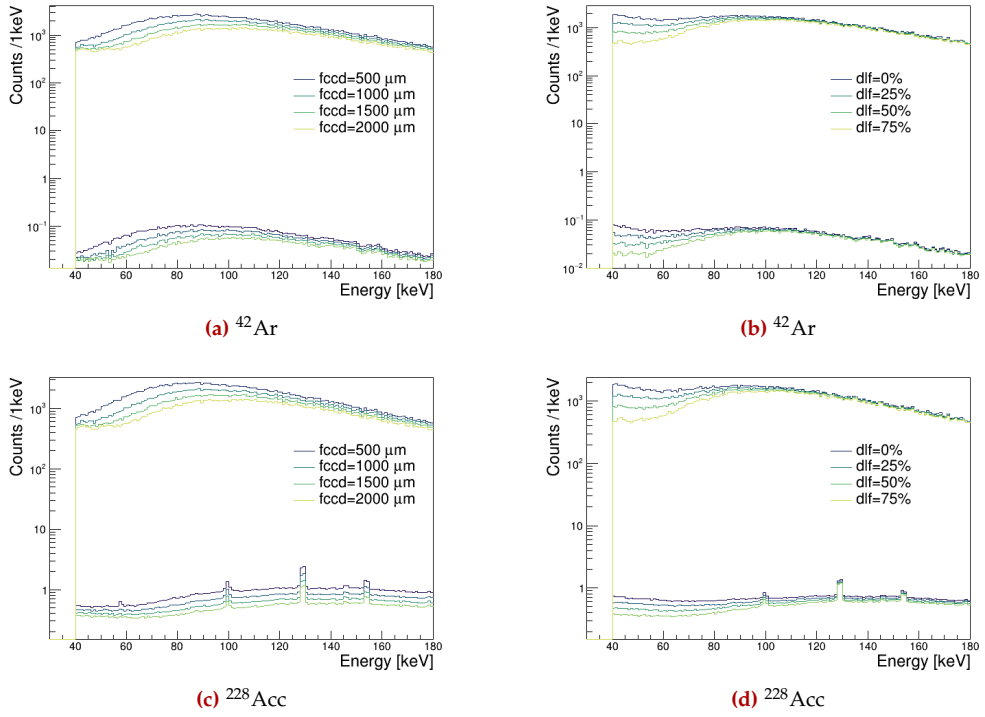

(a) ^{42}Ar **(b)** ^{42}Ar

(c) ^{228}Acc **(d)** ^{228}Acc

Figure 7.19: *pdf*s of ^{39}Ar compared with ^{42}Ar (top) and ^{228}Ac (bottom). The plots on the right(left) show the comparison setting different FCCD (DLF) and fixing the DLF (FCCD) at reasonable values. The amplitudes of these two background sources are still too low to explain the ^{39}Ar rate anomaly, even with the application of the FCCD/DLF effects.

7.5.2 *Event statistic in the simulation*

As explained in Sec.7.2.2, the statistics of the generated MCs is greater by a factor of 10 than the data. In order to check if this statistics is enough, a new *pdf* is generated using a different seed. The best-fit point of `channel 1` (FCCD= 1377 μm and DLF= 0.72) is chosen to perform this test. Toys are then generated from this *pdf* and are fitted with the same models used so far. There is no variation on the best fit as shown in Fig.7.20, with and without the systematics.

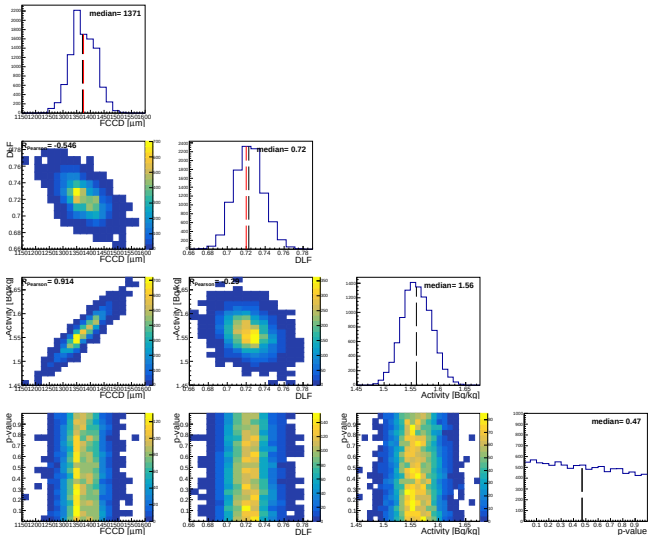

Figure 7.20: Parameter distribution and correlation of using toys generated from the *pdf* at the best-fit point of `channel 1` using a different seed. There is no variation in the best-fit values, it implies that the statistics used in MC is enough.

7.5.3 *Argon simulation volume*

To choose an optimal LAr simulation volume, the sampling distribution of ^{39}Ar decay vertex with an associated energy deposition in germanium is produced. The distributions are obtained from a MaGe simulation of ^{39}Ar decays homogeneously distributed in a large LAr volume. Looking at the cumulative distributions in Fig.7.21, the chosen cylinder centered around the array of height 70 cm and radius 30 cm is clearly large enough to enclose the vast majority of decays that produce an HPGe signal.

The charge-collection efficiency is assumed to be 1 in the entire detector volume.

7.6 RESULTS

7.6.1 *Best-fit values*

The best-fit of the FCCD and DLF parameters are estimated via likelihood profile for each detector, as explained in Sec.7.3.1. A typical likelihood

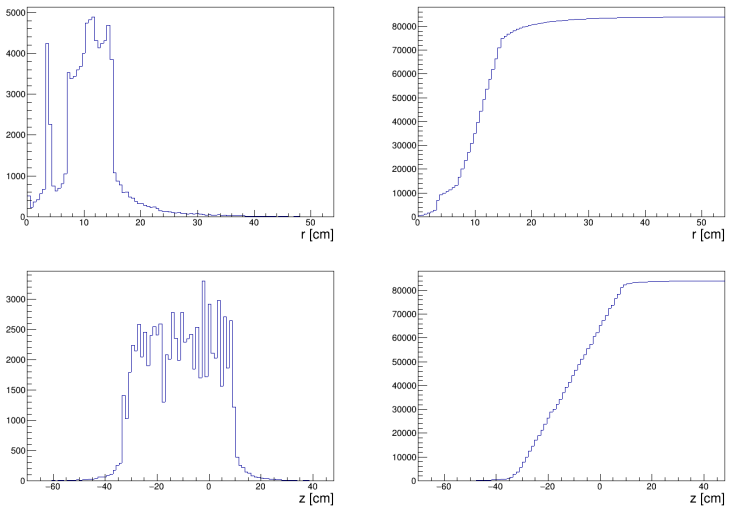

Figure 7.21: Left column: sampling distribution of ^{39}Ar decay vertex with associated energy deposition in any detector in the array. Right column: cumulative distribution. Top row: distribution projected in the radial coordinate r. Bottom row: distribution projected in the vertical coordinate z. The array center is located approximately at $(r = 0, z = -11.5\ \text{cm})$. Structures in the bulk of the distribution are generated by the presence of the germanium array.

profile of data on the 2D grid with different FCCD and DLF values is illustrated in Fig.7.22, with the projections on the two axes.

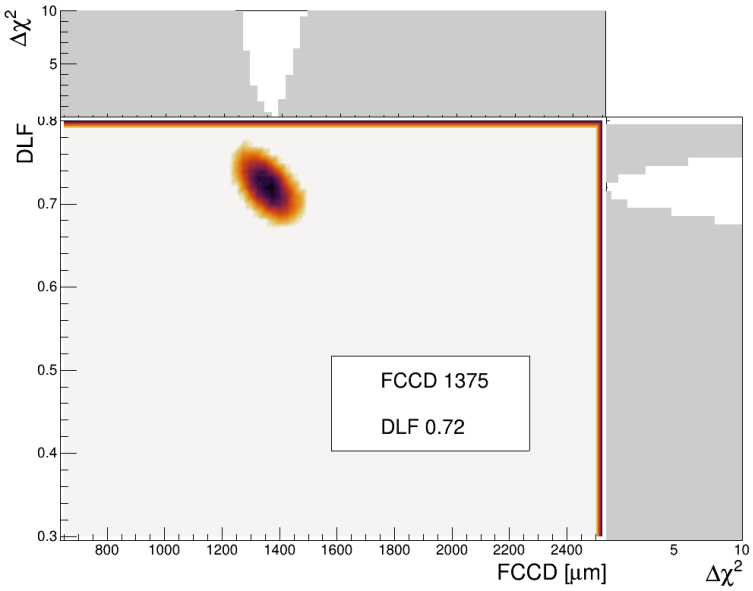

Figure 7.22: Likelihood profile of `channel 1`. In the main box, the best FCCD and DLF related to the minimum t_s ($\Delta\chi^2$) are indicated. The projections of the likelihood profile on the FCCD and DLF are illustrated on the axes.

Fig.7.23 shows the comparison between data and simulated *pdf* at the best-fit FCCD and DLF for `channel 1`. The black points mark the data while the continuous blue line indicates the total *pdf* with all contributions added. The amplitude of the β component of ^{39}Ar is set to 1 Bq/kg of activity. The

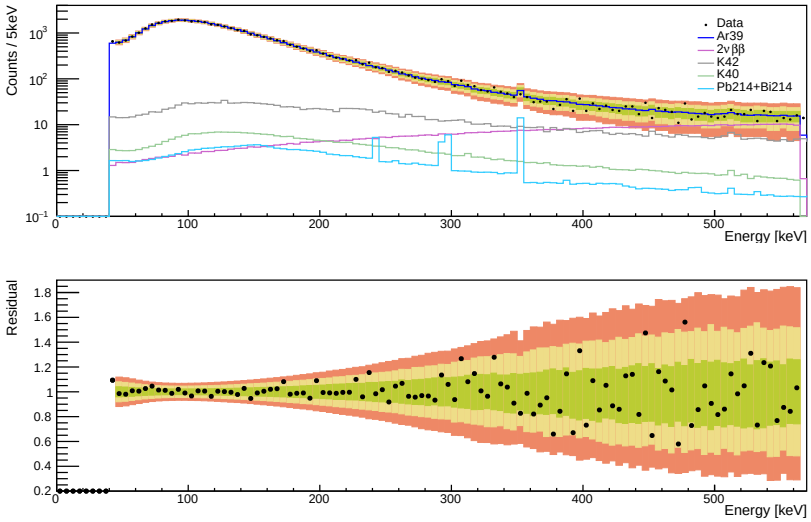

Figure 7.23: Comparison of data (black points) and best-fit model (blue line) on the low-energy spectrum. The best-fit model consists of the γ and β *pdf*s of ^{39}Ar and the four background *pdf*s (colored lines) taken at the best values of FCCD and DLF found for the detector. In the bottom panel, the ratio between data and model in units of Poisson standard deviations is shown together within 1σ, 2σ, 3σ.

four selected background sources ($2\nu\beta\beta$, ^{40}K, ^{42}K, ^{214}Pb+^{214}Bi) are added with the expected number of counts. The amplitude of $2\nu\beta\beta$ stemmed from the known half-life of the process which is $T_{1/2}^{2\nu\beta\beta} = 2.022 \cdot 10^{21}$ yr (see Sec.8.2). The amplitude of the γ component of ^{39}Ar is computed by the amplitude difference between data and all simulated components at their proper rate. The numbers of counts of each component in the analysis range are required for the generation of the toys MC to compute the confidence intervals (see next section). The residuals and the Poisson bands for 1σ, 2σ and 3σ fluctuations are also shown. The residuals are in good agreement with the expected Poisson fluctuations, and it also implies a positive double-check on the number of events seen from the value of $T_{1/2}^{2\nu\beta\beta}$.

An additional test is to reproduce the previous comparison with the *pdf*s adjusted to the overall range (till 565 keV) instead focused only on the analysis range. The plot is shown in Fig.7.24 and, even with the bigger range, the simulated *pdf*s look in agreement with the observed one.

7.6.2 *Confidence intervals*

The profile likelihood for the FCCD and the DLF found previously is compared with the critical thresholds of the test statistic corresponding to the 68% probability, with and without including the systematics. The intersection of the lines indicating the critical threshold with the profile likelihood of data gives the confidence intervals, as explained in Sec.7.3.4. For instance, Fig.7.25 illustrates the estimation of the confidence intervals of FCCD and DLF for `channel 1`. App.G reports the confidence intervals for

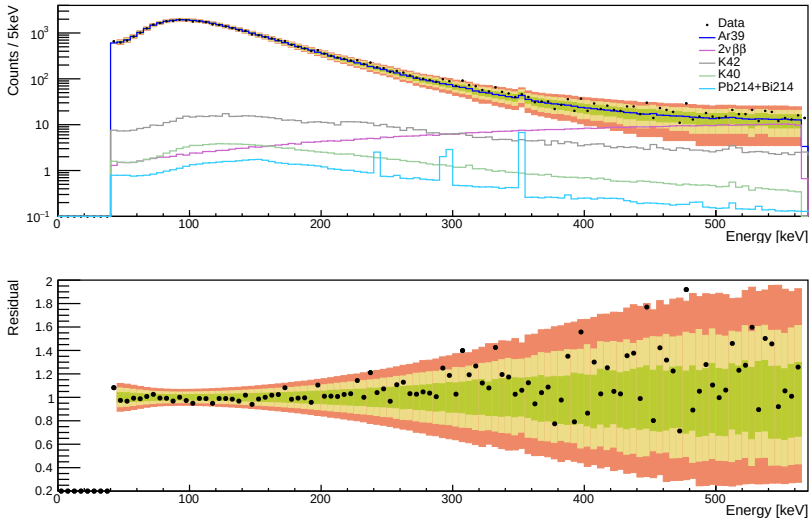

Figure 7.24: Comparison of data (black points) and best-fit model (blue line), as in Fig.7.23, on the overall energy range till 565 keV.

all detectors. The critical threshold of the test statistic without the inclusion of systematics (blue line) is in good agreement with the expected value of 2.3, indicating the critical threshold of the χ^2 distribution with 2 *dof* at 68% probability. On average among the detectors, the resulting statistical uncertainty is $\sim$ 5% and the total uncertainty is $\sim$ 12%.

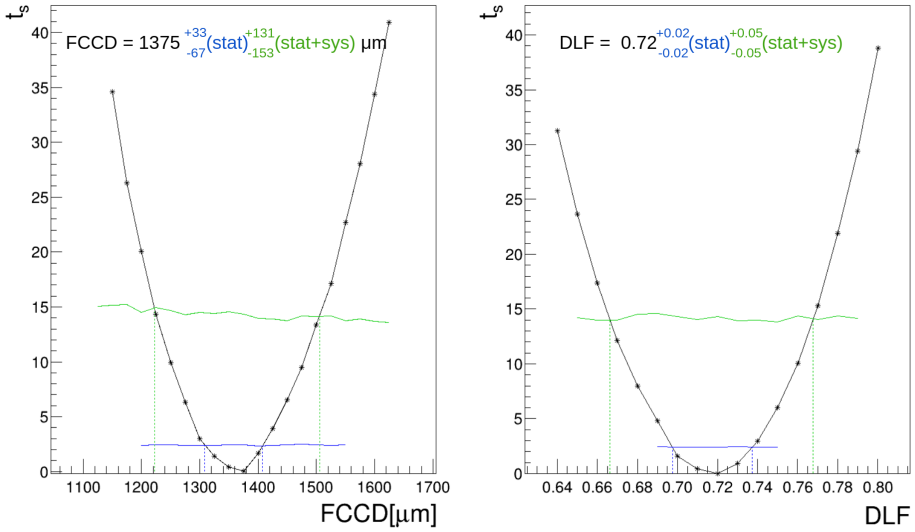

Figure 7.25: Likelihood profile for the FCCD (left) and DLF (right) parameters obtained from the fit on the data (black points). The blue and green lines show the critical threshold for the test statistic corresponding to the 68% probability, respectively with and without the systematics included.

To better understand the overall shift of the critical threshold produced by the additional effects of the systematics (green line), Fig.7.26 shows the parameter distributions and correlations obtained by using toys deformed with all the systematics components. The median of the distribution with-

out systematics is in good agreement with the injected parameter values, as already discussed in Sec.7.3.3. The introduction of the systematics in the MC data set has the effect of both creating biases in the fit and enlarging the distributions. Below, Fig.7.27 and Fig.7.28 respectively illustrate the

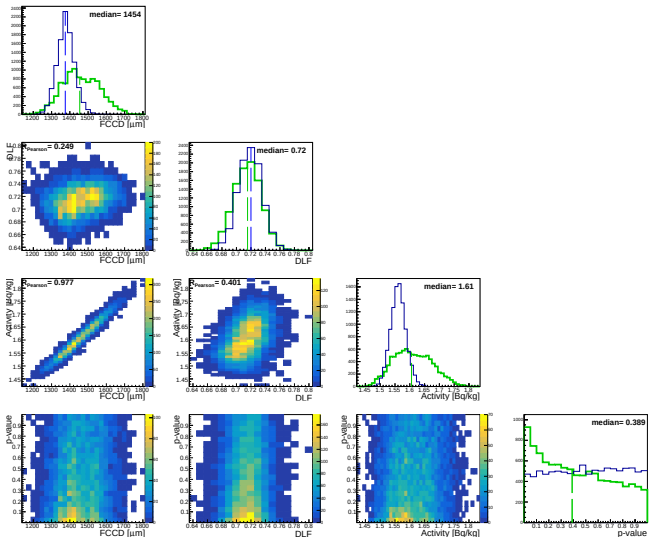

Figure 7.26: Parameter distributions and correlations obtained with toys distorted by all systematics. The overall effects are visible on the shift of the mean values and the increase of the width of distributions.

comparisons of the FCCD and DLF distributions, with and without the indicated systematic components, the injected median and the extracted medians. The FCCD distributions are more deformed by the three systematics than the DLF distributions. The overall distributions and correlations of the FCCD, DLF, ^{39}Ar activity, and p-value for each systematics component are illustrated in App.G.

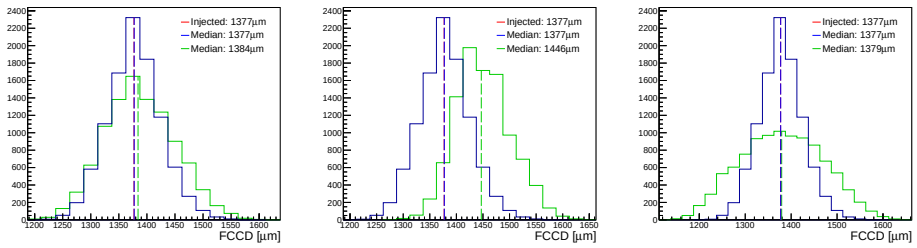

(a) TL model **(b)** Background model **(c)** Energy scale

Figure 7.27: Distribution the FCCD parameter in 10^4 toys MC. The blue distributions are obtained with only statistical fluctuation of the MC, while the green ones include systematic uncertainties. The median of each distribution and the injected FCCD are also indicated.

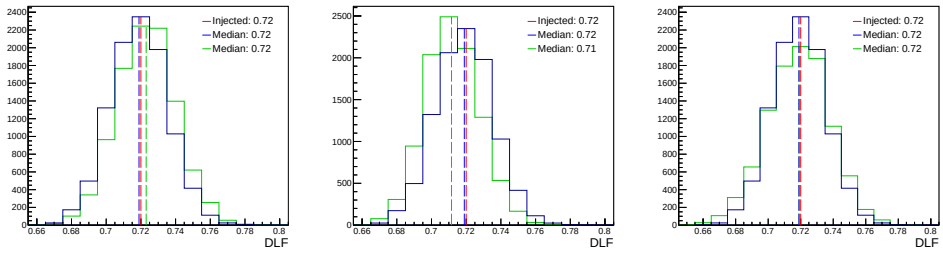

(a) TL model **(b)** Background model **(c)** Energy scale

Figure 7.28: Distribution the DLF parameter in 10^4 toys MC. The blue distributions are obtained with only statistical fluctuation on the MC, while the green ones include systematic uncertainties. The median of each distribution and the injected DLF are also indicated.

7.6.3 *Conclusion*

The final results of the estimated FCCD and DLF parameters are listed in Tab.7.3 with their statistical and systematic uncertainties; the latter is computed by the quadratic difference of total uncertainties found by the green lines and the statistical uncertainties found by the blue lines (see Fig.7.25). The extracted AV and f_{AV} are also listed together with their propagated uncertainties. In Fig.7.29, the FCCD and DLF results (in red) are compared with the official results (in black), including their total uncertainties. The results of the ICPCs look in good agreement for both parameters. The uncertainties of the points of the first measurement of Coax detectors are too large to compare them properly; however, the mean values are mainly in agreement. The results of BEGes obtained via the ^{39}Ar analysis are higher than the official GERDA results, which consider the FCCD growth at RT with the average speed of 0.1 mm/yr. A better comparison with the *in-situ* ^{39}Ar measurements would be with the results obtained from the interpolation of the first and the second measurements of BEGe detectors in HADES. Unfortunately, this kind of comparison is possible with only the FCCD parameters of nine BEGe (see the previous chapter). Fig.7.30 compares the FCCD from the ^{39}Ar analysis with the values obtained from the first and second detector characterization in HADES, and the estimated values at the time of GERDA Phase II from the two characterizations (Sec.6.4). Although the ^{39}Ar values are larger than the other FCCDs, the points appear to follow the same overall trend among the detectors, except for GD02C. It is clearly visible especially for the FCCD referring at the time of data taking (from the ^{39}Ar analysis in blue line and the estimation from HADES measurements in red line).

In conclusion, this innovative analysis uses for the first time a technique to estimate the AV of HPGe detectors *in-situ* by studying the energy spectra of the ^{39}Ar collected at low energy. The ICPC results are in good agreement with the official GERDA results while the BEGe value presents the same behavior of the estimations at the time of the data-taking from the two detector characterizations.

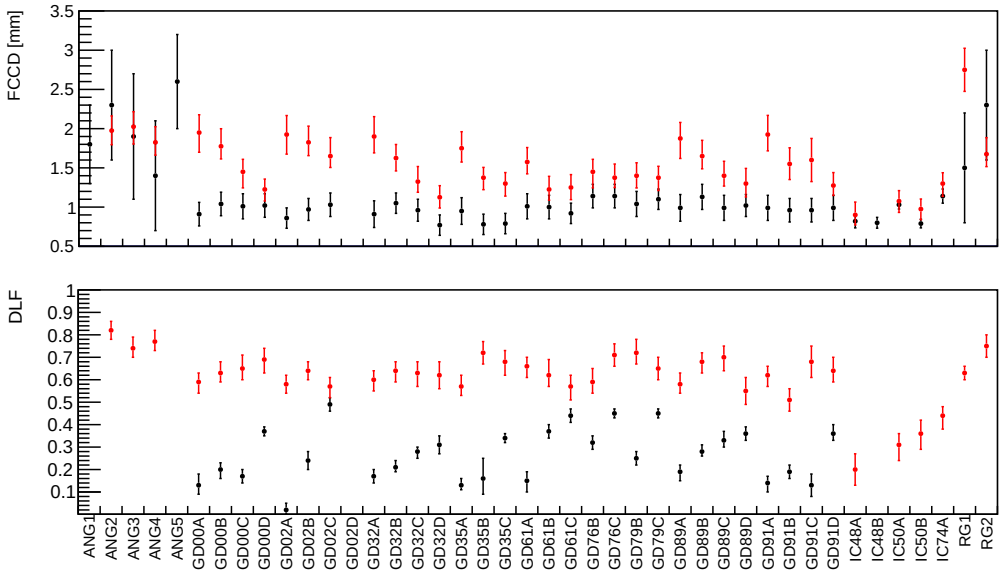

Figure 7.29: FCCD and DLF values for each detector in GERDA Phase II$^+$. The red points indicate the results with their total uncertainties obtained from the ^{39}Ar analysis. The black points are the *official* values of GERDA obtained by previous analyses.

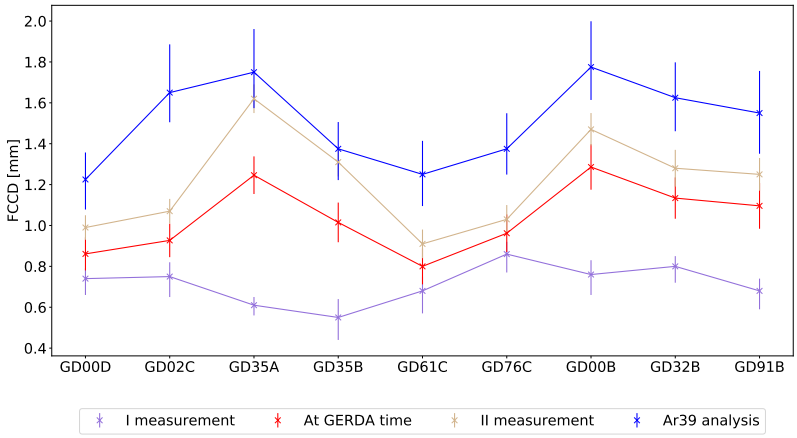

Figure 7.30: FCCD of the nine BEGe detectors re-characterized in HADES obtained by the ^{39}Ar analysis (blue) the first and second measurements in HADES (beige and purple, respectively), and the estimation of the FCCD at the time of GERDA Phase II$^+$ from the two measurements (red). All the point trends are similar among the detectors.

Table 7.3: List of the resulted FCCD, DLF, AV, and f_{AV} for each detector from the ^{39}Ar analysis. The uncertainties for each parameter indicate the statistical and systematic uncertainties. The horizontal lines are meant to divide the different detector types.

Detector	FCCD [mm]	DLF	AV [mm^3]	f_{AV}
ANG2	$1.975^{+0.085\,+0.166}_{-0.060\,-0.169}$	$0.82^{+0.02\,+0.02}_{-0.01\,-0.03}$	$467.5^{+2.0\,+5.5}_{-2.8\,-5.4}$	$0.873^{+0.004\,+0.010}_{-0.005\,-0.010}$
ANG3	$2.025^{+0.061\,+0.180}_{-0.081\,-0.205}$	$0.74^{+0.02\,+0.04}_{-0.01\,-0.03}$	$382.1^{+2.3\,+5.8}_{-1.7\,-5.0}$	$0.865^{+0.005\,+0.013}_{-0.004\,-0.011}$
ANG4	$1.825^{+0.065\,+0.189}_{-0.050\,-0.155}$	$0.77^{+0.02\,+0.04}_{-0.01\,-0.03}$	$384.8^{+1.4\,+4.4}_{-1.0\,-5.4}$	$0.876^{+0.003\,+0.010}_{-0.002\,-0.012}$
RG1	$2.750^{+0.030\,+0.273}_{-0.152\,-0.229}$	$0.63^{+0.01\,+0.02}_{-0.01\,-0.02}$	$312.0^{+3.7\,+7.0}_{-0.7\,-7.7}$	$0.813^{+0.010\,+0.018}_{-0.002\,-0.020}$
RG2	$1.675^{+0.083\,+0.192}_{-0.037\,-0.154}$	$0.75^{+0.02\,+0.04}_{-0.02\,-0.04}$	$338.5^{+1.0\,+4.0}_{-2.1\,-4.9}$	$0.883^{+0.002\,+0.010}_{-0.006\,-0.013}$
GD00A	$1.950^{+0.083\,+0.211}_{-0.139\,-0.208}$	$0.59^{+0.02\,+0.03}_{-0.02\,-0.04}$	$63.1^{+1.5\,+2.2}_{-0.9\,-2.2}$	$0.738^{+0.017\,+0.026}_{-0.010\,-0.026}$
GD00B	$1.775^{+0.114\,+0.192}_{-0.063\,-0.148}$	$0.63^{+0.02\,+0.04}_{-0.02\,-0.03}$	$101.2^{+0.8\,+2.0}_{-1.5\,-2.5}$	$0.801^{+0.007\,+0.016}_{-0.012\,-0.020}$
GD00C	$1.450^{+0.050\,+0.162}_{-0.054\,-0.154}$	$0.65^{+0.02\,+0.04}_{-0.02\,-0.04}$	$127.5^{+0.8\,+2.3}_{-0.7\,-2.4}$	$0.848^{+0.005\,+0.015}_{-0.005\,-0.016}$
GD00D	$1.225^{+0.052\,+0.121}_{-0.056\,-0.135}$	$0.69^{+0.02\,+0.04}_{-0.02\,-0.05}$	$128.2^{+0.9\,+2.1}_{-0.8\,-1.8}$	$0.868^{+0.006\,+0.014}_{-0.005\,-0.012}$
GD02A	$1.925^{+0.083\,+0.227}_{-0.153\,-0.197}$	$0.58^{+0.02\,+0.03}_{-0.02\,-0.03}$	$75.7^{+1.7\,+2.2}_{-0.9\,-2.5}$	$0.766^{+0.017\,+0.022}_{-0.009\,-0.025}$
GD02B	$1.825^{+0.101\,+0.180}_{-0.090\,-0.143}$	$0.64^{+0.02\,+0.03}_{-0.01\,-0.03}$	$89.4^{+1.1\,+1.7}_{-1.2\,-2.2}$	$0.790^{+0.010\,+0.015}_{-0.011\,-0.019}$
GD02C	$1.650^{+0.138\,+0.191}_{-0.054\,-0.134}$	$0.57^{+0.02\,+0.03}_{-0.02\,-0.04}$	$118.1^{+0.8\,+1.9}_{-2.0\,-2.7}$	$0.825^{+0.005\,+0.013}_{-0.014\,-0.019}$
GD32A	$1.900^{+0.134\,+0.214}_{-0.093\,-0.187}$	$0.60^{+0.02\,+0.03}_{-0.03\,-0.04}$	$63.6^{+0.9\,+1.8}_{-1.3\,-2.1}$	$0.759^{+0.011\,+0.022}_{-0.015\,-0.025}$
GD32B	$1.625^{+0.066\,+0.159}_{-0.058\,-0.153}$	$0.64^{+0.02\,+0.03}_{-0.02\,-0.04}$	$107.2^{+0.8\,+2.0}_{-0.9\,-2.1}$	$0.823^{+0.006\,+0.016}_{-0.007\,-0.016}$
GD32C	$1.325^{+0.084\,+0.172}_{-0.044\,-0.128}$	$0.63^{+0.02\,+0.04}_{-0.02\,-0.05}$	$115.3^{+0.6\,+1.8}_{-1.2\,-2.4}$	$0.857^{+0.005\,+0.013}_{-0.009\,-0.018}$
GD32D	$1.125^{+0.060\,+0.135}_{-0.054\,-0.125}$	$0.62^{+0.02\,+0.05}_{-0.02\,-0.05}$	$115.2^{+0.8\,+1.8}_{-0.8\,-1.9}$	$0.876^{+0.006\,+0.013}_{-0.006\,-0.014}$
GD35A	$1.750^{+0.063\,+0.201}_{-0.042\,-0.170}$	$0.57^{+0.03\,+0.04}_{-0.02\,-0.03}$	$113.6^{+0.6\,+2.3}_{-0.9\,-2.7}$	$0.815^{+0.004\,+0.017}_{-0.006\,-0.020}$
GD35B	$1.375^{+0.033\,+0.126}_{-0.067\,-0.137}$	$0.72^{+0.02\,+0.04}_{-0.02\,-0.04}$	$124.9^{+1.0\,+2.1}_{-0.5\,-1.9}$	$0.853^{+0.007\,+0.014}_{-0.003\,-0.013}$
GD35C	$1.300^{+0.055\,+0.128}_{-0.083\,-0.136}$	$0.68^{+0.02\,+0.04}_{-0.03\,-0.05}$	$97.3^{+1.1\,+1.8}_{-0.7\,-1.7}$	$0.843^{+0.010\,+0.016}_{-0.006\,-0.015}$
GD61A	$1.575^{+0.095\,+0.157}_{-0.054\,-0.141}$	$0.66^{+0.01\,+0.03}_{-0.02\,-0.04}$	$110.5^{+0.7\,+1.9}_{-1.3\,-2.1}$	$0.830^{+0.006\,+0.014}_{-0.010\,-0.016}$
GD61B	$1.225^{+0.073\,+0.150}_{-0.038\,-0.131}$	$0.62^{+0.03\,+0.06}_{-0.02\,-0.04}$	$117.9^{+0.6\,+1.9}_{-1.1\,-2.2}$	$0.863^{+0.004\,+0.014}_{-0.008\,-0.016}$
GD61C	$1.250^{+0.043\,+0.158}_{-0.057\,-0.144}$	$0.57^{+0.02\,+0.04}_{-0.03\,-0.05}$	$97.8^{+0.8\,+1.9}_{-0.6\,-2.1}$	$0.849^{+0.007\,+0.017}_{-0.005\,-0.018}$
GD76B	$1.450^{+0.076\,+0.139}_{-0.107\,-0.174}$	$0.59^{+0.04\,+0.04}_{-0.02\,-0.04}$	$56.5^{+0.9\,+1.5}_{-0.6\,-1.2}$	$0.810^{+0.013\,+0.021}_{-0.009\,-0.017}$
GD76C	$1.375^{+0.082\,+0.153}_{-0.036\,-0.120}$	$0.71^{+0.02\,+0.04}_{-0.02\,-0.04}$	$127.8^{+0.5\,+1.8}_{-1.2\,-2.3}$	$0.855^{+0.004\,+0.012}_{-0.008\,-0.015}$
GD79B	$1.400^{+0.097\,+0.133}_{-0.078\,-0.135}$	$0.72^{+0.04\,+0.04}_{-0.02\,-0.04}$	$113.1^{+1.1\,+1.9}_{-1.4\,-1.9}$	$0.842^{+0.008\,+0.015}_{-0.010\,-0.014}$
GD79C	$1.375^{+0.043\,+0.138}_{-0.078\,-0.144}$	$0.65^{+0.02\,+0.04}_{-0.02\,-0.04}$	$125.4^{+1.2\,+2.2}_{-0.7\,-2.1}$	$0.850^{+0.008\,+0.015}_{-0.004\,-0.014}$
GD89A	$1.875^{+0.101\,+0.177}_{-0.149\,-0.206}$	$0.58^{+0.03\,+0.04}_{-0.02\,-0.03}$	$72.0^{+1.6\,+2.2}_{-1.1\,-1.9}$	$0.768^{+0.017\,+0.024}_{-0.011\,-0.020}$
GD89B	$1.650^{+0.107\,+0.170}_{-0.055\,-0.152}$	$0.68^{+0.02\,+0.03}_{-0.02\,-0.04}$	$89.8^{+0.7\,+2.0}_{-1.4\,-2.2}$	$0.798^{+0.006\,+0.018}_{-0.012\,-0.019}$
GD89C	$1.400^{+0.088\,+0.161}_{-0.047\,-0.123}$	$0.70^{+0.02\,+0.04}_{-0.03\,-0.05}$	$89.3^{+0.6\,+1.6}_{-1.1\,-2.0}$	$0.826^{+0.006\,+0.015}_{-0.010\,-0.019}$
GD89D	$1.300^{+0.095\,+0.168}_{-0.082\,-0.150}$	$0.55^{+0.04\,+0.04}_{-0.02\,-0.05}$	$80.1^{+1.0\,+1.8}_{-1.1\,-2.0}$	$0.829^{+0.010\,+0.019}_{-0.012\,-0.021}$
GD91A	$1.925^{+0.151\,+0.191}_{-0.110\,-0.176}$	$0.62^{+0.02\,+0.03}_{-0.02\,-0.04}$	$88.2^{+1.3\,+2.1}_{-1.8\,-2.2}$	$0.782^{+0.012\,+0.019}_{-0.016\,-0.020}$
GD91B	$1.550^{+0.074\,+0.192}_{-0.091\,-0.154}$	$0.51^{+0.02\,+0.04}_{-0.02\,-0.04}$	$97.3^{+1.1\,+1.9}_{-0.9\,-2.4}$	$0.824^{+0.010\,+0.016}_{-0.008\,-0.020}$
GD91C	$1.600^{+0.044\,+0.116}_{-0.114\,-0.154}$	$0.68^{+0.02\,+0.03}_{-0.02\,-0.03}$	$93.1^{+1.4\,+1.9}_{-0.5\,-1.4}$	$0.817^{+0.012\,+0.017}_{-0.005\,-0.012}$
GD91D	$1.275^{+0.067\,+0.150}_{-0.024\,-0.123}$	$0.64^{+0.03\,+0.05}_{-0.02\,-0.04}$	$109.0^{+0.3\,+1.7}_{-0.9\,-2.0}$	$0.858^{+0.003\,+0.013}_{-0.007\,-0.016}$
IC48A	$0.900^{+0.060\,+0.152}_{-0.023\,-0.124}$	$0.16^{+0.02\,+0.06}_{-0.02\,-0.06}$	$323.8^{+0.6\,+3.3}_{-1.6\,-4.0}$	$0.930^{+0.002\,+0.009}_{-0.005\,-0.011}$
IC50A	$1.075^{+0.044\,+0.127}_{-0.055\,-0.132}$	$0.31^{+0.02\,+0.04}_{-0.03\,-0.06}$	$306.0^{+1.4\,+3.1}_{-1.1\,-3.2}$	$0.916^{+0.004\,+0.009}_{-0.003\,-0.010}$
IC50B	$0.975^{+0.039\,+0.121}_{-0.041\,-0.128}$	$0.36^{+0.02\,+0.05}_{-0.02\,-0.06}$	$323.9^{+1.1\,+3.4}_{-1.0\,-3.2}$	$0.925^{+0.003\,+0.010}_{-0.003\,-0.009}$
IC74A	$1.300^{+0.034\,+0.133}_{-0.080\,-0.142}$	$0.44^{+0.01\,+0.03}_{-0.02\,-0.05}$	$339.7^{+2.2\,+3.9}_{-0.9\,-3.6}$	$0.903^{+0.006\,+0.010}_{-0.002\,-0.010}$

Part IV

$T^{2\nu}_{1/2}$ measurement in GERDA Phase II

8

EFFECTS OF THE AV ON THE $T^{2\nu}_{1/2}$ MEASUREMENT

The measurements of the FCCD and AV in HPGe detectors are essential to model the detector response. However, the various techniques presented in the previous chapters report different results. The origin of this systematic shift remains unknown but suggested explanations are discussed qualitatively in Sec.8.1.

The AV of detectors affects the detection efficiency in many analyses of GERDA and LEGEND experiments. As an example among many, the measurement of the $2\nu\beta\beta$ half-life is influenced by the uncertainty on f_{AV}. GERDA Phase II has collected sufficient statistics to compute the $T^{2\nu}_{1/2}$ precisely. In Sec.8.1, a solid and reliable estimation of this observable is obtained thanks to the new f_{AV} of the re-characterized BEGe detectors. This choice drastically reduces the systematic uncertainties compared to previous measurements and obtains the most precise determination of $T^{2\nu}_{1/2}$ with ^{76}Ge.

8.1 OFFSET AMONG THE FCCD RESULTS

During the ICPC characterization campaign, the use of different radioactive sources has produced values of FCCD, which differ in a systematic manner. For example, there is an offset of 12% between the FCCD obtained with ^{241}Am respect to what is obtained with ^{133}Ba. This shift is also observed for the two characterizations of the BEGes in GERDA. For instance, the second campaign registers a difference of around 16% FCCD. Furthermore, the ^{39}Ar analysis applied on the data collected by GERDA Phase II^{+} gives interesting results *in-situ* but affected by an offset compared with the other analysis (around 37% FCCD w.r.t. ^{241}Am).

A complete comparison among all approaches can be achieved by focusing on the nine BEGe detectors re-measured. For these detectors, results from four different approaches are available for these detectors: ^{39}Ar analysis, and from the interpolation of the values of the first and second measurement in HADES with the ^{241}Am, ^{133}Ba, and ^{60}Co (see App.H) source. Due to very different and large systematic uncertainties, the figure shows only the statistical uncertainties for ^{39}Ar and ^{60}Co results. All the FCCDs show a similar trend among the detectors, and the ^{39}Ar and ^{60}Co results are in good agreement for most of the detectors. In addition, the correlation between these two point sets is illustrated with a dashed line bisecting the plane in Fig.8.1(right). It remains unclear the reason behind this compatibil-

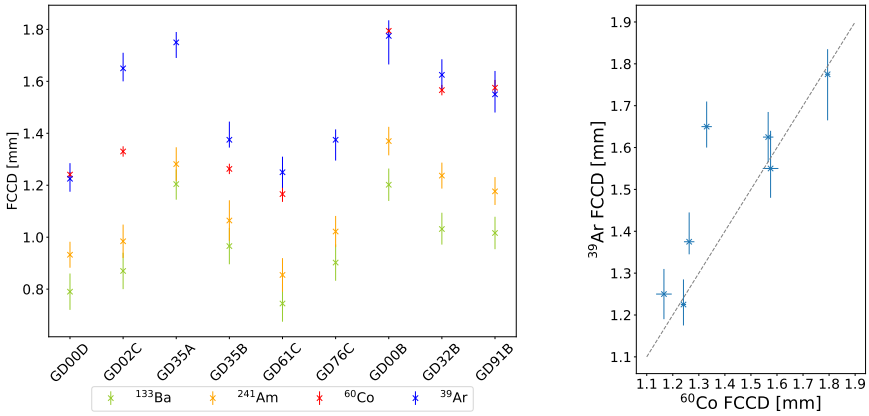

Figure 8.1: Left: FCCD results obtained by different analyses, using radioactive sources and the ^{39}Ar. The results show the same behavior despite the offset from different analyses. Right: Correlation between the results obtained from the ^{39}Ar analysis and the ^{60}Co measurements.

ity since these two analyses are based on different approaches focusing on different energy regions of the spectrum.

On the other hand, suggested explanations may clarify the offset among the ^{241}Am ^{133}Ba and ^{60}Co analyses which are all based on the γ-peak count. Several factors connected to systematics uncertainties on the analysis method or to the lack of additional physical effects on the simulations may affect the final results [108]. For instance, the depth at which the events are absorbed in the detector is different varying the energy of γs. It is also shown in the scatterplots (Fig.6.2, Fig.6.6, Fig.H.2) at x-z plane of the events depositing energy in the detector from a source placed at its top surface. Focusing on the single peaks, while at 60 keV peak of ^{241}Am the events deposit their energy mostly within 3 mm, for the 356 keV of ^{133}Ba they can exceed 5 cm. This may induce an estimation of a bigger FCCD at lower energies like for the ^{241}Am analysis w.r.t. the ^{60}Co analysis. On the contrary, the size of the charge cloud formed by charge carrier separation in the semiconductor may affect the FCCD determination in reverse. In case of significant energy deposition, the charges tend expand and can escape into the FCCD. Since it is not described in the simulations, the analysis would report a greater FCCD for full charge collection at higher energies. Furthermore, the energy resolution may impact the technique used to count the events under the γ-peak. Even without a transition layer, it is likely that an event is seen at lower energies than the total energy deposited in the detector since some of its energy depositions may appear inside the FCCD region. Counting these peculiar events under the peak leads to overestimating the FCCD, and this systematics may be generated by the energy smearing on the simulated peaks which is characterized by the energy resolution. For instance, Fig.8.2 shows the lost energy in the FCCD per event normalized to the initial energy for a simulated γ-line

at 60 keV, 356 kev, and 1332 keV, reproducing the main peaks of ^{241}Am, ^{133}Ba, and ^{60}Co spectra, respectively. The three spectra are normalized to the unity for a better visualization among them. They present a different shape along the lost energy. The right region of the plot shows the events that are not detected since the entire energy deposition is lost in the dead region. As expected, the majority of the ^{241}Am events lose their total energy (peak at 100%) because most of the energy depositions appear near the surface. While, the events which lose little energy in FCCD are placed in the left region of the plot. The amount of events within the energy resolution, which is around 0.80%, 0.24%, 0.12% for the 60 keV, 356 keV, 1332 keV respectively, may affect the FCCD determination.

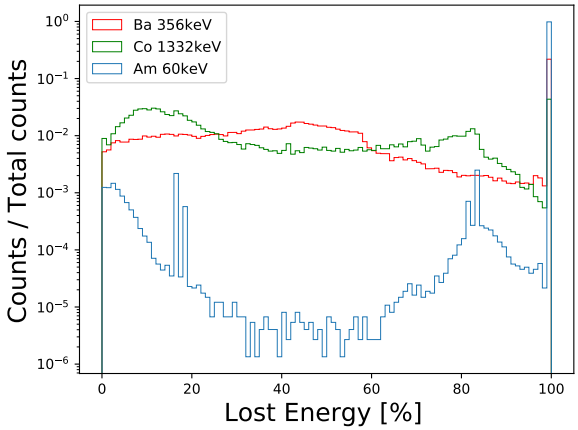

Figure 8.2: Lost energy in the dead region of a BEGe detector per event with initial energy of 60 keV, 356 keV, and 1332 keV (from the γ-peaks considered in ^{241}Am,^{133}Ba,^{60}Co analyses). The event energy is normalized to the total γ-peak energy. The histograms are normalized to 1 for a better visualization.

The combination of all these effects may results in what Fig.8.1 shows, with the $\mathrm{FCCD}_{^{133}\mathrm{Ba}} < \mathrm{FCCD}_{^{241}\mathrm{Am}} < \mathrm{FCCD}_{^{60}\mathrm{Co}}$. However, so far there is no compelling evidence to support an energy dependence in the measurement of the FCCD. Detailed pulse shape simulation and further investigation of the energy resolution are required but are beyond the scope of this work.

8.2 $2\nu\beta\beta$ HALF-LIFE WITH NEW FCCD

The two neutrino double beta decay is a process predicted by the Standard Model, as described in Sec.2.1, and it is one of the rarest radioactive processes ever observed. Precise measurements of its half-life could help the theory to constrain better the evaluation of the nuclear matrix elements of the various isotopes. Furthermore, many exotic processes produce characteristic distortions of the $2\nu\beta\beta$ event distribution.

The precision of previous measurements of the half-life of $2\nu\beta\beta$ decay in GERDA was limited by the uncertainty on the active volume, which is the primary source of uncertainty in the standard $T^{2\nu}_{1/2}$ determination since

the other contributions – LAr veto model, fit model, enrichment fraction, background model, etc. – are at the sub-percent level. As mentioned in Chap.6, the BEGe detectors were stored at room temperature before the GERDA deployment in 2015, causing an FCCD growth. The f_{AV} introduced in the previous $T^{2\nu}_{1/2}$ measurement took into account this effect which was roughly estimated with a growth speed of 0.1 ± 0.04 mm/yr. The second characterization of the nine BEGes is essential to investigate the FCCD growth and to obtain more reliable results to include in many analyses.

The half-life $2\nu\beta\beta$ is extracted from the number $\mathrm{N_{obs}}$ of measured $2\nu\beta\beta$ events in the analysis range [560, 2000] keV. The relation between the number of signal counts and the corresponding process half-life can be expressed as:

$$T^{2\nu}_{1/2} = \left[\frac{\mathcal{N}_A \log 2}{M_{76}}\, f_{76}\, \mathcal{E}_{QC}\, \mathcal{E}_{LAr}\, m_{BEGe}\, t_{PhaseII}\, \mathcal{E}_{MC}\right] \frac{1}{N_{obs}} \tag{8.1}$$

with

$$\mathcal{E}_{MC} = \frac{\sum_i \left(\mathcal{E}_{c,i}\, f_i^{AV}\, m_i^{tot}\, t_i\right)}{m_{BEGe}\, t_{PhaseII}}\,. \tag{8.2}$$

$\mathcal{N}_A$ is the Avogadro number, M_{76} is the ^{76}Ge molar mass, $f_{76} = 0.874 \pm 0.003$ is the enrichment fraction, $f_{LAr} = (97.7 \pm 0.1)\%$ is the probability for a signal event to survive the LAr veto cut, $\mathcal{E}_{QC} = (99.922 \pm 0.002)\%$ is the quality cuts signal efficiency, m_{BEGe} stands for the total mass of the nine detectors and $t_{PhaseII}$ for the total run time of GERDA Phase II. $\mathcal{E}_{MC}$ indicates the detection efficiency obtained through MC simulations for $2\nu\beta\beta$ decay events in the analysis range, and it is expressed by the product over the nine detectors of the AV fraction f_i^{AV}, the detector containment efficiency $\mathcal{E}_{c,i}$ corresponding to the probability that a $2\nu\beta\beta$ decay taking place in the AV of the detector deposits energy in the analysis window, the total detector mass m_i^{tot} and the time of measurement t_i. Since the efficiency is computed normalized to the total exposure, $m_{BEGe} \cdot t_{PhaseII}$ needs to be included in Eq.8.1.

$\mathcal{E}_{c,i}$ also accounts for the presence of a transition layer.

8.2.1 *Analysis*

The data used in this analysis correspond to the data set collected by the nine BEGe detectors, chosen for the re-characterization, in Phase II between December 2015 and April 2018 – from `Run 53` to `Run 93` – with a total exposure of 11.8 kg·yr. The reason for using only these selected detectors is justified by the negligible statistical uncertainty, expected by such an amount of exposure, compared to the systematic uncertainty on the active volume. Moreover, since the MC modeling of the LAr veto system assumes only the pre-upgrade LAr instrumentation, only data from Phase II are chosen. The multiplicity cut is applied as $2\nu\beta\beta$ events deposit their energy in a single detector with high probability. The non-physical events and those in coincidence with the muon veto are removed by the quality cut

and the muon veto cut, respectively. To further reduce the background, events tagged simultaneously in the germanium detectors and in the liquid argon are removed by the LAr veto cut.

The test statistic used in the analysis is based on the likelihood-ratio:

$$t_s = -2 \ln \frac{\mathcal{L}(S, \widehat{\mathrm{B}})}{\mathcal{L}(\widehat{S}, \widehat{\widehat{\mathrm{B}}})} \tag{8.3}$$

where S is the number of $2\nu\beta\beta$ decay events in the fit range $[560, 2000]$ keV, and B is the set of nuisance parameters given by the number of background events in the fit range. The likelihood function $\mathcal{L}$, bringing data and expectations together, is based on the product of Poisson probabilities for all bins. The theoretical models for signal and background event distributions are obtained from Monte Carlo simulations through the MaGe software framework. Not all the regularity conditions required by Wilk's theorem are satisfied, and toys MC are generated to investigate the analysis's performance and to compute the uncertainties thanks to the capability of *pdf*s to be distorted. The toy experiments are firstly generated by assuming a fixed model and varying the event number of each signal and background component according to statistical fluctuations. Each toy experiment is then processed in the analysis framework and fitted with the same model. Then, the generation of the MC toys is repeated, including the systematic uncertainties related to the background model and the detector response which introduce distortions in the shape of the signal and background *pdf*s. The systematic uncertainty due to the choice of the location of each background source in the fit model is estimated by comparing the reference location with the alternative mentioned in [100]. Uncertainties related to modeling the LAr veto response, which is affected by uncertainties in the optical parameters used in the MC simulations, are considered. The estimations of the transition region of FCCD are extracted using a simplified linear model for the CCE. In the generation of the toy experiments, the TL of each detector is varied in a conservative range of $\pm 5\sigma$ from the central value. Moreover, uncertainties in the theoretical calculations of the shape of $2\nu\beta\beta$ decay are studied assuming the Higher-State Dominance (HSD) and the Single-State Dominance (SSD) models in the calculations. All these uncertainties contribute to the systematic uncertainty of the half-life. More details on the analysis are reported in [109].

8.2.2 *Results*

The number of expected $2\nu\beta\beta$ events in the nine BEGe detectors, with a total exposure of 11.8 kg·yr, is $\mathrm{N_{obs}} = 16911 \pm 147(stat) \pm 112(sys)$ in the fit range $[560, 2000]$ keV. Fig.8.3 compares the observed data with the total best-fit model. The single contributions of the $2\nu\beta\beta$ decay and background are also shown. The $2\nu\beta\beta$ decay clearly dominates this energy region. In the bottom panel, the residuals are shown in number of standard deviations.

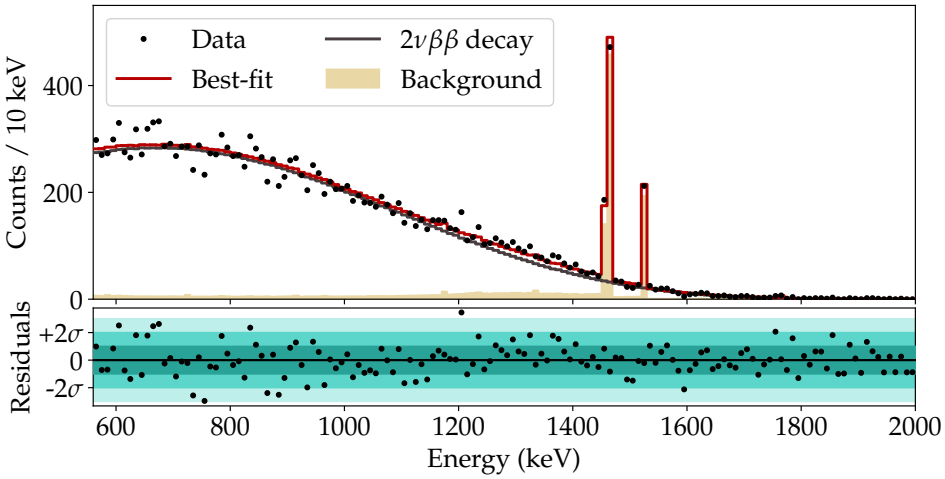

Figure 8.3: Best-fit signal and background decomposition of the nine BEGe energy spectrum. In the bottom panel, the ratio between data and model in units of Poisson standard deviations is shown together within 1σ, 2σ, 3σ.

The uncertainties on the f_{AV} of each detector are statistically propagated into the efficiency $\mathcal{E}_{MC}$ by properly treating the correlated and uncorrelated uncertainties with Monte Carlo methods. The efficiency is sampled according to the sum of Gaussian distributions over the nine detectors:

$$F(\mathcal{E}_{MC}) = \sum_i Gauss(\mathcal{E}_{MC,i} + r \cdot \sigma^{corr}_{\mathcal{E}_{MC,i}},\ \sigma^{uncorr}_{\mathcal{E}_{MC,i}}) \tag{8.4}$$

where $\sigma^{corr}_{\mathcal{E}_{MC,i}}$ and $\sigma^{uncorr}_{\mathcal{E}_{MC,i}}$ are the correlated and uncorrelated uncertainties of $\mathcal{E}_{MC}$ translated from the correlated and uncorrelated uncertainties of f_{AV}, respectively. To describe the correlation between the uncertainties, r is common to all the terms and is randomly sampled by a normal Gaussian. Finally, the efficiency and its uncertainty are extracted by the mean and the RMS of the resulting distribution $F(\mathcal{E}_{MC})$, respectively.

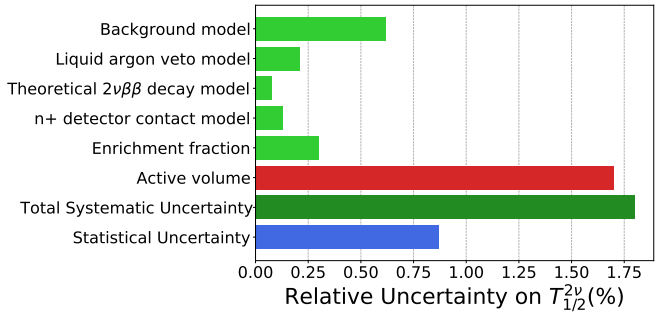

Figure 8.4: Uncertainties affecting the $2\nu\beta\beta$ decay half-life estimate. The statistical uncertainty is shown separately from the dominant total systematic uncertainty. The systematics related to the AV is indicated in red.

The f_{AV} extracted from the interpolation of the two characterizations are listed in Tab.6.5 with their correlated and uncorrelated uncertainties. The computed $\mathcal{E}_{MC}$ uncertainty of 1.7% can be propagated linearly to the

corresponding half-life estimation and then summed in quadrature with the other contributions, shown in Fig.8.4. The final estimation of the half-life with its total uncertainty is $T^{2\nu}_{1/2} = (2.022 \pm 0.018_{\text{stat}} \pm 0.036_{\text{sys}}) \cdot 10^{21}$ yr $= (2.022 \pm 0.041) \cdot 10^{21}$ yr. The total uncertainty (2%) is dominated by the systematic uncertainty on the AV (1.7%), while the statistical uncertainty contributes only at 0.9%.

Fig.8.5 shows the comparison among the new value and previous measurements from several experiments using ^{76}Ge and from the GERDA data-set in Phase I and Phase II. In particular, the total uncertainty of the measurement with the coaxial detectors in Phase I was dominated by the f_{AV} uncertainties, the background model, and MC simulation. Then, progress has been made for BEGe detectors in terms of analysis methods and uncertainty treatment, which are by far more elaborate than those for Coax detectors, in addition to a stronger background reduction.

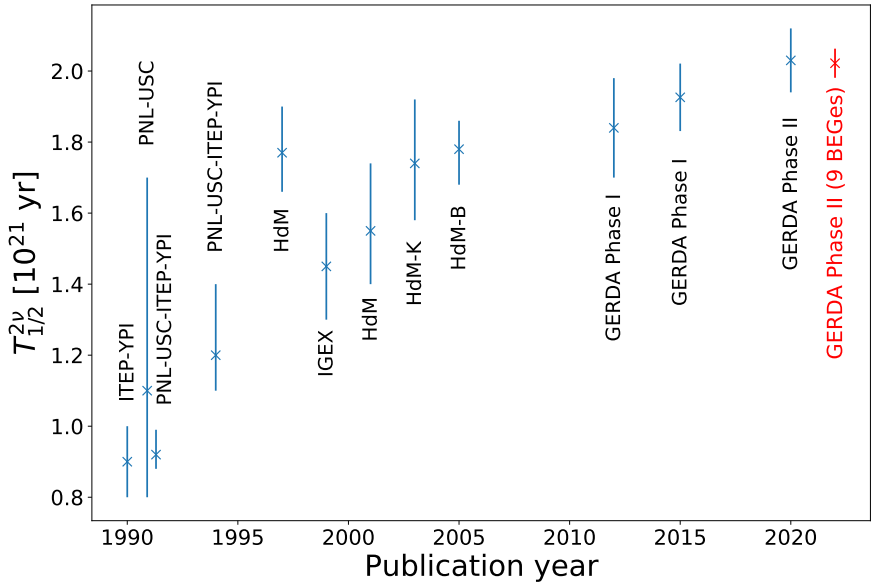

Figure 8.5: Experimental results for $T^{2\nu}_{1/2}$ of ^{76}Ge over the year since 1990. The plot includes results from the experiments ITEP-YPI [110], PNL-USC (natGe) [111] PNL-USC-ITEP-YPI [112, 113], Heidelberg-Moscow (HdM) [114, 115] and Igex [116], as well as the re-analysis of the HdM data by Klapdor-Kleingrothaus et al. [117] (HdM-K) and by Bakalyarov et al [118] (HdM-B). From 2012 on, two measurements from GERDA Phase I [119, 120] and one measurement from GERDA Phase II [100] are shown together with the value presented in this work.

All GERDA results are compatible within the uncertainties, and a general increase in the central value is observed due to a systematic underestimation of the background in the past experiments, which keeps increasing the signal-to-background ratio over time. The systematic uncertainty on the half-life is mainly reduced thanks to the better estimation of the f_{AV} and its uncertainty.

In conclusion, this new solid estimation of $T^{2\nu}_{1/2}$ is the most precise and reliable determination of the $2\nu\beta\beta$ decay half-life with ^{76}Ge. This record might be surpassed in the future only through a reduction of the systematic uncertainty related to the active volume fraction, since it dominates the total uncertainty. The reduction can be obtained by minimizing the time passed by the detectors at RT (maintaining them at low temperature even if they are not used) so stopping the growth of the dead layer and understanding better all the open questions discovered in this work.

CONCLUSIONS AND OUTLOOK

In this thesis work, a detailed investigation of the active volume of HPGe detectors used in the GERDA and LEGEND experiments is performed. Its effect on the measurement of the $2\nu\beta\beta$ half-life is studied.

All the first 29 ICPC detectors produced at the time of writing for the LEGEND-200 experiment are characterized in terms of active volume, which is a necessary ingredient for all future physics analyses in LEGEND. The detectors are placed in vacuum cryostats in the HADES underground facility, and two different radioactive sources set nearby each detector are used to determine the FCCD. A new versatile software framework is developed to automatically characterize the surfaces of a large number of detectors with high precision and to be efficiently adapted for the new upcoming detectors to be installed in the LEGEND cryostat. A special study on the FCCD at the bore-hole surfaces is examined and reveals a spread of results among the detectors in the range of $[50, 78]$% FCCD at the top surface. They are mostly larger than half of FCCD, which is the expected value due to the detectors' production chain. Furthermore, the assumption of the FCCD homogeneity on the top and lateral sides is validated with scan runs and, in general, no significant in-homogeneity is observed. A deeper investigation into the transition layer is suggested to give a complete model of the HPGe detectors surfaces. Potential new MC simulations should study various elaborate functions modeling the CCE parameterized by the FCCD and the DLF. An alternative strategy would be a Machine Learning approach to compare the energy spectra of data and simulations without executing a count ratio analysis.

Focusing on the official values of AV of the detectors in GERDA Phase II, the main contribution of their uncertainties is related to the unknown FCCD growth of the BEGe detectors stored at room temperature before the GERDA deployment in 2015. To find better AV values at the time of GERDA data-taking, nine BEGes were transferred back to the HADES facility to be characterized again after the GERDA decommissioning. A robust estimation is achieved by interpolating linearly the new results with the ones from the first measurement. Two different growth speeds are observed among the detectors and are included in the computation of the systematics.

An innovative technique has also been used to estimate the active volume *in-situ*. The ^{39}Ar data set offers the unique opportunity to estimate the active volume of the detectors in the same experimental conditions in which the GERDA physics data is recorded. The spectrum of low-energy events of Phase II^{+} is compared with different Monte Carlo models given by *pdf*s in a 2D grid defined by varying the FCCD and the DLF parameters. A statistical analysis consisting of the scanning of the test statistic based on the likelihood-ratio is performed to determine the dead layer and the transition

region for each detector, with the statistical and systematic uncertainties estimated by extracting confidence intervals from toy experiments. With respect to the official GERDA results, which take in consideration the FCCD growth of BEGe at room temperature with an average speed of 0.1 ± 0.04 mm/yr, the BEGes results of FCCD and DLF look larger while the ICPCs are in good agreement for both parameters. Comparing the former with the FCCD estimated by the nine BEGe re-characterized, ^{39}Ar values appear to follow the same overall trend among the detectors. Despite the promising results, the ambiguity on the ^{39}Ar activity remains unclear. Many tests have tried to solve this mismatch, and the cause could be related to a potential mis-modeling of the *bremsstrahlung* contribution, but no unambiguous results have proven it so far. A careful analysis of this puzzle may bring more reliable AV values to be included in many analyses. This investigation is strongly advised in the absence of a complete FCCD growth model in order to have more homogeneous AV results in the time of GERDA data-taking for all BEGes.

Finally, the effects of the new FCCD in GERDA obtained via the second characterization, have been studied on the measurement of the $2\nu\beta\beta$ half-life. The uncertainty of the active masses limited the precision of previous measurements of the half-life in GERDA. With the exposure of the nine BEGes, the extracted $2\nu\beta\beta$ half-life is $T^{2\nu}_{1/2} = (2.022 \pm 0.041) \cdot 10^{21}$ yr. With a total uncertainty of 2%, this is the most precise determination of $2\nu\beta\beta$ half-life with ^{76}Ge.

Future improvement in the measurement of $T^{2\nu}_{1/2}$ requires a precision determination of the active volume of the HPGe detectors. In GERDA, the ^{39}Ar analysis could seriously improve the estimation since it allows extraction of the AV *in-situ*. While in the future LEGEND-200 experiment, particular attention to the temperature storage of the ICPC detectors could improve the estimation even with a low exposure.

A

CHARACTERIZATION COMPONENTS

A.1 LEAD CASTLE

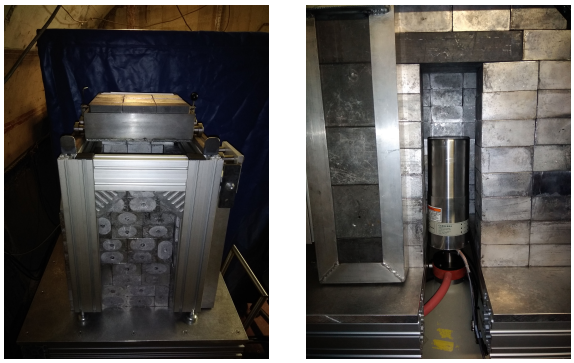

Figure A.1: Images of the lead castle in the static table in HADES. The inner position of the cryostat is visible in the photo on the left.

A.2 SOURCES AND SOURCE HOLDERS

A.2.1 *Source Activity*

L200 ID	2012 ID	Nuclid	Half-life (yr)	Ref. act. (kBq)	Unc. (%)	Ref. date (dd/mm/yy)	Activity shape	Origin	Owner	Reference
HS1	HS17	^{241}Am	432.20	4330.00	8	01/04/2012	1x1x2 mm^3	EuZ	MPIK	149473 UD 177
HS2	-	^{228}Th	1.91	87.0	7	01/11/2013	1x1x1 mm^3	EuZ	IRMM	026609 AC 9448
HS3	HS27	^{133}Ba	10.53	116.1	1.5	01/01/1993	point-like	PTB	IRMM	151-91
HS4	HS26	^{133}Ba	10.53	290.0	1.5	01/01/1984	point-like	PTB	IRMM	355-83
HS5	HS4	^{60}Co	5.26	413	1	01/01/1984	point-like	PTB	IRMM	233-82
HS6	HS21	^{241}Am	432.20	396.00	3	01/09/2008	point-like		MPIK	020294 RH 255

Figure A.2: Table of the HADES radioactive sources used in LEGEND.

A.2.2 ^{228}Th *HS2*

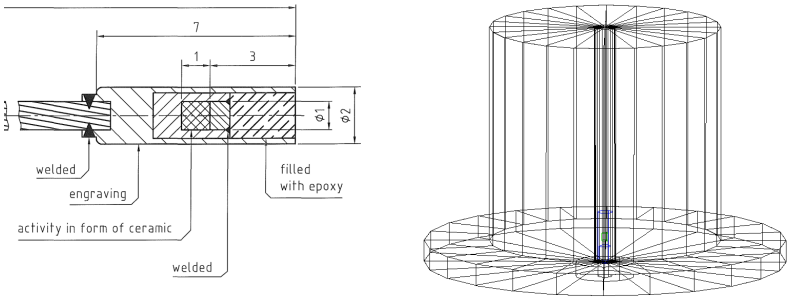

Figure A.3: Scheme of the ^{228}Th source components (left) and the structure of its copper holder (right).

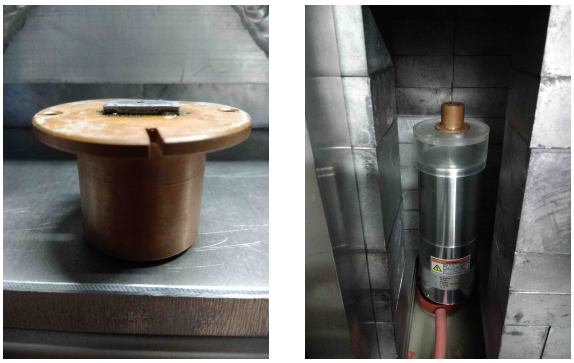

Figure A.4: Images of the copper source holder and its position upon the plexiglass source holder.

A.2.3 ^{133}Ba *HS4*

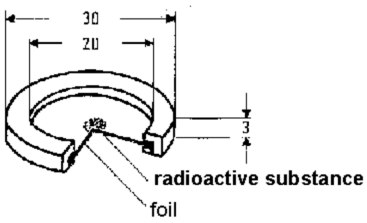

Figure A.5: Scheme of the ^{133}Ba source components.

A.2.4 ^{241}Am HS1

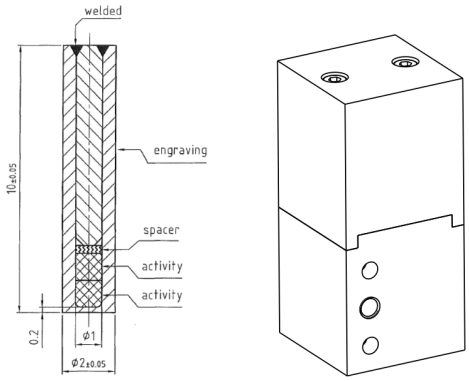

Figure A.6: Scheme of the ^{241}Am source components (left) and the structure of the copper collimator (right).

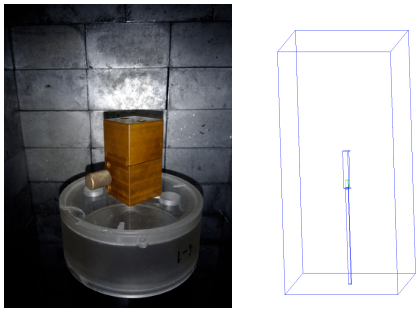

Figure A.7: Images of the real (left) and simulated (right) collimated ^{241}Am source.

A.2.5 ^{241}Am HS6

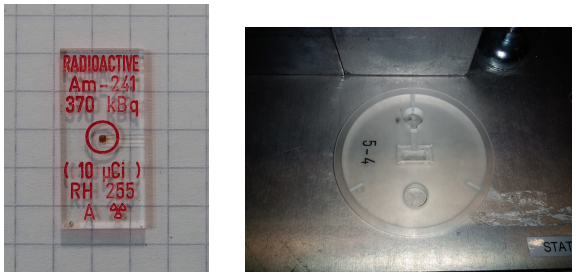

Figure A.8: Images of the uncollimated ^{241}Am source (HS6) and the top-end of the source holder fitting the source geometry.

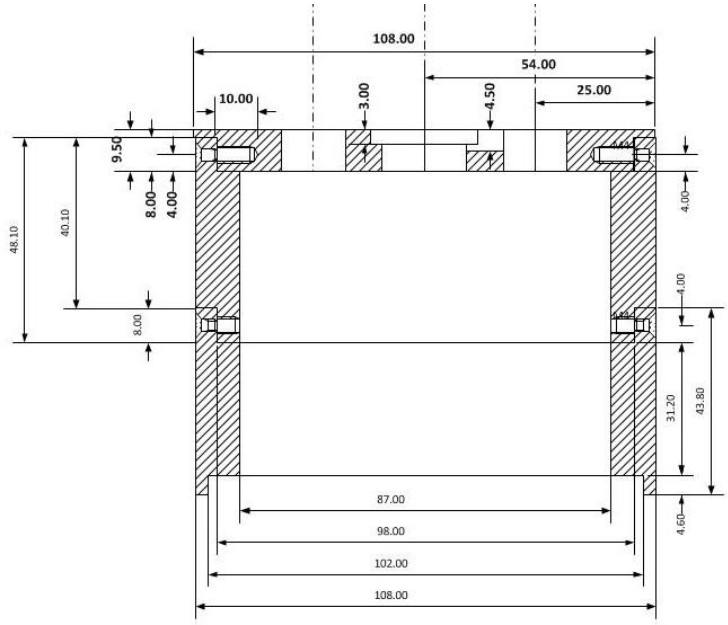

Figure A.9: Scheme of the plexiglass source holder. It consists of different piled-up sections.

A.3 CRYOSTAT, HOLDER, WRAP

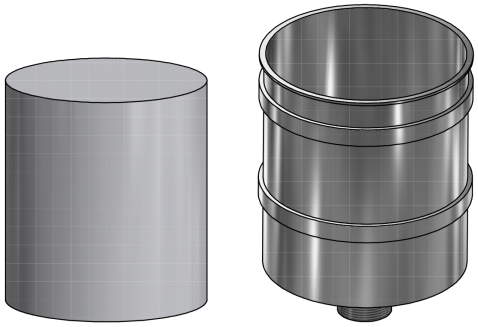

Figure A.10: Drawings of the standard wrap (left) and holder (right) components surrounding the detector.

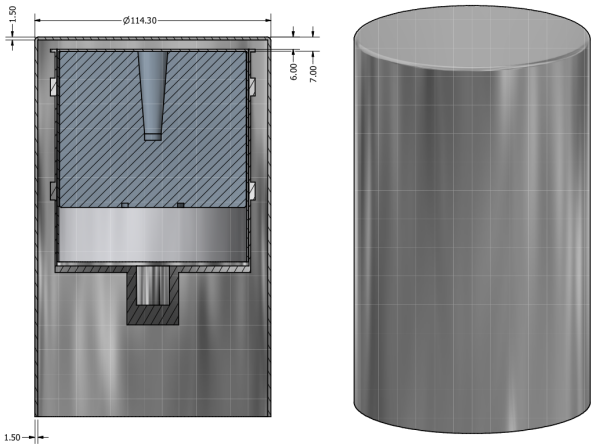

Figure A.11: Drawing of the inner (left) and outer (right) view of the cryostat.

A.4 DETECTORS

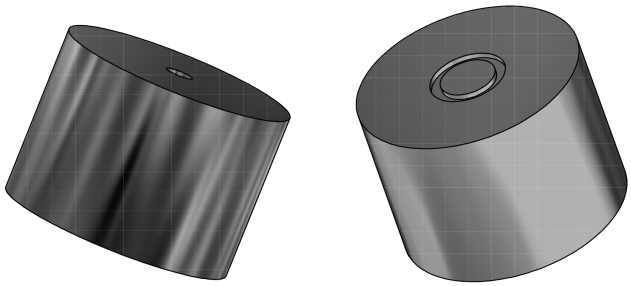

Figure A.12: Drawings of the standard geometry of the ICPC HPGe detector. Visualization of the bore-hole at the top surface (left) and the groove at the bottom surface (right)

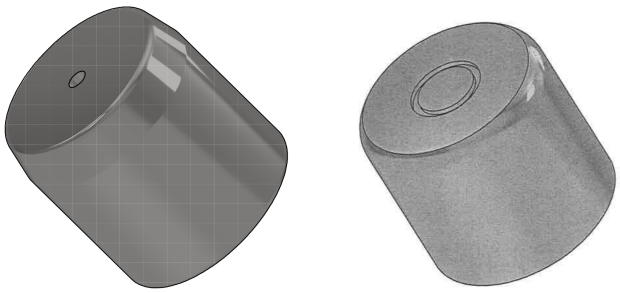

Figure A.13: Drawings of typical cases of outer tapering on the top (left) and the bottom (right) detector surface.

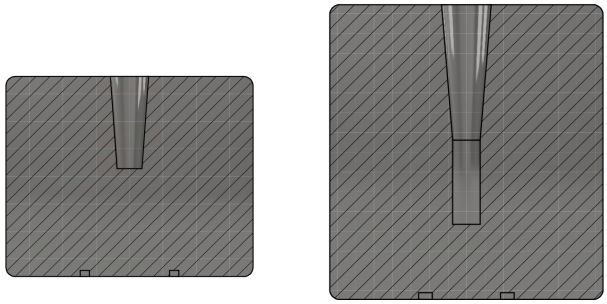

Figure A.14: Drawings of different cases of inner taper detector surface.

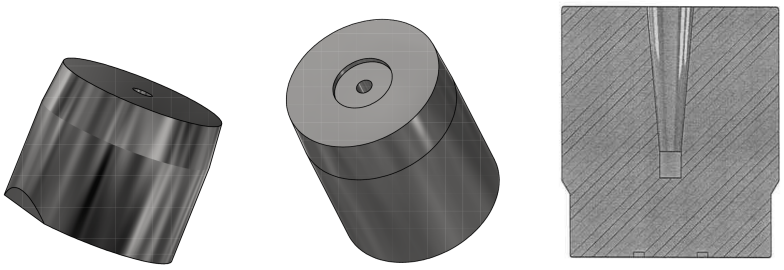

Figure A.15: Drawings of special cases of crack at the bottom (left), second groove (center) and multiradius (right) detectors.

B

EXAMPLES OF GDML FILE AND G4SIMPLE MACRO

```
<gdml xmlns:xsi="http://www.w3.org/2001/XMLSchema-instance"
xsi:noNamespaceSchemaLocation="http://service-spi.web.cern.ch/service-spi/app/
releases/GDML/schema/gdml.xsd">

 <define>

       <quantity name="solid_x" type="length" value="10" unit="cm" />
       <quantity name="solid_y" type="length" value="10" unit="cm"/>
       <quantity name="solid_z" type="length" value="30" unit="cm"/>

       <quantity name="inn_solid_x" type="length" value="5" unit="cm"/>
       <quantity name="inn_solid_y" type="length" value="5" unit="cm"/>
       <quantity name="inn_solid_z" type="length" value="20" unit="cm"/>

       <position name="pos_inner_solid" x="0" y="0" z="-solid_z/2" />

 </define>

 <materials>

    <material name="Al" Z="13.0" >
        <D value="2.70" unit="g/cm3" />
        <atom value="26.98" />
    </material>

 </materials>

 <solids>

       <box name="solid" x="solid_x" y="solid_y" z="solid_z"/>
       <box name="inner_solid" x="inn_solid_x" y="inn_solid_y" z="inn_solid_z"/>

       <subtraction name="final_solid" >
              <first ref="solid"/> <second ref="inner_solid"/>
              <positionref ref="pos_inner_solid" />
       </subtraction>

 </solids>

 <structure>
       <volume name="physical_volume">
              <materialref ref="Al"/>
              <solidref ref="final_solid"/>
       </volume>
 </structure>

 <setup name="Default" version="1.0">
       <world ref="physical_volume"/>
 </setup>

</gdml>
```

Figure B.1: Example scheme of a simple GDML file for the implementation of a hollow aluminum box.

```
/run/verbose 1
/random/setSeeds 1 1
/g4simple/setReferencePhysList LBE

/g4simple/setDetectorGDML ../geometry/main_th_HS2_top.gdml
/g4simple/setOutputFormat hdf5
/analysis/setFileName ../hdf5/sim-V05266A-th_HS2_bi-top-0r-38z-01.hdf5

/g4simple/setVolID Detector_PV 1
/g4simple/recordAllSteps false
/run/initialize
/g4simple/listPhysVols

/gps/particle ion
/gps/ion 83 212 0 0
/gps/energy 0 MeV
/grdm/nucleusLimits 212 212 83 83
/gps/ang/type iso
/gps/ang/mintheta 150 deg
/gps/ang/maxtheta 180 deg
/gps/pos/type Volume
/gps/pos/shape Cylinder
/gps/pos/radius 0.5
/gps/pos/halfz 0.5
/gps/pos/centre 0.0 0.0 -41.5 mm
/gps/pos/confine Source_PV

/run/beamOn 10000
```

Figure B.2: Example scheme of a macro file run by G4simple for the generation of 1000 events stored in a hdf5 file. The geometry is implemented looking at the input GDML file and the ^{212}Bi source is confined in a volume.

C

ACTIVE VOLUME DETERMINATION FOR SPECIAL DETECTOR GEOMETRIES

The common ICPC detector features a simple geometry given by a cylindrical bulk with a bore-hole at the top and the region of the groove at the bottom. However, several detectors show non standard shape such as tapered sides, multi-radius, additional groove at the top side, and crack at the bottom side. Below, these geometries are analyzed to properly compute the AV. Table C.1 lists all the dimensions of the detectors, including the special geometries.

C.1 TAPERING

Fig.C.1 shows the labels used below in the computation of the AV for a tapered geometry. Detectors can show several tapering that are here called bottom-outer taper, top-outer taper and top-inner taper based on the position of the tapered surface.

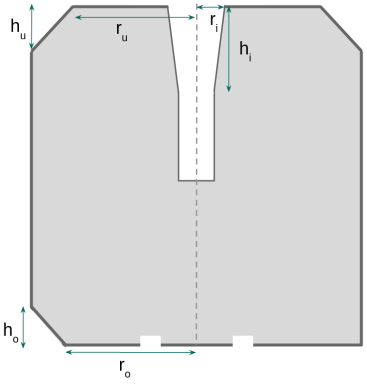

Figure C.1: Sketch of the r-z plane of a typical ICPC detector. with several tapered surface: bottom-outer taper (h_o, r_o), top-outer taper (h_u, r_u), top-inner taper (h_i, r_i).

Assuming the FCCD is homogeneous for the entire n+ surface (but for the bore-hole), Fig.C.2 shows the geometry of a tapered side. The light-gray region indicates the bulk volume with the decreased size, required for the computation of the AV. The figure reproduces the geometry for the case of a top outer tapered detector but the computation can be extended to the other cases in the same way. The new height (h_s) of the seized tapered bulk is given by the corner height shift ($B^{'}$):

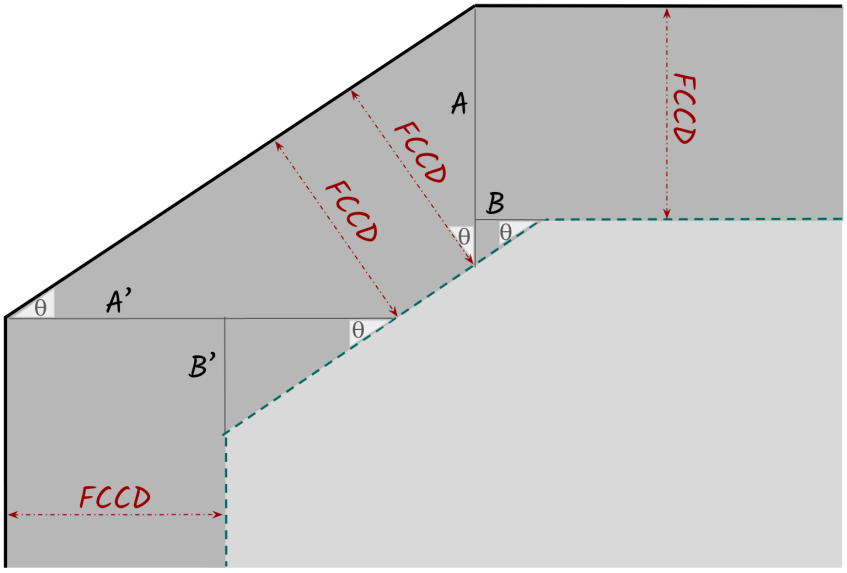

Figure C.2: Illustration of tapered ICPC for the AV calculation.

$$\begin{aligned} t &= h/(R-r) = \tan(\theta) \\ B^{'} &= t \cdot (1/\sin(\arctan(t)) - 1) \cdot FCCD \\ h_s &= h - FCCD + B^{'} \end{aligned} \tag{C.1}$$

where h, R, and r refer to the height, the greater radius and the smaller radius of the tapered bulk, respectively. The new radius (h_r) of the tapered bulk derived from the corner radius shift (B) is

$$\begin{aligned} t &= (R-r)/h = \arctan(\theta) \\ B &= t \cdot (1/\sin(\arctan(t)) - 1) \cdot FCCD \\ r_s &= r - B \end{aligned} \tag{C.2}$$

From the previous definition, one can also derive the new inner (r_s) radius when the bore-hole is tapered, where now h and r are referring to the dimensions of that tapered side:

$$\begin{aligned} t &= (R-r)/h \\ s &= t \cdot |FCCD - FCCD_{bh}/\sin(\arctan(t))| \\ r_s &= s \end{aligned} \tag{C.3}$$

C.1.1 *Bottom-Outer Taper*

The bottom side presents a tapered shape. $h_{o_{new}}$ and $r_{o_{new}}$ are the sized height and radius computed from Eq.C.1 and Eq.C.2 with h_o, r_o, and R_c in place of h, r, and R, respectively

$$\begin{aligned} AV = & AV_{standard} \\ & - \pi \cdot h_{o_{new}} \cdot (R_c - FCCD)^2 \\ & + \pi/3 \cdot h_{o_{new}} \cdot \left[r_{o_{new}}^2 + r_{o_{new}} \cdot (R_c - FCCD) + (R_c - FCCD)^2 \right] \end{aligned} \tag{C.4}$$

R_c is the radius of the bulk (see Fig. 5.40) and FCCD and $FCCD_{bh}$ are the FCCD at top and side, and at the bore-hole, respectively. These three parameters can be found in the computation below, as well.

C.1.2 *Top-Outer Taper*

The top side presents a tapered shape in the outer region. $h_{u_{new}}$ and $r_{u_{new}}$ are the sized height and radius computed from Eq.C.1 and Eq.C.2 with h_u, r_u, and R_c instead of h, r, and R, respectively.

$$\begin{aligned} AV = & AV_{standard} \\ & - \pi \cdot h_{u_{new}} \cdot (R_c - FCCD)^2 \\ & + \pi/3 \cdot h_{u_{new}} \cdot \left[r_{u_{new}}^2 + r_{u_{new}} \cdot (R_c - FCCD) + (R_c - FCCD)^2 \right] \end{aligned} \tag{C.5}$$

C.1.3 *Top-Inner Taper*

The top side presents a tapered shape in the inner region. $r_{i_{new}}$ is the sized radius computed from Eq.C.3 with h_i, r_w, and r_i instead of h, r, and R, respectively. If the bore-hole is a cone,

$$\begin{aligned} AV = & AV_{standard} \\ & + \pi \cdot (h_w + FCCD_{bh} - FCCD) \cdot (r_w + FCCD_{bh})^2 \\ & - \pi/3 \cdot h_{i_{new}} \cdot (r_{i_{new}}^2 + r_{i_{new}} \cdot r_{w_{new}} + r_{w_{new}}^2) \end{aligned} \tag{C.6}$$

where the sized height and radius are given by $h_{i_{new}} = h_i + FCCD_{bh} - FCCD$ and $r_{w_{new}}$ from Eq.C.2 with h_i, r_w, and r_i instead of h, r, and R, respectively. While, if the bore-hole shows both the cone and the cylinder shape at different height, then

$$\begin{aligned} AV = & AV_{standard} \\ & + \pi \cdot (h_w + FCCD_{bh} - FCCD) \cdot (r_w + FCCD_{bh})^2 \\ & - \pi/3 \cdot h_{i_{new}} \cdot (r_{i_{new}}^2 + r_{i_{new}} \cdot r_{w_{new}} + r_{w_{new}}^2) \\ & - \pi \cdot (h_{w_{new}} - h_{i_{new}}) \cdot r_{w_{new}}^2 \\ & - \pi \cdot (h_w - h_{i_{new}} + FCCD_{bh}) \cdot r_{w_{new}}^2 \end{aligned} \tag{C.7}$$

where the sized height and radius are given by $r_{w_{new}} = r_w + FCCD_{bh}$, $h_{w_{new}} = h_w + FCCD_{bh} - FCCD$, and $h_{i_{new}}$ from Eq.C.1 with h_i, r_w, and r_i instead of h, r, and R, respectively.

C.2 TOP GROOVE

The top side presents a second groove, like the one sketched in Fig.C.3. The AV sized by the FCCD region is

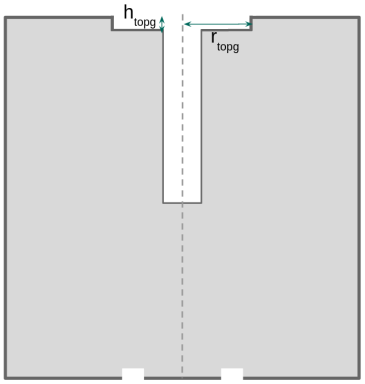

Figure C.3: Sketch of the r-z plane of a detector with a second groove at the top surface (h_{topg}, r_{topg}).

$$\begin{aligned} AV = & AV_{standard} \\ & - \pi \cdot h_{topg} \cdot (r_{topg} + FCCD)^2 \\ & + \pi \cdot h_{topg} \cdot (r_w + FCCD_{bh})^2 \end{aligned} \tag{C.8}$$

C.3 MULTI-RADIUS

The detector present multi-radius configuration like the one shown in Fig C.4. The AV sized by the FCCD region is

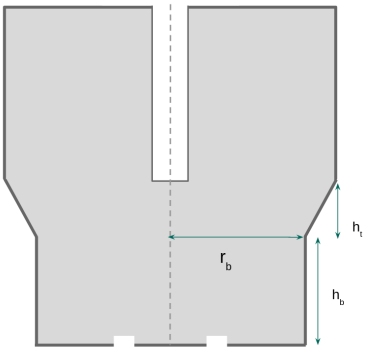

Figure C.4: Sketch of the r-z plane of a detector with a narrowing bulk. It presents the so called multi-radius geometry (h_t, r_b, h_b).

$$
\begin{aligned}
AV =& AV_{standard} \\
& - \pi \cdot (h_{b_{new}} + h_t) \cdot (R_c - FCCD)^2 \\
& + \pi \cdot h_{b_{new}} \cdot (r_b - FCCD)^2 \\
& + \pi/3 \cdot h_t \cdot \left[(r_b - FCCD)^2 + (r_b - FCCD) \cdot (R_c - FCCD) + (R_c - FCCD)^2 \right]
\end{aligned}
\tag{C.9}
$$

where $h_{b_{new}}$ is the size height computed from Eq.C.1 with h_t, r_b, and R_c in place of h, r, and R, respectively.

C.4 BOTTOM CRACK

Fig.C.5 displays the sketch of a detector with a bottom crack. Since it is asymmetrical along the z-axis, it cannot be treated only in the r-z plane like the other detectors. The sized corner radius r_s is stemmed from the crack

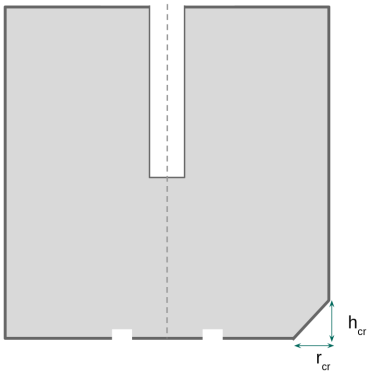

Figure C.5: Sketch of the r-z plane of a detector with a crack at the bottom side (h_{cr}, r_{cr}).

corner radius shift (s) as:

$$
\begin{aligned}
t &= (R - r)/h \\
s &= t \cdot (1/\sin(\arctan(t)) - 1) \cdot FCCD \\
r_s &= r - FCCD + s
\end{aligned}
\tag{C.10}
$$

The AV sized by the FCCD layer is

$$
\begin{aligned}
AV =& AV_{standard} \\
& - \frac{2h_{cr_{new}}}{r_{cr_{new}}} (R - FCCD)^2 \left[\frac{(R - r_{cr_{new}} - FCCD)^2}{2(R - FCCD)} - \frac{(R - r_{cr_{new}} - FCCD)}{4} \cdot \right. \\
& \left. \cdot \sin\left(\frac{2(R - r_{cr_{new}} - FCCD)}{R - FCCD} \right) - \frac{R - FCCD}{3} \sin^3\left(\frac{R - r_{cr_{new}} - FCCD}{R - FCCD} \right) \right]
\end{aligned}
\tag{C.11}
$$

where $h_{cr_{new}}$ and $r_{cr_{new}}$ are the sized height and radius computed from Eq.C.1 and Eq.C.10 with h_{cr}, r_{cr}, and R_c instead of h, r, and R, respectively.

Table C.1: Dimensions in mm of the diodes characterized at the time of writing. See Fig.5.40, Fig. C.1, Fig. C.3, Fig. C.4, Fig. C.5 for label references.

ICPC	H_c	R_c	h_w	r_w	h_g	r_{g_o}	r_{g_i}	h_o	r_o	h_u	r_u	h_i	r_i	h_{topg}	r_{topg}	h_b	r_b	h_t	h_{cr}	r_{cr}
V02160A	65.4	39.9	33.7	4.7	2.0	15.5	11.3	0	39.9	20.1	37.8	0	4.7	0	0	0	39.9	0	8	5
V02160B	59.3	41.0	30.0	4.8	2.0	13.9	10.1	0	41.0	0	41.0	0	4.8	0	0	0	41.0	0	0	0
V02162B	90.4	40.0	55.0	4.0	3.0	15.8	10.5	0	40.0	25.0	39.2	0	4.0	2.7	15.3	0	40.0	0	0	0
V02166B	95.5	40.0	61.6	4.3	2.0	13.9	9.7	0	40.0	0	40.0	0	4.3	0	0	0	40.0	0	0	0
V04199A	100.4	42.0	70.0	4.0	2.0	14.0	10.0	0	42.0	20.0	41.0	70.0	9.8	0	0	0	42.0	0	0	0
V04545A	100.5	42.5	69.2	4.0	2.0	14	10.0	0	42.5	0	42.5	0	4.0	0	0	0	42.5	0	0	0
V04549A	80.5	37.5	49.0	5.0	2.0	14.0	10.0	0	37.5	0	37.5	0	5.0	0	0	0	37.5	0	0	0
V04549B	65.4	37.5	50.9	4.0	2.0	20.0	37.5	0	37.5	0	37.5	50.9	8.7	0	0	0	37.5	0	0	0
V05261A	65.2	40.1	30.0	4.0	2.0	16.0	13.0	0	40.1	0	40.1	30.0	6.2	0	0	0	40.1	0	0	0
V05261B	87.0	40.1	64.8	4.0	2.0	14.0	10.0	0	40.1	0	40.1	40.0	7.2	0	0	0	40.1	0	0	0
V05266A	75.2	40.0	42.0	4.0	2.0	16.0	13.0	0	40.0	0	40.0	0	4.0	0	0	0	40.0	0	0	0
V05266B	72.0	40.1	41.9	4.0	2.0	14.0	10.0	0	40.1	0	40.1	0	4.0	0	0	0	40.1	0	0	0
V05267A	80.2	40.0	40.2	4.0	2.0	18.0	15.0	0	40.0	17.0	36.0	0	4.0	0	0	0	40.0	0	0	0
V05267B	85.5	40.1	51.6	4.0	2.0	16.0	13.0	0	40.1	0	40.1	35.0	6.51	0	0	0	40.1	0	0	0
V05268A	83.2	40.1	45.1	4.0	2.0	18.0	15.0	0	40.1	0	40.1	35.0	6.5	0	0	0	40.1	0	0	0
V05268B	65.2	40.1	49.0	4.0	2.0	18.0	15.0	0	40.1	0	40.1	45.0	7.2	0	0	0	40.1	0	0	0
V05612A	80.1	40.0	40.0	4.0	2.0	18.3	14.8	0	40.0	0	40.0	30.0	6.3	0	0	0	40.0	0	0	0
V05612B	85.0	38.0	70.1	4.0	2.0	18.0	15.0	0	38.0	0	38.0	50.0	7.8	0	0	0	38.0	0	0	0
V07646A	95.1	41.0	65.0	4.0	2.0	14.0	10.0	0	41.0	0	41.0	55.0	8.8	0	0	24.0	38.0	5.1	0	0
V07302A	65.0	40.0	35.0	4.0	2.0	14.0	10.0	0	40.0	0	40.0	0	4.0	0	0	0	40.0	0	0	0
V07302B	57.4	40.1	30.0	4.0	2.0	12.5	8.5	0	40.1	0	40.1	0	4.0	0	0	0	40.1	0	0	0
V07647A	70.3	39.8	37.0	4.0	2.0	15.0	12.0	8.0	35.8	0	39.8	0	4.0	0	0	0	39.8	0	0	0
V07647B	66.1	39.8	42.0	4.0	2.0	13.0	10.0	0	39.8	9.0	36.8	0	4.0	0	0	0	39.8	0	0	0
V07298B	75.3	40.0	48.2	4.0	2.0	13.0	10.0	0	40.0	0	40.0	0	4.0	0	0	0	40.0	0	0	0
V08682A	95.7	45.0	61.0	4.0	2.0	15.0	12.0	0	45.0	0	45.0	50.0	8.3	0	0	0	45.0	0	0	0
V08682B	43.3	45.0	17.1	4.1	2.0	13.0	10.0	0	45.0	0	45.0	0	4.1	0	0	0	45.0	0	0	0
V09374A	75.6	45.2	43.1	4.0	2.0	15.0	12.0	0	45.2	0	45.2	40.0	7.2	0	0	0	45.2	0	0	0
V09724A	75.6	45.1	43.1	4.0	2.0	15.0	12.0	0	45.1	0	45.1	40.0	7.2	0	0	0	45.1	0	0	0
V09372A	111.8	46	79.0	4.0	2.0	15.0	12.0	0	46.0	0	46.0	60.0	9.0	0	0	0	46.0	0	0	0

D

ALTERNATIVE FCCD RESULTS FROM ICPC CHARACTERIZATION

This section reports the FCCD obtained from the three radioactive sources used during the characterization in HADES: *ba_HS4*, *am_HS1*, and *am_HS6*. The results from *am_HS1* are calibrated with the uncollimated *am_HS6* results of `V07302A`, `V07302B`, `V07647A`, and `V07647B`, as explained in Sec.5.5.4. Fig.D.1 compares the three result sets of the detectors characterized by all sources. As expected, the ^{133}Ba values are lower than the two ^{241}Am results. Tab.D.1 lists the values presented in Tab.5.7, but replaces the calibrated FCCD from *am_HS1* with the values from *am_HS6* for the detectors shown in Fig.D.1, which have been characterized also by this additional source. In this way, even if the listed Am values are not homogeneous regarding the technique used among the detectors, some of them are at least more reliable without the additional uncertainty due to the calibration.

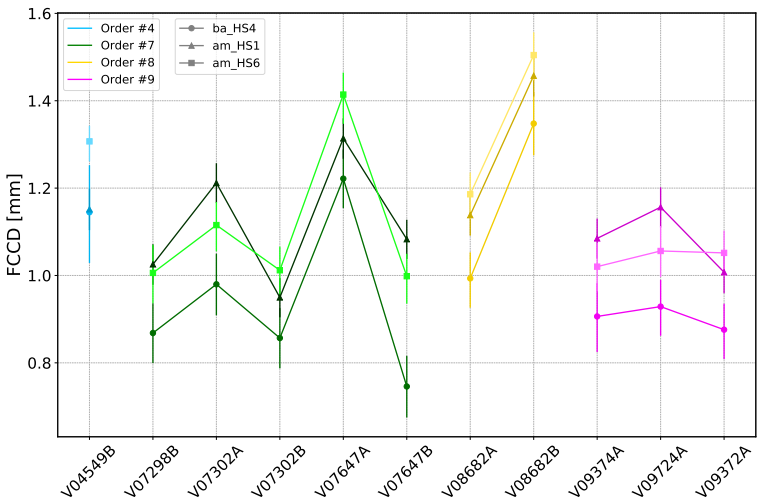

Figure D.1: Comparison of the FCCD results of the detectors characterized by the ^{133}Ba source and the collimated and uncollimated ^{241}Am sources.

Table D.1: List of the FCCD, AV and f_{AV} for each detector, obtained with the ^{133}Ba and ^{241}Am analyses. The detectors characterized by also the *am_HS6* present the results from this source in the column of ^{241}Am. The uncertainties are separated into correlated and uncorrelated components.

ICPC	FCCD [mm]		AV [mm^3]		f_{AV}	
	^{133}Ba	^{241}Am	^{133}Ba	^{241}Am	^{133}Ba	^{241}Am
V02160A	$0.65^{+0.05\,+0.03}_{-0.5\,-0.03}$	-	$302.5^{+1.3\,+0.7}_{-1.3\,-0.7}$	-	$0.949^{+0.004\,+0.002}_{-0.004\,-0.002}$	-
V02160B	$0.66^{+0.05\,+0.03}_{-0.05\,-0.03}$	$0.63^{+0.03\,+0.01}_{-0.3\,-0.01}$	$293.9^{+1.4\,+0.6}_{-1.3\,-0.6}$	$294.6^{+0.8\,+0.3}_{-0.8\,-0.3}$	$0.947^{+0.004\,+0.002}_{-0.004\,-0.002}$	$0.949^{+0.003\,+0.001}_{-0.003\,-0.001}$
V02162B	$0.69^{+0.05\,+0.02}_{-0.05\,-0.02}$	-	$423.8^{+1.7\,+0.7}_{-1.7\,-0.8}$	-	$0.950^{+0.004\,+0.002}_{-0.004\,-0.002}$	-
V02166B	$0.76^{+0.05\,+0.02}_{-0.05\,-0.02}$	$0.61^{+0.03\,+0.02}_{-0.03\,-0.02}$	$450.3^{+1.8\,+0.7}_{-1.8\,-0.7}$	$455.4^{+1.1\,+0.5}_{-1.1\,-0.5}$	$0.946^{+0.004\,+0.001}_{-0.004\,-0.002}$	$0.957^{+0.002\,+0.001}_{-0.002\,-0.001}$
V04199A	$1.15^{+0.05\,+0.01}_{-0.06\,-0.03}$	$1.09^{+0.03\,+0.01}_{-0.03\,-0.01}$	$510.9^{+2.1\,+0.9}_{-1.6\,-0.5}$	$513.3^{+1.2\,+0.5}_{-1.2\,-0.5}$	$0.942^{+0.004\,+0.002}_{-0.003\,-0.001}$	$0.947^{+0.002\,+0.001}_{-0.002\,-0.001}$
V04545A	$0.86^{+0.05\,+0.03}_{-0.05\,-0.03}$	$1.08^{+0.03\,+0.01}_{-0.03\,-0.01}$	$533.8^{+2.0\,+1.0}_{-1.9\,-1.0}$	$525.7^{+1.2\,+0.4}_{-1.2\,-0.4}$	$0.943^{+0.004\,+0.002}_{-0.003\,-0.002}$	$0.929^{+0.002\,+0.001}_{-0.002\,-0.001}$
V04549A	$1.11^{+0.05\,+0.02}_{-0.05\,-0.02}$	$1.07^{+0.03\,+0.02}_{-0.03\,-0.02}$	$320.9^{+1.4\,+0.4}_{-1.4\,-0.4}$	$322.1^{+0.9\,+0.5}_{-0.9\,-0.5}$	$0.914^{+0.004\,+0.001}_{-0.004\,-0.001}$	$0.917^{+0.003\,+0.002}_{-0.002\,-0.002}$
V04549B	$1.15^{+0.05\,+0.06}_{-0.06\,-0.07}$	$1.31^{+0.03\,+0.04}_{-0.02\,-0.02}$	$268.5^{+1.3\,+1.5}_{-1.1\,-1.3}$	$265.0^{+0.9\,+0.5}_{-0.7\,-0.3}$	$0.931^{+0.004\,+0.005}_{-0.004\,-0.004}$	$0.919^{+0.003\,+0.002}_{-0.002\,-0.001}$
V05261A	$0.90^{+0.05\,+0.02}_{-0.05\,-0.02}$	-	$305.1^{+1.3\,+0.5}_{-1.2\,-0.4}$	-	$0.937^{+0.004\,+0.002}_{-0.004\,-0.001}$	-
V05261B	$1.01^{+0.05\,+0.02}_{-0.06\,-0.03}$	$1.19^{+0.03\,+0.01}_{-0.03\,-0.01}$	$403.7^{+1.7\,+0.9}_{-1.5\,-0.7}$	$398.4^{+1.0\,+0.4}_{-1.0\,-0.4}$	$0.931^{+0.004\,+0.002}_{-0.003\,-0.002}$	$0.919^{+0.002\,+0.001}_{-0.002\,-0.001}$
V05266A	$0.91^{+0.05\,+0.03}_{-0.05\,-0.03}$	$1.02^{+0.03\,+0.01}_{-0.03\,-0.01}$	$349.8^{+1.5\,+0.8}_{-1.5\,-0.9}$	$346.7^{+0.9\,+0.4}_{-0.9\,-0.4}$	$0.932^{+0.004\,+0.002}_{-0.004\,-0.002}$	$0.924^{+0.002\,+0.001}_{-0.002\,-0.001}$
V05266B	$0.91^{+0.05\,+0.02}_{-0.05\,-0.02}$	$1.00^{+0.03\,+0.01}_{-0.03\,-0.01}$	$335.2^{+1.5\,+0.6}_{-1.4\,-0.6}$	$332.8^{+0.9\,+0.3}_{-0.9\,-0.3}$	$0.931^{+0.004\,+0.002}_{-0.004\,-0.002}$	$0.924^{+0.003\,+0.001}_{-0.002\,-0.001}$
V05267A	$1.13^{+0.05\,+0.04}_{-0.05\,-0.04}$	-	$360.7^{+1.5\,+1.0}_{-1.5\,-1.1}$	-	$0.920^{+0.004\,+0.003}_{-0.004\,-0.003}$	-
V05267B	$0.81^{+0.05\,+0.02}_{-0.05\,-0.02}$	$1.09^{+0.03\,+0.01}_{-0.03\,-0.01}$	$403.0^{+1.7\,+0.7}_{-1.5\,-0.6}$	$394.7^{+1.0\,+0.4}_{-1.0\,-0.4}$	$0.945^{+0.004\,+0.002}_{-0.004\,-0.001}$	$0.926^{+0.002\,+0.001}_{-0.002\,-0.001}$
V05268A	$0.96^{+0.05\,+0.02}_{-0.05\,-0.02}$	$1.04^{+0.03\,+0.01}_{-0.03\,-0.01}$	$388.3^{+1.6\,+0.7}_{-1.4\,-0.5}$	$385.9^{+1.0\,+0.4}_{-1.0\,-0.4}$	$0.936^{+0.004\,+0.002}_{-0.003\,-0.001}$	$0.930^{+0.002\,+0.001}_{-0.002\,-0.001}$
V05268B	$0.85^{+0.05\,+0.02}_{-0.06\,-0.02}$	-	$306.0^{+1.4\,+0.6}_{-1.2\,-0.5}$	-	$0.945^{+0.004\,+0.002}_{-0.004\,-0.001}$	-
V05612A	$1.33^{+0.05\,+0.03}_{-0.06\,-0.04}$	$1.44^{+0.03\,+0.01}_{-0.03\,-0.01}$	$362.2^{+1.6\,+1.0}_{-1.4\,-0.8}$	$359.3^{+0.9\,+0.4}_{-0.9\,-0.4}$	$0.908^{+0.004\,+0.002}_{-0.003\,-0.002}$	$0.901^{+0.002\,+0.001}_{-0.002\,-0.001}$
V05612B	$0.89^{+0.05\,+0.02}_{-0.06\,-0.03}$	$0.97^{+0.03\,+0.01}_{-0.03\,-0.01}$	$356.6^{+1.6\,+0.9}_{-1.3\,-0.7}$	$354.4^{+0.9\,+0.3}_{-0.9\,-0.4}$	$0.943^{+0.004\,+0.002}_{-0.004\,-0.002}$	$0.937^{+0.003\,+0.001}_{-0.002\,-0.001}$
V07298B	$0.87^{+0.05\,+0.02}_{-0.05\,-0.02}$	$1.01^{+0.06\,+0.07}_{-0.04\,-0.05}$	$351.0^{+1.5\,+0.6}_{-1.5\,-0.6}$	$347.2^{+1.8\,+1.3}_{-1.7\,-1.2}$	$0.934^{+0.004\,+0.002}_{-0.004\,-0.002}$	$0.924^{+0.005\,+0.003}_{-0.004\,-0.003}$
V07302A	$0.98^{+0.05\,+0.02}_{-0.05\,-0.02}$	$1.12^{+0.05\,+0.06}_{-0.03\,-0.04}$	$299.4^{+1.4\,+0.6}_{-1.3\,-0.6}$	$296.0^{+1.4\,+0.9}_{-1.2\,-0.8}$	$0.923^{+0.004\,+0.002}_{-0.004\,-0.002}$	$0.913^{+0.004\,+0.003}_{-0.004\,-0.002}$
V07302B	$0.86^{+0.05\,+0.02}_{-0.05\,-0.02}$	$1.01^{+0.05\,+0.06}_{-0.03\,-0.04}$	$266.8^{+1.3\,+0.5}_{-1.2\,-0.5}$	$263.2^{+1.3\,+0.9}_{-1.1\,-0.7}$	$0.929^{+0.004\,+0.002}_{-0.004\,-0.002}$	$0.916^{+0.004\,+0.003}_{-0.004\,-0.003}$
V07646A	$1.11^{+0.06\,+0.06}_{-0.03\,-0.03}$	$1.25^{+0.03\,+0.06}_{-0.03\,-0.05}$	$456.7^{+2.0\,+0.8}_{-1.9\,-0.9}$	$452.0^{+1.8\,+1.7}_{-0.9\,-0.8}$	$0.964^{+0.004\,+0.002}_{-0.004\,-0.002}$	$0.954^{+0.004\,+0.004}_{-0.002\,-0.002}$
V07647A	$1.22^{+0.05\,+0.02}_{-0.05\,-0.02}$	$1.41^{+0.05\,+0.06}_{-0.03\,-0.04}$	$312.3^{+1.4\,+0.5}_{-1.3\,-0.5}$	$307.5^{+1.5\,+1.1}_{-1.1\,-0.7}$	$0.909^{+0.004\,+0.001}_{-0.004\,-0.001}$	$0.895^{+0.004\,+0.003}_{-0.003\,-0.002}$
V07647B	$0.75^{+0.05\,+0.02}_{-0.06\,-0.02}$	$1.00^{+0.03\,+0.04}_{-0.03\,-0.04}$	$304.2^{+1.4\,+0.5}_{-1.4\,-0.5}$	$298.0^{+1.0\,+1.0}_{-0.7\,-0.7}$	$0.942^{+0.004\,+0.002}_{-0.004\,-0.002}$	$0.922^{+0.003\,+0.003}_{-0.002\,-0.002}$
V08682A	$0.99^{+0.05\,+0.01}_{-0.06\,-0.02}$	$1.19^{+0.03\,+0.04}_{-0.03\,-0.03}$	$567.7^{+2.1\,+0.8}_{-1.8\,-0.5}$	$560.4^{+1.5\,+1.3}_{-1.2\,-1.0}$	$0.944^{+0.004\,+0.001}_{-0.003\,-0.001}$	$0.932^{+0.002\,+0.002}_{-0.002\,-0.002}$
V08682B	$1.35^{+0.05\,+0.02}_{-0.06\,-0.02}$	$1.50^{+0.03\,+0.04}_{-0.03\,-0.03}$	$242.2^{+1.3\,+0.5}_{-1.3\,-0.5}$	$238.6^{+0.9\,+0.8}_{-0.8\,-0.7}$	$0.883^{+0.005\,+0.002}_{-0.005\,-0.002}$	$0.936^{+0.003\,+0.002}_{-0.002\,-0.002}$
V09374A	$0.91^{+0.05\,+0.03}_{-0.05\,-0.04}$	$1.02^{+0.03\,+0.04}_{-0.03\,-0.03}$	$452.6^{+1.8\,+1.2}_{-1.6\,-1.0}$	$448.9^{+1.2\,+1.1}_{-1.1\,-1.0}$	$0.944^{+0.004\,+0.002}_{-0.003\,-0.002}$	$0.936^{+0.003\,+0.002}_{-0.002\,-0.002}$
V09724A	$0.93^{+0.05\,+0.02}_{-0.05\,-0.02}$	$1.06^{+0.04\,+0.04}_{-0.03\,-0.04}$	$449.8^{+1.8\,+0.7}_{-1.6\,-0.5}$	$445.7^{+1.2\,+1.2}_{-1.1\,-1.1}$	$0.942^{+0.004\,+0.001}_{-0.003\,-0.001}$	$0.934^{+0.003\,+0.002}_{-0.002\,-0.002}$
V09372A	$0.88^{+0.05\,+0.02}_{-0.05\,-0.02}$	$1.05^{+0.03\,+0.04}_{-0.03\,-0.03}$	$700.3^{+2.4\,+1.0}_{-2.1\,-0.7}$	$692.6^{+1.7\,+1.3}_{-1.5\,-1.3}$	$0.955^{+0.003\,+0.001}_{-0.003\,-0.001}$	$0.944^{+0.002\,+0.002}_{-0.002\,-0.002}$

E

TRANSITION LAYER MODEL APPLIED TO THE ^{228}Th ENERGY SPECTRUM

The presence of a non-null transition layer (TL) distort the shape of background source and, in particular, of the $2\nu\beta\beta$ distribution that can potentially mimic the presence of new-physics phenomena. An alternative way to extract the TL from the one reported in Chap.7 via ^{39}Ar analysis, is a count ratio method similar to that used for the FCCD determination. The effect of the TL in the characterization energy spectrum appears to be strong in the lower energy tail of γ peaks. FEP events are shifted out of the peak to lower energies since the reconstructed energy is smaller when interacting in the TL. The high-statistics 2615 keV line from ^{208}Tl source is suitable to determine the size of the transition region. Fig.E.1(left) shows the overlap of the data spectrum and several MC spectra with different DLF, assuming a linear model for the TL. The DLF is the dead layer fraction with respect to the entire FCCD. As the DLF decrease (so the TL grows), more events of the peak are counted at lower energies in the tail region. A count ratio analysis is performed taking into account the counts in two different regions. The region $[2500, 2600]$ keV before the peak is affected by the TL size while the region around the peak $[2610, 2620]$ keV is not. The ratio of the counts in the regions is computed for the observed energy spectrum and for simulated energy spectra obtained varying the DLF from 0 to 0.9 in steps of 0.1. The FCCD is fixed at the best value estimated before by the ^{241}Am analysis. The uncertainty on the count ratio accounts only for statistical uncertainty stemming from the error propagation of the Poisson uncertainties on the two region counts. Since the count ratio is observed to change linearly with respect to the dead-layer fraction, a linear fit is performed on the simulated values. The best DLF value is found by comparing the observable from the data with the simulated interpolation. Fig. E.1(right) graphically shows the determination of the best DLF. The final comparison of the data spectrum and the simulated spectrum obtained with the best FCCD determined by the ^{241}Am analysis and the best DLF obtained with the count ratio described above is plotted in Fig.E.2. The non-null TL allows a better match between the two spectra. More sophisticated CCE functions are suggested to be applied to better reproduce the observed energy spectrum.

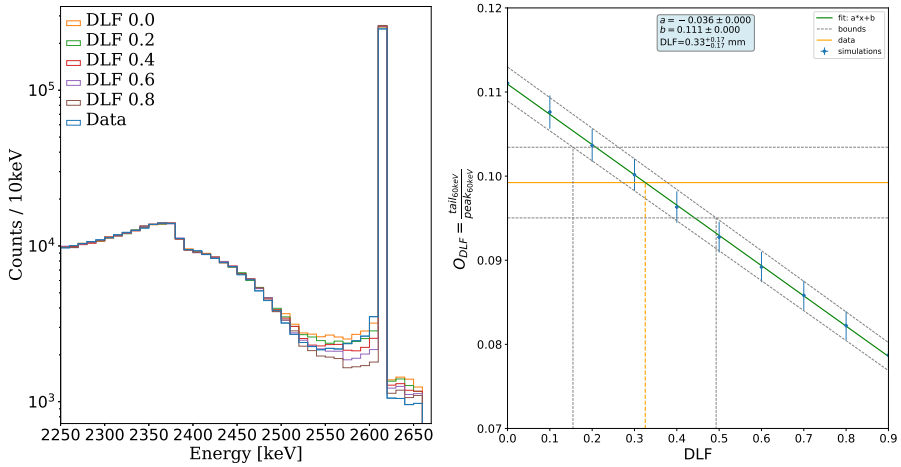

Figure E.1: Example of the optimization of the DLF. Left: effect of the DLF on the tail of the ^{208}Tl peak at 2615 keV. Right: Extraction of the best DLF, in orange, by the count ratio analysis; the statistical uncertainties are indicated with dotted gray lines.

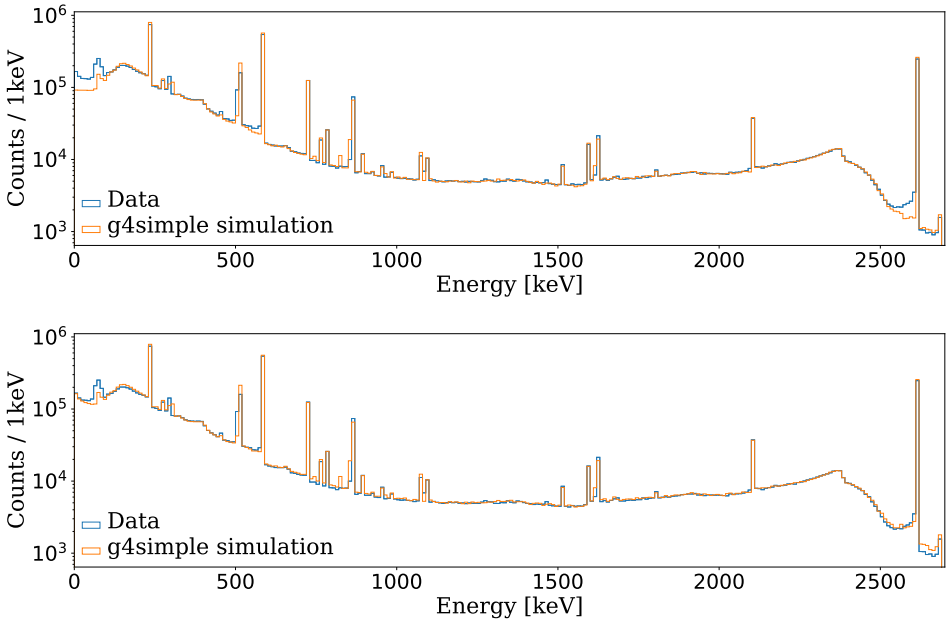

Figure E.2: Comparison between the data energy spectrum and the simulated energy spectrum. Top: the simulated energy spectrum presents the best FCCD extracted from previous analysis with null transition layer. Bottom: the simulated energy spectrum presents the FCCD fixed at the same value and the TL is the one estimated by this analysis.

F

MISCELLANEA

F.1 MASS ATTENUATION COEFFICIENT AND ATTENUATION LENGTH

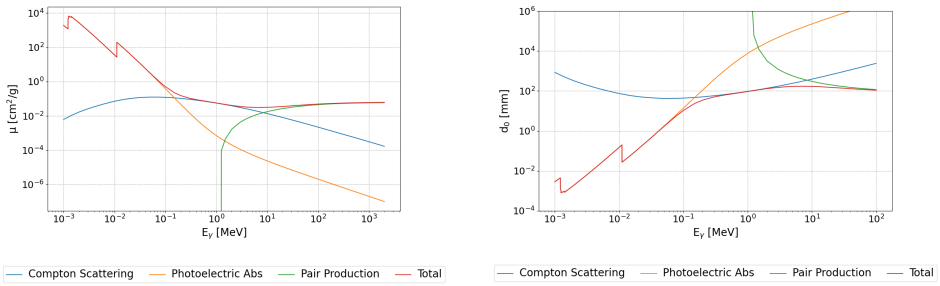

Figure F.1: Left: γ-ray mass attenuation μ in germanium as a function of the energy and contribution of different interaction processes. Right: Attenuation length d_0 in germanium as a function of the energy for different interaction processes. Data from [121].

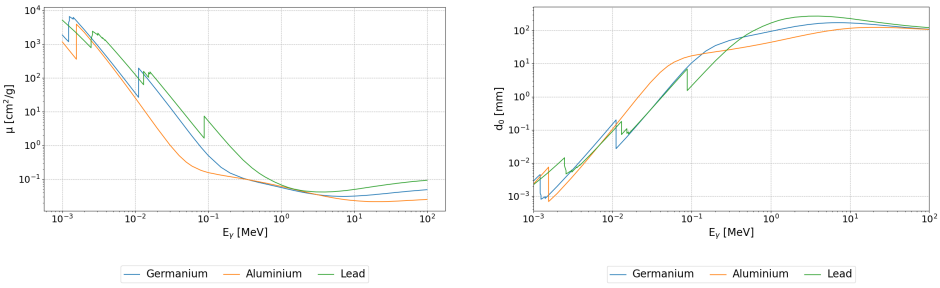

Figure F.2: Left: total mass attenuation μ for γ-rays as a function of the energy in different materials. Right: attenuation length d_0 as a function of the energy of different materials in standard densities. Data from [121].

F.2 DETECTOR DIMENSIONS IN GERDA PHASE II$^+$

Table F.1: Summary of detector names, channel numbers, heights and radii of the cylinder (H, R), heights and internal and external radii of the groove (h_g, r_{g_o}, r_{g_i}), and heights and radii of the bore-wall (h_w, r_w) for BEGe, Coax and ICPC detectors used during the GERDA Phase II$^+$. In the table, horizontal lines are used to distinguish detectors belonging to different strings.

Detector	Channel	H [mm]	R [mm]	h_g [mm]	r_{g_o} [mm]	r_{g_i} [mm]	h_w [mm]	r_w [mm]
GD91A	0	31.18	35.27	2	10.5	7.5	0.0	0.0
GD35B	1	32.1	38.16	2	10.5	7.5	0.0	0.0
GD02B	2	28.66	35.51	2	10.5	7.5	0.0	0.0
GD00B	3	29.46	36.98	2	10.5	7.5	0.0	0.0
GD61A	4	33.57	36.74	2	10.5	7.5	0.0	0.0
GD89B	5	24.85	38.02	2	10.5	7.5	0.0	0.0
GD91C	7	29.79	34.95	2	10.5	7.5	0.0	0.0
RG1	9	84	38.25	2	20	17	73	6.75
ANG3	10	93	39	2	20	17	83	7.5
GD02A	11	27.55	35.23	2	10.5	7.5	0.0	0.0
GD32B	12	32.16	35.95	2	10.5	7.5	0.0	0.0
GD32A	13	24.9	33.13	2	10.5	7.5	0.0	0.0
GD32C	14	33.15	35.99	2	10.5	7.5	0.0	0.0
GD89C	15	24.75	37.35	2	10.5	7.5	0.0	0.0
GD61C	16	26.45	37.28	2	10.5	7.5	0.0	0.0
GD76B	17	26.29	29.14	2	10.5	7.5	0.0	0.0
GD00C	18	33.64	37.76	2	10.5	7.5	0.0	0.0
GD35C	19	26.32	37.42	2	10.5	7.5	0.0	0.0
GD76C	20	33.18	37.92	2	10.5	7.5	0.0	0.0
GD89D	21	22.89	36.72	2	10.5	7.5	0.0	0.0
GD00D	22	32.28	38.2	2	10.5	7.5	0.0	0.0
GD79C	23	30.22	39.48	2	10.5	7.5	0.0	0.0
GD35A	24	35.34	36.77	2	10.5	7.5	0.0	0.0
GD91B	25	30.26	35.29	2	10.5	7.5	0.0	0.0
GD61B	26	30.21	37.98	2	10.5	7.5	0.0	0.0
ANG2	27	107	40	2	18	15	94	7
RG2	28	84	38.25	2	20	17	70	6.5
ANG4	29	100	37.5	2	18	15	89	7
GD00A	30	26.41	35.16	2	10.5	7.5	0.0	0.0
GD02C	31	32.59	37.44	2	10.5	7.5	0.0	0.0
GD79B	32	29.04	38.42	2	10.5	7.5	0.0	0.0
GD91D	33	31.88	35.65	2	10.5	7.5	0.0	0.0
GD32D	34	32.12	36.15	2	10.5	7.5	0.0	0.0
GD89A	35	28.34	34.31	2	10.5	7.5	0.0	0.0
IC50B	37	85.4	36.3	2	13.5	9.5	53.9	5.25
IC48A	38	80.4	37.3	2	13	10	47.4	5.25
IC50A	39	80.4	37.35	2	13.5	9.5	40.0	5.25
IC74A	40	82.3	38.3	2	13.5	9.5	52.4	5.25

F.3 EXPOSURE IN GERDA PHASE II$^+$

Table F.2: Single-detector exposures corresponding to the selected Phase II$^+$ data. Detector GD02D is not fully depleted and is therefore excluded from the analysis [93].

Detector	Exp. (kg·yr)	Detector	Exp. (kg·yr)	Detector	Exp. (kg·yr)
GD00A	0.58	GD61A	0.86	ANG2	2.75
GD00B	0.79	GD61B	0.83	ANG3	2.71
GD00C	0.96	GD61C	0.74	ANG4	2.79
GD00D	0.95	GD76B	0.45	ANG5	-
GD02A	0.64	GD76C	0.97	RG1	2.39
GD02B	0.73	GD79B	0.48	RG2	2.54
GD02C	0.93	GD79C	0.95	IC48A	2.25
GD02D	-	GD89A	0.62	IC48B	-
GD32A	0.54	GD89B	0.73	IC50A	1.83
GD32B	0.81	GD89C	0.70	IC50B	2.27
GD32C	0.87	GD89D	0.62	IC74A	2.43
GD32D	0.83	GD91A	0.74		
GD35A	0.90	GD91B	0.73		
GD35B	0.95	GD91C	0.74		
GD35C	0.74	GD91D	0.81	Total	44.1

G

PARAMETER DISTRIBUTIONS AND CRITICAL THRESHOLDS OF ^{39}Ar ANALYSIS

The effects of each systematics in the ^{39}Ar analysis (Sec.7.6.2) – the background model, the transition layer model, and the energy scale – are visible in the distributions of FCCD, DLF, ^{39}Ar activity, and goodness of fit. The *pdf* distortions from the background model are shown in Fig.G.1. They feature a distinct bias on the FCCD (and activity) and DLF mean value estimations. Furthermore, the *p*-value distribution results deformed due to the additional background components added in the toys but not in the MC grid *pdf* used in the analysis. The effects of the transition layer model on the parameter distributions are illustrated in Fig.G.2. They produce a distortion, by enlarging especially the FCCD and activity distribution. Fig.G.3 shows the effects of the energy scale, and a large effect from ± 1 keV energy shift is clearly visible on the width of the FCCD and activity distributions.

The results of the critical thresholds to compute the statistical and systematic uncertainties of the ^{39}Ar analysis (Sec.7.6.2) parameters are reported below. The two following series of plots represents the critical thresholds of statistical (blue line) and statistical+systematic (green line) for each detector of GERDA Phase II^{+} for the FCCD and DLF parameters, respectively. While the statistical function is around the expected value of 2.3 – indicating the critical threshold of the χ^2 distribution with 2 *dof* at 68% probability – for every detector, the green line differs around a range of $[9, 22]$ among the detectors. The intersection of the critical threshold with the profile likelihood of data gives the related uncertainties of the two parameters. In the regions near the borders, the lines cannot intersect properly (`channel 9` in FCCD plot, and `channel 27`, `channel 38` in DLF plots), and a symmetrical systematic is taken from the only intersection point obtained.

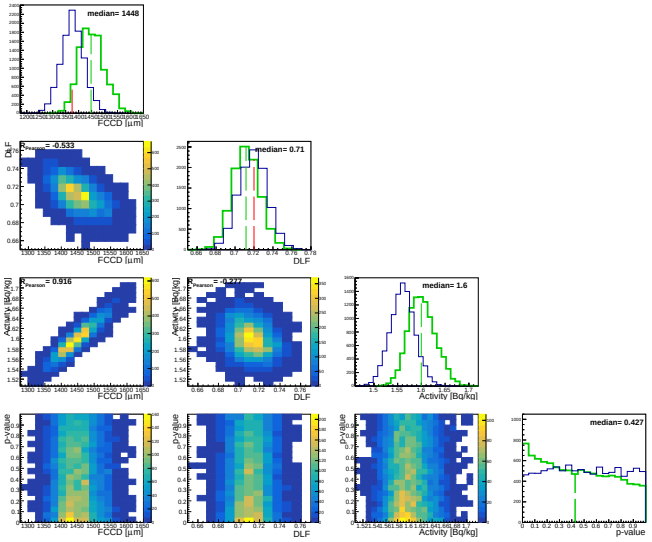

Figure G.1: Effects of the background sources, applied as additional component in the toy experiments production, on the fit parameters. Correlations between the fit parameters and the distributions (on the diagonal) of the reconstructed parameters are shown. From the right: FCCD, DLF, activity, *p*-value.

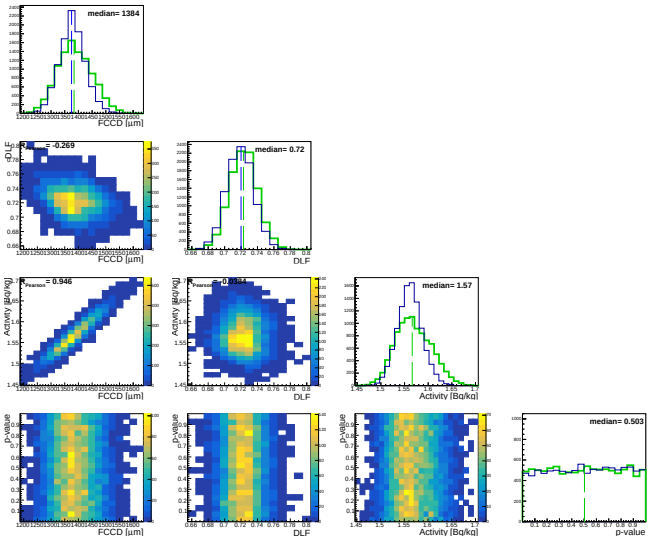

Figure G.2: Effects of the transition layer model, applied as a global distortion in the toy experiment production, on the fit parameters. Correlations between the fit parameters and the distributions (on the diagonal) of the reconstructed parameters are shown. From the right: FCCD, DLF, activity, *p*-value.

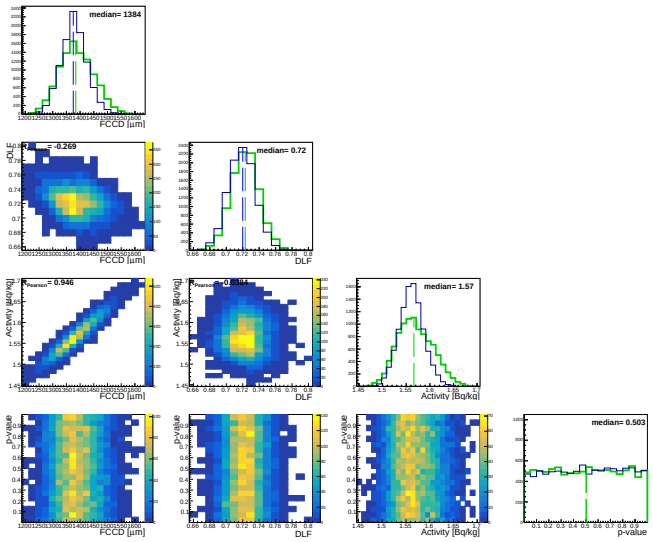

Figure G.3: Effects of the energy scale, applied as a global distortion in the toy production, on the fit parameters. Correlations between the fit parameters and the distributions (on the diagonal) of the reconstructed parameters are shown. From the right: FCCD, DLF, activity, p-value.

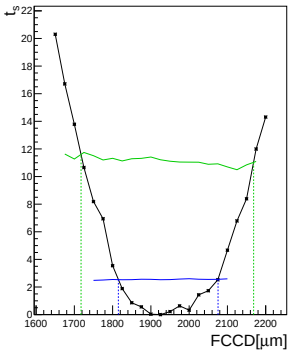

ch0

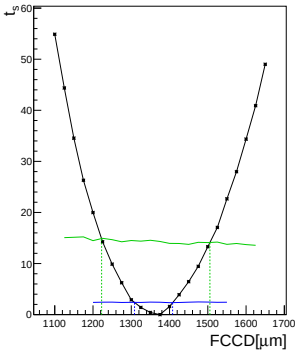

ch1

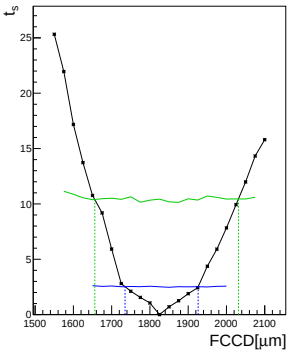

ch2

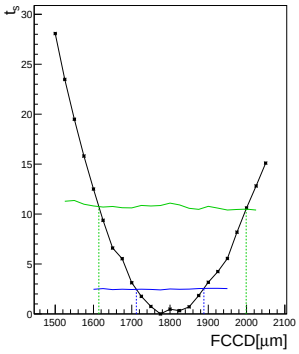

ch3

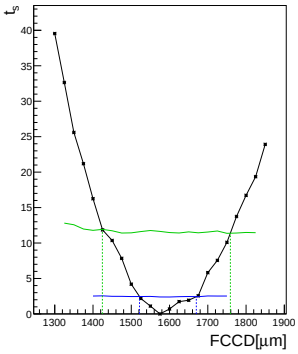

ch4

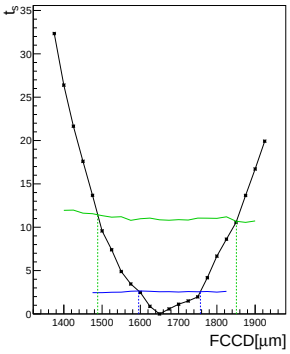

ch5

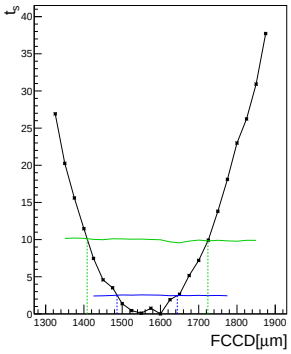

ch7

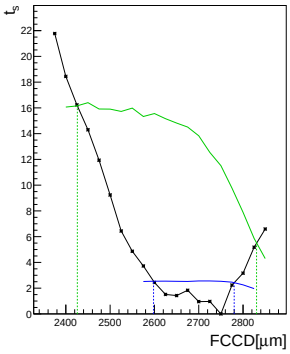

ch9

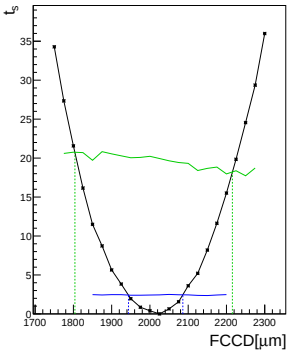

ch10

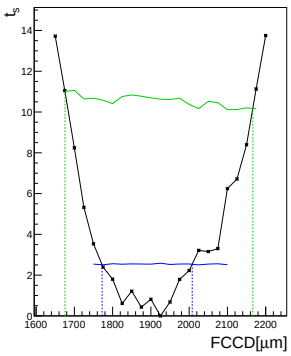

ch11

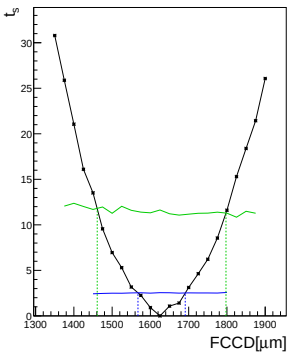

ch12

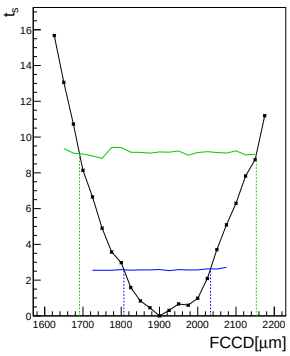

ch13

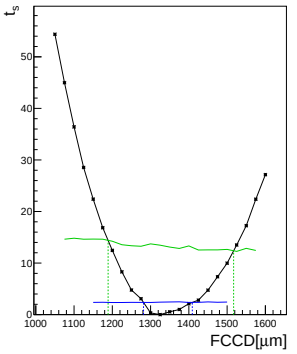

ch14

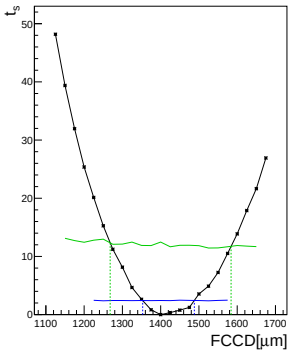

ch15

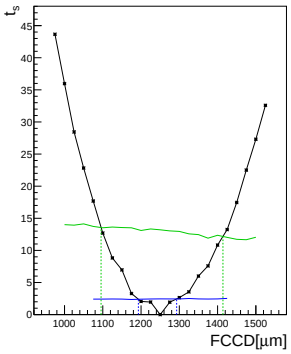

ch16

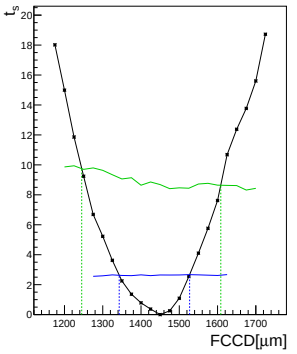

ch17

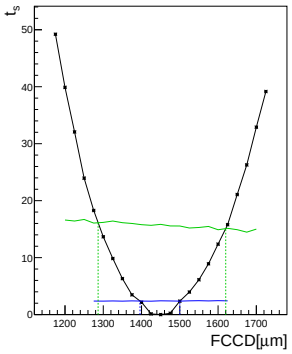

ch18

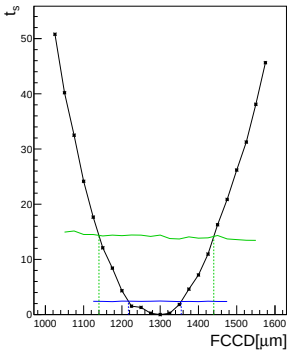

ch19

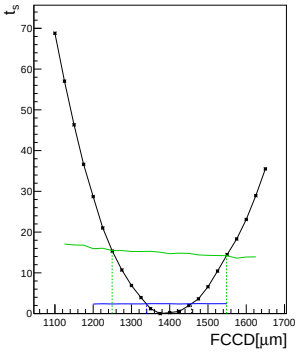

ch20

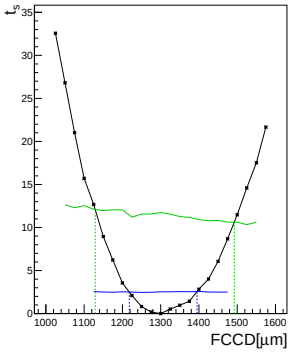

ch21

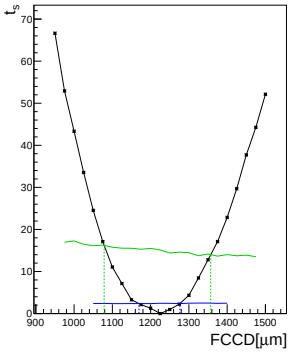

ch22

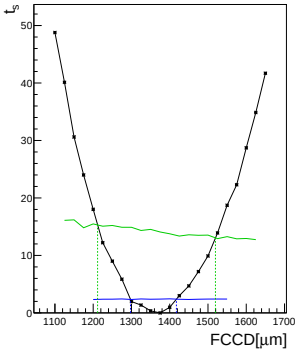

ch23

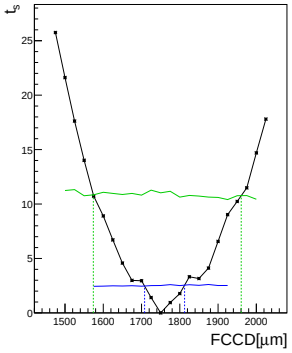

ch24

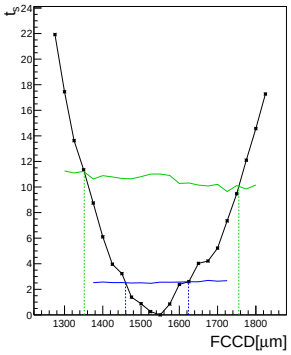

ch25

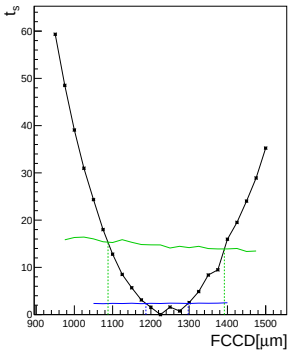

ch26

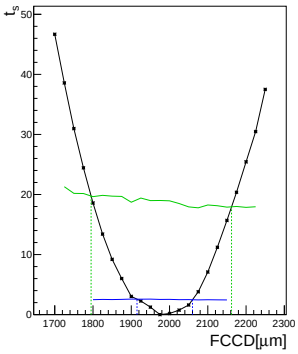

ch27

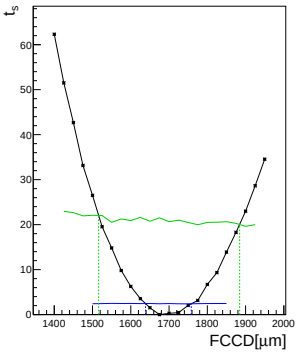

ch28

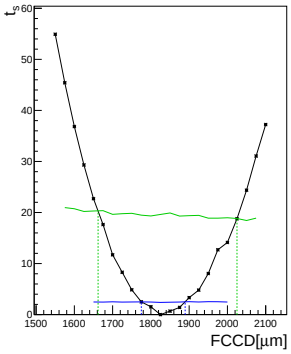

ch29

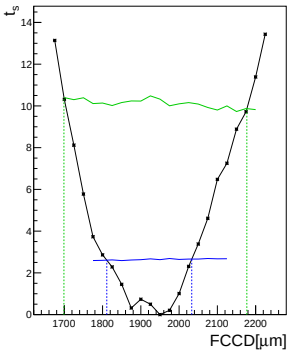

ch30

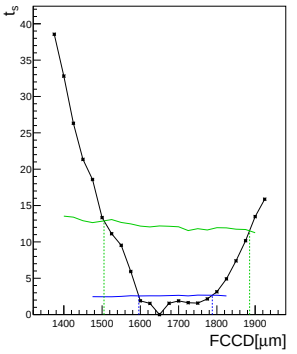

ch31

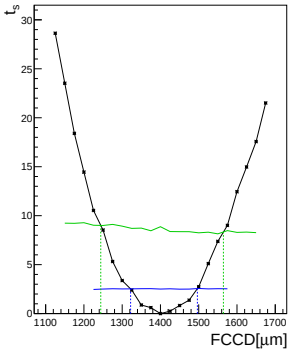

ch32

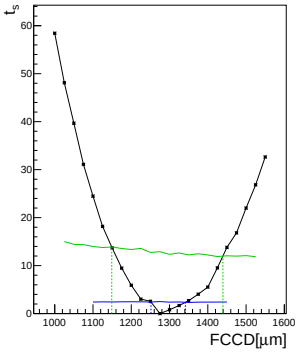

ch33

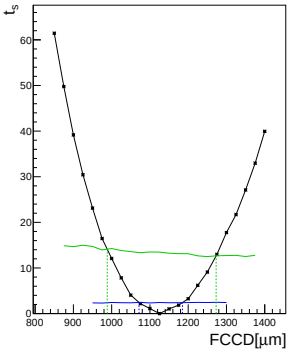

ch34

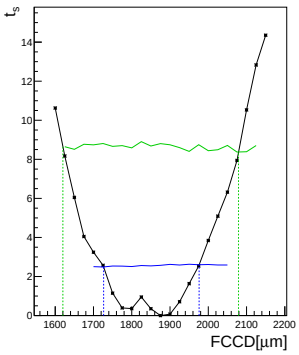

ch35

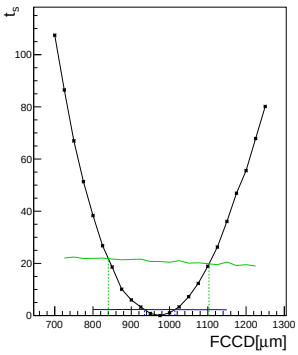

ch37

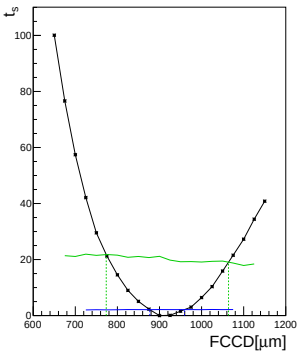

ch38

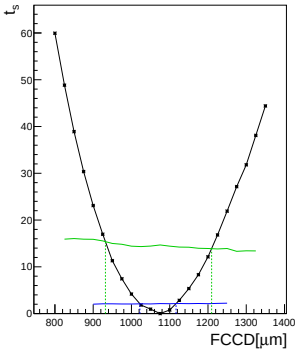
t_s
60
50
40
30
20
10
0
800
900
1000
1100
1200
1300
1400
FCCD[μm]

ch39

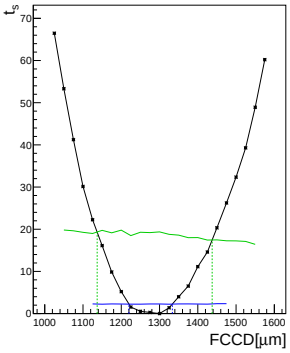
t_s
70
60
50
40
30
20
10
0
1000
1100
1200
1300
1400
1500
1600
FCCD[μm]

ch40

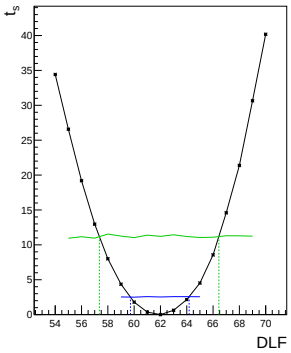

ch0

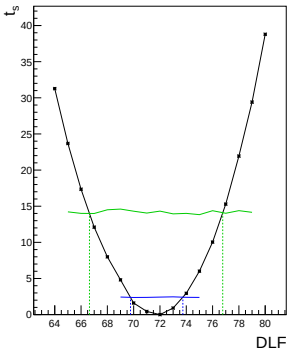

ch1

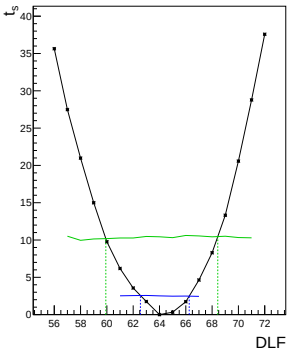

ch2

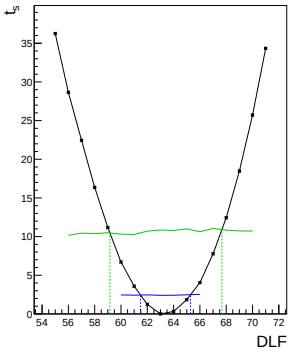

ch3

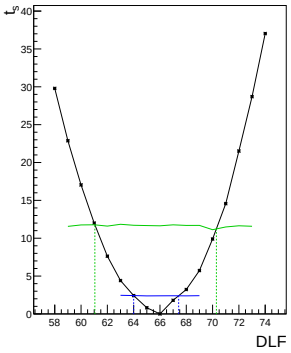

ch4

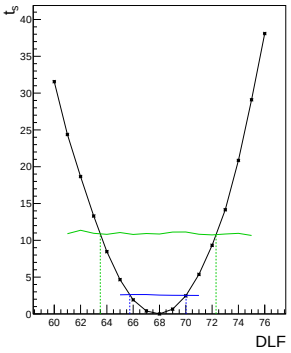

ch5

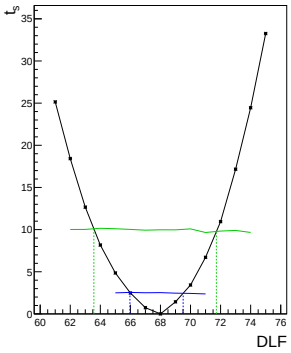

ch7

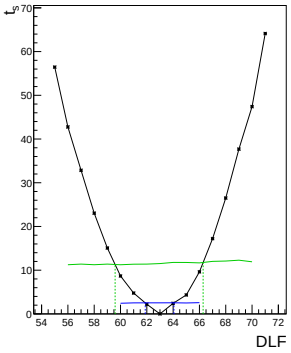

ch9

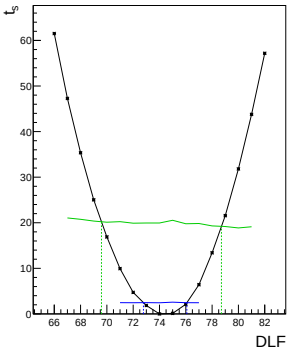

ch10

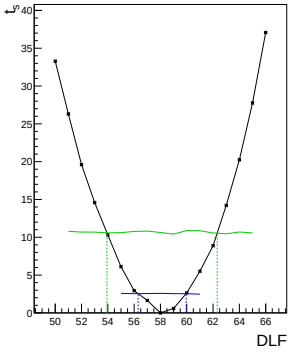

ch11

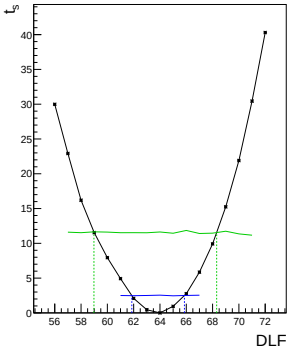

ch12

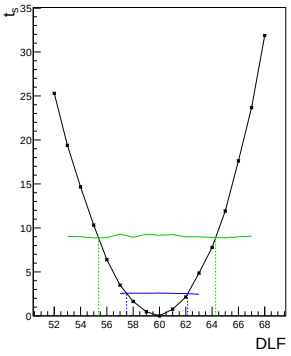

ch13

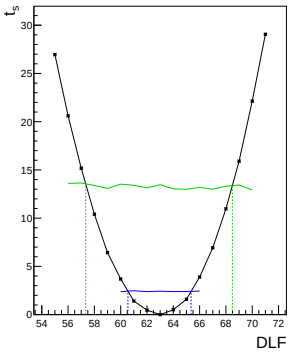

ch14

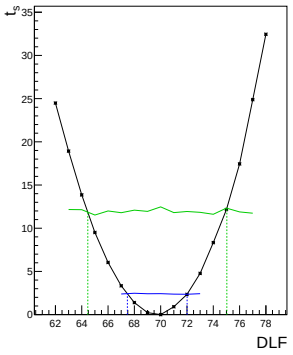

ch15

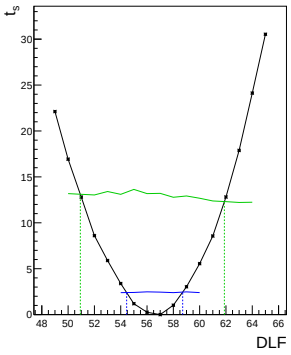

ch16

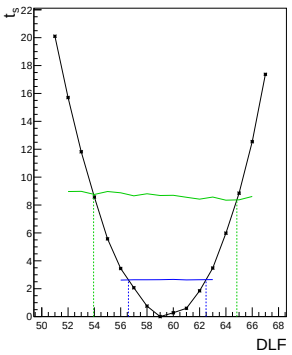

ch17

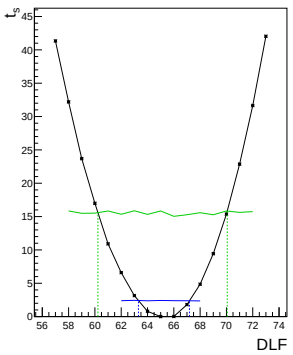

ch18

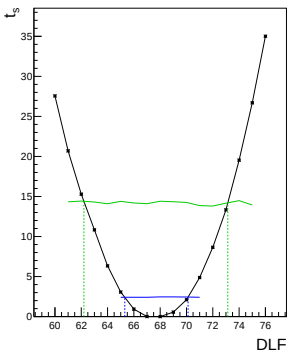

ch19

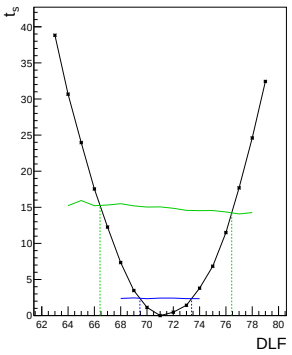

ch20

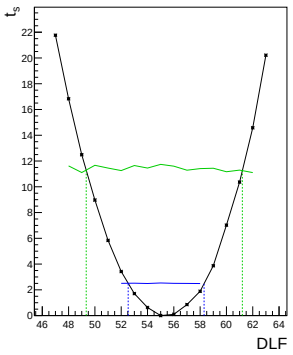

ch21

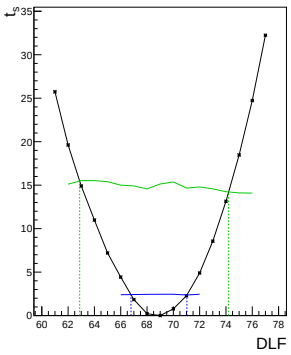

ch22

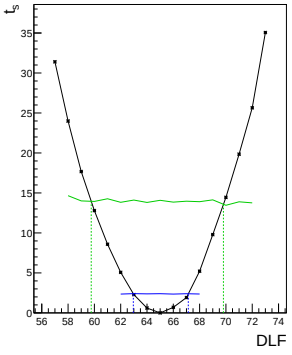

ch23

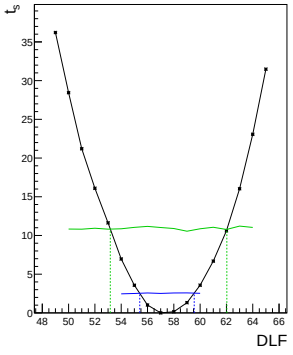

ch24

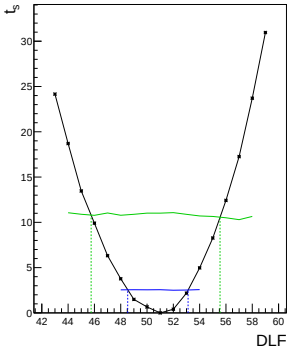

ch25

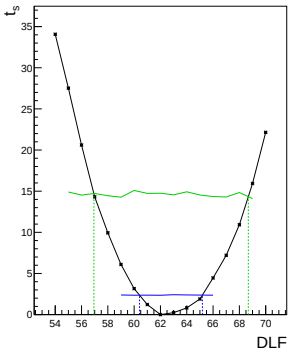

ch26

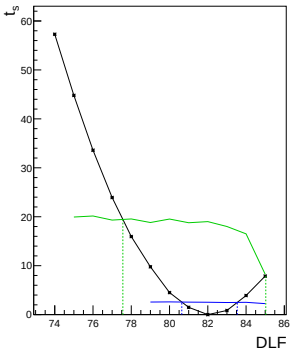

ch27

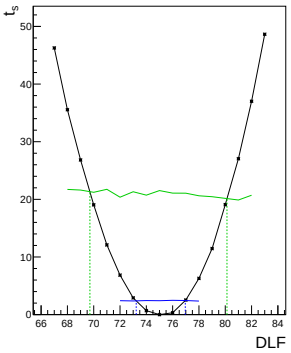

ch28

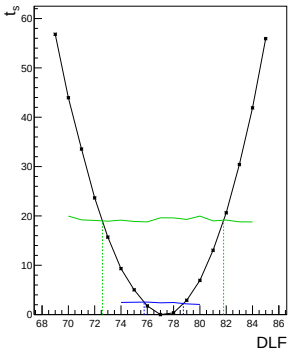

ch29

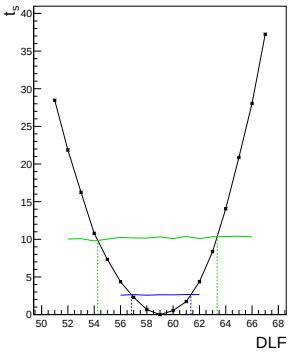

ch30

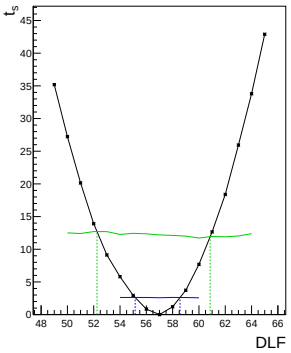

ch31

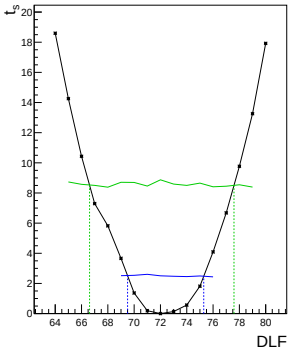

ch32

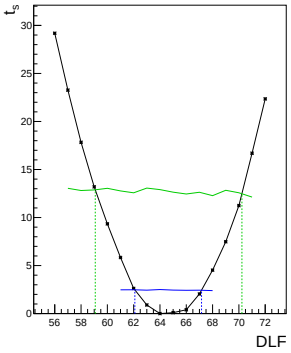

ch33

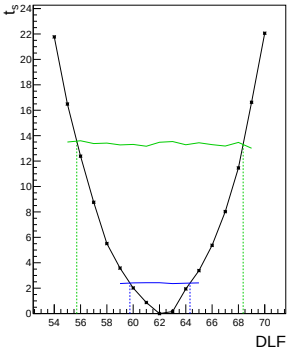

ch34

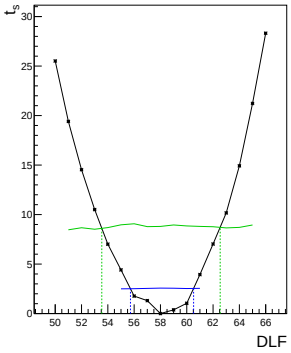

ch35

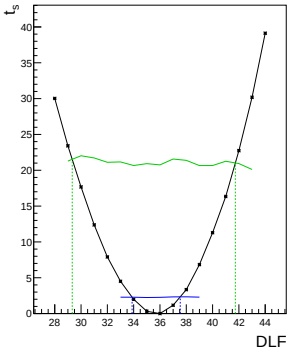

ch37

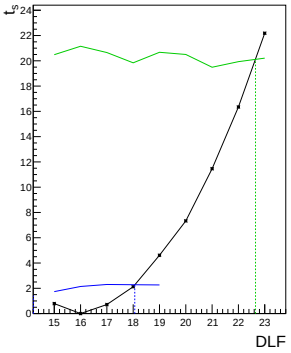

ch38

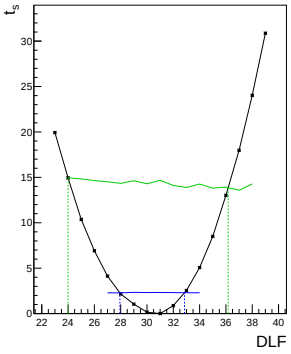

ch39

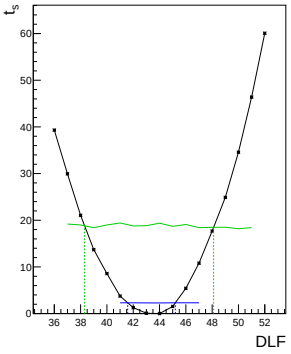

ch40

H

^{60}Co MEASUREMENT OF BEGES FOR THE FCCD DETERMINATION

An additional radioactive source that can be used for the FCCD determination of BEGe is the uncollimated ^{60}Co source (*co_HS5*), which irradiates the detector at a distance of 198 mm from the top side of the BEGe set in the HADES facility. The FCCD obtained from these measurements are used for the comparison with the values got from the ^{241}Am and ^{133}Ba second measurement campaign (Ch.6) and from ^{39}Ar analysis (Ch.7). The source has exactly the same geometry and material of the ^{133}Ba source shown in Fig.A.5. Fig.H.1 shows the typical energy spectrum from 1 h data taking (left) and the related A/E spectrum as a function of the energy. In both plots the two main peaks at 1173.2 keV and 1332.5 keV are clearly visible.

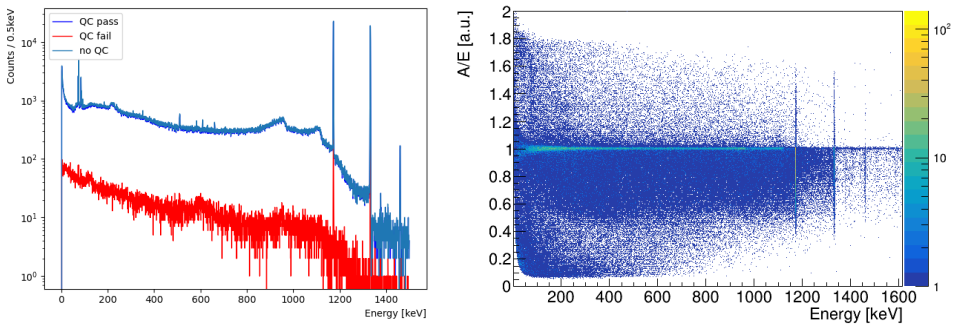

Figure H.1: Left: observed energy spectrum from a BEGe irradiated by the ^{60}Co source placed at the top of the detector. Right: A/E data as function of the energy; it clearly shows the two SEP events used in the analysis (see text).

The ^{60}Co method used for the FCCD determination takes into account the two prominent γ-lines for a direct comparison with the MC simulations. It implies that the observable $O_{^{60}Co}$ is not a count ratio as done for the ^{133}Ba and ^{241}Am methods, but the counts C_{peak} under the peaks are separately compared between the data and simulation:

$$O_{^{60}Co_1} = C_{1173.2keV} \tag{H.1}$$

$$O_{^{60}Co_2} = C_{1332.5keV} \tag{H.2}$$

The emission probabilities are $p_{1173.2\ keV} = 99.85(3)\%$ and $p_{1332.5keV} = 99.9826(6)\%$ [77]. For a correct comparison between MCs and data, a proper knowledge of the source activity is required since the observable of the ^{60}Co measurement is not a count ratio. The activity is listed in Tab.A.2 with the related reference date. At the time of the second measurement, the ^{60}Co activity is estimated to be lowered to 2.76 kBq. Unlike the ^{241}Am and ^{133}Ba

sources, ^{60}Co is a volume probe source. Fig.H.2 shows the distributions of the events depositing the energy in the detector volume for the γ-lines at 1173 keV and 1332 keV. In the same way, they spread throughout the full detector volume, and it implies that the FCCD effects are significantly reduced on the ^{60}Co γ-lines intensity with respect to those observed in ^{241}Am and ^{133}Ba peaks (see Fig.H.3).

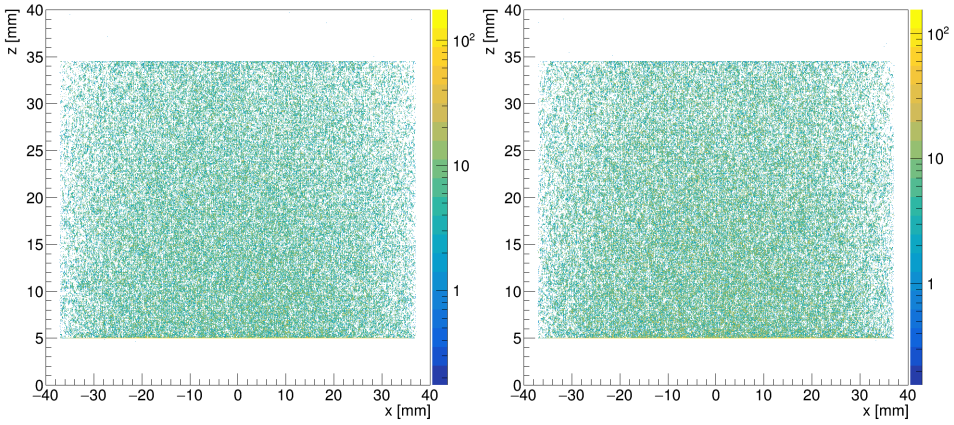

Figure H.2: Scatterplot in the x-z plane of hits from 1173 keV (left) and 1332.5 keV (right) γ-lines of the ^{60}Co source placed at the top of the detector.

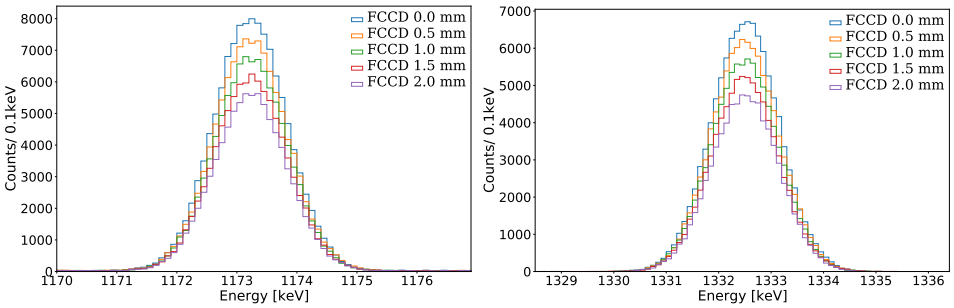

Figure H.3: Variation of the ^{60}Co peaks for different FCCD values. They are less affected than the ^{133}Ba and ^{241}Am since they are at higher energy and can reach the entire volume of the detector even without interacting nearby the surfaces.

Data and simulations need to be prepared before making the analysis, which is similar to that used for the ^{133}Ba and ^{241}Am analysis. The data is firstly calibrated comparing the mean values obtained from the fitting of the ^{60}Co peaks and their nominal values. The MCs are generated simulating the entire ^{60}Co decay and the hits are smeared by a Gaussian function whose parameters are taken from the energy resolution of the detector. The simulations are then post-processed setting different values of the FCCD thickness, in a range of $[0, 2]$ mm with a step of 0.1 mm. To determine the peak counts in Eq.H.1, the observed and simulated peaks are fitted with a Gaussian function and a Step function. Fig.H.4 shows the fit on the data

for the detector GD32B. The counts are computed by the integral of the Gaussian component of the fit within 3σ.

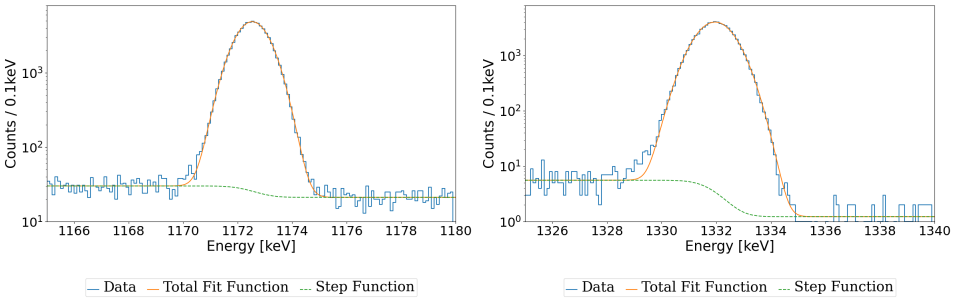

Figure H.4: Example of fit of the observed γ peaks at 1173 keV (left) and 1332 keV (right). The total function is given by the combination of a Gaussian function and a Step function.

Finally, the observables $O_{^{60}Co_1}$ and $O_{^{60}Co_2}$ are plotted as a function of the FCCD values and are fitted by an exponential function. An alternative fit function that takes into account the volume effect (cubic function) has been tried but no difference in the finals results has been observed. The intersection between the data count and the simulation function returns the estimation of the FCCD value and its uncertainty (dashed lines) for the detector. This process is repeated for both γlines. For instance, Fig.H.5 shows the comparison of the counts under the peak at 1173 keV (top) and the comparison of the energy spectra of data and simulation at the best FCCD (bottom).

Beyond the same systematics found already for ^{133}Ba and ^{241}Am, additional components are required, to be added in quadrature, that are not negligible since the ^{60}Co analysis is not based on a count-ratio analysis. They are related to the distance of the source and the detector from the cryostat, the source activity, the detector dimension, and the dead time of a measurement. However, since this analysis is performed only to compare the results with those obtained previously by the other radioactive sources and the ^{39}Ar analysis, only the statistical uncertainties (indicated with dashed lines in Fig.H.5(top)) are recorded due to different systematics uncertainties among the results.

The ^{60}Co results from the two different γ-lines are practically the same. The final FCCD value is computed from the weighted average of the estimations from the two peaks. The final results for the BEGes of the second measurement are listed in Tab.H. The detector GD76C has some issue with the HV estimation of the data and the FCCD estimation is not allowed. The detector GD35A has some issue in the simulation process. The comparison of these values with those obtained from the ^{133}Ba and ^{241}Am sources and the ^{39}Ar analysis can be found in Sec.7.6.3.

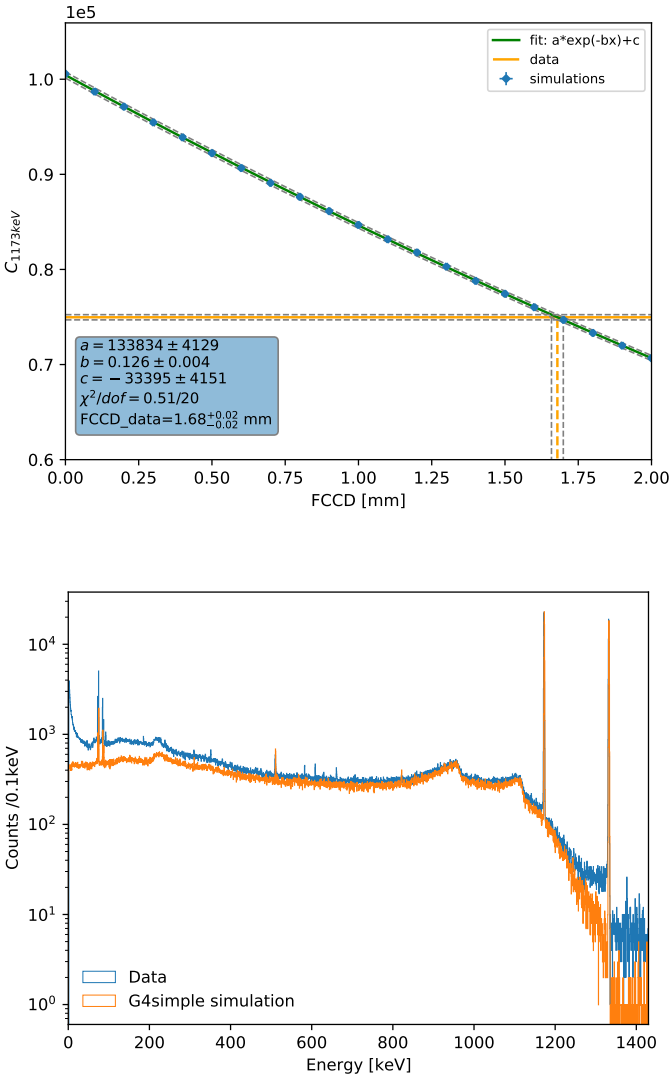

Figure H.5: Top: peak count as a function of simulated FCCD (see text). Bottom: comparison of the observed and simulated (at the best FCCD) energy spectra.

BEGe	^{60}Co FCCD [mm]
GD35B	1.63 ± 0.02
GD00D	1.43 ± 0.01
GD02C	1.66 ± 0.02
GD61C	1.46 ± 0.02
GD00B	2.04 ± 0.01
GD32B	1.77 ± 0.03
GD91B	1.77 ± 0.03

Table H.1: FCCD results from the ^{60}Co source without the application of QC. They derive from the weighted mean of the results obtained from the two peak counts. The uncertainties are only statistical.

ACRONYMS

$0\nu\beta\beta$	neutrinoless double beta decay
$2\nu\beta\beta$	two-neutrino double beta decay
ANN	artificial neural network
AV	active volume
BEGe	Broad Energy Germanium
BI	background index
C.I.	confidence interval
CCE	charge collection efficiency
CP	charge conjugation parity
DAQ	data acquisition
DEP	double escape peak
DL	dead layer
DLF	dead layer fraction
DLT	dead layer thickness
DSP	digital signal processing
FADC	fast analog-to-digital converter
FCCD	full charge collection depth
FEP	full energy peak
FWHM	full width at half maximum
GELATIO	GErda LAyouT for Input/Output
GERDA	GERmanium Detector Array
HADES	High Activity Disposal Experimental Site
HDPE	high-density polyethylene
HEROICA	Hades Experimental Research Of Intrinsic Crystal Appliances
HPGe	High Purity Germanium
HV	high voltage

INFN Istituto Nazionale di Fisica Nucleare

LAr liquid argon

LEGEND Large Enriched Germanium Experiment for Neutrinoless double beta Decay

LNGS Laboratori Nazionali del Gran Sasso

MC Monte Carlo

MGDO Majorana-Gerda Data Object

MJD Majorana Demonstrator

MSE multi-site event

NME nuclear matrix element

pdf probability density function

PEN polyethylene naphthalate

PMT photomultiplier tube

PPC P-type Point Contact

PSD pulse shape discrimination

ROI region of interest

RT room temperature

SEP single escape peak

SiPM silicon photomultipliers

SM Standard Model

SSE single site event

TL transition layer

TLT transition layer thickness

TPB tetraphenyl butadiene

TPC time projection chamber

UGLAr underground-sourced liquid argon

BIBLIOGRAPHY

[1] R. L. Workman et al. "Review of Particle Physics." *PTEP* (2022). DOI: 10.1093/ptep/ptac097.

[2] J.Schwinger. "The theory of quantized fields. I." *Phys. Rev.* 82 (1951). DOI: 10.1103/PhysRev.82.914.

[3] E. C. Sudarshan et al. "Chirality invariance and the universal Fermi interaction." *Phys. Rev.* 109.5 (1958). DOI: 10.1103/PhysRev.109.1860.2.

[4] R. P. Feynman et al. "Theory of the fermi interaction." *Phys. Rev.* 109.1 (1958). DOI: 10.1103/PhysRev.109.193.

[5] M. Goldhaber et al. "Helicity of neutrinos." *Phys. Rev.* 109.3 (1958). DOI: 10.1103/PhysRev.109.1015.

[6] C. L. Cowan et al. "Detection of the Free Neutrino: a Confirmation." *Science* 124.3212 (1956). DOI: 10.1126/science.124.3212.103.

[7] B. Pontecorvo. "The Small Probability of the Processes $\mu \longrightarrow e + \gamma$, $\mu \longrightarrow e + e + e$ and Neutral Currents in Weak Interactions." *JETP* 16.4 (1963).

[8] G. Danby et al. "Observation of High-Energy Neutrino Reactions and the Existence of Two Kinds of Neutrinos." *Phys. Rev.* 9.1 (1962). DOI: 10.1103/PhysRevLett.9.36.

[9] K. Kodama et al. "Observation of tau neutrino interactions." *Phys. Lett. B* 504.3 (2001). DOI: 10.1016/S0370-2693(01)00307-0.

[10] R. Davis et al. "Search for Neutrinos from the Sun." *Phys. Rev. Lett.* 20.21 (1968). DOI: 10.1103/PhysRevLett.20.1205.

[11] K. Abe et al. "Atmospheric neutrino oscillation analysis with external constraints in Super-Kamiokande I-IV." *Phys. Rev. D* 97.7 (2018). DOI: 10.1103/PhysRevD.97.072001.

[12] K. Eguchi et al. "First Results from KamLAND: Evidence for Reactor Antineutrino Disappearance." *Phys. Rev. Lett.* 90.2 (2003). DOI: 10.1103/PhysRevLett.90.021802.

[13] K. Hoepfner. "Results from the CHORUS neutrino oscillation experiment." *Nucl. Phys. B* 65.1-3 (1998). DOI: 10.1016/S0920-5632(97)00996-1.

[14] I. Esteban et al. "Global analysis of three-flavour neutrino oscillations: synergies and tensions in the determination of θ_{23}, δ_{CP}, and the mass ordering." *J. High Energy Phys.* 2019.1 (2018). DOI: 10.1007/JHEP01(2019)106.

[15] B. Abi et al. "Long-baseline neutrino oscillation physics potential of the DUNE experiment." *Eur. Phys. J. C* 80.10 (2020). DOI: 10.1140/epjc/s10052-020-08456-z.

[16] K. Abe et al. "Physics potential of a long-baseline neutrino oscillation experiment using a J-PARC neutrino beam and Hyper-Kamiokande." *PTEP* 2015.5 (2015). DOI: 10.1093/ptep/ptv061.

[17] M. Duerr et al. "On the Quantitative Impact of the Schechter-Valle Theorem." *J. High Energy Phys.* 2011.91 (2011). DOI: 10.1007/JHEP06(2011)091.

[18] W. Rodejohann. "Neutrinoless double beta decay and neutrino physics." *J. Phys. G* 39 (2012). DOI: 10.1088/0954-3899/39/12/124008.

[19] J. Kotila et al. "Phase space factors for double-β decay." *Phys. Rev. C* 85.3 (2012). DOI: 10.1103/PhysRevC.85.034316.

[20] S. Stoica et al. "New Calculations for Phase Space Factors Involved in Double Beta Decay." *Phys. Rev. C* 88.3 (2013). DOI: 10.1103/PhysRevC.88.037303.

[21] J. Engel et al. "Status and Future of Nuclear Matrix Elements for Neutrinoless Double-Beta Decay: A Review." *Rep. Prog. Phys* 80.4 (2016). DOI: 10.1088/1361-6633/aa5bc5.

[22] M. Fukugita et al. "Barygenesis without grand unification." *Phys. Lett. B* 174.1 (1986). DOI: 10.1016/0370-2693(86)91126-3.

[23] N. Aghanim et al. "Planck 2018 results: VI. Cosmological parameters." *Astronomy and Astrophysics* 641 (2020). DOI: 10.1051/0004-6361/201833910.

[24] M. Aker et al. "Direct neutrino-mass measurement with sub-electronvolt sensitivity." *Nature Physics* 18.2 (2022). DOI: 10.1038/s41567-021-01463-1.

[25] M. Agostini et al. "Probing Majorana neutrinos with double-β decay." *Science* 365.6460 (2019). DOI: 10.1126/science.aav8613.

[26] A. Gando et al. "Search for Majorana Neutrinos near the Inverted Mass Hierarchy Region with KamLAND-Zen." *Phys. Rev. Lett.* 117 (8 2016). DOI: 10.1103/PhysRevLett.117.082503.

[27] R. Arnold et al. "First results of the search of neutrinoless double beta decay with the NEMO 3 detector." *Phys. Rev. Lett.* 95 (18 2005). DOI: 10.1103/PhysRevLett.95.182302.

[28] R. Arnold et al. "Probing new physics models of neutrinoless double beta decay with SuperNEMO." *Eur. Phys. J. C* 70 (4 2010). DOI: 10.1140/epjc/s10052-010-1481-5.

[29] C. Alduino et al. "CUORE-0 detector: design, construction and operation." *JINST* 11.07 (2016). DOI: 10.1088/1748-0221/11/07/P07009.

[30] K. Alfonso et al. CUPID pre-CDR. 2019. arXiv: 1907.09376.

[31] M. Auger et al. "The EXO-200 detector, part I: detector design and construction." *JINST* 7.05 (2012). DOI: 10.1088/1748-0221/7/05/P05010.

[32] nEXO Collaboration et al. nEXO Pre-Conceptual Design Report. 2018. arXiv: 1805.11142.

[33] H. V. Klapdor-Kleingrothaus et al. "Latest Results from the Heidelberg-Moscow Double Beta Decay Experiment." *Eur. Phys. J A* 12 (2001). DOI: 10.1007/s100500170022.

[34] H. V. Klapdor-Kleingrothaus et al. "Search for neutrinoless double beta decay with enriched ^{76}Ge in Gran Sasso 1990-2003." *Phys. Lett. B* 586.3 (2004). DOI: 10.1016/j.physletb.2004.02.025.

[35] C. E. Aalseth et al. "Comment on "Evidence for Neutrinoless Double Beta Decay"." *Modern Phys. Lett. A* (2002). DOI: 10.1142/S0217732302007715.

[36] V. Guiseppe et al. "The MAJORANA neutrinoless double-beta decay experiment." IEEE, 2008. DOI: 10.1109/NSSMIC.2008.4774740.

[37] K. H. Ackermann et al. "The GERDA experiment for the search of $0\nu\beta\beta$ decay in ^{76}Ge." *Eur. Phys. J. C* 73.2330 (2013). DOI: 10.1140/epjc/s10052-013-2330-0.

[38] F. T. Avignone et al. "Ge Detectors and $0\nu\beta\beta$: The Search for Double Beta Decay with Germanium Detectors: Past, Present and Future." *Frontiers in Physics* 7 (2019). DOI: 10.3389/fphy.2019.00006.

[39] M. Agostini et al. "Final Results of GERDA on the Search for Neutrinoless Double-β Decay." *Phys. Rev. Lett.* 125.25 (2020). DOI: 10.1103/PhysRevLett.125.252502.

[40] I. J. Arnquist et al. "Final Result of the MAJORANA DEMONSTRATOR 's Search for Neutrinoless Double-β Decay in ^{76}Ge". 2022. arXiv: 2207.07638.

[41] "First Search for the Majorana Nature of Neutrinos in the Inverted Mass Ordering Region with KamLAND-Zen". 2022. arXiv: 2203.02139.

[42] G. Anton et al. "Search for Neutrinoless Double-Beta Decay with the Complete EXO-200 Dataset." *Phys. Rev. Lett.* 123.16 (2019). DOI: 10.1103/PhysRevLett.123.161802.

[43] I. Nutini et al. "New results from the CUORE experiment." *International Journal of Modern Physics A* 37.07 (2022). DOI: 10.1142/S0217751X22400140.

[44] N. Abgrall et al. "LEGEND-1000 Preconceptual Design Report". 2021. arXiv: 2107.11462.

[45] J. Detwiler. 2020. DOI: 10.5281/zenodo.3959552.

[46] K. Freund et al. "The performance of the Muon Veto of the GERDA experiment." *Eur. Phys. Jour. C* 76.5 (2016). DOI: 10.1140/epjc/s10052-016-4140-7.

[47] Photo courtesy of Kai Freund, GERDA collaboration.

[48] M. Agostini et al. "Upgrade for Phase II of the GERDA Experiment." *Eur. Phys. J. C* (2018). DOI: 10.1140/epjc/s10052-018-5812-2.

[49] C. E. Aalseth et al. "The Igex ^{76} Ge Neutrinoless Double-Beta Decay Experiment: Prospects for Next Generation Experiments." *Phys. Rev. D* 65.9 (2002). DOI: 10.1103/PhysRevD.65.092007.

[50] M. Agostini et al. "Results on neutrinoless double beta decay of ^{76}Ge from GERDA Phase I." *Phys. Rev. Lett.* 111.12 (2013). DOI: 10.1103/PhysRevLett.111.122503.

[51] M. Agostini et al. "Background-free search for neutrinoless double beta decay with GERDA Phase II." *Nature* 544.7648 (2017). DOI: 10.1038/nature21717.

[52] R. Cooper et al. "A novel HPGe detector for gamma-ray tracking and imaging." *Nucl. Instrum. Meth.* 665 (2011). DOI: 10.1016/j.nima.2011.10.008.

[53] A. Domula et al. "Pulse shape discrimination performance of Inverted Coaxial Ge detectors." *Nucl. Instrum. Meth.* 891 (2017). DOI: 10.1016/j.nima.2018.02.056.

[54] M Agostini et al. "First results of GERDA Phase II and consistency with background models." *J. Phys. Conference Series* 798.1 (2017). DOI: 10.1088/1742-6596/798/1/012106.

[55] M. Agostini et al. "Pulse shape discrimination for GERDA Phase I data." *Eur. Phys. J. C* 73.10 (2013). DOI: 10.1140/epjc/s10052-013-2583-7.

[56] M. Agostini et al. "GELATIO: a general framework for modular digital analysis of high-purity Ge detector signals." *JINST* 6.08 (2011). DOI: 10.1088/1748-0221/6/08/P08013.

[57] R. Brun et al. "ROOT — An object oriented data analysis framework." *Nucl. Instrum. Meth.* 389.1-2 (1997). DOI: 10.1016/S0168-9002(97)00048-X.

[58] M. Agostini et al. "The MGDO software library for data analysis in Ge neutrinoless double-beta decay experiments." *J. Phys. Conference Series* 375.4 (2011). DOI: 10.1088/1742-6596/375/1/042027.

[59] O. Schulz et al. "BAT.jl – A Julia-based tool for Bayesian inference." *SN Computer Science* 2.3 (2020). DOI: 10.1007/s42979-021-00626-4.

[60] N. Abgrall et al. "The Large Enriched Germanium Experiment for Neutrinoless Double Beta Decay (LEGEND)." *AIP Conference Proceedings* 1894 (2017). DOI: 10.1063/1.5007652.

[61] J. Hyvärinen et al. "Nuclear matrix elements for $o\nu\beta\beta$ decays with light or heavy Majorana-neutrino exchange." *Phys. Rev. C* 91.2 (2015). DOI: 10.1103/PhysRevC.91.024613.

[62] J. Barea et al. "$0\nu\beta\beta$ and $2\nu\beta\beta$ nuclear matrix elements in the interacting boson model with isospin restoration." *Phys. Rev. C* 91.3 (2015). DOI: 10.1103/PhysRevC.91.034304.

[63] L. Coraggio et al. "The calculation of the neutrinoless double-beta decay matrix element within the realistic shell model." *Phys. Rev. C* 101.4 (2020). DOI: 10.1103/PhysRevC.101.044315.

[64] J. Hardy et al. "Precise efficiency calibration of an HPGe detector: source measurements and Monte Carlo calculations with sub-percent precision." *Applied Radiation and Isotopes* 56.1-2 (2002). DOI: 10.1016/S0969-8043(01)00168-3.

[65] J. Boson et al. "A detailed investigation of HPGe detector response for improved Monte Carlo efficiency calculations." *Nucl. Instrum. Meth, A* 587.2-3 (2008). DOI: 10.1016/j.nima.2008.01.062.

[66] D. Budjáš et al. "Optimisation of the MC-model of a p-type Ge-spectrometer for the purpose of efficiency determination." *Applied Radiation and Isotopes* 67.5 (2009). DOI: 10.1016/j.apradiso.2009.01.015.

[67] B. Bruyneel et al. "Characterization of large volume HPGe detectors. Part I: Electron and hole mobility parameterization." *Nucl. Instrum. Meth, A* 569.3 (2006). DOI: 10.1016/j.nima.2006.08.130.

[68] E. Aguayo et al. "Characteristics of signals originating near the lithium-diffused N+ contact of high purity germanium p-type point contact detectors." *Nucl. Instrum. Meth, A* 701 (2013). DOI: 10.1016/j.nima.2012.11.004.

[69] Z. He. "Review of the Shockley-Ramo theorem and its application in semiconductor gamma-ray detectors." *Nucl. Instrum. Meth, A* 463.1-2 (2001). DOI: 10.1016/S0168-9002(01)00223-6.

[70] M. Agostini et al. Characterization of inverted coaxial ^{76}Ge detectors in GERDA for future double-β decay experiments. 2021. DOI: 10.1140/epjc/s10052-021-09184-8.

[71] EURIDICE (European Underground Research Infrastructure for Disposal of nuclear waste in Clay Environment). URL: http://www.euridice.be.

[72] E Andreotti et al. "HEROICA: an underground facility for the fast screening of germanium detectors." *JINST* 8.06 (2013). DOI: 10.1088/1748-0221/8/06/P06012.

[73] In 2016 Mirion Technologies Inc. acquired CANBERRA Industries Inc. URL: https://www.mirion.com/.

[74] M. Agostini et al. "Production, characterization and operation of ^{76}Ge enriched BEGe detectors in GERDA." *Eur. Phys. J. C* 75.39 (2014). DOI: 10.1140/epjc/s10052-014-3253-0.

[75] ^{133}Ba. URL: http://www.nucleide.org/DDEP_WG/Nuclides/Ba-133_tables.pdf.

[76] ^{241}Am. URL: http://www.nucleide.org/DDEP_WG/Nuclides/Am-241_tables.pdf.

[77] ^{260}Co. URL: http://www.nucleide.org/DDEP_WG/Nuclides/Co-60_tables.pdf.

[78] ^{228}Th. URL: http://www.nucleide.org/DDEP_WG/Nuclides/Th-228_tables.pdf.

[79] Y. Kermaidic and M. Redchuck. LEGEND Internal Documentation.

[80] B. Lowe. "Measurements of Fano factors in silicon and germanium in the low-energy X-ray region." *Nucl. Instrum. Meth* 399.2-3 (1997). DOI: 10.1016/S0168-9002(97)00965-0.

[81] B. Lehnert. "Search for $2\nu\beta\beta$ Excited State Transitions and HPGe Characterization for Surface Events in GERDA Phase II." PhD thesis. 2016.

[82] G. Marshall, S. Sullivan, A. Alexander and M. Agostini. LEGEND Internal Documentation.

[83] G4simple. URL: https://github.com/legend-exp/g4simple.

[84] legend-g4simple-simulation. URL: https://github.com/legend-exp/legend-g4simple-simulation.

[85] A. Alexander, personal communication.

[86] M. Miloradovic. "Characterisation of Inverted Coaxial Detectors and Calibration Source Production for the GERDA experiment." PhD thesis. 2020.

[87] L. Lyons et al. "How to combine correlated estimates of a single physical quantity." *Nucl. Instrum. Meth., A* 270.1 (1988). DOI: 10.1016/0168-9002(88)90018-6.

[88] S. Hauf et al. "Validation of Geant4-based radioactive decay simulation." *IEEE Transactions on Nuclear Science* 60.4 (2013). DOI: 10.1109/TNS.2013.2271047.

[89] G. A. Cirrone et al. "Validation of the Geant4 electromagnetic photon cross-sections for elements and compounds." *Nucl. Instrum. Meth, A* 618.1-3 (2010). DOI: 10.1016/j.nima.2010.02.112.

[90] Private communication of LEGEND with Mirion.

[91] GERDA Internal Documentation.

[92] M. B. Heider. "Performance and stability tests of bare high purity germanium detectors in liquid argon for the GERDA experiment." PhD thesis. 2009.

[93] M. Agostini et al. "Characterization of 30 ^{76}Ge enriched Broad Energy Ge detectors for GERDA Phase II." *Eur. Phys. J. C* 79.11 (2019). DOI: 10.1140/epjc/s10052-019-7353-8.

[94] J. Kostensalo et al. "Spectral shapes of forbidden argon β decays as background component for rare-event searches." *J. Phys. G* 45.2 (2018). DOI: 10.1088/1361-6471/aa958e.

[95] R. Saldanha et al. "Cosmogenic production of ^{39}Ar and ^{37}Ar in argon." *Phys. Rev. C* 100.2 (2019). DOI: 10.1103/PhysRevC.100.024608.

[96] J. Calvo et al. "Backgrounds and pulse shape discrimination in the ArDM liquid argon TPC." *JCAP* 12 (2018). DOI: 10.1088/1475-7516/2018/12/011.

[97] P. Benetti et al. "Measurement of the specific activity of ar-39 in natural argon." *Nucl. Instrum. Meth. A* 574 (2007). DOI: 10.1016/j.nima.2007.01.106.

[98] M. G. Dunford. "A Search for the Neutrinoles Double Electron Capture of ^{36}Ar and a Measurement of the Specific Activity of ^{39}Ar in Atmospheric Argon with the DEAP-3600 Detector." PhD thesis. 2018.

[99] M. Boswell et al. "MaGe-a geant4-based monte carlo application framework for low-background Germanium experiments." *IEEE Transactions on Nuclear Science* 58.3 (2011). DOI: 10.1109/TNS.2011.2144619.

[100] M. Agostini et al. "Modeling of GERDA Phase II data." *J. High Energy Phys.* 2020.3 (2019). DOI: 10.1007/JHEP03(2020)139.

[101] R. Ajaj et al. "Electromagnetic Backgrounds and Potassium-42 Activity in the DEAP-3600 Dark Matter Detector." *Phys. Rev. D* 100.7 (2019). DOI: 10.1103/PhysRevD.100.072009.

[102] G. Cowan et al. "Asymptotic formulae for likelihood-based tests of new physics." *Eur. Phys. J. C* 71.2 (2010). DOI: 10.1140/epjc/s10052-011-1554-0.

[103] P. A. Zyla et al. "Review of Particle Physics." *PTEP* 2020.8 (2020). DOI: 10.1093/ptep/ptaa104.

[104] S. Algeri et al. "Searching for new phenomena with profile likelihood ratio tests." *Nature Reviews Physics* 2.5 (2020). DOI: 10.1038/s42254-020-0169-5.

[105] Geant4. URL: https://geant-val.cern.ch/.

[106] L. Pandola, personal communication.

[107] R. Hiller. GERDA Internal Documenation.

[108] T. Comellato, B. Lehnert, personal communication.

[109] E. Bossio. "Beyond the Standard Model physics searches with double-beta decays." PhD thesis. 2022.

[110] A. Vasenko et al. "New results in the ITEP/YePI double beta-decay experiment with enriched germanium detectors." *Modern Physics Lett. A* 05.17 (1990). DOI: 10.1142/s0217732390001475.

[111] H. S. Miley et al. "Suggestive evidence for the two-neutrino double-decay of Ge76." *Phys. Rev. Lett.* 65.25 (1990). DOI: 10.1103/PhysRevLett.65.3092.

[112] F. T. Avignone et al. "Confirmation of the observation of 2 $\nu\beta\beta$ decay of ^{76}Ge." *Phys. Lett. B* 256.3-4 (1991). DOI: 10.1016/0370-2693(91)91810-I.

[113] F. T. Avignone. "Double-beta decay: Some recent results and developments." *Progress in Particle and Nuclear Physics* 32.C (1994). DOI: 10.1016/0146-6410(94)90022-1.

[114] M. Günther et al. "Heidelberg-Moscow $\beta\beta$ experiment Ge-76: Full setup with five detectors." *Phys. Rev. D* 55.1 (1996). DOI: 10.1103/PhysRevD.55.54.

[115] H. V. Klapdor-Kleingrothaus et al. "Latest Results from the Heidelberg-Moscow Double Beta Decay Experiment." *Eur. Phys. J. A* 12.2 (2001). DOI: 10.1007/s100500170022.

[116] A. Morales. "Review on Double Beta Decay Experiments and Comparison with Theory." *Nucl. Phys. B* 77.1-3 (1998). DOI: 10.1016/S0920-5632(99)00440-5.

[117] C. Dörr et al. "New Monte-Carlo simulation of the HEIDELBERG-MOSCOW double beta decay experiment." *Nucl. Instrum. Meth, A* 513.3 (2003). DOI: 10.1016/j.nima.2003.07.018.

[118] A. M. Bakalyarov et al. "Results of the experiment on investigation of Germanium-76 double beta decay. Experimental data of Heidelberg-Moscow collaboration November 1995 - August 2001". 2003. arXiv: http://arxiv.org/abs/hep-ex/0309016.

[119] M. Agostini et al. "Measurement of the half-life of the two-neutrino double beta decay of ^{76}Ge with the Gerda experiment." *J. Phys. G* 40.3 (2012). DOI: 10.1088/0954-3899/40/3/035110.

[120] M. Agostini et al. "Results on $\beta\beta$ decay with emission of two neutrinos or Majorons in ^{76}Ge from GERDA Phase I." *Eur. Phys. J. C* 75.9 (2015). DOI: 10.1140/epjc/s10052-015-3627-y.

[121] XCOM: Photon Cross Sections Database. URL: http://www.nist.gov/pml/data/xcom/.

ACKNOWLEDGEMENTS

The success of these three years would not have been possible without the guidance and collaboration of several people.

I owe my deepest gratitude to Riccardo Brugnera, my mentor; your advice and support were essential to growing and becoming a better physicist. Thank you for the time you dedicated to me, you always gave importance to my work contributing with constructive criticism. Thank you for the opportunities you offered me to share and increase my knowledge by working with students and attending schools, conferences, workshops, even during the difficult time of COVID. I would like to thank Alberto Garfagnini for welcoming me to this outstanding research group at the time of my master thesis, and your kind and unlimited support was also crucial for this thesis work. I consider myself very lucky to have met such a supportive research group and very honored to be part of it.

Thank you, Katharina von Sturm and Luigi Pertoldi, for your continuous help and stimulating exchanges of ideas; working with you was a source of inspiration and motivation. Thank you, Abi Alexander, for the great job we did together for the ICPC characterization and for reminding me that we really did a great job. Thank you, Yoann Kermaidic and Bjoern Lehnert, your guidance and fruitful discussions were fundamental to starting the characterization work and pursuing new ideas. Thank you Tommaso Comellato and Elisabetta Bossio for collaborating on the work presented in the final chapter of this thesis.

Finally, thank you, Roberto and Veronica, for your constant unconditional support for the realization of this thesis.